Department of Applied Geology

The Evolution of the Metamorphic Series in the NW Fujian Province, the NE Cathaysia Block, and the Significance in the Reconstruction of Precambrian Supercontinents

Wen Zeng

This thesis is presented for the Degree of
Doctor of Philosophy
of
Curtin University of Technology

October 2010

DECLARATION

According to the Cooperative Agreement on Jointly Supervised PhD Awards by China University of Geosciences (Wuhan) and Curtin University of Technology, this thesis is to be sent to both universities.

To the best of my knowledge and belief this thesis contains no material previously published by any other person except where due acknowledgement has been made. This thesis contains no material which has been accepted for the award of any other degree or diploma in any university

Signature: Wen Zeng

Date: October 20, 2010

ABSTRACT

This thesis focuses on the Paleoproterozoic to Late Paleozoic basement evolution of the metamorphic rocks scattered in the NW Fujian Province, the NE Cathaysia Block the southeastern area of South China. Field observation, systematic sampling and petrographic investigation combined with of whole rock geochemistry, zircon U-Pb, Lu-Hf isotopes, trace elements, amphibole and biotite $^{40}Ar/^{39}Ar$ analyses and mineral chemistry study were applied in this project to determine the nature, ages and relations of the leucosomes, felsic paragneiss and mafic metamorphic rocks in study area and their implications to the reconstruction of the Precambrian Rodina Supercontinent.

Following conclusions are made:

1. Based on this study, according to their metamorphism and deformation characteristics, the metamorphic rock series in the study area can be divided into two types, moderately to strongly metamorphosed rock series that experienced ductile deformation and moderately metamorphosed rock series that have experienced ductile deformations. New La-ICPMS U-Pb zircon ages presented here and in previous study suggest that the original litho-stratigraphy should be abandoned and the terminology “Complex” should be used instead of “Group” and “Formation” for the high grade metamorphic rock series in northwestern Fujian, where the protoliths were strongly reworked by Early Paleozoic tectono-thermal events.

2. Obvious zircon U-Pb age peaks of ~1800 Ma suggest that the protoliths of the Cathaysia Block be comparable to the basements of North America rather than those of Eastern India and East Antarctica. Although the peaks of ~1800 Ma are also present in Western Australia, their $^{176}Hf/^{177}Hf$ ratios (0.280706 - 0.281510) are apparently lower than those of zircons from SW Cathaysia

(0.281515 - 0.282098) and from this study (0.281232 - 0.282213, NE Cathaysia). Besides, detrital zircons in Cathaysia and NW Yangtze indicate significant juvenile input during Paleo- to Mesoproterozoic according to the zircon Hf isotopes, which are distinctly different from Western Australia. These evidences suggest that the basement of the Cathaysia share similarities with that of North America, lending support for the Rodinia configuration proposed by Li et al. (2008), in which Cathaysia was next to western Laurentia before and during the late Mesoproterozoic assembly of Rodinia.

3. The protoliths of the felsic paragneiss in the NW Fujian area are immature sediments, consisting of greywacke, arkose and lithic arenite compositions. The significant input of the paragneiss protolith was dominantly formed by several magmatic events during Neoproterozoic (820 ± 6 Ma, 780 ± 6 Ma, 776 ± 6 Ma, 758 ± 3 Ma, 740 ± 8 Ma and 722 ± 9 Ma), probably deposited not early than middle Neoproterozoic (~680 Ma). Many metamorphic rocks contain 0.99 - 0.72 Ga detrital magmatic zircons, which are interpreted as reflecting the tectono-thermal events related to the assembly and break-up of the Rodinia supercontinent during the Neoproterozoic.

4. In this study, new La-ICPMS U-Pb anatectic zircon data from the NW Fujian area suggest that the strong and widespread tectono-thermal events were related to the orogeny probably having started during the Middle Cambrian and lasted until the Middle Devonian, consisting of at least three main episodes (~473 Ma, ~445 Ma, ~423 Ma), with major orogeny events (including syn- to post-orogenic melting) constrained between ~473 Ma and ~407 Ma in the NE Cathaysia, and between ~468 Ma and ~415 Ma in the SW Cathaysia. The age peaks in the Cathaysia Block (ca. 488, 471, 455, 440 and 415 Ma) are within the age range of the Qinling-Tongbai-Dabie orogen during 512 - 406 Ma. This suggests a possible linkage or interaction of the two orogens.

5. The duration of the "Caledonian" orogeny in the NW Fujian area was no shorter than ~50 Myr, starting at ~473 Ma (~Early Ordovician) or earlier, and terminating at ~423 Ma (~Middle Silurian) or later. The "Caledonian" orogenic event in the Cathaysia Block was likely due to an intracontinental collision rather than the subduction of oceanic crust or arc-continental collision. Considering the inhomogeneous cooling paths for the Tianjingping, the Jiaoxi and Mayuan complexes, and different time restraint of the widespread anatectic and magmatic events occurred in different places, the "Caledonian" tectono-thermal events in the Cathaysia Block might vary between different segments of the orogen.

KEY WORDS: Zircon U-Pb age, Hf isotope, geochemistry, $^{40}Ar/^{39}Ar$ analyses, the Cathaysia Block, South China, Rodinia Supercontinent, Caledonian orogeny

ACKNOWLEDGMENTS

First and foremost, I would like to thank my parents for their parental guidance and financial support for my education.

Special thanks go to my supervisor Prof. Zengqiu Zhong for taking me on since I was an undergraduate student, and for his supervision and direction. His invaluable advice and assistance in how to systematically characterize a small yet complicated geological outcrop have contributed to my fascination and love for uncovering the evolution history of the Cathaysia Block. I also thank Prof. Hanwen Zhou and A/Prof. Li Zhang for providing thorough, detailed and constructive reviews on my papers. I am particularly grateful to my supervisor Prof. Zheng-Xiang Li of Curtin University of Technology for his great help in completing the thesis. I appreciate the time that he spent revising the text, talking through ideas and teaching me about geochronology and tectonics. Prof. Ian Fitzsimons and Prof. Simon Wilde are gratefully acknowledged for reviewing and commenting on my writing of both the research proposal and final thesis chapters.

I would like to extend my thanks to Xinqian Lv and Chunzhong Li, who provided warm hospitality and logistic support for the field work in northwestern Fujian Province.

Many people provided invaluable helps to my analytical work including advices, supports and helps with analytical procedures. They are sincerely thanked here. These include Yongsheng Liu, Zhaochu Hu, Haihong Chen, Keqing Zong, Chunlin Tong and Changgui Gao of the State Key Laboratory of Geological Processes and Mineral Resources, China University of Geosiences(Wuhan), Hujun Gong, Xiaoming Liu, Honglin Yuan, Mengning

Dai and Chunrong Diwu of the State Key Laboratory of Continental Dynamics, Northwest University, Pete Kinny, Alan Kennedy, Elaine Miller, Fred Jourdan, Chris Clark, Katy Evans, Hao Gao and Min Gao of Curtin University of Technology, and Janet Muhling of the University of Western Australia. I also thank Prof. Wu Yuanbao and Qiang Wang for the helpful discussions on U-Pb ages and Hf isotopes.

I wish to express my gratitude to fellow students Rui Liu, Hua Xiang and Song Jin who participated in the fieldwork and discussions, and assisted with sample preparation and some analyses. I also wish to thank my friends Jiawen Niu, Mahbubul Ameen, Jinrong Wang, Jing Wan, Min Peng, Jing Wang and Xiaochi Liu, Cheng Lei for giving me confidence and guiding me through at times of doubt and despair.

Financial support for the project came from the National Natural Science Foundation of China (grant No. 40372094), the Opening Foundation of State Key Laboratory of Continental Dynamics, Northwest University (grant No. 06LCD12), the Bureau of Land and Resources of Zhejiang Province (grant No. 2004005), the Australian Research Council (grant No. DP0770228) that supported the analytical costs in Australia, a Curtin University CIPRS scholarship, a top-up scholarship from Curtin's The Institute for Geoscience Research (TIGeR), and a visiting scholarship from the China Scholarship Council. All these support are gratefully acknowledged.

CONTENTS

LIST OF FIGURES AND TABLES

Chapter 1 Introduction

Continental blocks form through crustal growth events, terrane or continental collisions, and tectonic modifications. The Asian continent formed predominantly through progressive amalgamation of continental blocks during the Phanerozoic[2-3], and could become the centre of a future supercontinent Amasia[4]. The tectonic events leading to the formation of Asia are part of the global tectonic system, including the formation and breakup of supercontinents of Pangaea (ca. 320 - 170 Ma[5]), Gondwanaland (650 - 500 Ma assembly, 320 Ma merger in Pangea and 185 - 100 Ma breakup[6]), Rodinia (ca. 1100 - 750 Ma[7-13]), and Columbia (ca. 2.0 - 1.2 Ga[12, 14-19]). East Asia, as one of the tectonically most mobile areas in the current world, may thus hold more clues about the geological history of the dynamic Earth.

East Asia contains three major Precambrian cratonic blocks, the North China, Tarim and the South China Blocks. They and other various allochthonous crustal fragments of East Asia have been brought into close juxtaposition by geological convergent plate tectonic processes. The South China Block, which is the largest one of all East Asian blocks and has played a key role during the amalgamation and evolution of continental Southeast Asia, could probably maintain abundant geological records during its existence (Figure 1.1).

This thesis focuses on the Paleoproterozoic to Late Mesozoic basement evolution of the metamorphic rocks scattered in the northwestern Fujian Province, southeastern area of South China (116.1° - 120.4° E, 23.8° - 28.3° N, Figure 1.2). The Province is bordered by Zhejiang Province to the north and by Jiangxi and Guangdong Provinces to the west. And to the south-east of the Province is the East China Sea.

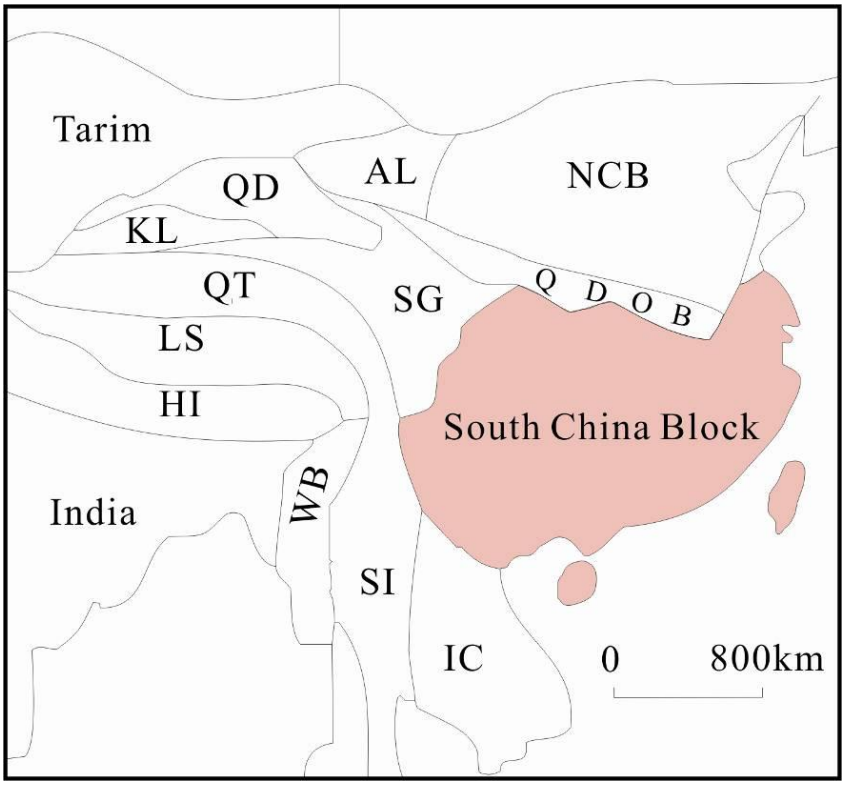

Figure 1.1 A schematic map showing the major tectonic units in East Asia

AL, Alashan Terrane; NCB, North China Block; HI, Himalaya; IC, Indochina Block; KL, Kunlun Terrane; LS, Lhasa Block; QD, Qaidam Terrane; QDOB, Qinling-Dabie Orogenic Belt; QT, Qiangtang; SI, Sibumasu Block; SG, Songpan-Ganzi Accretionary Complex; WB, West Burma; Modified after [3].

Figure 1.2 Location of the study area in Fujian province, south-east China.

§ 1.1 A summary of major tectonic events of Yangtze and Cathaysia blocks, South China

The South China Block is bounded to the north by the Qinling-Dabie orogenic belt, to the northwest the Longmenshan Fault, to the southwest the Red River Fault, and to the southeast the continental slope of the East and the South China Seas (Figure 1.3). It is a composite terrane with Yangtze Block accepted as the northwestern portion. However, the composition of the southeastern portion of South China Block still remains controversial.

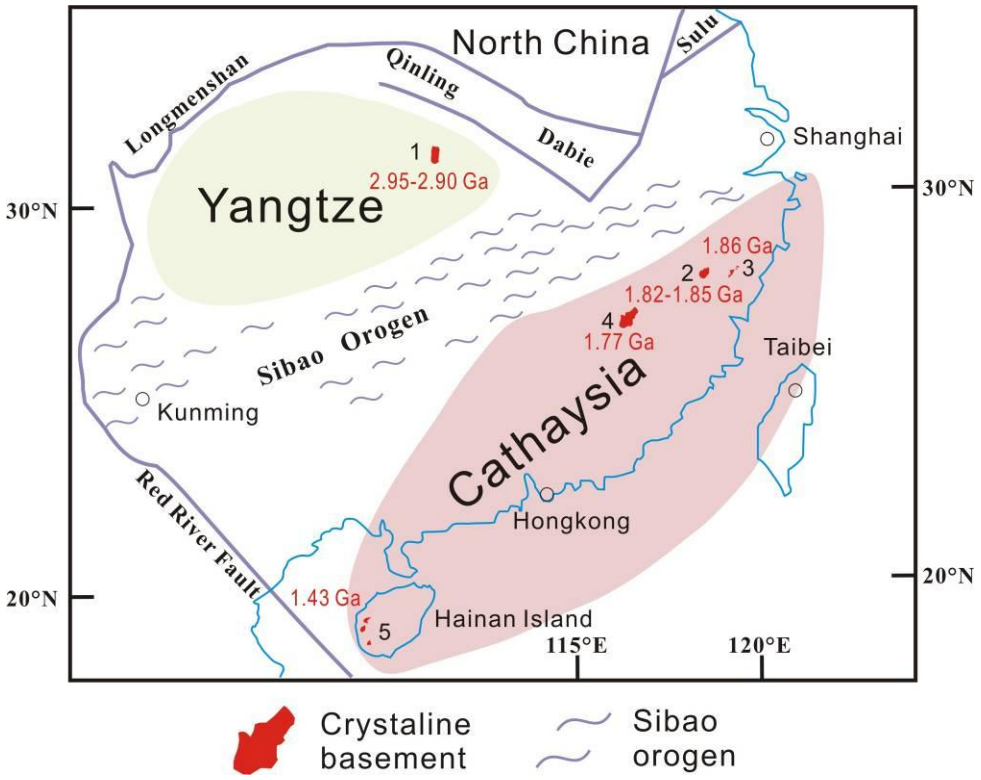

Figure 1.3 Tectonic framework of the South China Block

1-Kongling complex; 2-Danzhu granitic gneiss; 3-Sanzhishu granitic gneiss; 4-Tianjingping amphibolites; 5-Baoban complex (modified after [20]).

Grabau[21] firstly suggested that the metamorphic rock series widespread in southeastern South China overlain unconformably by late Palaeozoic strata formed from Archaean to Proterozoic, and named the coastal region as the "Cathaysia Paleocontinent", which has held worldwide geologists" interests since the 1980s. Alternatively, some authors[22-23] suggested that the southeastern South China Block be a Caledonian fold belt developed over a miogeosyncline, due to the strong imprint of the Ordovician-Silurian orogenesis on thick sedimentary-volcanic successions in the region. Hsü et al.[24-25] proposed a coastal terrane called Huanan Block being

separated from Yangtze by a Mesozoic suture, recognizing the widespread Mesozoic thrusting in southeastern South China. With a new round of investigations being carried out since the 1990s, more systematic and reliable geochronology, geochemistry, and basin history data have been collected to revise the tectonic models. The "Cathaysia Block" has presently been referred to as the description of the coastal region of the southeastern South China, probably including part of the continent "sinking" in the East and South China seas (Figure 1.3), other than a concept of the paleocontinent. Furthermore, a Neoproterozoic (Grenville) age suture named the Sibao Orogen was recognized between the Yangtze and Cathaysia terranes[26-27] (Figure 1.3), considering no reliable record for active margins in interior continent since the end of the Neoproterozoic and coherent distribution of sedimentary facies in South China across the proposed Mesozoic sutures since at least the Devonian[28].

A time-space diagram (Figure 1.4) is presented to illustrate the major tectonic events up to Late Mesozoic that shaped the South China Block as we know it today.

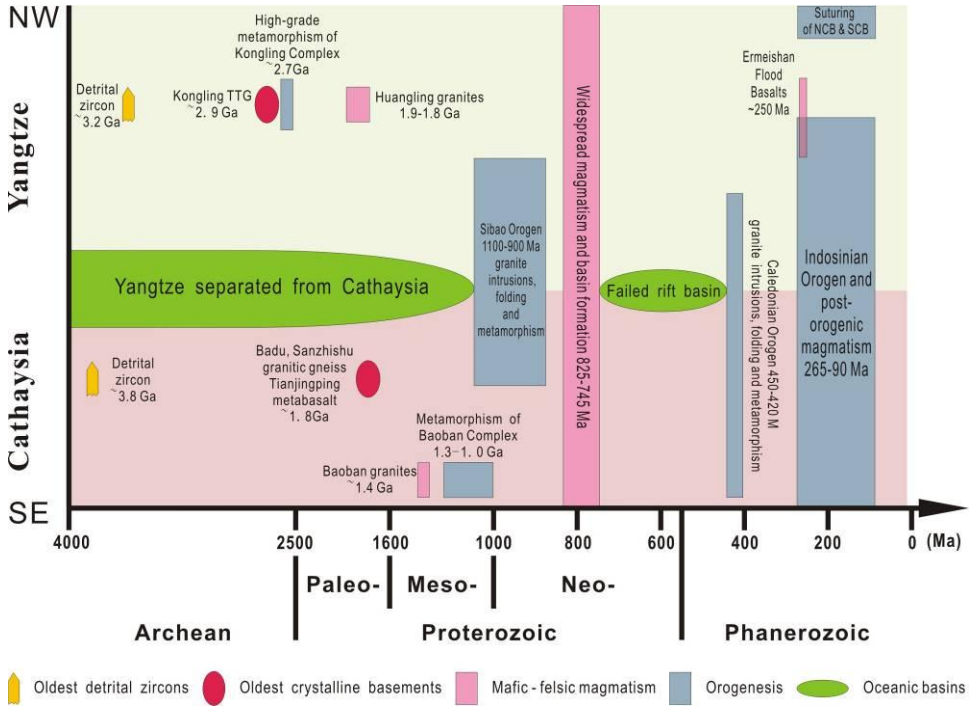

Figure 1.4 A schematic diagram illustrating the timing of the major tectonic events in South China up until late-Mesozoic.

1.1.1 Basement compositions formed before 1.0 Ga

The Yangtze Block is widely accepted as a coherent craton with the presence of an old core consisting of trondhjemitic gneiss and amphibolite in Kongling area of its

northern part (1 in Fig 1.3), which yielded SHRIMP U-Pb magmatic zircon ages of ca. 2.95 - 2.90 Ga[29-31] and experienced ca. 2.75 Ga high-grade metamorphism, and 1.9 - 1.8 Ga granitic intrusions[29]. Some older detrital zircons obtained from the pelite are dated between 3.28 and 2.87 Ma[29]. It may consist of Archaean basement widespread beneath Proterozoic upper-crustal rocks[31].

Pre-Neoproterozoic aged rocks are rarely found in the Cathaysia Block. Achaean ages from Cathaysia are only recorded in inherited zircon cores and detrital zircons, and there is still no report of Achaean rocks hitherto. SHRIMP U–Pb geochronology studies on detrital zircons shows minor Eoarchaean (ca. 3.8 Ga), Paleo- to Mesoarchaean (3.3 - 3.0 Ga) from late Neoproterozoic sediments in the Nanling-Yunkai area[32] and the oldest detrital zircons are ca. 3.8 Ga in the Wuyishan area[33]. And the oldest known crystalline rocks are recognized in the northeastern Cathaysia, consisting of the ca. 1.8 Ga Danzhu[20] (2 in Figure 1.3) and Sanzhishu[34] (3 in Figure 1.3) granitic gneisses in southwestern Zhejiang Province, and the ca. 1.8 Ga Tiajingping metabasalts which has experienced amphibolite facies metamorphism in northwestern Fujian Province (4 in Figure 1.3[35]). In addition, granodiorites in the Baoban Complex are dated at ca. 1.43 Ga in the Hainan Island, southern Cathaysia (5 in Figure 1.3[27, 36]). The high-grade (upper amphibolite facies) metamorphic basement rocks in the northeastern Cathaysia were regarded as part of the Precambrian crystalline basement of Cathaysia. However, recent geochronological work shows these rock series are probably Neoproterozoic to early Paleozoic in age[33, 37] (this study see description and discussion in Chapter 5 and 6).

1.1.2 The Meso-Neoproterozoic events and the relationship with Rodinia

The Meso-Neoproterozoic was the most active period of continental growth for the South China Block[27-28, 38]. The rocks during Late Meso- and Early Neoproterozoic are commonly metamorphosed to greenschist facies, and are tightly folded and eroded prior to the deposition of volcaniclastic rocks younger than 820 Ma. In eastern Sibao Orogen, the Shuangxiwu arc volcanic rocks yielded SHRIMP U-Pb zircon age of ca. 900 Ma[20]. Adakitic granite in Gan-Wan arc/ophiolitic belt was dated ca. 970 Ma, indicating an active subduction then[39-40]. Amphibolite from blueschists from the same area gave an Ar/Ar age of ca. 900 Ma[20]. In the western Sibao Orogen, granitic gneiss found in Sichuan Province was dated using SHRIMP U-Pb zircion method at 1007±14 Ma and siliciclastic rocks at the same locality have their youngest detrital zircon grains dated at ca. 1000 Ma. And the younger age limit for the orogeny is probably suggested by a 857±13 Ma granodiorite in southern Sichuan Province. In this case, the formation of the Sibao Orogen from ca 1000 -

900 Ma was caused by the collision of the Yangtze and Cathaysia blocs, which made the South China Block come to its present size and shape.

Neoproterozoic anorogenic magmatic rocks dated at ca. 830 - 750 Ma are widespread in South China[20, 41-47] including pre-rifting granitoids and rift-related volcanic rocks and mafic-ultramafic sills/dykes widespread in the Yangtze craton. Mineralogical, petrographic and geochemical characteristics of the granitoids indicate that they are S-type and I-type. However, they were formed during a short period of 825 - 820 Ma, such as the 819 ± 8 Ma Ershan K-rich granitoids in Yunnan, the 819 ± 9 Ma Jiuling cordierite-bearing granitoids in northern Jiangxi, the 823 ± 8 Ma Xuncun cordierite-bearing granitoids in southern Anhui[45], the 819 ± 8 Ma Bendong Granite, the 824 ± 4 Ma Granite and the 826 ± 10 Ma Sanfang Granite in north Guangxi[43], and the 819 ± 7 Ma Huanling Pluton in Hubei Province[48] (Figure 1.5). And their Sm–Nd isotopic data suggest that all were generated by partial melting of various crustal rocks without appreciable involvement of new mantle-derived magmas[45]. The rift-related volcanic rocks include the 817 ± 5Ma Tiechuanshan bimodal basalte-dacite/rhyolite in Hannan area at the northwestern margin[47], the 803 ± 12 Ma Suxiong bimodal basalt-dacite/rhyolite in the western margin[44], and volcanic rocks along the southern to southeastern margin, such as the 819 ± 11 Ma Yingyangguan spilite-keratophyre[49], the 814 ± 12 Ma Changshuipu dacitic agglomerate[50], the 797 ± 11 Ma Hongchicun-Shangshu bimodal basalt-rhyolite[46], and the 818 ± 12 Ma Taoyuan bimodal basalt-rhyolite[51]. Besides, the rift-related mafic-ultramafic sills/dykes occurred both around and inside the Yangtze Block, including the 788 ± 2 Ma Jiabang dolerite sills in southeastern Guizhou[52], the 770 ± 3 Ma[53] /806 ± 3 Ma[20] Huangling mafic dike swarm in Hubei, and the 761 ± 8 Ma mafic-ultramafic dykes in north Guangxi[54].

A recent study on the Mamianshan rift-related bimodal volcanic rocks in northwestern Fujian area, Cathaysia Block, which are dominantly transitional to mildly alkaline basalts and subordinate alkaline rhyolite, give an eruption age of 818 ± 9 Ma.

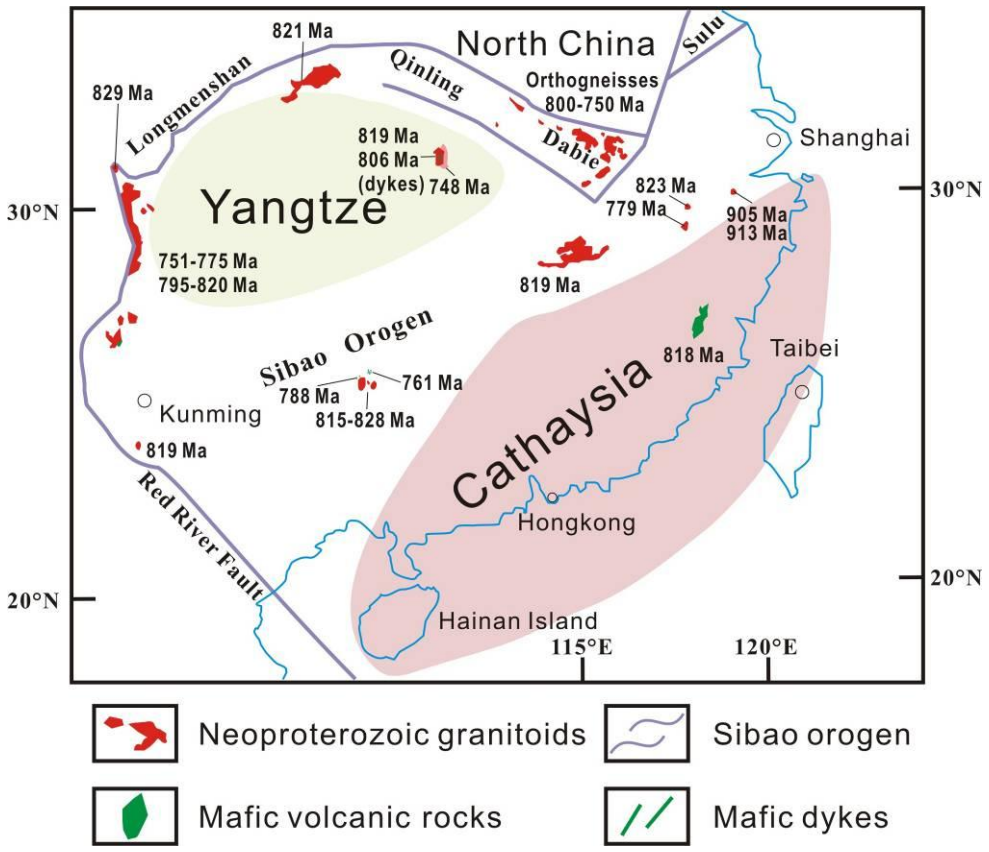

Figure 1.5 Simplified map showing the distribution of the Neoproterozoic granitoids in South China Block, modified after [20, 45].

The abundance of Meso-Neoproterozoic aged rocks in South China has led many geologists to examine its involvement in the formation and breakup of a late Mesoproterozoic supercontinent, firstly proposed by Valentine and Moores[55], later termed Rodinia[56], which was composed of almost all Precambrian cartons. The Grenville-aged or Grenvillian orogenic events occurred between 1300 Ma and 900 Ma all over the world, including Antarctica, Australia, Baltica, the southern margin of Laurentia, North and South China and plenty of other continents[7-9, 13, 57-59] (Figure 1.6). With the accumulation of the geological and paleomagnetic evidences, more and more authors have accepted the Rodinia hypothesis and proposed their continental reconstructions[7-13, 56-57, 59-61].

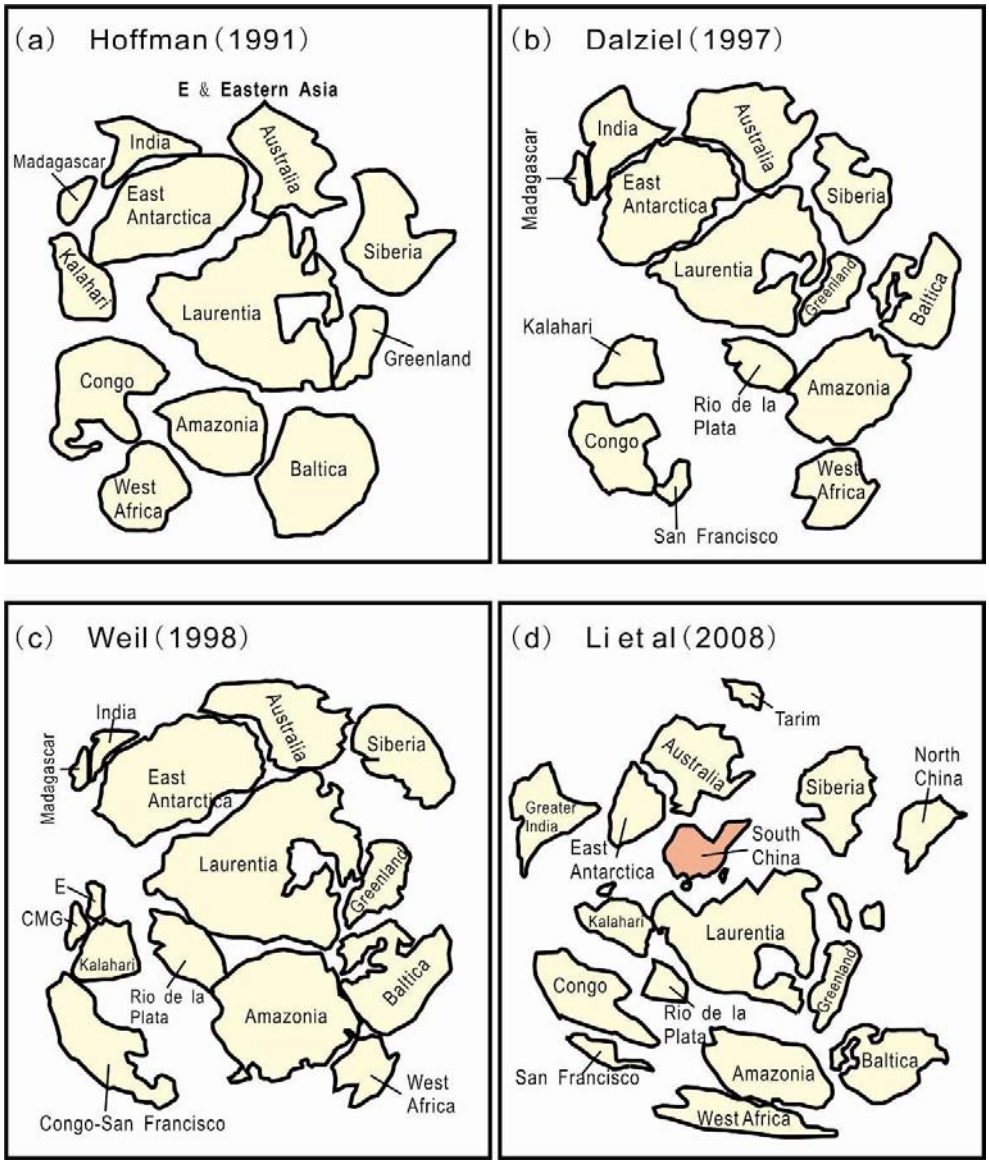

Figure 1.6 Paleogeographic reconstructions of Rodinia.

CMG, Coates Land-Maudheim-Grunehogna Province; E, Ellsworth-Whitmore Montain.

It is suggested that the fragmentation of Rodinia occurred in two distinct periods; the first one during 820 - 750 Ma and the second on between 600 and 550 Ma[10]. The 820-750 Ma event separated Australia from western Laurentia

The major magmatic and rifting events in the South China Block from late Mesoproterozoic to earliest Neoproterozoic (≥ 900 Ma) may reflect the dynamic changes in tectonic environment between the assembly of Rodinia, and breakup of the supercontinent during two phases of ca. 850 - 825 Ma and 750 - 700 Ma. Based on stratigraphic correlations, paleomagnetic and geochronology results Li et al.[27, 62] proposed South China was located in a central position between Australia-East Antarctica and Laurentia in Rodinia during the late Mesoproterozoic to Early Neoproterozoic in their “missing-link” model (Figure 1.7), in which the Cathaysia

Block is suggested to act as an extension of Laurentia from ca. 1800 Ma, having no connection between Australia-East Antarctica, Yangtze craton until 1100 - 900 Ma. This central position within Rodinia is also suggested as a site of rifting that led to the Neoproterozoic (ca. 820 - 750 Ma) break up of Rodinia[28, 63]. This reconstruction was supported by later paleomagnetic studies[11]. However, Jiang et al.[64] argued that the stratigraphic comparisons suggest that the SCB may have been linked to northwestern India in Neoproterozoic time and was probably separated from India and moved toward northwestern Australia in the early Cambria. Recently, paleomagnetic data have indicated that the SCB may have been connected with northwestern Australia and remote northeastern India during latest Neoproterzoic and early Paleozoic times[65]. Alternatively, Yu et al.[32] considered that the late Neoproterozoic sediments, from which ~3.8 Ga, 3.3 - 3.0 Ga, ~2.5 Ga, ~1.0 Ga and 0.70 - 0.54 Ga zircon populations were discovered, may have originated mainly from Eastern India-East Antarctica and thus suggested that the South China Block was linked with the Eastern India - East Antarctica continents in the Late Neoproterozoic (Figure 1.8). It seems that the location of the SCB relative to other microcontinents in Rodinia is still a contentious issue.

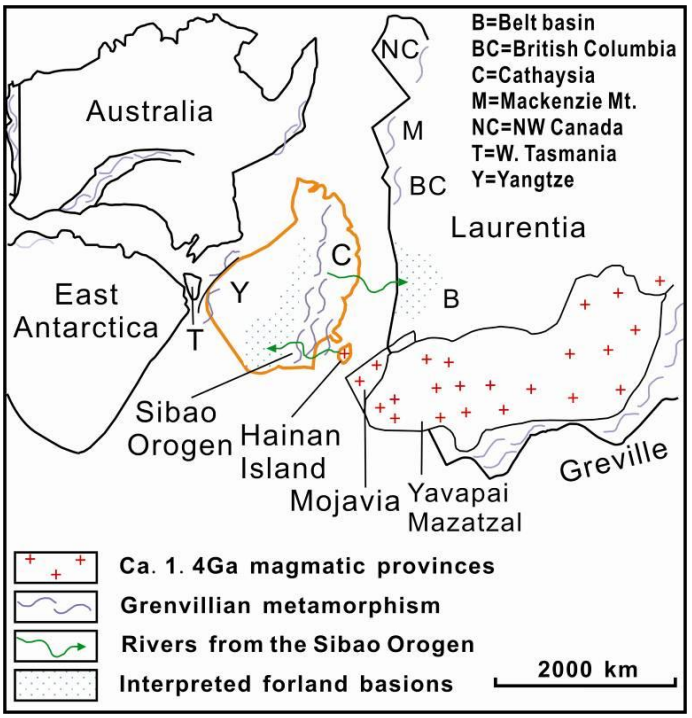

Figure 1.7 The "missing link" model for possible position of South China in Rodinia, modified after [27].

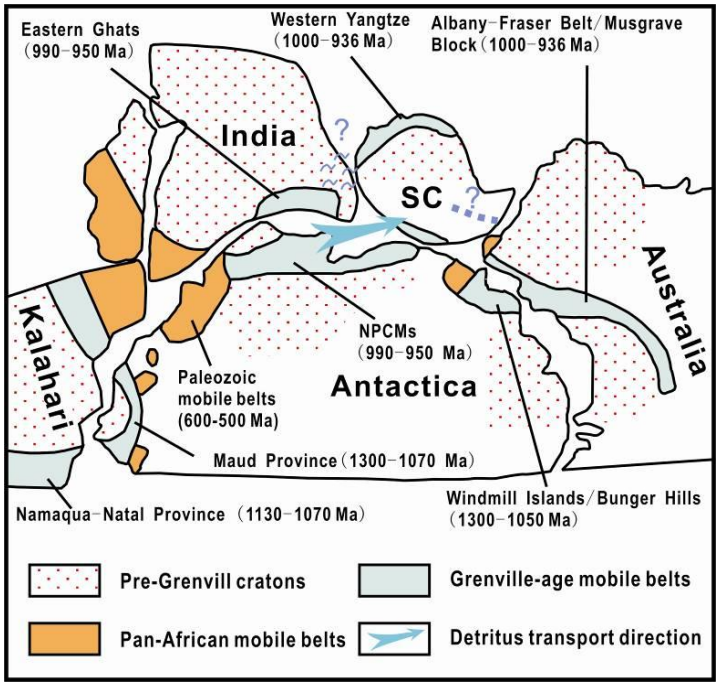

Figure 1.8 Paleoposition of the South China Block, modified after [32].

The heavy dotted line with "?" in the South China Block denotes a proposed Grenville belt; the wavy lines with "?" between India and SCB indicate possible connection between the Eastern Ghats in India and the western part of the Yangtze Block; SC, South China; NPCMs, northern Prince Charles Mountains.

However, because all these Neoproterozoic igneous rocks occurred mostly around the Yangtze Block, with some showing arc-like geochemical fetures, and a ~1.0 Ga ophiolite suite occurred in the southeastern Yangtze Block[66], Zhou et al.[67-70] consided that active continental margins existed around the Yangtze Block during the early Neoproterozoic, and the collision between the Yangtze and Cathaysia blocks did not start until ca. 800 Ma.

1.1.3 The Ordovician-Silurian "Caledonian" events and the relationship with Gandwanaland

It is suggested that continental rifting in South China ceased during ca 750 - 730 Ma[20], and the Nanhua Rift represented a failed rift from the late Neoproterozoic to earliest Palaeozoic[28]. These are supported by the sediments from Late Neoproterozoic to early Ordovician ages, which are dominantly carbonates, shales and some cherty units on the Yangtze side of the Nanhua Basin, whereas clastic marine deposits dominate the Cathaysia side of the basin. From ~450 Ma to ~400 Ma, the area of the Cathaysia Block was inverted into a Caledonian fold-thrust belt, with the Nanhua basin in front of it[23-25, 71] (Figure 1.9).

It is proposed that the Caledonian Orogeny represents the closure of a large

inter-continental ocean basin[72], requiring the consumption of considerable oceanic crust. However, although it is unclear if any oceanic crust was developed in the Nanhua Basin, there is not any post-Neoproterozoic arc or ophiolitic complexes having been reported between the Yangtze and Cathaysia blocks so far. Besides, an open ocean environment is not supported by the Sinian to early Paleozoic sedimentary facies in this region[72]. Recent study shows the Nanhua Basin had evolved into a foreland-basin similar to the Appalachian basin, based on the investigation of the Kbentonite, black-shale, and associated flysch deposition within South China near the Ordovician–Silurian transition, which can be regarded as distal, foreland responses to the continuous northwestward collision and accretion of the Cathaysia Block to the Yangtze Block[73] (Figure 1.9).

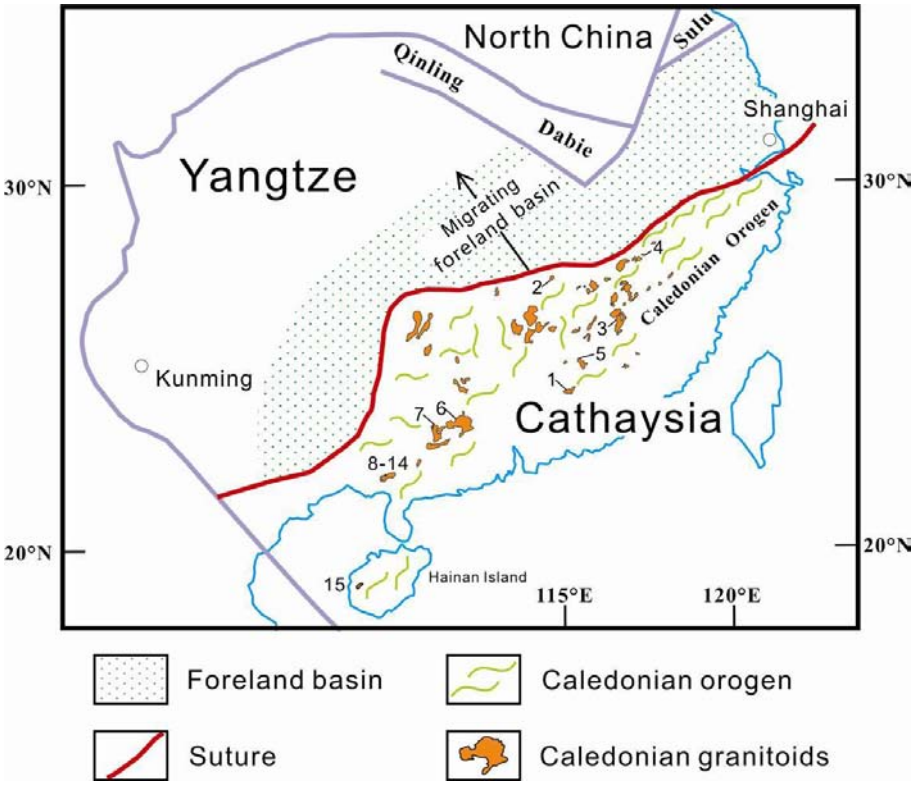

Figure 1.9 Schematic diagram showing the location of the Caledonian Orogen, related granitoids and foreland basin in South China, modified after [20, 73-74]; Numbers represent the dated granitoids listed in Table 1.1.

The Caledonian Orogeny in South China during the Early-Middle Paleozoic (542.0 - 359.2 Ma) was a strong tectonothermal event accompanied by intensive folding and ductile shearing deformation of the Sinian to early Paleozoic successions, the extensive granitic magmatism and the regional angular unconformity.

The thick Sinian to early Paleozoic sediments in the Cathaysia Block were generally involved into an intensive folding deformation and ductile slipping rheology including thrust and strike-slip deformation and were metamorphosed to

lower-greenschist facies. The peak period of deformation was during 420 Ma and 400 Ma[75]. At the same time, a violent granitic magmatism started all over the Cathaysia Block, forming numerous peraluminous S-type and rare I-type granites aging from 507 to 370 Ma[76-82]. The S-type granites formed a bit later (400 - 430 Ma) than the I-type (460 - 430 Ma, e.g. Cizhu granodiorite[79]; 4 in Figure1.9 and Table 1.1), and composed more than 90% of all the Caledonian granites, including both in-situ/semi-in-situ gneissic granite batholiths and homogeneous granite batholiths. Large-scale S-type granitoids were formed mainly by multiple intrusions (e.g. Wanyangshan-Zhuguangshan and Wugongshan complex granitic batholiths), mostly consisted of biotite monzinitic granite; whereas small-scale ones were formed once comprising granodiorites, monzonitic granites, quartz monzonitic granites and biotite granites (for detail information including the localities, ages and analytical methods of these granitoids, see Figure 1.9 and Table 1.1). Synchronously, migmatization of the Precambrian metamorphic rocks developed widely within the Cathaysia Block, e.g. ca. 470 Ma migmatic granite in the Wuyishan area[83], 394 - 449 Ma migmatites in Yunkai area[84], 447 Ma Tianjingping leucogranodiorite of migmatites in northwestern Fujian Province[85], 448 Ma Baiyunshan migmatic augen gneisse and 412 Ma Chendong nebulitic migmatitic granite near Guangzhou City[86]. Most of the Caledonian granites and migmatites exhibit low $\varepsilon_{Nd}(t)$ values of -18.4 to -2.1, high $(^{87}Sr/^{86}Sr)_i$ values of 0.7071 to 0.7287, and old Nd model ages very similar to those of the surrounding Precambrian metamorphic basement rocks. Hence they were mostly derived from partial melting of thickened continental crust[87].

After the violent granitic magmatism and migmatization, the whole South China Caledonian fold belt was overlain unconformably by the Late Devonian conglomerate and coarse sandstone, indicating the termination of folding and orogeny. From the Late Devonian, a united paleogeographic and sedimentary environment occurred really in the South China Block. Hence, the Ordovician-Silurian orogeny probably reflected the final phase of accretion between the Yangtze and the Cathaysia blocks.

From the global viewpoint, the tectonic evolution of South China during the Early-Middle Paleozoic has been marked by the break up and dispersion of Gondwanaland[88]. The main stable „„core“ of Lower Palaeozoic Gondwanaland[89] comprised a supercontinent including Africa, South America, Arabia, the Indian subcontinent, Antarctica and Australia (Figure. 1.10). Iberia and Armorica in the West, and South China and other terranes in the East are faunally contiguous to various parts of that core.

According to the faunal distribution, the biogeographic[2-3, 90] and the paleomagnetic

data[91], the South China Block had been located along the Great India - Australia region of the Gondwanaland margin during the Early-Middle Paleozoi. After the Early Devonian, South China was separated from Gondwanaland, and remained in a low latitude position thousands of kilometers away from the East Gondwanaland at the southern polar region[92], which are indicated by available biogeography[2-3], litho-facies and paleomagnetic[93-94] evidences.

The start of the Caledonian orogeny in South China may resulted from the major clockwise rotation of the Gondwanaland supercontinent, the opening of the Paleo-Tethys during Early to Middle Paleozoic and the closure of the late Neoproterozoic-Paleozoic Nanhua Rift basin which separated the Cathaysia and Yangtze blocks[95]. However, models for the formation of the orogen remain debeating[28].

Table 1.1 The zircon U-Pb dating data of Caledonian granitoids in the Cathaysia Block

No.	Locality	Rock	Age (Ma)	Method	Data Source
1	Guzhai	Granodiorite	507 ± 17	La-ICPMS	[76]
2	Wugongshan	Granodiorite	428 ± 1 - 462 ± 2	TIMS	[78]
3	Yiqian	Granite	445 ± 6	La-ICPMS	[79]
4	Cizhu	Granodiorite	432 ± 2	La-ICPMS	[79]
5	Sanbiao	Bt Granite	422 ± 11	La-ICPMS	[79]
6	Shidong	Bt Granite	461 ± 35	SHRIMP	[80]
7	Guangping	Bt Granite	444 ± 6	SHRIMP	[80]
8	Yunkai	Bt Monzonitic Granite	467 ± 10	SHRIMP	[81]
9	Yunkai	Granite	465 ± 10	SHRIMP	[81]
10	Yunkai	Charnockite	435 ± 11	SHRIMP	[81]
11	Yunkai	Gt-Bt Monzonitic Granite	413 ± 8	SHRIMP	[81]
12	Yunkai	Foliated Granite	441 ± 5	La-ICPMS	[82]
13	Yunkai	Granitic Gneiss	430 ± 5	La-ICPMS	[82]
14	Yunkai	Bt Orthogneiss	427 ± 4	La-ICPMS	[82]
15	Baoban	Anatectic Granite	370 ± 4	SHRIMP	[77]

§ 1.2 Previous Work in the NE Cathaysia Block

The Precambrian metamorphic basement rocks in the north were previously divided into two major units, Paleo-Mesoproterozoic unit and Neoproterozoic unit, due to the different metamorphic degrees and inaccurate dating data[96-97]. The rocks

experienced upper amphibolite facies metamorphism and migmatizaion were assigned to the Paleo-Mesoproterozoic unit including Tianjingping "Formation" and Mayuan "Group" in Fujian Province and Badu "Group" in Zhejiang Province, whereas others metamorphosed to greenschist-lower-aphibolite facies were attributed to the Neoproterozoic unit, composing Mamianshan and Wanquan "Group" in Fujian Province and Longquan "Group" in Zhejiang Province. Since the oldest known crystalline rocks were recognized in the Badu "Group" (1.8 Ga Danzhu[20] and Sanzhishu[34] orthogneisses) and the Tianjingping "Formaiton" (1.8 Ga metabasalts), they could be treated as Paleoproterozoic products. However, recent geochronology research for the metamorphic series in Fujian Province shows that the rocks in Mayan "Group" are Neoproterozic rift successions deposited not earlier than 800 Ma, and the Mamianshan and Wanquan "Groups" were formed during the Neoproterozoic from 751 Ma to 728 Ma[33]. Considering these rocks experienced strong metamorphism, deformation and anatexis, the original lithostratigraphy and the previous "Group" and "Formation" terminology should be abandoned. The names of each metamorphic unit hereinafter are referred to as "Complex".

Nd isotopic studies of many granitic and sedimentary rocks indicate that the Palaeoproterozoic (2.2 - 1.7 Ga) was an important period of formation and accretion of continental crust in the Cathaysia Block[98-100], main part of the Tianjingping Complex. The other suite is composed principally of fine-grained biotite gneiss and amphibolite, the protoliths of which are intermediate to felsic volcano-sedimentary rocks and basic volcanic rocks. They are poorly exposed, and mainly occur near Tianjingping, southwest of Jianning. A 2682 ± 148 Ma Sm-Nd whole-rock isochron age for amphibolite is the main evidence used to propose that the Tianjingping Formation formed in the Neoarchean[101]. However, Li[35] obtained a zircon age of 1766 ± 19 Ma from the same amphibolites and interpreted this as formation age for the Tianjingping Complex. The amphibolite is LREE-enriched with highly positive $\varepsilon_{Nd}(t)$ values and a mean crustal residence model age (T_{DM}) of 1.77 Ga[102]. The Mayuan Complex is widespread in Fujian area (Figure 1.10) and has been extensively modified by anatexis. The metamorphic temperature and pressure conditions were 570 - 680 °C and 4.3 - 7.0 kbar[103-104], or 590 - 625 °C and 4.2 - 4.5 kbar[105]. The Mamianshan and Wanquan Complexes in northwestern Fujian and the neighboring Longquan Group in southwestern Zhejiang, shows a northeast-trending distribution (Figure 1.10), which is roughly parallel to the Neoproterozoic Nanhua rift basin[63]. The Mamianshan Complex underwent intense deformation and was metamorphosed to upper-greenschist to lower-amphibolitefacies at pressures of 3 - 4.5 kbar and temperatures of 530 - 600 °C[104].

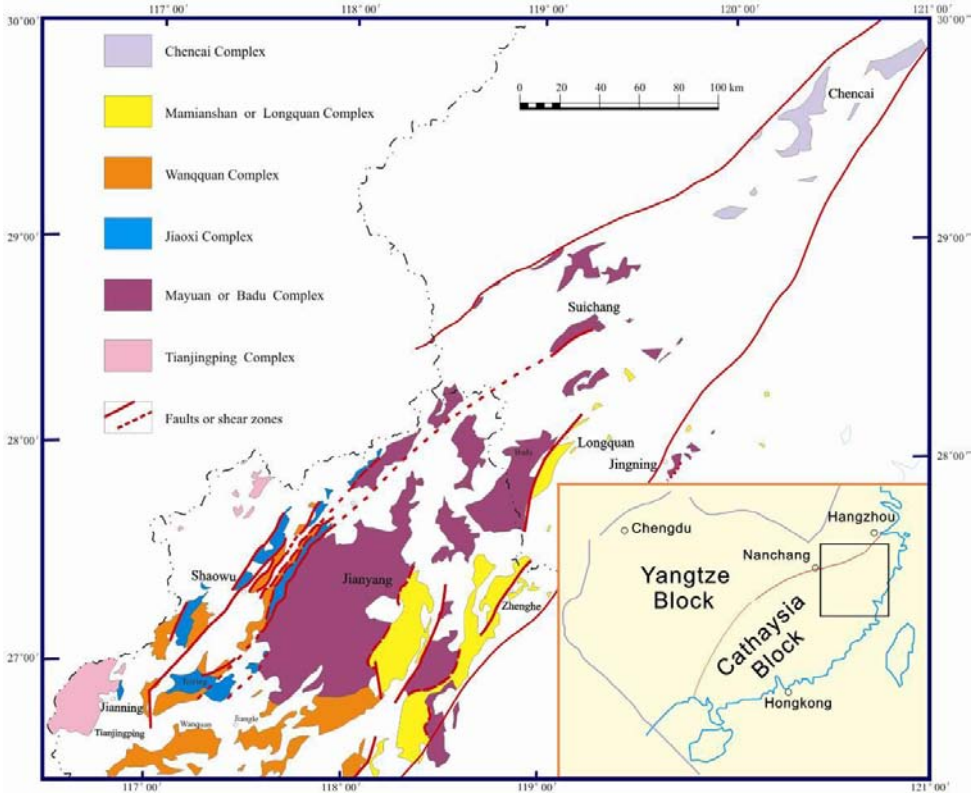

Figure 1.10 Simplified geologic map of the Precambrian metamorphic rocks in Fujian and Zhejiang Provices.

§ 1.3 Aims and Objectives

The metamorphic basement rocks of the Cathaysia Block were chosen as the research project because it may hold some key information for understanding the geodynamic evolution of a long duration from Paleoproterozoic to Late Mesozoic. These include the ~2.7 - ~1.8 Ga inherited zircons from leucogranite and metabasite that may be sourced from other continent (e.g. Laurentia[26-27], or India and East Antarctica[32]) during the evolvement of the Columbia Supercontinent, the ~1000 - ~700 Ma magmatic activities that were probably related to the assembly and breakup of Rodinia, the records of the magmatic metamorphism and anatexis extensively developed from ~500 Ma to ~430 Ma when it was located along the margin of Gondwanaland, and the metamorphic and resetting information from ~240 Ma to 150 Ma which may be caused by the closure of the Paleo-Tethys and the subduction of the Pacific plate during the assembly of Pangea.

The major objectives of this thesis are to:

1. Establish the T-t conditions of the metamorphic rocks and the lithosphere growth history of the major metamorphic complexes in northeastern Cathaysia Block, South China,
2. Propose a testable hypothesis on the basement evolution of the northeastern

Cathaysia Block,

3. Discuss the major tectonothermal events in the Paleozoic in relation to global tectonic evolution.

§ 1.4 Approaches

The methods employed during this project are outlined below:

- ✧ Structural and lithological mapping was carried out during three field seasons in Fujian and Zhejiang Provinces. Samples were collected from key areas for petrology, geochemistry and geochronology studies;
- ✧ The field data and published data were collated and presented in a GIS format to allow spatial analyses and map preparation;
- ✧ Whole rock geochemical analyses were performed on the gneisses, amphibloltes, and leocosomes;
- ✧ Geochronology research were carried out for U-Pb analyses of zircon, titanite, monazite and $^{40}Ar/^{39}Ar$ analyses of hornblende, biotite and muscovite;
- ✧ Hf isotopic analyses for zircon grains compiled with the trace element analyses;
- ✧ Mineral chemistry analyses for garnet, biotite, muscovite, hornblende, plagioclase, sillimanite, and monazite.

§ 1.5 Thesis Structure

An outline of each chapter is presented as follow:

Chapter 1, the introduction chapter (current chapter), presents a broad background about the historical geology of the South China building on precursors‟ work.

Chapter 2 provides an overview of regional geology based on the field observations and previous geochronology data in the study area.

Chapter 3 gives analytical background information regarding the methodology employed in this study.

Chapter 4 and 5, which form the main part of this thesis, focus on the whole rock geochemical characteristics, the geochronological framework, and the geochemical and Hf isotopic features of zircons, and the T-t paths establishment for two adjacent complex units, the Tianjingping Complex, the Jiaoxi and Mayuan complexes, the northeastern Cathaysia Block. The geochemistry analyses are based on an extensive investigation into various samples, consisting metabasite, metasedimentary rocks and

migmatites formed by anatexis. The geochronology data were obtained from different minerals, including zircon, monazite, titanite, hornblende and biotite. And the geochemical and Hf isotopic features of zircons record the lithosphere evolution history of the study area.

Chapter 6 uses all the data in combination to propose a testable hypothesis on the basement evolution of the northeastern Cathaysia Block, and to discuss the major tectonothermal events in Paleozoic in relation to global tectonic evolution.

Chapter 2 Regional geology and sampling

Precambrian metamorphic basement rocks in Fujian Province have a total exposure of about 15000 km^2, mainly in the north and northwestern part of the province, which has been subdivided into western and eastern regions according to different working teams (Figure 2.1). They are mostly layered metamorphic terranes, with the major protoliths being sedimentary and volcano-sedimentary rock series with scarcely exposed metamorphosed and deformed intrusions. The metamorphic rocks have previously been divided into the Archaean or Palaeoproterozoic Tianjingping "Formation", the Palaeoproterozoic Mayuan "Group", and the Neoproterozoic Wanquan "Group", Mamianshan "Group" and Jiaoxi "Formation". They are mostly not in direct contact, or in fault contact with each other[106] and their detailed features will be discussed later (Table 2.1, Figure 2.1).

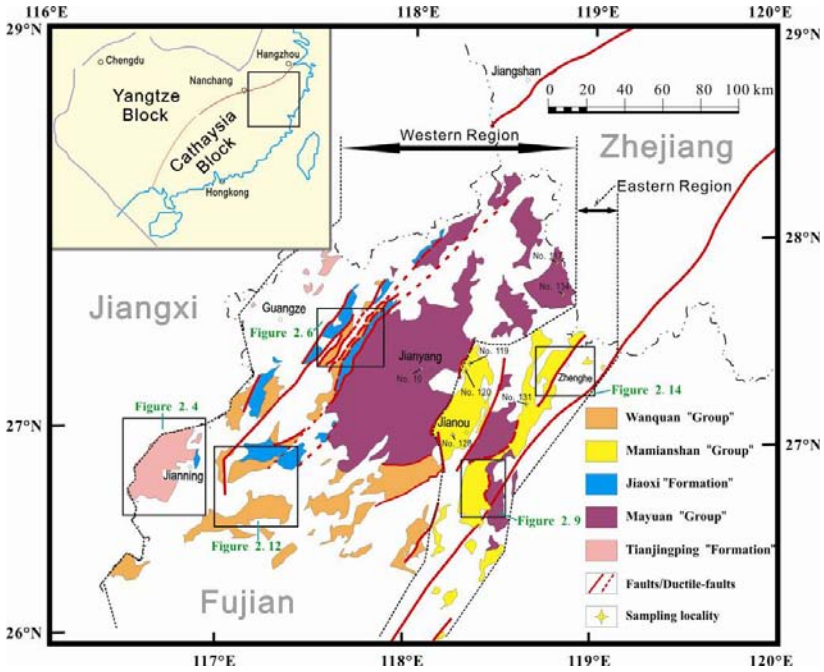

Figure 2.1 Geological sketch map of the northwest Fujian Province (modified after references [37, 106]; the boundary lines of western and eastern regions are not geological boundaries); Rock samples from the sampling localities are listed in APPENDIX A.

Table 2.1 A previous subdivision of Precambrian rocks in northwestern Fujian Province (modified after reference [106])

<table>
<tr><td colspan="2">Western Region</td><td colspan="2">Eastern Region</td></tr>
<tr><td rowspan="3">Wanquan “Group”</td><td>Xiafeng “Formation” 728 ± 8 Ma[33]</td><td rowspan="3">Mamianshan “Group”</td><td>Longbeixi “Formation”</td></tr>
<tr><td>Huangtan “Formation”</td><td>Dongyan “Formation” 818 ± 9 Ma[37]</td></tr>
<tr><td>Dutan “Formation”</td><td>Daling “Formation” 751 ± 7 Ma[33]</td></tr>
<tr><td colspan="2">Jiaoxi “Formation” younger than 0.8 Ga[33]</td><td colspan="2"></td></tr>
<tr><td rowspan="2">Mayuan “Group”</td><td>Nanshan “Formation” 807 ± 12 Ma[33]</td><td>Dikou “Formation” younger than 0.8 Ga[33]</td></tr>
<tr><td>Dajinshan “Formation”</td><td>Dajinshan “Formation”</td></tr>
<tr><td colspan="2">Tianjingping “Formation” 1766 ± 19 Ma[35]</td><td colspan="2"></td></tr>
</table>

728 ± 8 Ma, protolith age; - - - - - -, fault contact; ……, unknown contact; ——stratigraphic contact
their detailed features will be discussed later

Based on this study, according to their metamorphism and deformation characteristics, the metamorphic rock series in the study area can be divided into two types:

(1) Moderately to strongly metamorphosed rock series that experienced ductile deformation, as exampled by the Tianjingping and Mayuan Complexes. In these rock units granitic and quartzofeldspathic veins and folds are “open” with more variable geometry (Figure 2.2). Such rock units have undergone amphibolite facies metamorphism and migmatization.

(2) Moderately metamorphosed rock series that have experienced ductile deformations, such as the Mamianshan and Wanquan Complexes, in which there are quartz veins of variable widths (Figure 2.3). Such rock units have dominatingly undergone upper greenschist facies metamorphism, but locally up to lower amphibolite facies metamorphism.

a. Photo of the Mayuan Complex at location No. 65

b. Photo of the Tianjingping Complex at location No. 125

Figure 2.2 Granitic and quartzofeldspathic veins and ductile folds in high grade metamorphic rocks. Location numbers are shown in Figure 2.4 and 2.6.

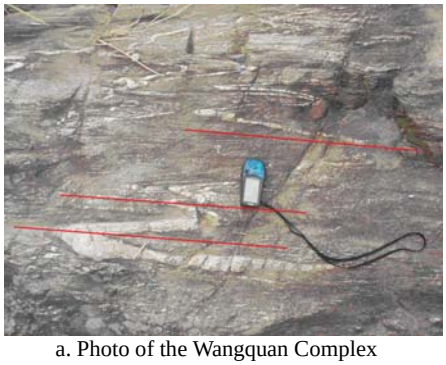

a. Photo of the Wangquan Complex at location No. 51

b. Photo of the Mamianshan Complex at location No. 119

Figure 2.3 Quartz veins and regular folds in low-grade metamorphic rocks. The axes of the folds are parallel to the gneissosity. Location numbers are shown in Figure 2.1 and 2.12.

§ 2.1 The Tianjingping Complex

The oldest metamorphic rocks of the region, the Tianjingping Complex, have an exposure of about 840 km^2, mainly in the Jianning and Guangze areas (Figure 2.1). Figure 2.4 shows the detailed geological features of the Tianjingping Complex and the sampling locality numbers.

It consists predominantly of graphite-bearing sillimanite-garnet-mica schist, sillimanite-plagioclase-mica schist, sillimanite-bearing biotite-plagioclase gneiss, fine-grained biotite-plagioclase gneiss, fine-grained garnet-bearing biotite gneiss and hornblende-biotite gneiss with mica schist, gneiss and amphibolite enclaves. Their protolith is a suite of volcanic flysch that has undergone amphibolite facies metamorphism and local modification by anatexis, forming leucosomes of different sizes and resulting in their strong plastic deformation and migmatization (Figure 2.5).

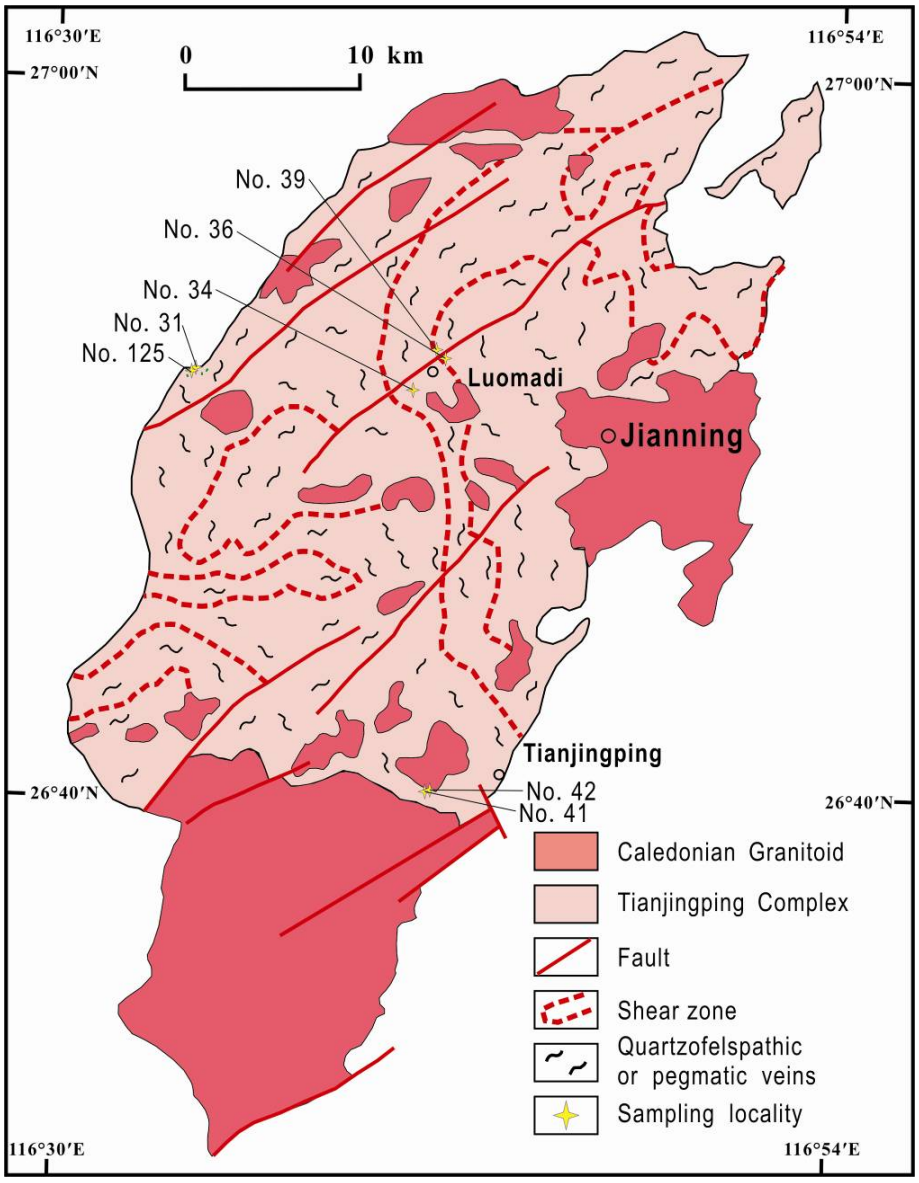

Figure 2.4 Geological map of the Tianjingping Complex, modified after the Geological Map of Fujian Province[1]. Rock samples from the sampling localities are listed in APPENDIX A.

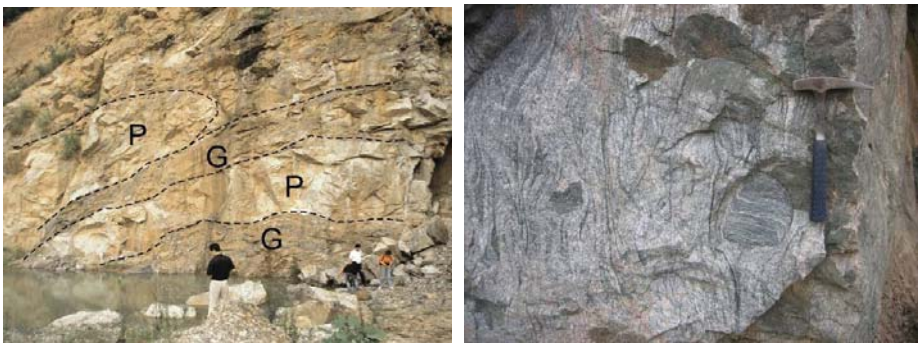

a. Pegmatite (P) intruding into hornblende -biotite gneiss (G) (No. 34)

b. Banded migmatite with amphibolite and gneiss enclaves (No. 125)

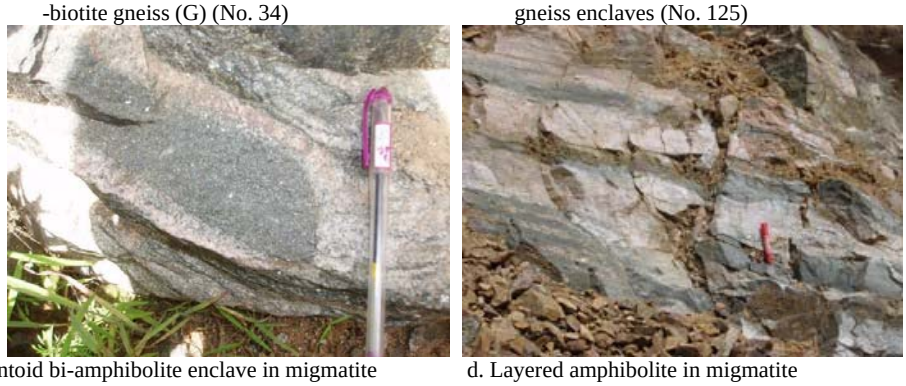

c. Lentoid bi-amphibolite enclave in migmatite (No. 125)

d. Layered amphibolite in migmatite (No. 39)

Figure 2.5 Field features of the Tianjingping Complex. Location numbers are shown in Figure 2.4.

The Tianjingping Complex was previously considered to be of late Archean age based on a whole rock Sm-Nd isochron age of 2682 ± 148 Ma for amphibolite in the nearby Yijiawan district[101]. However, Li et al.[35] considered the Sm-Nd isochron a likely "pseudo-isochron", and concluded that the protolith formed in the Paleoproterozoic, based on a SHRIMP U-Pb zircon isotopic age of 1766 ± 19 Ma they obtained from amphibolite exposed in the Tianjingping area. The amphibolite displays geochemical characteristics of enriched LREE, highly positive $\varepsilon_{Nd}(t)$ values and a mean crustal residence model age (T_{DM}) of the Tianjingping Complex[102]. Recently, Wan et al.[33] analyzed detrital zircons from fine-grained biotite gneiss of the Tianjingping Complex and obtained SHRIMP U-Pb isotopic ages of 2.79-1.76 Ga for the magmatic cores of zircons and an age of 446 - 425 Ma from the metamorphic rims. It suggests that the Tianjingping Complex was possibly formed no earlier than 1.76 Ga and was reworked in the Paleozoic.

§ 2.2 The Mayuan Complex

The Mayuan Complex forms the main part of the metamorphic series and has an exposure of approximately 5370 km^2 (Figure 2.1). It is previously divided into the Dajinshan and Nanshan "Formations" in the western region, the Dajinshan and

Dikou “Formations” in the eastern region (Table 2.1).

2.2.1 The Dajinshan “Formation”

The Dajinshan “Formation” is composed mainly of amphibolite facies graphite-bearing sillimanite–garnet–biotite schist, fine-grained biotite-plagioclase gneiss with amphibolite layers and small amounts of quartzite and marble. Figure 2.6 shows the western Mayuan Complex located northwest of Jianyang. The rocks have been extensively modified by anatexis, with portion of granitic melt in migmatite increasing from the east to the west (Figure 2.7). Previously estimated metamorphic temperatures and pressures range from 570 °C to 680 °C and 4.3 kbar to 7.0 kbar[103-104] , or from 590 °C to 625 °C and 4.2 kbar to 4.5 kbar [105].

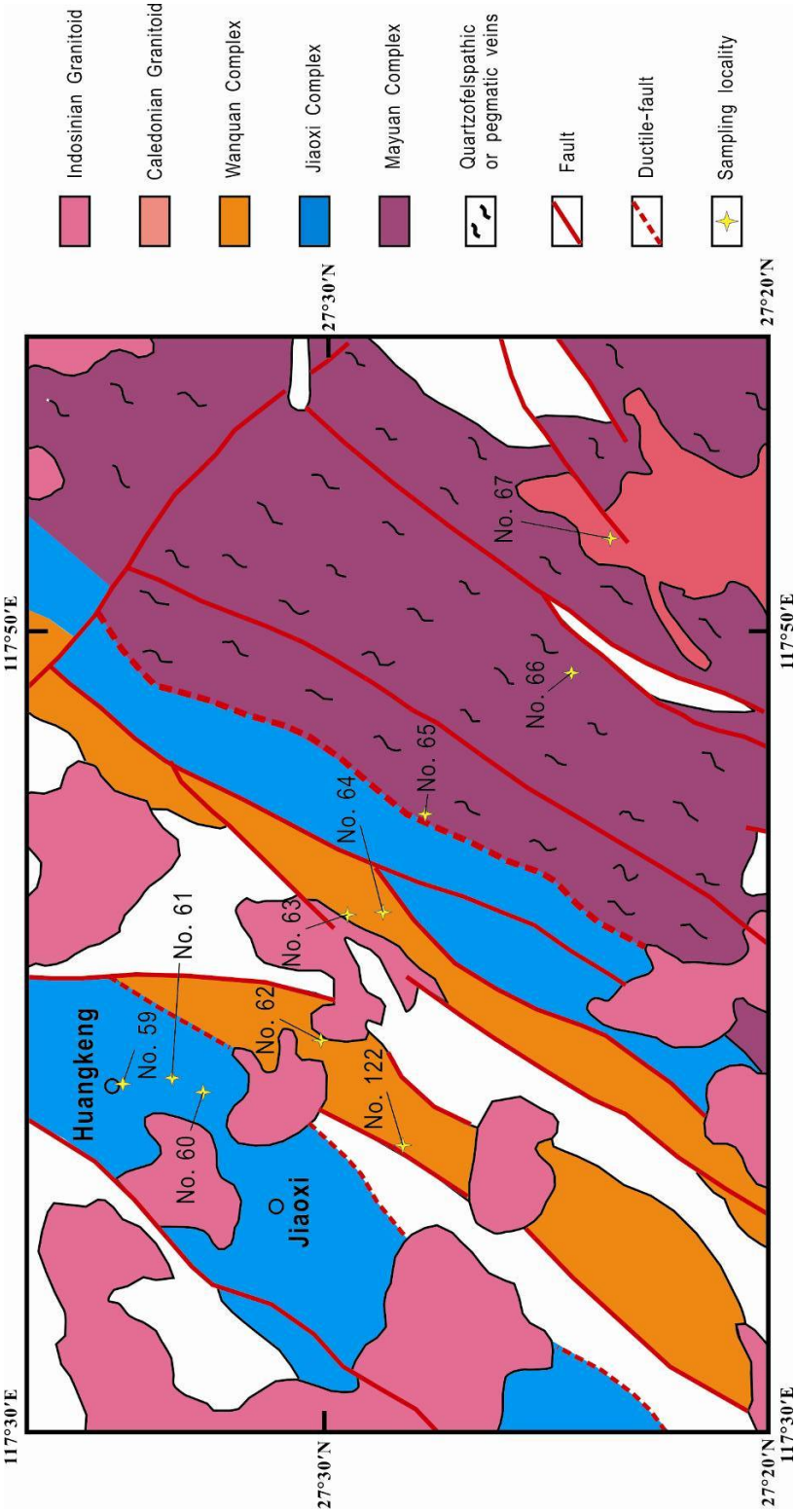

Figure 2.6 Geological map of the northwestenern Jiaoxi and Mayuan Complexes, modified after the Geological Map of Fujian Province[1]; Rock samples from the sampling localities are listed in APPENDIX A.

a. Fine-grained biotite gneiss with a small amount of quartzofeldspathic veins (No. 66)

b. Irregular folds of quartzofeldspathic veins in migmatite (No. 65)

c. Granitic and quartzofeldspathic veins and irregular folds (No. 65)

d. A lager amount of granitic leucosome in migmatite (No. 65)

Figure 2.7 Field features of the Dajinshan "Formation". Location numbers are shown in Figure 2.6.

2.2.2 The Nanshan and Dikou "Formations"

The Nanshan "Formation" is exposed mainly in the Jianyang area (Figure 2.1). It consists predominantly of fine-grained biotite gneiss and biotite–quartz schist and has experienced strong deformation and anatexis with Quartzofeldspathic veins and folds (Figure 2.8). The Complex is interpreted to have been derived mainly from sedimentary rocks with small amounts of volcano-sedimentary rocks.

The Dikou "Formation" is distributed mainly in the Dikou area (Figure 2.9). It consists predominantly of fine-grained amphibolite facies garnet and sillimanite-bearing biotite gneiss, migmatic biotite gneiss, schist and quartzite, the protoliths of which are sedimentary rocks. Irregular folds of quartzofeldspathic veins are widely developed in the migmatic biotite gneiss (Figure 2.10). The Dikou "Formation" was previously considered to have formed during the Paleoproterozoic because of its high-grade metamorphism, deformation and migmatization[106]. However, based on the SHRIMP U-Pb zircon study, the Dikou "Formation" is determined to be formed later than 0.8 Ga[33].

a. Tight folds of quartzofeldspathic veins b. Irregular folds of quartzofeldspathic veins

Figure 2.8 Field features of the Nanshan “Formation” (No. 10). Location numbers are shown in Figure 2.1.

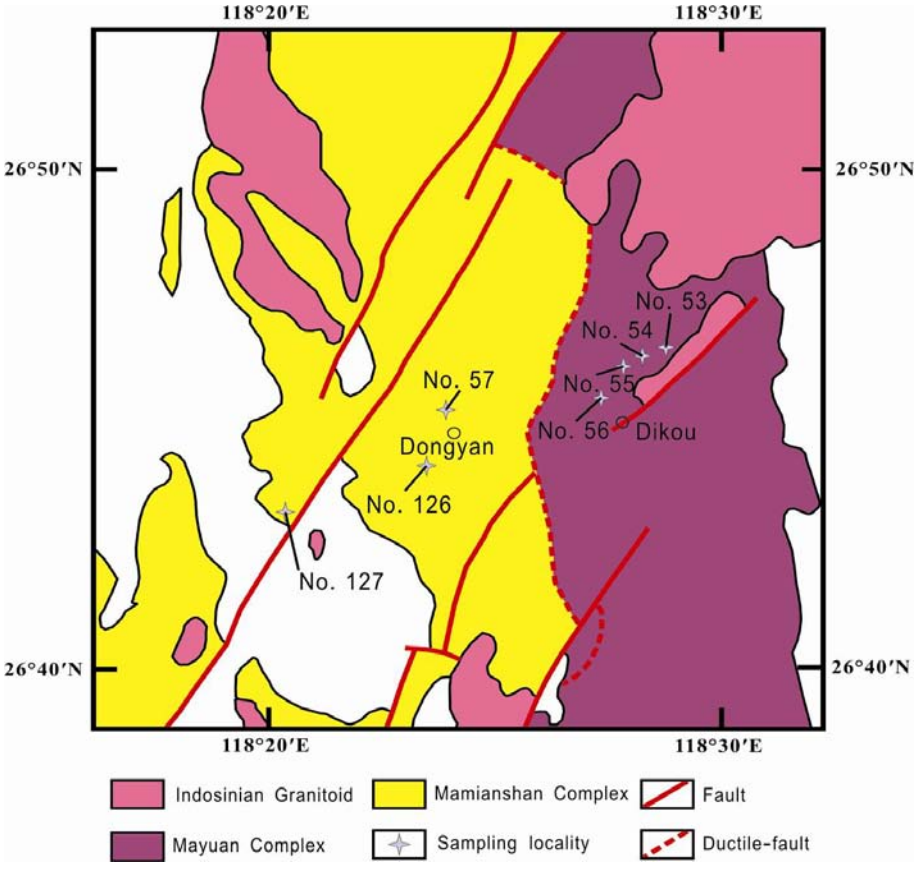

Figure 2.9 Geological map of the Tianjingping Complex, modified after the Geological Map of Fujian Province[1]; Rock samples from the sampling localities are listed in APPENDIX A.

a. Migmatic biotite gneiss with quartzofeldspathic veins (No. 53)

b. Irregular folds of quartzofeldspathic veins in migmatite (No. 56)

Figure 2.10 Field features of the Dikou "Formation". Location numbers are shown in Figure 2.9.

§ 2.3 The Jiaoxi "Formation"

The Jiaoxi "Formation" is mainly exposed ca. 8.5 km southwest of the Huangkeng Town along ductile faults (Figure 2.6). It consists predominantly of banded biotite gneiss and hornblende gneiss with interlayers of biotite-quartz schist. The protoliths were intermediate to felsic volcano-sedimentary and sedimentary rocks[106]. The metamorphic minerals, including biotite, garnet, sillimanite and kyanite, suggest an amphibolite-facies metamorphism. They have generally experienced migmatization and intense ductile deformation (Figure 2.11).

These rocks were previously regarded as of Meso- to Palaeoproterozoic ages according to four $^{207}Pb/^{206}Pb$ ages of 1500 - 1890 Ma zircons from the paragneiss[106]. Recent geochronology studies revealed abundant 1040 - 800 Ma detrital zircons from fine-grained biotite gneiss in the Jiaoxi "Formation", implying that the protoliths were deposited no earlier than 0.8 Ga[33].

a. Irregular folds of quartzofeldspathic

b. Pegmatite vein intruding into migmatitic

veins in migmatite (No. 59) biotite gneiss (No. 61)

c. Granitic and quartzofeldspathic veins and irregular folds (No. 61)

d. A lager amount of granitic leucosome in migmatite (No. 61)

Figure 2.11 Field features of the Jiaoxi Complex.

§ 2.4 The Wanquan Complex

The Wanquan Complex is widespread in the Wanquan and Taining areas with ductile fault contact to the Jiaoxi "Formation" (Figure 2.12). It is previously divided, in ascending order, into the Dutan, Huangtan and Xiafeng "Formations". Their protoliths are a suite of marine facies volcano-sedimentary series that were metamorphosed to upper greenschist-facies and locally lower amphibolite-facies.

The Dutan "Formation" consists predominantly of fine-grained biotite gneiss and mica-quartz schist, and their protoliths are dominantly sedimentary rocks with some intermediate to felsic volcanic rocks. The Huangtan "Formation" is mainly composed of fine-grained biotite-albite gneiss, fine-grained biotite two-feldspar gneiss and quartz veins. The protoliths are mainly Na-rich intermediate to felsic volcanic rocks with intercalations of sedimentary rocks. The Xiafeng "Formation" consists chiefly of micaceous schist, locally containing graphite, intercalated with small amounts of fine-grained quartzo-feldspathic gneiss. Its protoliths were sedimentary and intermediate to felsic volcano-sedimentary rocks. All rocks of the Wanquan formation are intensively deformed and the folds axes are parallel to the gneissosity or schistosity (Figure 2.13).

Conventional U-Pb zircon dating of intermediate to felsic metavolcanic rocks of the Wanquan Complex yielded ages of 1320 - 1050 Ma[106]. But latest SHRIMP U-Pb zircon study yielded a weighted mean $^{206}Pb/^{238}U$ age of 728 ± 8 Ma, indicating the formation age of the original volcanic rock in the Xiafeng "Formation"[33].

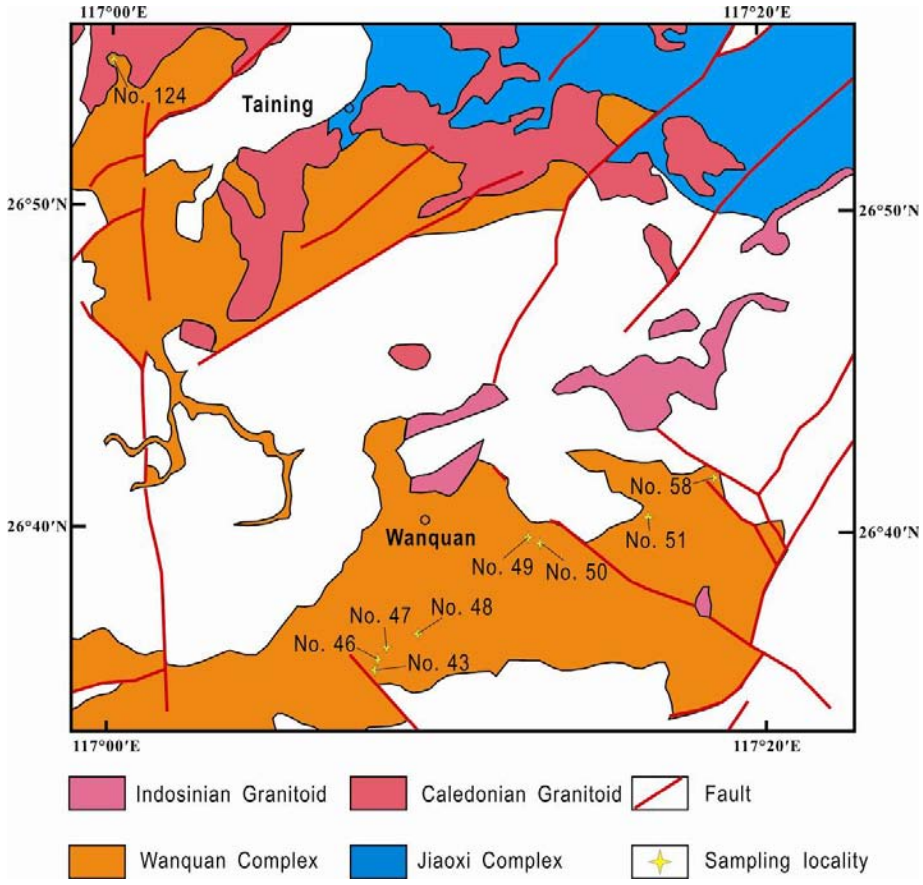

Figure 2.12 Geological map of the western Wanquan Complex, modified after the Geological Map of Fujian Province[1]; Rock samples from the sampling localities are listed in APPENDIX A.

a. Deformed quartz veins in paragneiss (No. 121)

b. Quartz veins in paragneiss (No. 121)

c. The axes of the folds are parallel to the gneissosity (No. 50)

d. The axes of the folds are parallel to the gneissosity (No. 49)

Figure 2.13 Field features of the Wanquan Complex.

§ 2.5 The Mamianshan Complex

The Mamianshan Complex is well exposed along the Zhenghe-Jianou-Dongyan and Longbeixi-Youxi-Anxi areas, showing a northeast-trending distribution, and was formerly subdivided, from bottom to top, into the Daling, Dongyan and Longbeixi "Formations" (Figure 2.9, Figure 2.14 and Table 2.1).

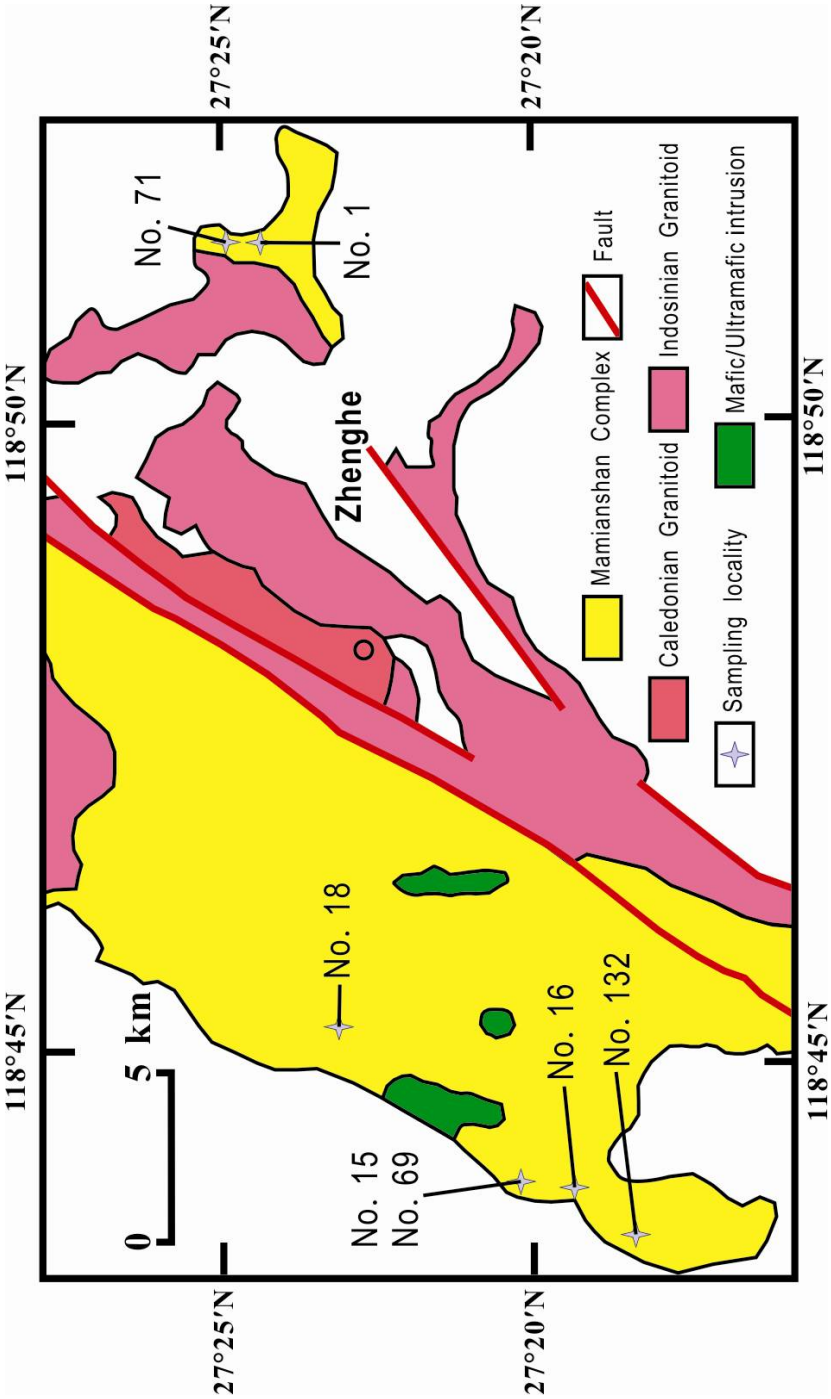

Figure 2.14 Geological map of the northern Mamianshan Complex, modified after the Geological Map of Fujian Province[1]; Rock samples from the sampling localities are listed in APPENDIX A.

The Daling "Formation" consists predominantly of fine-grained gneiss (Figure 2.14 a, b, c) and several micaceous- and quartz-schist with the meta-keratophyric volcanic rocks and marbles (Figure 2.14 d).

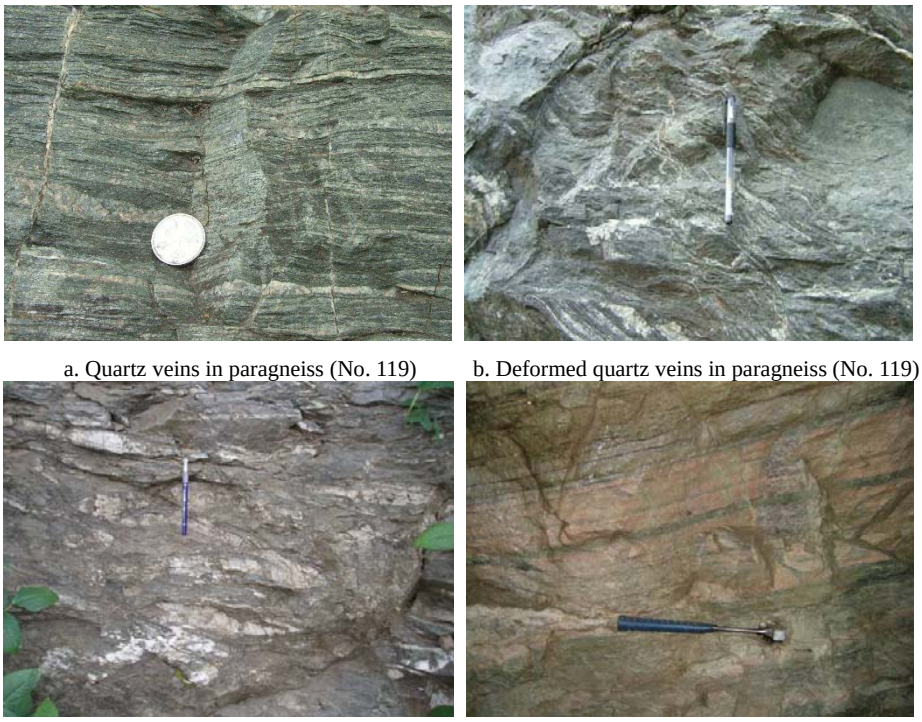

a. Quartz veins in paragneiss (No. 119) b. Deformed quartz veins in paragneiss (No. 119)

c. The axes of the folded quartz veins parallel to the gneissosity (No.120) d. Marble with pelitic layers (No. 13)

Figure 2.15 Field features of the Mamianshan Complex.

The Dongyan "Formation" is composed of actinolite schist, amphibolite, biotite gneiss, mica-bearing quartz schist and marble. Their protoliths are spilite, quartz-keratophyre and sediments such as marls and carbonates. The Longbeixi "Formation" consists dominantly of micaceous schist and quartzite which have sedimentary protoliths with some marble lens. The metamorphic grade of the Mamianshan Complex rocks reached upper greenschist- to amphibolite-facies, and the metamorphic temperatures and pressures estimated were 530 - 600 °C and 3 - 4.5 kbar[103-104], or 459-612 °C and 5.6-7.7 kbar[105]. Four phases of deformation have been identified[105, 107]. A conventional U–Pb zircon age of 1100 ± 19 Ma was obtained for a metamorphosed quartz-keratophyre of the Daling "Formation"[108-109], but a SHRIMP zircon U-Pb age of 818 ± 9 Ma (MSWD = 1.1) has recently been reported for magmatic zircon from felsic metavolcanic rocks of the Dongyan "Formation"[37].

a. Outcrop of the greenschist (No. 15) b. Quartz and calcite veins in greenschist (No. 69)

Figure 2.16 Field features of the greenschist in the Mamianshan Complex.

The Mamianshan Complex is similar in many cases to the Wanquan Complex, with both dominated by Na-rich volcano-sedimentary rocks. However, in the Wanquan Complex basic metavolcanic rocks are not found, and quartzite and marble are also limited. The lithological boundaries in theWanquan Complex are oriented in an EW direction whereas those in the Mamianshan Complex are oriented in an NNE direction.

Comparing the components and the field characteristics of these complexes, the Tianjingping, Mayuan and Jiaoxi Complexes have experienced higher-degree metamorphism, anatexis, migmatization and strong deformation, with quarzofelsdparic veins or leucogranites inside, whilst the Wanquan and Mamianshan Complexes have been metamorphosed to a lower degree, with quartz veins and regular folds. The intensity of the anatexis increases from southeast to the northwest. Since the Jiaoxi and Mayuan complexes almost share similar ages for their youngest detrital zircons (Table 2.1), they could be amalgamated as a single unit. Because the protolith of Mamianshan Complex could have been deposit earlier than that of Wanquan Complex, they should remain separated, although they have semblable features.

§ 2.6 Field Sampling

Samples for this study were collected in the study area during 3 field seasons of 2005 and 2006. They include schist, gneiss, metabasite and leucogranitoid from all the five complexes (sample names and GPS are listed in APPENDIX A). Field observations include Global Positioning System (GPS) readings of sites and attitudes of rocks structures and rock types. Sample locations were recorded with a hand held Garmin eTrex Legend Mapping Handheld GPS. Samples sites include commercial quarries, small excavations for local village uses, road cuts, natural outcrops at ridge tops, riverbeds, and excavated material from adits. At each site a single of block up

to ~3 kg was collected with the aid of sledgehammers and geopicks. All the rock samples were cleaned and weathered surfaces were completely removed by hammer and rock saw. Thin-sections were made for each sample.

Chapter 3 Methodology

§ 3.1 Whole Rock Geochemistry

Forty-nine samples were analyzed by X-ray fluorescence (XRF) for major elements. These rock samples were also analyzed for the full suite of rare earth elements (REE) and selected trace elements using an Inductively Coupled Plasma Mass Spectrometry (ICP-MS).

3.1.1 Sample preparation

Each sample consists 150 - 300 g of about washed whole rock, trimmed of any stained or weathered surfaces, and crushed using a jaw crusher into chips of smaller than ~2 cm. And the resulting chips were then cleaned on a 2mm mesh using tap water, which ensured that small grains and surficial dust were removed prior to crushing in the mill. Dried sample fragments were put into a tungsten bowl Tema mill and ground for several seconds. After that, the sample was sieved over 74 μm sieve. The portion of sample not passing the sieve was put back into the mill, together with next amount of sample. The entire sample was reduced to powder by repeating the procedure until the whole sample passed through the sieve. About 100 g of homogeneous sample powder was set aside for geochemistry. Between samples, all apparatus were brushed, washed firstly in water and then in acetone, and finally cleaned using a self contamination run of the next sample to be crushed.

3.1.2 Analysis of major elements through XRF

Major elements of rock samples were analyzed using an X-ray Fluorescence (XRF) (PANalytical, Holland) at the Huadong Mineral Resources Supervision and Testing Center, Ministry of Land and Resources Research, Nanjing, China. The samples were prepared as 40 mm fused beads using the PANalytical Perl'X 3 fusion machine. The beads were prepared in a 4:1 dilution using 2.5 g of sample and 10 g of $Li_2B_4O_7$ Flux.

Major element oxide contents (SiO_2, Al_2O_3, FeO, Fe_2O_3, CaO, MgO, Na_2O, K_2O, TiO_2, MnO, and P_2O_5) were obtained by comparing peak positions and intensities to traces of geological standards. All major element oxide contents for these replicates were within 0.5% (absolute) of the first analysis. Approximately 10 g of each sample

was weighed into a porcelain crucible and heated at 1000 °C for 10 h in a muffle furnace to measured the loss on ignition (LOI). A critical check on the quality of XRF analyses is that the sum of major element oxides and LOI is 100 ± 5%.

3.1.3 Analysis of trace and rare earth elements through ICP-MS

Inductively coupled plasma mass spectroscopy (ICP-MS) is capable of trace multielement analysis, often at the part per trillion level. A schematic representation of an ICP-MS system is displayed in Figure 3.1. Trace elements of the samples were analyzed using an Agilent 7500a ICP-MS (Agilent, USA) at the State Key Laboratory of Geological Processes and Mineral Resources, China University of Geosciences (Wuhan), where the following sample preparation technique was used; (1) Crushed sample powders were dried in an oven at a temperature of 105 °C for 12 hours. (2) 50 mg of each sample was digested in a Teflon bomb with a 2.0 ml mixture of subboiling distilled superpure HF and HNO_3 (1:1), and heated for 48 hours at a temperature of 190 °C. (3) After digestion, the sample was evaporated to incipient dryness at a temperature of 115 °C, refluxed with 3 ml HNO_3, and heated again to incipient dryness. (4) The sample was re-dissolved using 2-3 ml HNO_3 (30%) and heated for 12 hours at a temperature of 190 °C. (5) After cooled, the solution was diluted with a mixture of HF (0.1%) and HNO_3 (2%) to a final dilution factor of 1:1500.

Each analysis of trace elements consisted of a 60 second uptake, 90 second analysis, and 60 second washout sequence, with two scans per second over the range of elements. 19 channels per atomic mass unit were used to do the registration; during dwell time of 320 ms. Standards were introduced with concentration of 1, 2, 5, 10 and 20 ppb. Internal Rh and Ir standards were applied for internal drift correction. Two international standard reference samples, AGV-2, BCR-2, BHVO-2, G-2, and GSR-1 were used to monitor accuracy and precision.

For the analysis of trace elements through ICP-MS, the digested rock sample (liquid) was introduced by way of a nebulizer, which aspirated the sample with high velocity carrier gas of argon, forming a fine mist, into hot plasma. The aerosol then passed into a spray chamber where larger droplets were removed via a drain. Droplets small enough produced by this process were vaporized in the plasma torch. Temperature inside the plasma reached to 6000 ~ 10000 K, with pressure up to ~760 Torr, stripping the atoms of their valence electrons rapidly. The positively charged ions were accelerated to a set of apertures into an interface region, which enables extraction of the ions without compromising the high vacuum (10^{-4} Pa) in the mass spectrometer. Once the ions were in the mass spectrometer chamber, they were

focused by an electromagnetic lens system and directed down the mass analyzer. Ions with specific mass-to-charge rations (m/z) were transmitted sequentially to the ion detection system, while ions with lower or higher m/z ratios have different trajectories and were lost. The detector consisted of combined electron multiplier and low gain analog detector, one of which was selected depending on the ion-beam intensity.

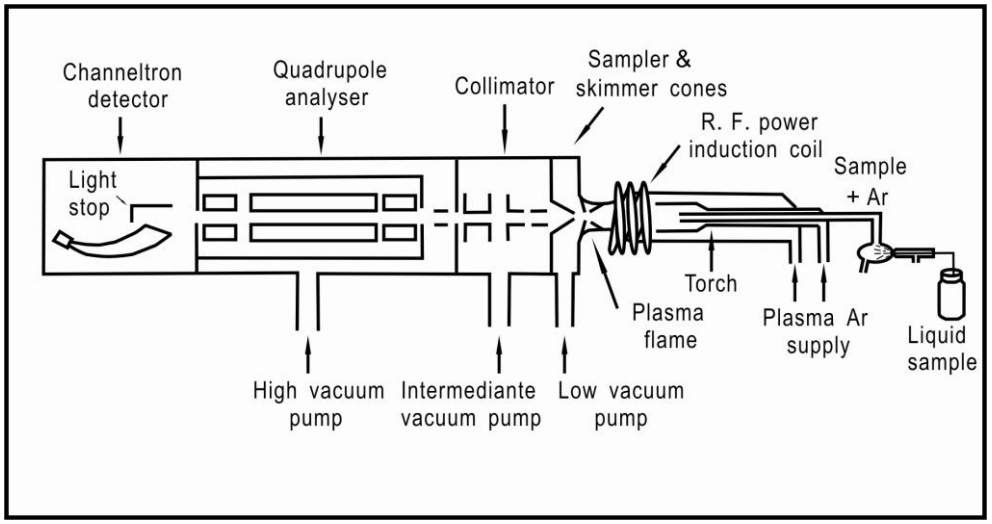

Figure 3.1 Schematic of ICP-MS main processes (modified after [110-111]).

§ 3.2 Geochronology

3.2.1 Mineral separation

Mineral separation of zircon, titanite, and part of hornblende, biotite and muscovite was processed in the Academe of Regional Geological Survey, Langfang, China. Firstly, fresh rock samples (1 - 3 kg) were crushed to grain sizes of < 245 μm, using a steel jaw crusher, and then were ground down to 74 μm using a percussion mill. Between samples, all apparatus were brushed, washed firstly in water and then in acetone, and finally cleaned using a self contamination run of the next sample to be crushed. Then the minerals were separated by a combination of Wilfley-table washing, heavy liquid separation (1,1,2,2-tetrabromoethane and diiodomethane), magnetic separation and hand-picking.

3.2.2 Cathodoluminescence imaging of zircon

Selected zircon grains from the least magnetic fractions were different in shapes and colors with high transparency and few inclusions. They were set in 2-part epoxy resin along with a portion of standards. Epoxy mounts were then cut back to half the thickness of the mounted minerals and hand polished. To remove the contamination of the mounts, a three stage ultrasonic cleaning process was used.

Cathodoluminescence (CL) imaging of zircons prior to ion-microprobe analysis are used to reveal the interior structures of the minerals, such as core/rim, and zoning structures, which are commonly related to different ages. These ages may be used to interpret the magmatic, metamorphic or anatectic history a zircon or a titanite has undergone. All CL images of zircons in the LA-ICP-MS mounts were acquired using a Mono CL3 + (Gatan, USA) attached to a scanning electron microscope (Quanta 400 FEG) at the State Key Laboratory of Continental Dynamics, Northwest University, Xi'an, China. Operating conditions of the SEM used an accelerating voltage of 12 kV, with a spot size of 6 and a primary beam current 20.

Core/rim structures are common to many of the samples. Brightness of CL response, usually inversely associated with the trace elements content such as U, REE and Th etc. of zircon [112-115], vary greatly between samples, and often even within a single grain. Where U content between individual zones in a single grain varies significantly, adequate contrast often cannot be resolved within the capabilities of the machine. Consequently, the common practice of post imaging manipulation of zircon images has in some cases been employed to remove noise and enhance the visible structures within the raw grayscale images. For the titanite with higher U and Th contents, BSE images were taken for this purpose.

Obtained images were directly saved as digital files and were printed out for selection of analytical points during analyses. The sites were marked and labeled during the ion microprobe analytical sessions.

3.2.3 Laser Ablation Microprobe ICP-MS U-Pb analyses

Zircon U-Pb dating and trace element analyses were carried out at the La-ICP-MS Lab in the State Key Laboratory of Geological Processes and Mineral Resources, China University of Geosciences (Wuhan), using an Agilent 7500a ICP-MS (Agilent, USA) coupled with a GeoLas 2005 laser-ablation system (DUV 193 nm ArF-excimer laser) (MicroLas, Germany). A schematic representation of an ICP-MS system is given in Figure 3.2. A spot size of 32 μm with a repetition rate of 8 Hz was applied to all analyses. Helium was used as the carrier gas to enhance transport efficiency of ablated material. Standard zircon 91500 was used for external calibration. NIST610 was used for external calibration of element contents and ^{29}Si was used for internal calibration. For details of the analytical processes and parameters of the equipment see reference [116]. Pb isotopic data, U-Pb surface ages and the U-Th-Pb contents of the zircon spot analyses were processed using the GLITTER software (Version 4.0). ISOPLOT software[117] was used for calculating weighted zircon ages (1σ error) and

a concordia plot.

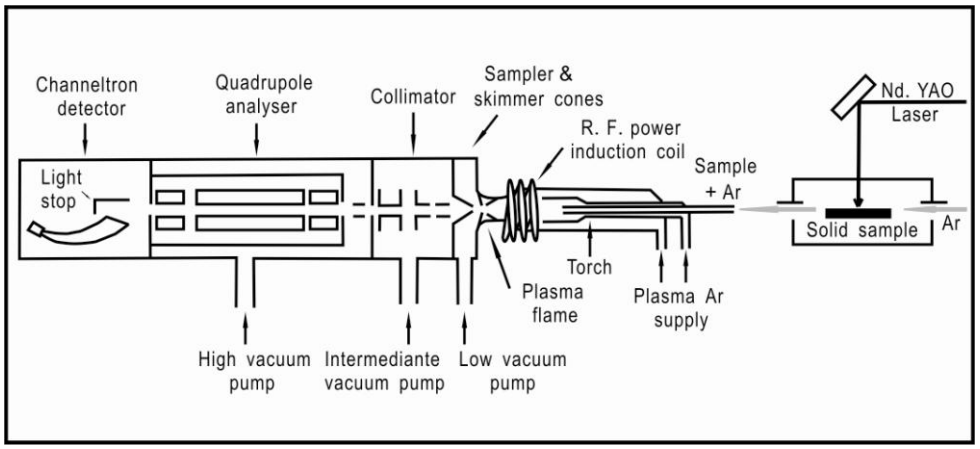

Figure 3.2 Schematic of La-ICP-MS main processes (modified after [110]).

3.2.4 $^{40}Ar/^{39}Ar$ Analyses for hornblende and biotite

K-bearing minerals used for $^{40}Ar/^{39}Ar$ dating each possess a characteristic narrow thermal closure interval, termed the closure temperature, below which argon is retained within the mineral lattice [118]. All hornblende and biotite from samples (see Table3.1) were carefully handpicked under a binocular microscope to avoid impurities or inclusions such as quartz or microcline.

Table 3.1 Samples for $^{40}Ar/^{39}Ar$ analyses

Mineral	Sample
Hornblende	114-1, 114-2, 29-2, 109-4, 88-13, 61-3, 39-1, 82-2, 15-2, 69-1, 86-5, 122-1, 125-4
Biotite	101-2, 109-3, 65-2, 31-7, 43-1, 86-5, 122-1, 125-4

HF leaching for hornblende

After hand-picking to greater than 99% purity and weighing, hornblende samples were processed by HF leaching, when the following preparation technique was used.

(1) Putting sample into a small beaker using deionized H_2O;
(2) Moving excess water into a second beaker;
(3) Putting HF (5%) into the beaker with sample;
(4) Leaching the sample for 45 s by laying the beaker in an ultrasonic;
(5) Adding H_2O to dilute HF before remove all the liquid from the beaker to a large beaker carefully;
(6) Repeating step (5) for three times;
(7) Putting H_2O into the beaker and washing the samples using an ultrasonic for one minute, then removing all the liquid to the large beaker carefully;
(8) Repeating step (7) twice;

(9) Transferring the sample back to the petri dish using methanol;
(10) Removing methanol from prei dish;
(11) Rinsing one large and two small beakers;
(12) Next sample, repeating steps above;
(13) Drying all the samples under a heat lamp.

$^{40}Ar/^{39}Ar$ analytical procedure

Samples for $^{40}Ar/^{39}Ar$ analyses were packaged into aluminium foil containers. The packages were Cd-shielded and irradiated for 90 h in position 5C (i.e. in the high flux area and receiving flux from all directions), in the McMaster University Reactor, Hamilton, Canada, along with the neutron flux monitor Biotite standard Tinto B (K-Ar age = 409.24 ± 0.71 Ma). K_2SO_4 salts were used for determining correction factors for K-produced ^{40}Ar. Correction factors for interfering reactions are as follow: $(^{36}Ar/^{37}Ar)_{Ca}$ = 2.54 (± 0.09)×10^{-4}; $(^{39}Ar/^{37}Ar)_{Ca}$ = 6.51 (± 0.31)×10^{-4} [119]; $(^{40}Ar/^{39}Ar)_K$ = 0.0010 (± 0.0005).

Analyses of hornblende, biotite, and muscovite from samples (see Table 3.2 for sample list) were carried out at the Western Australian Argon Isotope Facility, John de Laeter Centre, Curtin University of Technology. Argon data were collected by infrared laser step-heating of single and multiple grains (see individual sample description for details). Irradiated mineral samples were loaded into an ultra-high vacuum laser chamber and baked to 120 °C overnight to remove adsorbed atmospheric argon from the samples and chamber walls. Prior to analysis, the dimensions of each grain were measured using the calibrated stage system.

A 110 W Spectron Laser Systems continuous-wave neodymium–yttrium–aluminium–garnet (CW–Nd–YAG) laser (λ = 1064 nm), fitted with a TEM00 aperture, was used to step-heat each sample at increasing laser power (9.9–10.1 A). The gases released were purified using three SAES AP10 getter pumps to remove all active gases (i.e. CO_2, H_2O, H_2, N_2, O_2, and CH_4). The remaining noble gases were equilibrated into a high-sensitivity mass spectrometer (MAP 215–50) fitted with a Balzers SEV 217 multiplier, operated at a mass-resolution of 600. System blanks were measured between every two unknowns, and the unknowns were corrected using the unweighted mean of the bracketing blank determinations. Mean 5 min extraction system blanks obtained during data collection were: $^{40}Ar = 6.5 \times 10^{12}$ cm^3, $^{39}Ar = 8.6 \times 10^{-15}$ cm^3, $^{38}Ar = 8.1 \times 10^{-15}$ cm^3, $37Ar = 1.1 \times 10^{-13}$ cm^3 and $^{36}Ar = 4.5 \times 10^{-14}$ cm^3 at standard temperature and pressure. Data were corrected for mass-spectrometer discrimination and nuclear interference reactions. $^{40}Ar/^{39}Ar$ ages were calculated using the decay constant recommended by reference [120].

§ 3.3 Mineral Chemistry

Selected uncovered and polished thin sections of sample rocks were carbon coated. Hornblende, biotite, plagioclase, sillimanite and garnet mineral assemblages were circled using a STAEDTLER Lumocolor permanent marker pen, which contains ink showing up with electron imaging. They were analyzed for major element compositions (SiO_2, TiO_2, Al_2O_3, FeO, MnO, MgO, CaO, Na_2O, K_2O) using a JEOL JSM-6400 Scanning Microscope equipped with a Wavelength-dispersive X-ray Detector (WDS) and MORAN SCIENTIFIC WDS SOFTWARE at the Center for Microscopy, Characterisation & Analysis in University of Western Australia.

For electron microprobe analyses, the following steps were carried out.

Step 1 Loading the sample and getting an image

The thin-section sample was secured on the holder with appropriate standards by using carbon tape which also provided electrical conductivity. After the sample was loaded, the air in the specimen chamber was pumped out until the pressure fell below 10^{-5} torr. Then required accelerating voltage was chosen and the brightness, contrast, focus and correct astigmatism were adjusted to obtain the best Secondary Electrons (SE) and Backscattered Electrons (BSE) images.

Step 2 Storing rough locations for all standards and sample analysis areas using the Deben Stage Controller

A highest Speed Level (level 3) was used and the X and Y coordinates were controlled by a joystick to find analysis areas of necessary standards or sample using the Deben Stage Controller. Store the rough locations which could be recalled when analyzing.

Step 3 Inserting the optical microscope, focusing the reflected light image of the sample, focusing the electron image of the sample, and marking the position of the beam on the monitor screen

When the optical microscope was inserted, the field of view would be reduced, and the signal received by the SE detector would be compromised. This would have some detrimental effects on normal SEM operation. Thus, before inserting the optical microscope we performed imaging, stored and recorded positions of standards and samples. After the optical microscope being inserted, the TV monitor and the DC power box were turned on. Both the reflected light image and the secondary electron image were focused. The position of the beam on the monitor was marked while the electron beam was focused to a point (x 300,000) on the wollastonite standard (a cathodoluminescent mineral).

Step 4 Standardizing on standards and analyzing samples using the Moran Scientific WDS software

The Moran Scientific WDS software was started and “Wavelength Dispersive

Analyser" was selected. The analysis file "15sil_masa.wds" was loaded. To standardise on all silicate standards, 15 kV of accelerating voltage and 20 nA of beam current were set. The counting times for upper background, peak and lower background were set to 10, 40 and 10 seconds respectively (suggested value).The elements Na, Mg, Al, Si, Mn, Fe, K, Ca, and Ti were standardised using standard minerals including albite, olivine, garnet, pyroxene, apatite, orthoclase, wollastonite and rutile. Then the selected minerals (hornblende, plagioclase, biotite, muscovite, garnet, sillimanite, monazite, etc) were analyzed.

Step 5 Routine WDS analysis and multi-piont automated WDS analysis.

When the samples were analyzed using routine WDS analysis, operating conditions were checked to be identical to those used for standardization (15 kV of accelerating voltage and 20 nA of beam current). The elements to analyze were selected and the relevant analysis file was saved. The number of oxygens for the structural formula was entered for each mineral (see Table 3.3 below).

Table 3.3 the number of oxygens in the structural formula of minerals

Mineral	Olivine	Pyroxene	Plagioclase	Garnet	Biotite	Muscovite	Hornblende
No. of O	4	6	8	12	22	22	23

For large mineral grains and night sessions, multi-point automated WDS analysis is sometimes could be used. Firstly, we moved the stage to find the first analysis position and focused both optical microscope and secondary electron image. Then the backslash from the drives was removed by pressing ***bklsh*** button on the stage controller to make sure that the stage returned to the desired location and that the image remained in focus. After that, the coordinates and the number of oxygens for the structural formula (see Table 3.4) were saved to the run table. Other analysis points were added following the same procedure. They could be analyzed together by selecting ***Multi-Point Analyse*** in the WDS CONTROL window.

§ 3.4 Hf-isotope Geochemistry

Zircon Hf isotope analyses reported in this thesis were carried out in situ using a Nu Plasma HR MC-ICP-MS (Nu Instruments Ltd., UK) coupled with a GeoLas 2005 laser-ablation system, at the State Key Laboratory of Continental Dynamics, Northwest University, Xi'an. The laser system delivers a beam of 213 nm UV light from a frequency-quintupled Nd:YAG laser. Most analyses were carried out with a beam diameter of 44 μm, a repetition rate of 10 Hz, and energies of 0.6 - 1.3 mJ/pulse. This resulted in total Hf signals of (1 - 6) × 10^{-11} A, depending on conditions and the Hf contents. Typical ablation times were 30 - 120 s, resulting in

pits 20 - 60 μm deep. Ar was used as carrier gas for transporting the ablated sample from the laser-ablation cell via a mixing chamber to the ICP-MS torch. The Nu Plasma MC-ICP-MS system features a unique geometry with a fixed detector array of 12 Faraday cups, and three ion counters. Beams are directed into the collectors by varying the dispersion of the instrument using an electrostatic zoom lens. For this work masses 172, 175, 176, 177, 178, 179 and 180 were analyzed simultaneously in Faraday cups; and all analyses were carried out in static-collection mode. Data were normalized to $^{179}Hf/^{177}Hf = 0.7325$, using an exponential correction for mass bias. Initial setup of the instrument was performed using a 1 ppm solution of JMC475 Hf, spiked with 80 ppb Yb, which typically yielded a total Hf beam of $(10 - 14) \times 10^{-11}$ A. The laser-ablation analyses were carried out using the Nu Plasma time-resolved analysis software, in which the signal for each mass and each ratio is displayed as a function of time during the analysis. This allows the more stable portions of the ablation to be selected for analysis, before the data are processed to give the final results. The selected interval is divided into 40 replicates for the calculation of the standard error. Background was collected on peak for 45 s before ablation began.

A correction of the isobaric interferences of ^{176}Lu and ^{176}Yb on ^{176}Hf is required for the measurement of accurate $^{176}Hf/^{177}Hf$ ratios in zircon. This correction is relatively straightforward for the Nu Plasma, because the mass bias of the instrument is independent of mass over the mass range considered here[121]. Interference of ^{176}Lu on ^{176}Hf was corrected by measuring the intensity of an interference-free ^{175}Lu isotope and also a recommended $^{176}Lu/^{175}Lu$ ratio of 0.02669[122] to calculate $^{176}Lu/^{177}Hf$. Similarly, the interference of ^{176}Yb on ^{176}Hf was corrected by measuring an interference-free ^{172}Yb isotope and using a $^{176}Yb/^{172}Yb$ ratio of 0.5886[123] to calculate $^{176}Yb/^{177}Hf$. Zircon 91500 was used as the reference standard, with a recommended $^{176}Hf/^{177}Hf$ ratio of 0.282295 ± 0.000027 (n = 33, 115). A decay constant for ^{176}Lu of 1.865×10^{-11} $year^{-1}$ [124], the present-day chondritic ratios of $^{176}Hf/^{177}Hf = 0.282772$ and $^{176}Lu/^{177}Hf = 0.0332$ [125] were adopted to calculate ε_{Hf} values. Single-stage model ages (T_{DM}) were calculated by reference to depleted mantle with a present-day $^{176}Hf/^{177}Hf$ ratio of 0.28325 and $^{176}Lu/^{177}Hf$ ratio of 0.0384[126]. Two-stage model ages (T_{DM}^{UC}/T_{DM}^{LC}) were calculated with an assumed $^{176}Lu/^{177}Hf$ ratio of 0.0093 for the average upper continental crust[127]. All zircons analyzed in this study have much lower $^{176}Yb/^{177}Hf$.

Chapter 4 Ordovician-Silurian migmatization and partial melting of Precambrian crustal and mantle materials in the Tianjingping Complex

§ 4.1 Petrography

Twenty-six rock samples were collected from the Tianjingping Complex (for sampling localities see Figure 2.4 and Table 2.2), including ten leucosome samples, nine felsic gneiss samples and seven mafic gneiss samples. Textures of leucosome are massive, granoblastic and medium grained, commonly with a mineral assemblage of biotite + plagioclase + quartz ± K-feldspar ± muscovite, and minor apatite, zircon and opaque minerals (Figure 4.1). Felsic gneiss samples are grey in color and massive, and usually have gneissic structure and a mineral assemblage of biotite + plagioclase + quartz ± amphibole ± garnet, with minor apatite, zircon, titanite and opaque minerals (Figure 4.2). They range from ultrabasic to acid rocks with the increase of quartz content. Samples of biotite-amphibole-plagioclase gneisses are dark green and massive, with the mineral assemblage of amphibole + plagioclase + quartz ± biotite and minor titanite, which are more or less oriented to a certain direction (Figure 4.3).

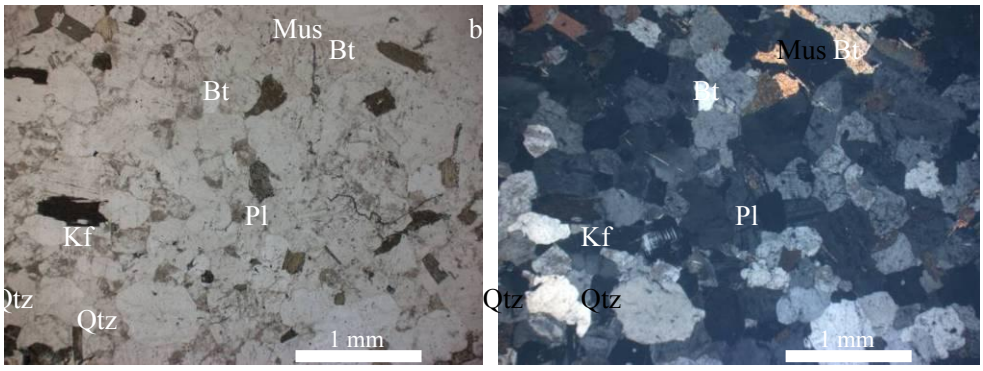

Figure 4.1 Typical granoblastic texture of leucosome (sample 125-5) under both (a) plane polarized and (b) cross polarized light. The composition is dominated by quartz (Qtz), plagioclase (Pl) and K-feldspar (Kf), with lesser amounts of biotite (Bt) and muscovite (Mus).

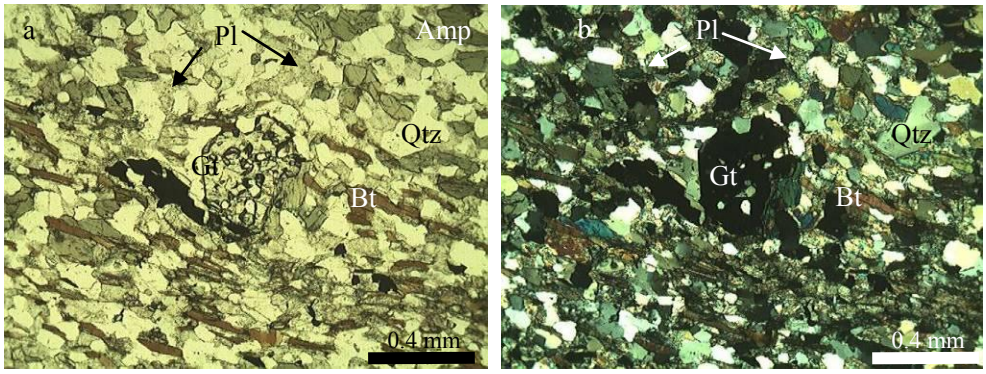

Figure 4.2 Typical gneissic structure of garnet-amphibole-biotite gneiss (sample 34-4) under both (a) plane polarized and (b) cross polarized light. The composition is dominated by plagioclase (Pl, altered to clay mineral) and quartz (Qtz), with lesser amounts of biotite (Bt), amphibole (Amp) and minor garnet (Gt) and opaque minerals.

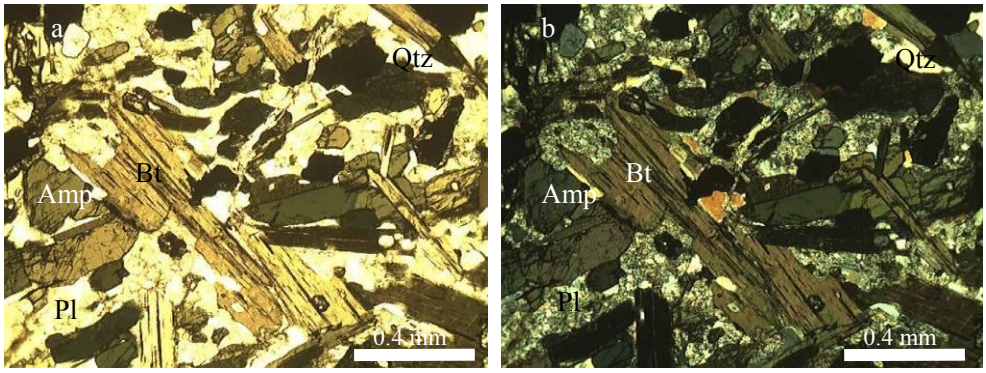

Figure 4.3 Typical biotite-amphibole-plagioclase gneiss with oriented minerals (sample 31-7) under both (a) plane polarized and (b) cross polarized light. The composition is dominated by biotite (Bt), amphibole (Amp), plagioclase (Pl, partly altered) and quartz (Qtz).

§ 4.2 Geochronological analyses

4.2.1 Zircon U-Pb ages

Samples selected for determining the formation time of the leucosomes and mafic gneiss rocks, and the time limit for the deposition of the meta-sediments were collected from two places, Min-Gan boundary area (samples 125-1, 125-2, 125-4) and Luomadi area (samples 34-4 and 39-1).

1) Samples from the Min-Gan boundary area

Age of leucogranodiorite (sample 125-1)

Sample 125-1 is a medium-grained (grain size 2 - 3 mm) intermediate rock, containing biotite, plagioclase, quartz, and minor apatite, zircon and opaque minerals. Its sampling locality is shown in Figure 2.4. Most of the zircon grains are elongated

prismatic almost euhedral and colorless crystals up to 100-350 μm in length with length/width ratios from 2:1 to 6:1. CL images reveal that most grains are strongly zoned (Figure 4.4a) showing the characteristics of magmatic genesis. Concordia diagrams for twenty-three zircon U-Pb analyses are displayed in Figure 4.4b, and the U-Pb analytical results are listed in APPENDIX B. The Th contents and U contents of the zircons are 10 to 1954 ppm and 253 to 3251 ppm, respectively and show an obvious positive correlation. Th/U ratios are from 0.02 to 0.61 and mostly higher than 0.1, which indicates that majority of the zircon grains are of igneous origin with few metamorphic ones. All the analytical data plot on or near the concordia (Figure 4.4b). Besides one grain produces an age of 471 ± 4 Ma, the rest of them yield a range of $^{206}Pb/^{238}U$ ages between 450 and 436 Ma, with a weighted mean $^{206}Pb/^{238}U$ age of 445 ± 3 Ma (95% conf., MSWD = 1.15) (Figure 4.4b).

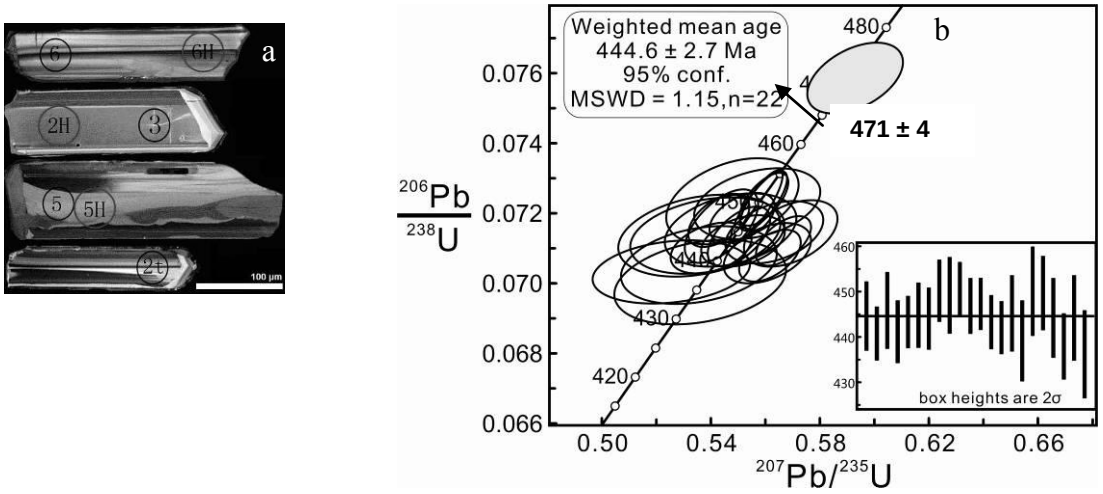

Figure 4.4 Cathodoluminescence (CL) images (a) and LA-ICP-MS U-Pb isotopes (b) of zircon grains in sample 125-1. Numbers and letters in circles (such as 6, 2t and 2H) in picture (a) represent analysis spots for U-Pb, Trace elements and Hf isotopes, respectively. The data are listed in APPENDIXES B, C and D.

Age of paragneiss (sample 125-2)

Sample 125-2 is a grey and medium-grained (grain size 1 - 2 mm) acid rock, containing biotite (partly altered to chlorite), plagioclase (partly altered), quartz, and minor accessory minerals, e.g. apatite, zircon and opaque minerals (Figure 4.1). Its sampling location is the same as sample 125-1. Zircon grains are most commonly subhedral to euhedral, with some grain fragments and elongated prismatic crystals up to 200 μm in length. Under plain polarized light, zircon grains of 125-2 are colorless to pale brown. Under CL imaging, the zircon grains display various internal structures. The elongated prismatic grains display fine scale oscillatory zonation. The smaller grains often show core/rim structure. Most cores are brighter, indicating lower thorium and uranium contents (Rubatto and Gebauer, 2000). Additionally, broad darker rims with fine oscillatory zonation are developed and occasionally

incursive into cores, forming embayments (Figure 4.5a).

Concordia diagrams for thirty-one zircon U-Pb analyses are displayed in Figure 4.5b, and the U-Pb analytical results are listed in APPENDIX B. Most of the Th/U ratios for sample 125-2 zircon analytic spots are between 0.17 and 1.28, besides four data from <0.01 to 0.05. There is a great variation in the ppm values for both Th and U contents, from about 1 to 999 ppm and 68 to 2104 ppm, respectively (APPENDIX B). Most of the analytical data plot on or near the concordia (Figure 4.5b). They produced a range of $^{206}Pb/^{238}U$ ages between 2280 and 440 Ma. The analytic spots of zircon cores yielded two clusters of older ages, 2.28 - 1.60 Ga and 780 - 729 Ma (with one age of 992 Ma). Two populations are identified from the ages between 780 and 729 Ma, with weighted average ages of 740 ± 8 Ma (95% conf., MSWD = 1.5) and 776 ± 6 Ma (95% conf., MSWD = 0.41), respectively (Figure 4.5c, 4.6). The data from rims or single magmatic grains always show younger ages, from 450 to 440 Ma, with a weighted average age of 445 ± 3 Ma (95% conf., MSWD = 0.75) (Figure 4.5c, 4.6). These three populations are also shown as principal peaks in the probability histogram (Figure 4.7). This indicates that the protolith of the paragneiss has been strongly reworked by later thermal events.

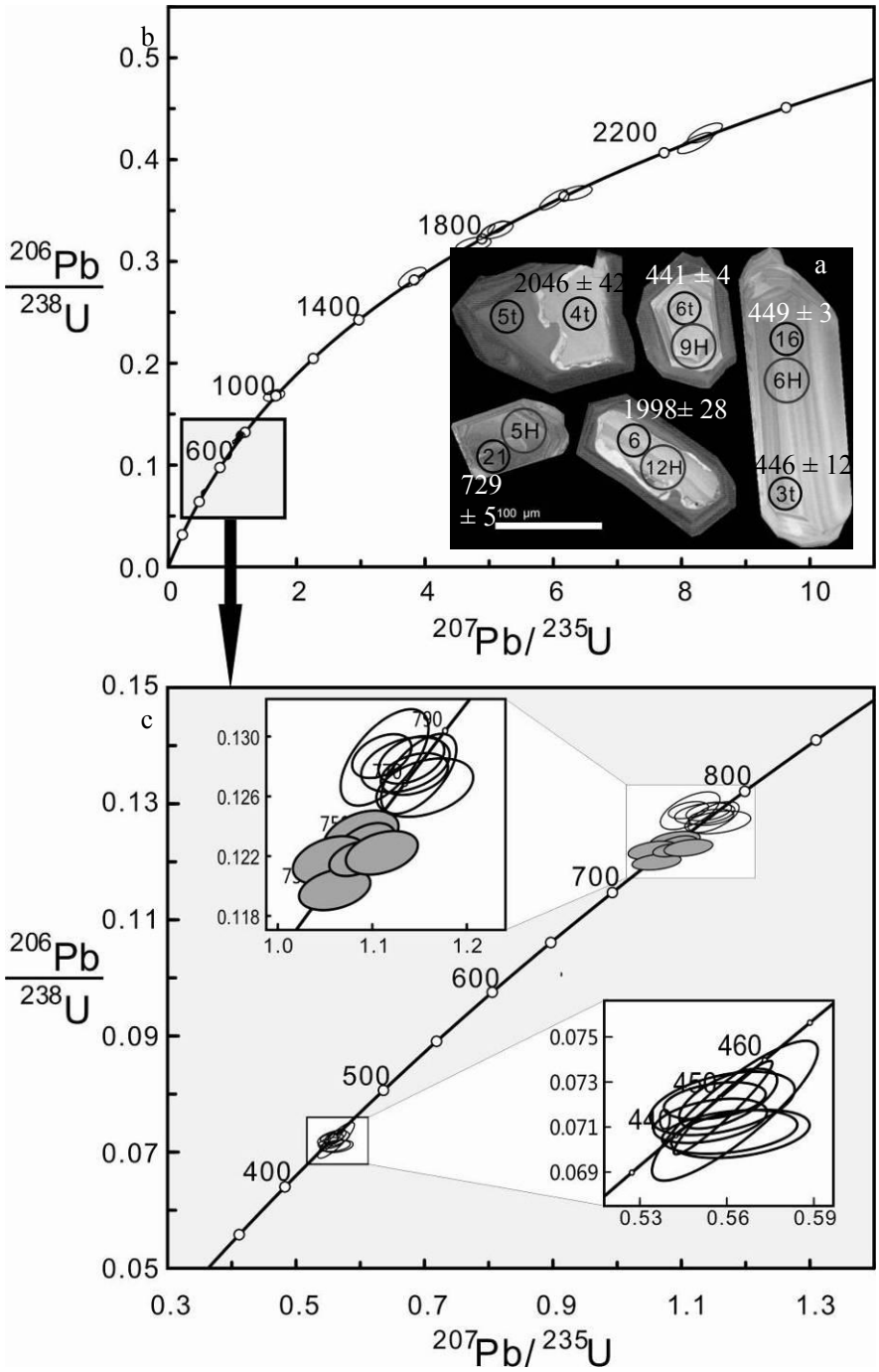

Figure 4.5 Typical cathodoluminescence (CL) images (a) and LA-ICP-MS zircon U-Pb isotopes concordia diagram (b) of zircon grains in sample 125-2. Numbers and letters in circles (such as 6, 3t and 5H) in picture (a) represent analysis spots for U-Pb, Trace elements and Hf isotopes, respectively. The data are listed in APPENDIX B, C and D. The weighted average ages of three populations (c) are 740 ± 8 Ma, 776 ± 6 Ma and 445 ± 4 Ma (shown in Figure 4.6)

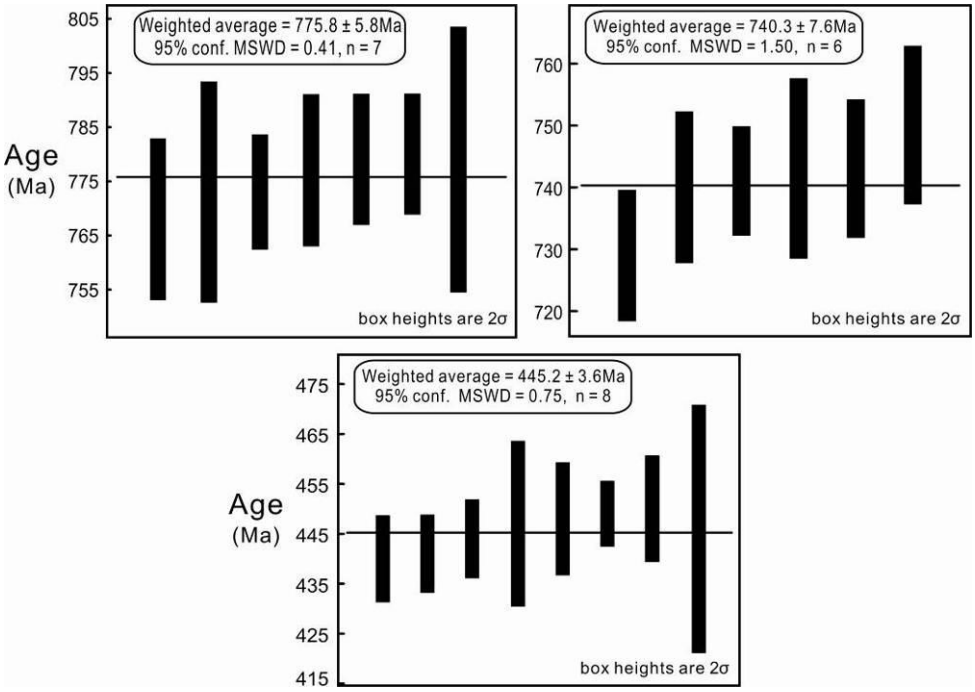

Figure 4.6 Histogram of weighted average zircon ages of three populations in sample 125-2.

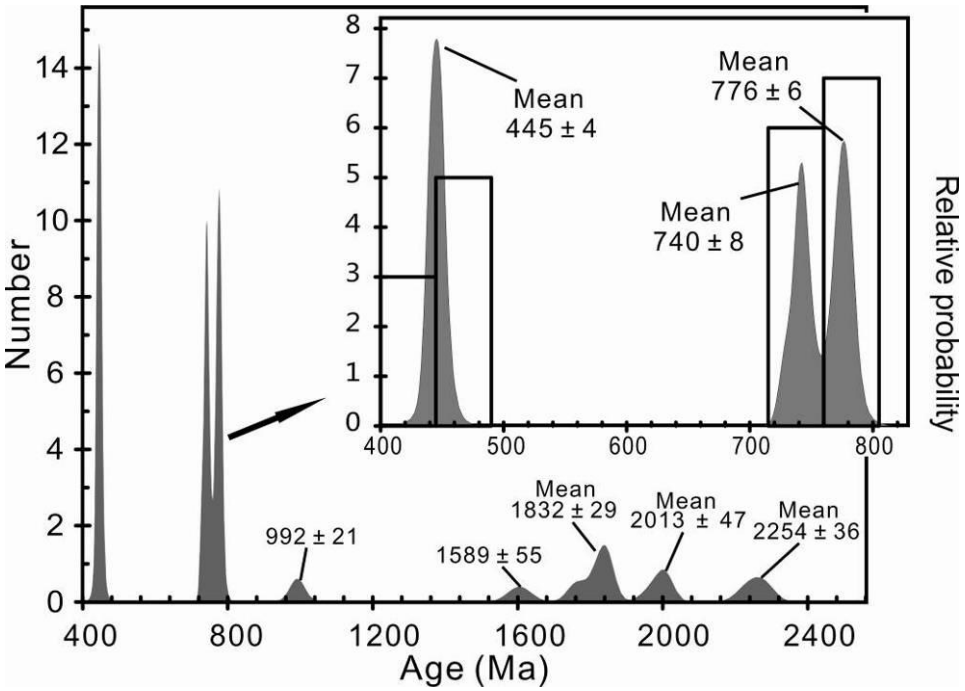

Figure 4.7 Probability histogram for U-Pb analyses from sample 125-2. Principle concordant age peaks are at ca. 445, 740 and 776 Ma. $^{206}Pb/^{238}U$ ages are used for analyses younger than 1000 Ma, and $^{207}Pb/^{206}Pb$ ages for the others. The number of grains between 400 and 800 Ma are indicated.

Age of biotite-amphibole-plagioclase gneiss 125-4

Sample 125-4 is a dark green massive and medium-grained (grain size 0.1-0.5 mm) basic rock, consisting of biotite, amphibole, plagioclase, quartz, and minor titanite,

zircon and some opaque minerals. Its sampling location is the same as sample 125-1. Zircon grains are most commonly subhedral to eueuhedral, with some grain fragments and elongated prismatic crystals up to 200 μm in length. Under plain polarized light, zircon grains of 125-4 are colorless to pale brown. Under CL imaging, the zircon grains are dark and some of them display complicated internal structures (Figure 4.8a), indicating higher Th and U contents and a possible fluid-present formation/recrystallization environment[128].

Concordia diagrams for 19 zircon U-Pb analyses are displayed in Figure 4.8b, and the U-Pb analytical results are listed in APPENDIX B. Th/U ratios for sample 125-4 zircon analytic spots varies in a wide range, from < 0.01 to 1.46. Both the Th and U contents of zircon grains are generally higher than other samples, and also show a huge variation, from less than 1 (0.67) to 17685 ppm and 327 to 13826 ppm, respectively (APPENDIX B). The zircon grains yielded a variant range of $^{206}Pb/^{238}U$ ages from 478 to 443 Ma. In the analytical data, all but one are no greater than 15% discordance and form two $^{206}Pb/^{238}U$ age populations (Figure 4.8b), with weighted average ages of 448 ± 3 Ma (95% conf., MSWD = 0.57) and 473 ± 4 Ma (95% conf., MSWD = 0.26), respectively (Figure 4.9), which are also shown in the population probability histogram (Figure 4.10). The zircon grains containing lower Th/U ratios (< 0.04) generally produce younger ages from 451 to 443 Ma, whereas ones consisting of higher Th/U ratios (> 0.7) yield both younger and older ages (Figure 4.11), which indicate that fluid-present metamorphism probably occurred at the latest period in the formation process of this rock and some analyses reflect partially recrystallized zircons with incompletely re-set U and Pb isotope compositions.

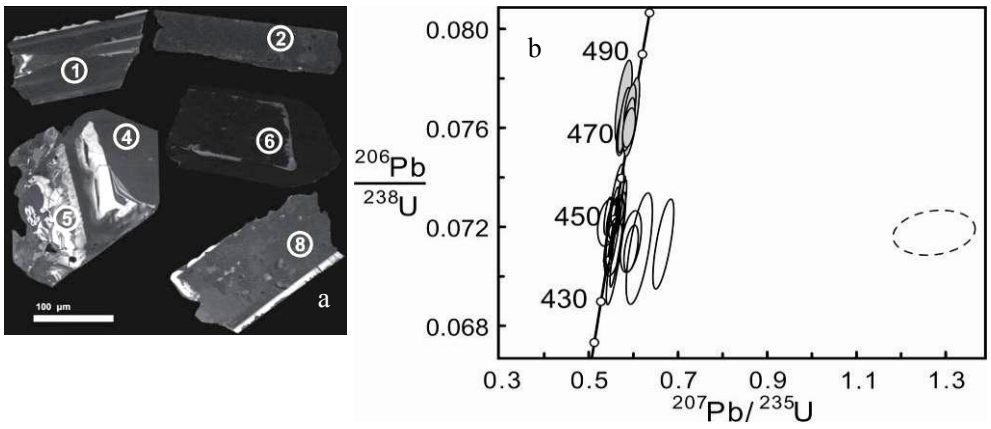

Figure 4.8 Typical cathodoluminescence (CL) images (a) and LA-ICP-MS zircon U-Pb isotopes concordia diagram (b) of zircon grains in sample 125-4. Numbers in circles (such as 1) in picture (a) represent analysis spots for U-Pb in APPENDIX B.

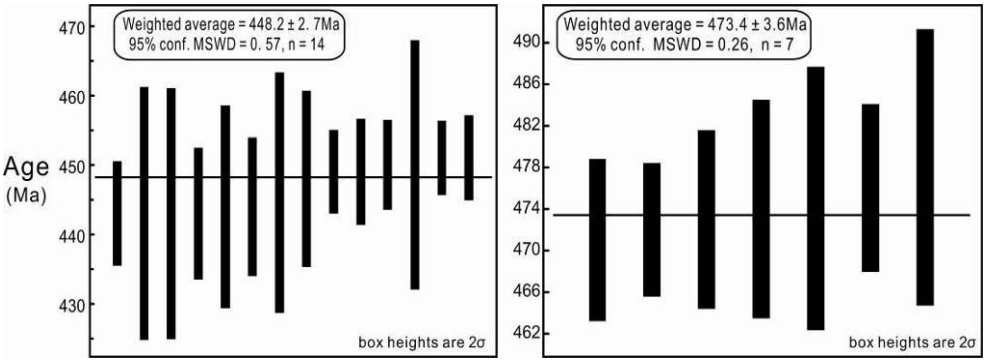

Figure 4.9 Histogram of weighted average ages of two zircon age populations in sample 125-4.

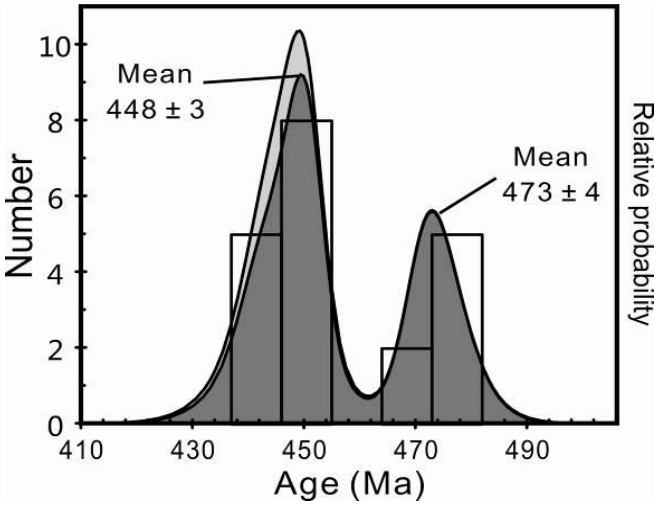

Figure 4.10 Probability histogram for <10% discordant U-Pb analyses from sample 125-4. The probability distribution plots (in light grey) include ages with >10% discordance. Principle concordant age peaks are at ca. 448 and 473 Ma. The number of grains >10% discordant are indicated.

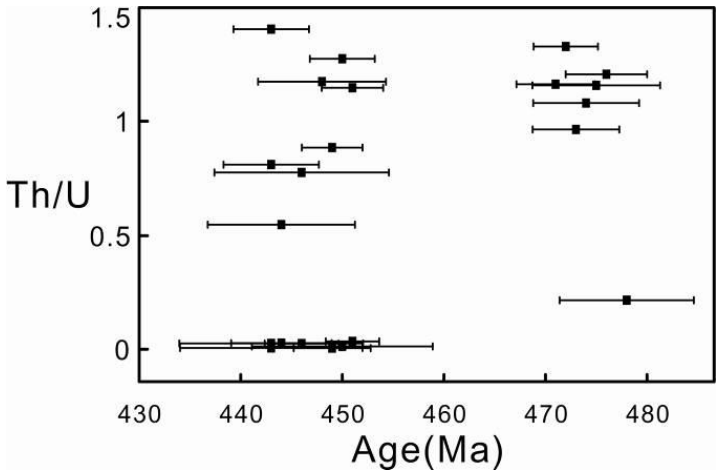

Figure 4.11 $^{206}Pb/^{238}U$ age vs. Th/U ratio plot for zircons from sample 125-4. The plot illustrates the large spread of ages and Th/U ratios that indicate some analyses on partially recrystallized zircon with incompletely re-set U and Pb isotope compositions.

2) Samples from the Luomadi area

Age of paragneiss 34-4

Sample 34-4 is a dark brown massive and fine-grained (grain size 0.1 - 0.5 mm) acid rock with gneissosity, containing biotite (partly altered to chlorite), plagioclase (altered), quartz, and minor apatite, zircon and opaque minerals (Figure 4.2). Its sampling locality is shown in Figure 2.4. Zircon grains are most commonly subhedral to rounded, with some grain fragments crystals shorter than 100 μm in length. Under plain polarized light, zircon grains of 34-4 are colorless to pale brown. Under CL imaging, three internal structure types of zircon grains could be identified. The subhedral prismatic grains display moderately well developed oscillatory zoning, with broad secondary sector zoning overprinting the oscillatory zoning. The rounded grains often show core/rim structure. Small cores of different sizes are surrounded by rims of fine oscillatory zoning or broad sector zoning then to unzoned quite thin rims. Big cores without zoning are always surrounded by very thin rims with fine oscillatory zoning (Figure 4.12a).

Concordia diagrams for thirty-four zircon U-Pb analyses are displayed in Figure 4.11b, and the U-Pb analytical results are listed in APPENDIX B. The Th/U values from 34-4 zircon analyses are fairly high, ranging from 0.26 to 2.44. Both Th and U contents are also relatively high, from 54 to 5657 ppm and 98 to 3768 ppm, respectively (APPENDIX B). Most of the analytical data plot on or near the concordia (Figure 4.12b) and yielded a range of $^{206}Pb/^{238}U$ ages between 675 and 2702 Ma. The main analytic age data are between 675 - 849 Ma, with several older inherited ages from 1115 - 2702 Ma. During young ages, two large and one small populations are displayed (Figure 4.12b). The larger populations (including 22 grains) yield two weighted average ages of 820 ± 6 Ma (95% conf., MSWD = 0.26) and 780 ± 6 Ma (95% conf., MSWD = 0.77), and the other 4 grains produce a mean age of 679 ± 10 Ma (95% conf., MSWD = 0.12) (Figure 4.13). This suggests that the significant input of the paragneiss protolith was dominantly formed by two magmatic events during Neoproterozoic (Figure 4.14). Although the very thin rims with fine oscillatory zoning are too narrow to analyze, they indicate that the protolith has been strongly reworked by later thermal events.

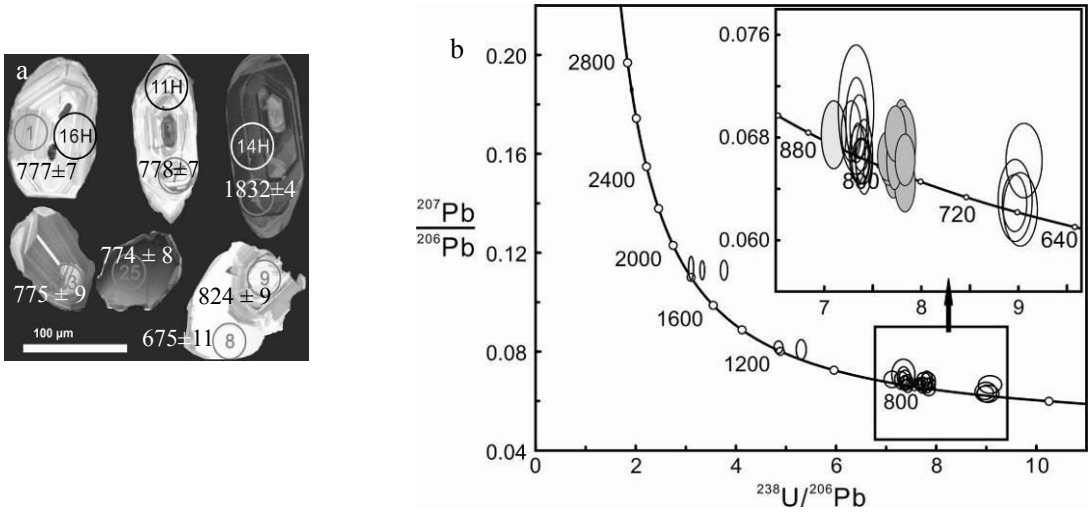

Figure 4.12 Typical cathodoluminescence (CL) images (a) and LA-ICP-MS zircon U-Pb isotopes concordia diagram (b) of zircon grains in sample 34-4. Numbers and letters in circles (such as 1, 11H) in picture (a) represent analysis spots for U-Pb, Hf isotopes in APPENDIXES B and D.

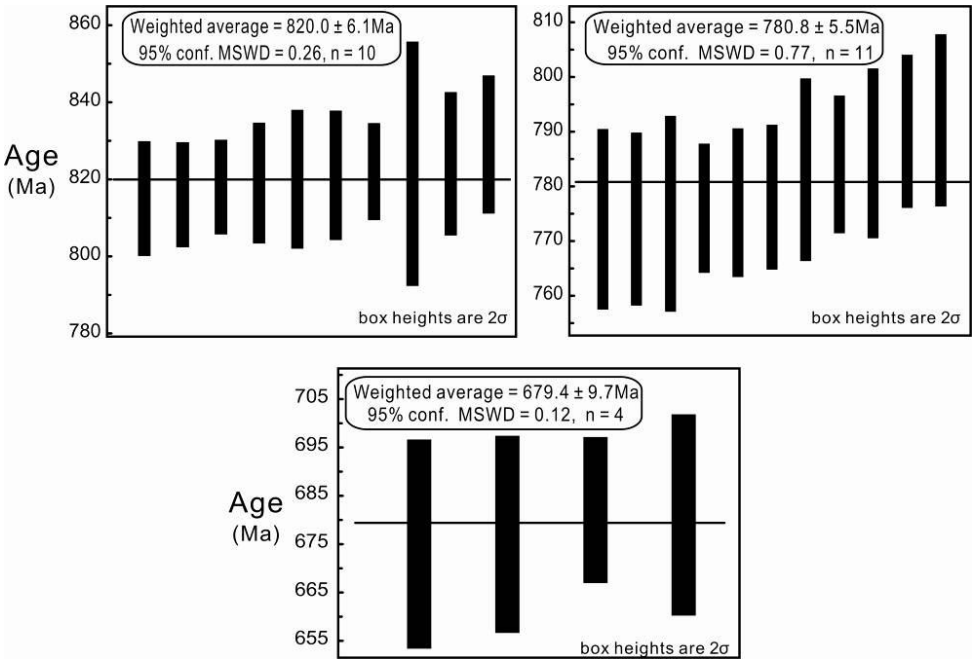

Figure 4.13 Histogram of weighted average ages of three main zircon age populations in sample 34-4.

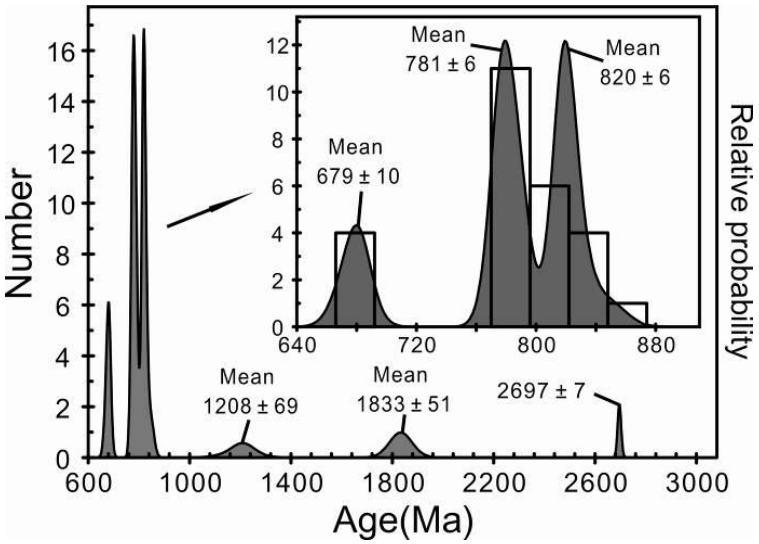

Figure 4.14 Probability histogram for the analyses of sample 34-4. Principle age peaks are at ca. 679 Ma, 781 Ma and 820 Ma.

Age of biotite-amphibole-plagioclase gneiss 39-1

Sample 39-1 is a massive and medium-grained (grain size 0.8-1.5 mm) basic rock, consisting of amphibole, biotite, plagioclase, quartz, and minor accessory minerals of titanite, zircon and opaque minerals. Its sampling location is shown on Figure 2.4. The zircon grains are either stunted or elongated prismatic almost euhedral and colorless crystals up to 100 - 300 μm in length with length/width ratios from 2:1 to 7:1. CL images reveal that most grains have core/rim structure, with strongly zoned cores surrounded by unzoned thin rims cutting their oscillatory zonation (Figure 4.15a). Some of the rims are occasionally incursive into cores, forming embayments (Figure 4.15a). Since the rims are too narrow, only 26 zircon cores were analyzed.

Concordia diagrams for zircon U-Pb analyses of sample 39-1 are displayed in Figure 4.13b, and the U-Pb analytical results are listed in APPENDIX B. The Th contents and U contents of the zircons are 20 to 545 ppm and 46 to 654 ppm, respectively and show a positive correlation. Th/U ratios are quite high, ranging from 0.75 to 2.27, which indicates that the zircon cores are of igneous origin[128]. Most of the analytical data are concordant (Figure 4.15b) and yielded a range of fairly close $^{206}Pb/^{238}U$ ages between 448 and 441 Ma with a weighted average age of 444 ± 3 Ma (95% conf., MSWD = 0.13).

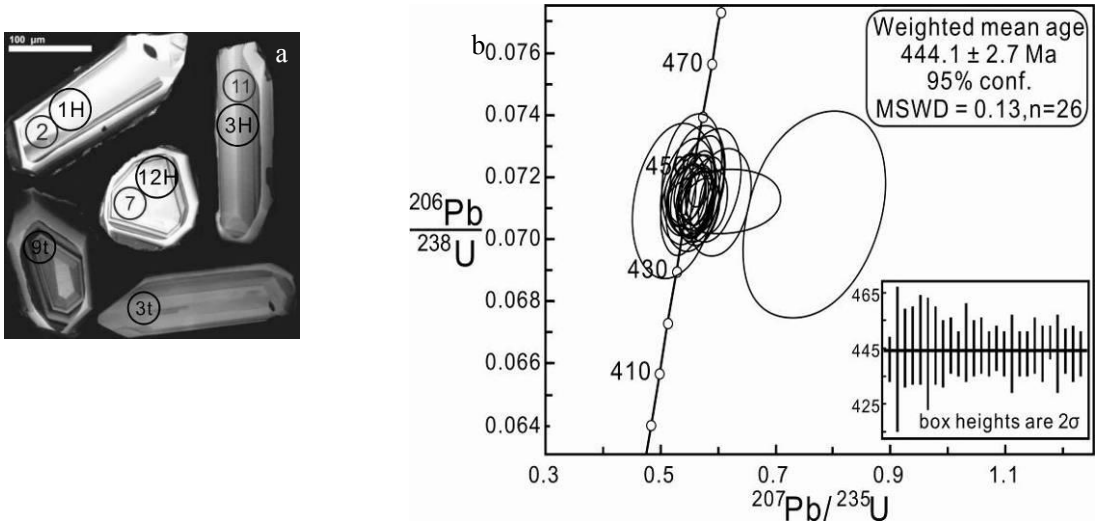

Figure 4.15 Cathodoluminescence (CL) images (a) and LA-ICPMS U-Pb isotopes (b) of zircon grains in sample 39-1. Numbers and letters in circles (such as 2, 3t and 1H) represent analysis spots for U-Pb, trace elements and Hf isotopes, respectively. The data are listed in APPENDIXES B, C and D.

§ 4.2.2 Zircon rare earth elements (REE) geochemistry

As shown in the APPENDIX C and Figure 4.16, almost all zircons yield similar REE distributions, although there are slight differences between the ones from felsic and mafic metamorphic rocks. The REE patterns are characterized by strong fractionation in both light REE (LREE) and heavy REE (HREE), with relatively smooth increases in Chondrite-normalized abundances from La to Lu, punctuated by excess Ce and Eu depletion. The intermediate and heavy REE patterns are comparability with typical magmatic zircons [129-130]. The "abnormities" appear in two samples, 125-2 and 34-4. For 125-2, spots 03t, 05t and 06t yielded same ages within error (446 ± 12, 440 ± 4 and 441 ± 4 Ma, respectively, APPENDIX B), but show different REE patterns from others. Spots 125-2-03t and 125-2-06t, showing a magmatic feature under the CL imaging (Figure 4.16a), with lower HREE than other older zircons, might suggest a slightly change of the mineral compositions in the host rocks, i.e. these zircons crystallized simultaneously with some minerals containing higher HREE. But it is still hard to explain why the spot 125-2-05 with the same age displays a different REE distribution. The analytic spot data 34-4-03t (818 ± 9 Ma), display enrichments of LREE contents, different from others. This probably indicates that some small phosphatic inclusions with higher LREE contents are present within the analytical spot, since the Th and U contents of it are not relatively much higher compared with the other studied spots (Whitehouse and Kamber, 2002; Wu and Zheng, 2004).

The size of the Ce anomaly is given by Ce/Ce* (δCe), where Ce is the chondrite-normalised Ce concentration and Ce* is the average of the chondrite-normalised La and Pr concentrations. Strongly positive Ce anomalies are found in all analyzed spots (δCe = 1 - 311). The Eu anomaly is calculated as Eu/Eu* (δEu), where Eu is the chondrite-normalised Eu value and Eu* is the average of the chondrite-normalised Sm and Gd concentrations. Zircons from felsic samples (125-1, 125-2, 34-4) display more pronounced Eu negative anomalies (δEu = 0.05 - 0.25) whereas weaker or absent Eu negative anomalies (δEu = 0.38 - 1.71) from mafic samples (125-4, 39-1) (Figure 4.16), which is in agreement with the REE distributions of the host rocks

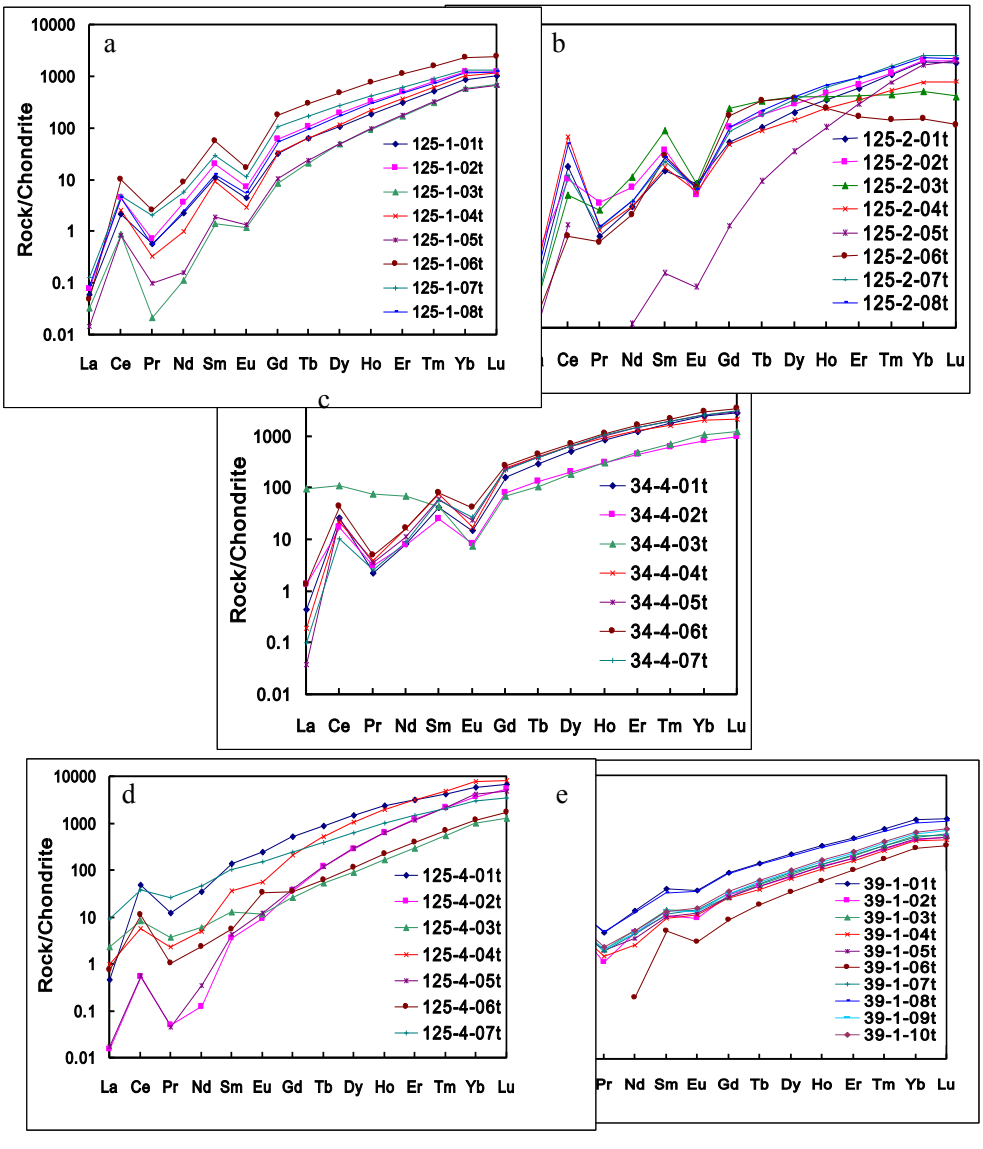

Figure 4.16 Chondritenormalized REE distributions of the zircon grains from from the samples (a) 125-1, (b) 125-2, (c) 34-4, (d) 125-4 and (e) 39-1 in the Tianjingping Complex. Positive Ce anomalies are shown in all analyzed grains. Negative Eu anomalies are strong in felsic samples and weak or absent in mafic samples.

(would be shown later). Furthermore, as shown in the δEu vs. δCe diagram, two groups of zircon grains could be identified depending on the host rocks or forming environment, from felsic and mafic samples, respectively (Figure 4.17). Thus Hf isotopes of the zircon grains from the Tianjingping Complex could be studied as two different types.

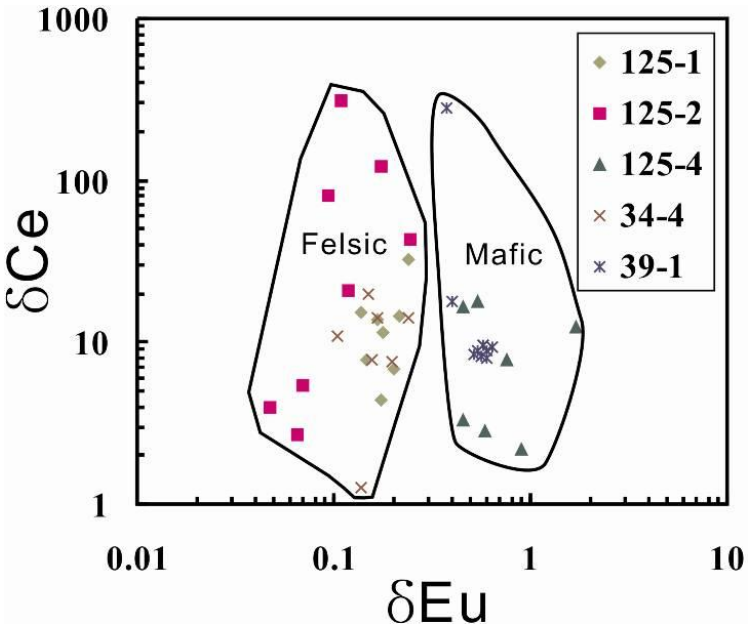

Figure 4.17 δEu and δCe correlations for zircons from different rock types

4.2.3 Hafnium (Hf) isotopes in zircon

The $^{176}Lu/^{177}Hf$ ratio of zircon is usually very low (< 0.0005), which means that time-integrated changes to the $^{176}Hf/^{177}Hf$ ratio as a result of *in situ* decay of ^{176}Lu proceed at virtually negligible rates. Therefore, zircon effectively preserves the initial $^{76}Hf/^{177}Hf$ ratio, providing an enduring record of the Hf isotopic composition of their source environment at the time of crystallization. This ratio can then be used to determine either a Hf model age or an initial ε_{Hf} value.

Lu-Hf isotopic compositions are sensitive tracers in mantle and crustal processes[126, 131], for more Hf is partitioned into the melts than Lu during mantle melting. As time goes on, the $^{176}Hf/^{177}Hf$ in the mantle would evolve to higher values than in crust.

Hence, the $^{176}Hf/^{177}Hf$ and the ε_{Hf} values can provide information about magma source and sediment provenance. Generally, high values of $^{176}Hf/^{177}Hf$ (or $\varepsilon_{Hf} >> 0$, Hf model age close to crystallization age) suggest „juvenile" mantle input, either directly via mantle-derived mafic melts, or by remelting of young, mantle-derived mafic lower crust. Low values of $^{176}Hf/^{177}Hf$ (or $\varepsilon_{Hf} << 0$, Hf model age >> crystallization age) indicate crustal reworking or contamination. Thus the former existence of old crust may be detected both directly if old detrital zircons are found and indirectly if younger detrital zircons with old Hf isotope signatures are present.

Leucogranodiorite 125-1

In-situ Lu-Hf isotope analyses were carried out alongside U-Pb dating on 12 zircons for sample 125-1. The $^{176}Hf/^{177}Hf$ ratios of the zircon grains range from 0.282121 to 0.282224. Calculated from the age of 445 Ma (471 Ma for spot 125-1-02t), The $\varepsilon_{Hf}(t)$ values are from -13.3 to -9.7, indicative for recycled continental crust. Since the $\varepsilon_{Hf}(t)$ values are all negative, more realistic Hf model ages (T_{DM}^{UC}, estimated by upper/felsic crust $^{176}Lu/^{177}Hf$ value of 0.015) are calculated. T_{DM}^{UC} values of 1728 to 1911 Ma (with a weighted mean of 1828 ± 39 Ma, Figure 4.18) imply a protolith derived from late Paleoproterozoic crust.

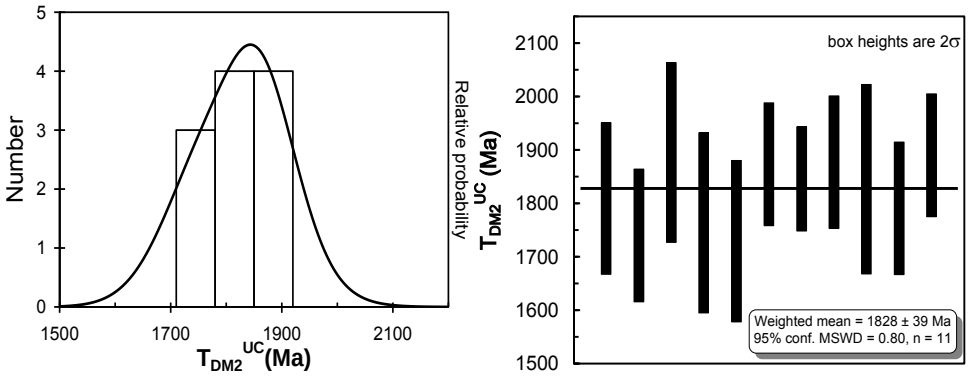

Figure 4.18 Histogram of probability and weighted average upper curst Hf model age (1828 ± 39 Ma) for sample 125-1.

Felsic Paragneiss 125-2

For sample 125-2, *in-situ* Lu-Hf isotopes of 14 zircon grains were analyzed beside the U-Pb dating spots. The $^{176}Hf/^{177}Hf$ ratios of the zircons lie between 0.281408 and 0.282203, calculated from different age populations of 445, 740, 776, 1832, 2013 and 2254 Ma according to the U-Pb dating spots. The younger zircons (445, 740 and 776 Ma) have obviously higher $^{176}Hf/^{177}Hf$ ratios than the older ones (> 1830 Ma), suggesting that the younger zircons contained more radiogenic Hf, and were probably crystallized in an environment when high HREE and Lu/Hf ratio minerals were decomposed and recrystallized. The $\varepsilon_{Hf}(t)$ values ranging from -16.7 to -1.9, except one inherited zircon with an age of 2254 Ma having a positive $\varepsilon_{Hf}(t)$

value of +4.6 (spot 125-2-11H), implying that their protolith may be derived from ancient crust or enriched mantle, with some additional depleted mantle materials. Hf model ages (T_{DM}) calculated for grain 125-2-10H Ma is 2422 ± 265 Ma. For the grains with negative $\varepsilon_{Hf}(t)$ values, upper crust Hf model ages (T_{DM}^{UC}) are calculated. T_{DM}^{UC} values exhibit two populations (Figure 4.19), one main peak from 1698 to 1978 Ma (with a 5 grains weighted mean age of 1816 ± 64 Ma), and the other from 2011 to 2764 Ma. It suggests protoliths were mostly derived from late Paleoproterozoic crust including some materials from early Paleoproterozoic to Archean crust and mantle.

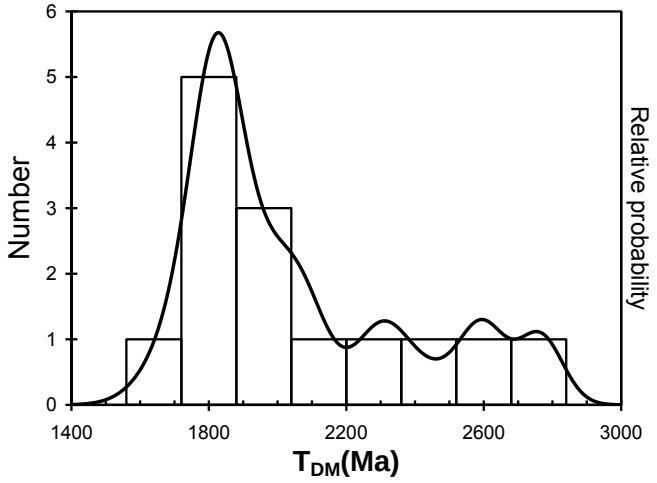

Figure 4.19 Probability histogram for the one grain of T_{DM} (2422 Ma) and T_{DM}^{UC} of sample 125-2. Principle age peak is at ca. 1840 Ma.

Biotite-amphibole gneiss 125-4

In-situ Lu-Hf isotopes of 11 zircon grains were analyzed alongside the U-Pb dating spots for sample 125-4. The $^{176}Hf/^{177}Hf$ ratios of the zircons range from 0.282014 to 0.282734, calculated from the age of 473 Ma. The $\varepsilon_{Hf}(t)$ values are from -16.6 to +7.1, suggesting that the protolith of the rocks was derived from ancient crust or enriched mantle, with additional depleted mantle materials. The spots with positive $\varepsilon_{Hf}(t)$ values have slightly higher $^{176}Hf/^{177}Hf$ ratios than ones with negative, suggesting that the mantle materials may contained higher radiogenic Hf content. Hf model ages (T_{DM}) are calculated for zircon grains with positive $\varepsilon_{Hf}(t)$ values, ranging from 853 to 1121 Ma (Figure 4.20). For the grains with negative $\varepsilon_{Hf}(t)$ values, lower crust Hf model ages (T_{DM}^{LC}, for mafic rocks) are calculated from 1880 to 3332 Ma (Figure 4.19). These imply younger mantle materials, possibly derived during late Mesoproterozoic to early Neoproterozic, were mixed with more ancient crust materials.

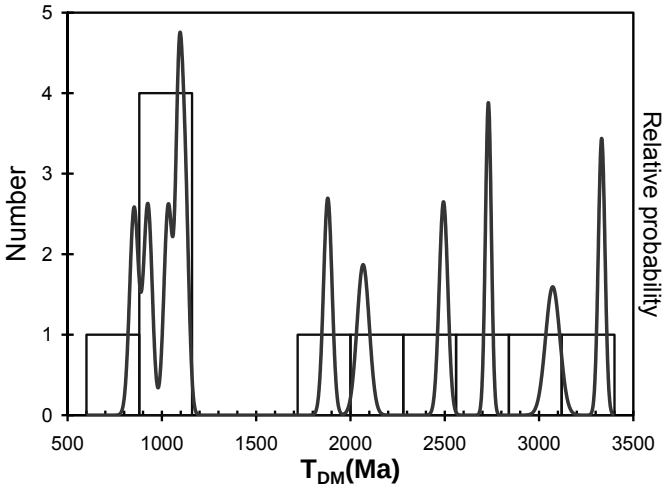

Figure 4.20 Probability histogram for the T_{DM} of sample 125-4. T_{DM} (<1200 Ma) and T_{DM}^{LC} (>1200 Ma) are presented for zircon grains with positive and negative $\varepsilon_{Hf}(t)$ values, respectively.

Felsic Paragneiss 34-4

For sample 34-4, *in-situ* Lu-Hf isotopes of 17 zircon grains were analyzed beside the U-Pb dating spots. The $^{176}Hf/^{177}Hf$ ratios of the zircons lie between 0.281943 and 0.282085, calculated from different age populations of 781, 820, 1208, 1833 Ma and single age data of 849 and 2696 Ma based on the U-Pb dating spots. The younger zircons (< 1300 Ma) have slightly higher $^{176}Hf/^{177}Hf$ ratios than the older ones (> 1800 Ma), suggesting that the younger zircons contained more radiogenic Hf. The $\varepsilon_{Hf}(t)$ values ranging from -24.0 to -1.4, implying that their protolith may be derived from ancient crust or enriched mantle. For the grains with negative $\varepsilon_{Hf}(t)$ values, upper curst Hf model ages (T_{DM}^{UC}) are calculated from 1874 to 3133 Ma (Figure 4.21). It suggests a protolith were mostly derived from crust materials older than late Paleoproterozoic.

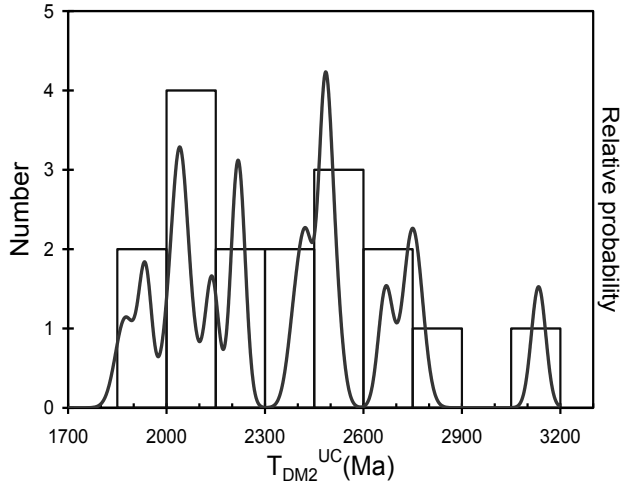

Figure 4.21 Probability histogram for the T_{DM}^{UC} of sample 34-4.

Amphibole-plagioclase gneiss 39-1

For sample 39-1, *in-situ* Lu-Hf isotopes analyses of 16 zircon grains were carried out alongside the U-Pb dating spots. The $^{176}Hf/^{177}Hf$ ratios of the zircons lie between 0.282086 and 0.282408, calculated from the age of 444 Ma. The $\varepsilon_{Hf}(t)$ values are from -14.8 to -3.3, suggesting that the protolith of the rocks was derived from ancient crust. Since the zircon $\varepsilon_{Hf}(t)$ values of the mafic sample 39-1 are all negative, lower crust Hf model ages (T_{DM}^{LC}) are calculated. T_{DM}^{LC} values of 2125 to 3153 Ma (Figure 4.22) imply a protolith derived from crust materials formed during Archean to Paleoproterozoic.

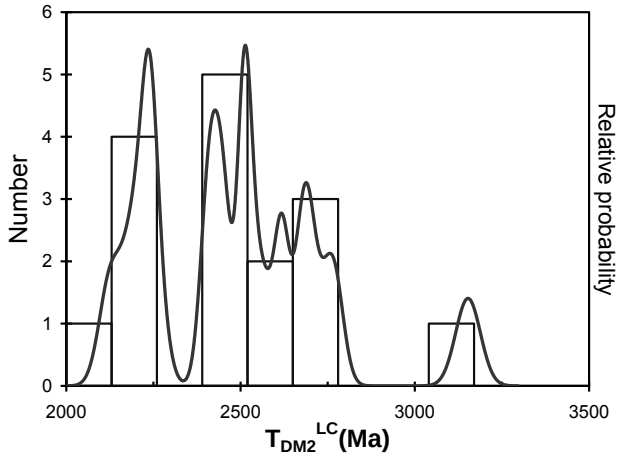

Figure 4.22 Probability histogram for the T_{DM}^{LC} of sample 39-1.

In sum, most of zircon grains analyzed contain high Th/U (0.13 - 2.44, n = 118) including all dated ages from ~2700 to ~440 Ma. The zircons with lower Th/U (> 0.06, n = 15) are always dated to be 440 - 451 Ma. Zircon grains selected from leocosome and metamafic samples (sample 125-1, 125-4 and 39-1) yield younger ages between 436 and 478 Ma, whereas those from paragneisses produce much wider range of ages from 681 to 2696 Ma. All these zircons could be divided into two types, one of which is from felsic samples and the other is from mafic samples, according to their REE patterns and trace element characteristics. The Hf model ages calculated for these zircons vary a lot in all the samples, ranging from ~853 to ~3613 Ma. Generally, zircon Hf model ages for mafic samples are slightly older than those for felsic samples, except the ones with positive $\varepsilon_{Hf}(t)$ values (0.2 - 7.1, T_{DM} = 853 - 1121 Ma).

4.2.4 Amphibole and biotite $^{40}Ar/^{39}Ar$ thermochronology

The goal of the $^{40}Ar/^{39}Ar$ thermochronology study part is to constrain the cooling and exhumation history of the high-grade metamorphic rocks of the Tianjingping Complex. Using different K-bearing mineral phases such as amphibole, muscovite, biotite, and K-feldspar, with different argon closure temperatures, the $^{40}Ar/^{39}Ar$ thermo- chronologic method allows the reconstruction of temperature-time curves,

which are an important guide in deciphering the exhumation history. In this study, because of the alteration of K-feldspar and lack of muscovite, only fresh amphibole and biotite were analyzed. Amphibole grains and biotite flakes were separated from amphibole-plagioclase gneiss boudins likely derived from mafic intrusives transposed and disrupted in the migmatite. Two biotite samples (125-4, 31-7) from the Min-Gan boundary area and one amphibole sample (39-1) from the Luomadi area were analyzed. The locations of these samples are shown in Figure 2.4

1) Samples from the Min-Gan boundary area

Age of biotite-amphibole-plagioclase gneiss 125-4

A biotite cleavage flake (690 × 380 μm) separated from sample 125-4 (Figure 4.23a) produced a concordant weighted mean plateau age of 370.1 ± 3.0 Ma (2σ, MSWD = 1.29, probability of fit = 0.26, including J-error), which were defined by seven consecutive gas fractions comprising 86% of released ^{39}Ar (Figure 4.23b & Appendix E). The two lowest temperature steps exhibit younger apparent ages, but together represent only 14% of the ^{39}Ar released. The plateau age is considered to represent the timing of cooling through the closure temperature for argon diffusion in biotite (ca. 300 °C, Grove and Harrison 1996).

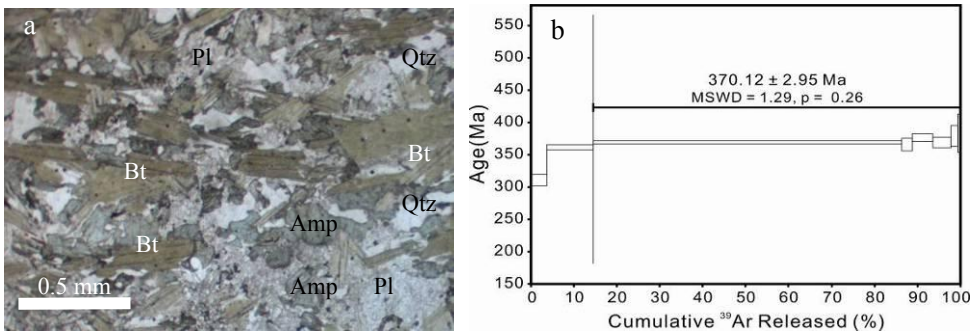

Figure 4.23 Photomicrograph of sample 125-4 (a) and associated biotite (b) ^{40}Ar/^{39}Ar age spectrum. Mineral abbreviations biotite (Bt), amphibole (Amp), plagioclase (Pl), quartz (Qtz).

Age of biotite-amphibole-plagioclase gneiss 31-7

A biotite (470 × 390 μm) from sample 31-7 (Figure 4.24a) yielded a flat age spectrum with a total fusion age of 384.1 ± 3.6 Ma (2σ) and a weighted mean plateau age of 391.8 ± 3.8 Ma (2σ, MSWD = 0.91, probability of fit = 0.47, including J-error), which were established by six successive gas fractions incorporating 84% of released ^{39}Ar (Figure 4.24b & Appendix E). The first two steps show younger apparent ages. The plateau age is considered to reflect the time of biotite cooling through ca. 300 °C[132].

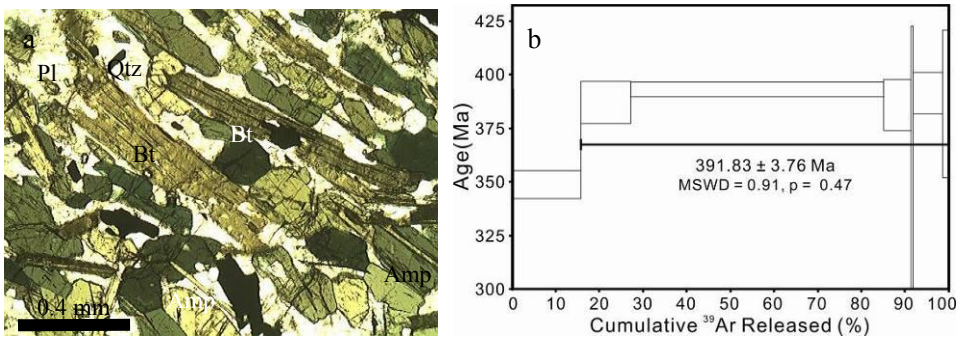

Figure 4.24 Photomicrograph of sample 31-7 (a) and associated biotite (b) $^{40}Ar/^{39}Ar$ age spectrum. Mineral abbreviations biotite (Bt), amphibole (Amp), plagioclase (Pl), quartz (Qtz).

2) Samples from the Luomadi area

Age of amphibole-plagioclase gneiss 39-1

Multiple amphibole grains (filled in a Nb package with size of 3467 × 2761 μm, 3mg) extracted from sample 39-1 (Figure 4.25a) yielded a more discordant age spectrum with apparent ages generally fluctuant with increasing temperature (Figure 4.25b), for a total fusion age of ~473 Ma with no geological meaning (Appendix E). The amphibole from this sample exhibits a complicated variation, suggesting that the discordance might be related to the inclusions of older events.

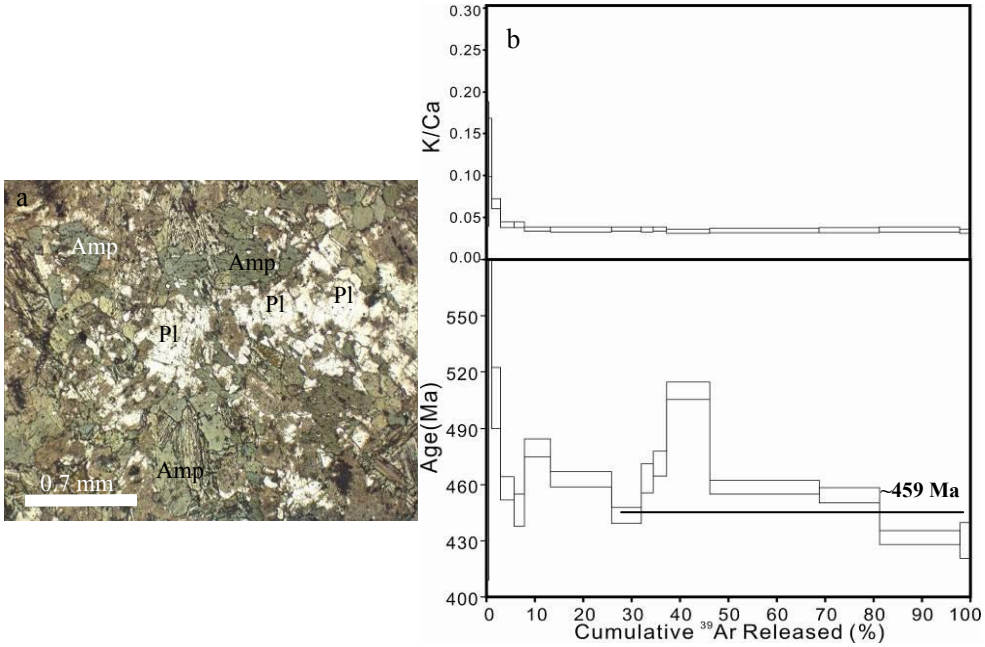

Figure 4.25 Photomicrograph of sample 39-1 (a) and associated biotite (b) $^{40}Ar/^{39}Ar$ age spectrum. Mineral abbreviations biotite (Bt), amphibole (Amp), plagioclase (Pl), quartz (Qtz).

§ 4.3 Whole rock geochemical analysis

The samples from the Tianjingping Complex for the geochemical analysis are classified into three types: leucosome, metamafic rocks and paragneiss.

4.3.1 Geochemistry features of leucosome

Major and trace elemental compositions of ten homogeneous leucosome samples from the Tianjingping Complex are listed in APPENDIX F. The leucosome samples have variable compositions with SiO_2 contents of 57.38 - 72.89%, K_2O + Na_2O contents from 5.20 to 10.83%. All the samples, except two (34-1, 125-5), have a range of Rittman index (δ) between 1.2 and 3.0 and thus belong to the calc-alkaline series. All samples but one are in the peraluminous field in the A/CNK-A/NK diagram (Figure 4.26a), with A/CNK from 0.97 to 1.11. All the samples plot in the granite and granodiorite fields in the An-Ab-Or diagram (Figure 4.26b).

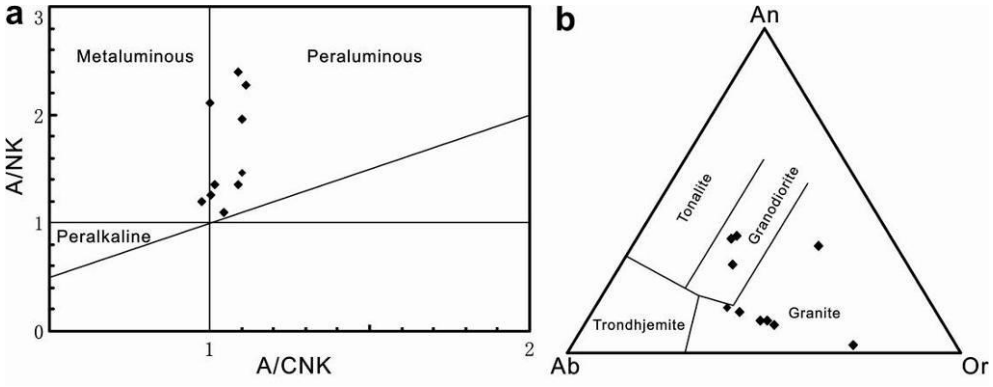

Figure 4.26 (a) A/NK-A/CNK diagram[133] and (b) molecular normative An-Ab-Or diagram[134] for leucosome from the Tianjingping area.

Samples 125-1 and 125-2, from which zircons for this study were collected, are in the granodiorite and granite fields, respectively. The samples have a range of total REE contents between 73 and 258 ppm. Chondrite-normalized REE patterns (Figure 4.27a) show that the samples are enriched in LREEs relative to HREEs (LREE/HREE = 2.15 to 20.94) and have a weak negative Eu anomaly (δEu = 0.48 to 1.19). Both REE patterns and spidergrams (Figure 4.27b) for the leucosome are comparable with those of middle to upper continental crust, for example by showing enrichment of Rb, Th, K and LREEs and relative depletion of HFSEs (Ba, Nb, Ta, Sr, Zr, Hf, Ti, ect.) and HREEs.

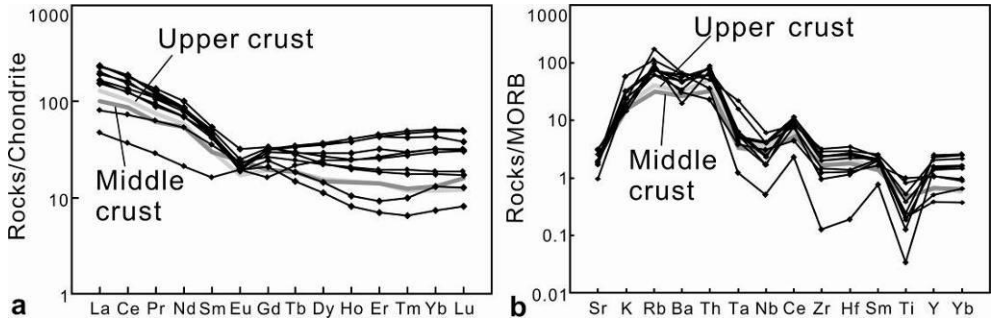

Figure 4.27 (a) Chondrite-normalized REE compositoinal patterns and (b) primitive mantle-normalized trace patterns for leucosomes from the Tianjingping area. Chondrite, MORB, upper and middle crust values are from references [135-137].

4.3.2 Geochemistry features of meta-mafic rocks

Seven metamafic rock samples from the Tianjingping area were analyzed in this study, and their major and trace elemental compositions are listed in APPENDIX F. Petrographic features indicated that these mafic rocks underwent varying degrees of alteration, consistent with their relatively high LOI (loss of ignition) values ranging from 0.28 to 7.60%. Therefore, the alteration effects on chemical compositions of these rocks need to be evaluated. Zirconium in mafic rocks is generally considered to be the most immobile during low- to medium-grade except severe seafloor-hydrothermal alteration[138-139]. A number of elements of different geochemical behaviors, including Ce, Y, TiO_2, Nb, V, Th, Ba, Sr and Rb, are plotted against Zr (Figure 4.28) to evaluate their mobility during alteration. Among the studied mafic rocks, sample 43-1 has the lowest LOI value (0.28%), suggesting insignificant alteration effect on their geochemical composition. The rare earth elements (REE) are tightly correlated with Zr, and the high-field-strength elements (HFSE such as Ti and Nb) increase with increasing Zr, despite slightly scattered samples, indicating that these elements are essentially immobile during alteration. On the contrary, alkaline (e.g. Rb), alkaline earth elements (e.g. Sr and Ba), siderophile (e.g. V) elements and Th are more or less scattered around, implying varying degrees of mobility during the alteration. Thus, only the immobile elements are used for rock classification and further petrogenetic discussions.

These mafic rocks have low SiO_2 (42.67 - 55.54%), high MgO (4.39 - 10.56%) and total alkalis ($Na_2O + K_2O$ = 3.82 - 5.86%) (APPENDIX F). On the Zr/TiO_2 vs. Nb/Y diagram[140], all samples plot into the subalkaline basalt filed (Figure 4.29a). On the TFeO/MgO versus SiO_2 plots[141] (Figure 4.29b), they plot into different fields. Samples 31-5, 31-7 and 41-3 (Group A1) exhibit typical tholeiitic composition, whereas samples 39-1, 39-2, 125-3 and 125-4 (Group A2) show calc-alkaline features. All the mafic rocks are highly evolved in compositions with Mg# ranging from 14 to

57. The samples have a range of total REE contents between 62 and 250 ppm.

The two groups of the metamafic rocks have distinctly different REE and trace elements characteristics, although the Chondrite-normalized REE patterns (Figure 4.30a) show that all the samples are slightly enriched in LREEs relative to HREEs (LREE/HREE = 4.35 to 7.03) and almost have no Eu anomaly (δEu = 0.85 to 1.06). Group A1 samples are significantly higher in total REE contents and total trace elements than those of Group A2. The primitive mantle-normalized spidergrams of Group A1 are characterized by moderate enrichments in most trace elements (Figure 4.30b), with slight depletions in Nb and Ta relative to La and Th, in P relative to Pr and Nd, in Zr and Hf relative to Nd and Sm, and in Ti relative to Eu and Gd, except the enrichment in Nb and Ta of sample 41-3 and in Ti of sample 31-7. In contrast, Group A2 samples exhibit a greater depletion in Nb and Ta relative to La and Th, in P relative to Pr and Nd and in Ti relative to Eu and Gd.

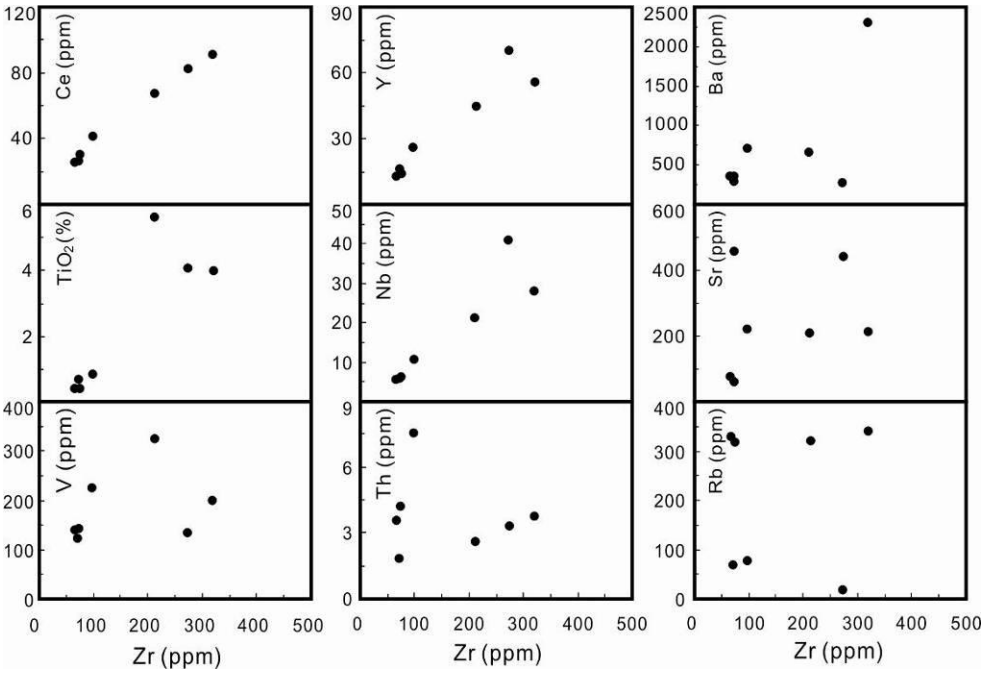

Figure 4.28 Plots of Ce, Y, TiO_2, Nb, V, Th, Ba, Sr, and Rb vs. Zr to evaluate the mobility of these elements of different geochemical behavior during alteration.

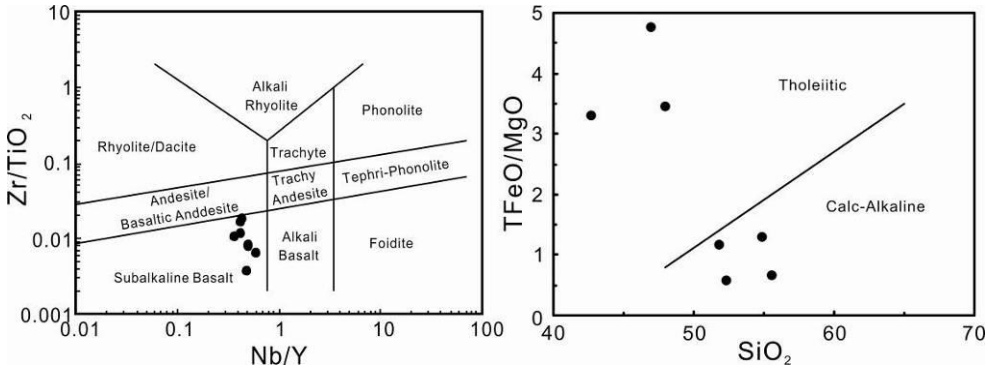

Figure 4.29 (a) Zr/TiO_2 vs. Nb/Y diagram classification[142] and (b) TFeO/MgO vs. SiO_2 plots[141] for the metamafic rocks in the Tianjingping Complex.

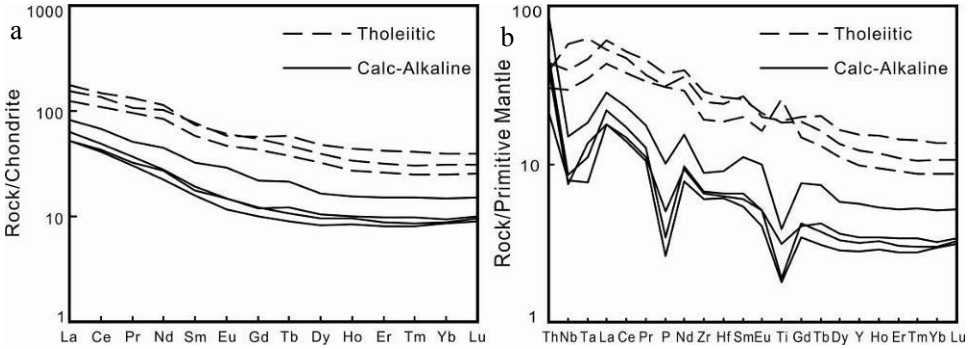

Figure 4.30 (a) Chondrite-normalized REE compositoinal patterns and (b) primitive mantle-normalized trace element distribution diagrams for metamafic rocks from the Tianjingping Complex. Chondrite and Primitive Mantle values are from reference [135] (not including Rb, Ba, U, K, Pb, Sr).

4.3.3 Geochemistry features of paragneiss

Major and trace elemental compositions of nine paragneiss samples from the Tianjingping Complex are listed in APPENDIX F. These rocks have variable SiO_2 (61.79 - 67.87%), Al_2O_3 (12.26 - 17.23%) and Na_2O (0.59 - 4.85%), relatively high K_2O (2.22 - 4.05%) and low MgO (1.35 - 3.51%). These samples are plotted in (Na + Ca) / (Na + Ca + K) versus Si / (Si + Al) (atomic proportions) in Figure 4.31 which defines compositional fields for various sedimentary rocks[143]. Most of the paragneiss samples plot in greywacke area with a few arkose and lithic arenite compositions, and two of them plot on the boundary line of graywacke and mudstone. These two samples (31-4 and 31-8) are intermediate rocks with biotite completely altered to chlorite which may slightly modified their initial compositions.

The samples have a relatively large variable range of total REE contents from 119 to 369 ppm. Chondrite-normalized REE patterns (Figure 4.32a) show that the samples are enriched in LREEs relative to HREEs (LREE / HREE = 7.26 - 12.96) and display well-developed negative Eu-anomalies (δEu = 0.41 - 0.73). Primitive mantle-normalized spidergrams (Figure 4.32b) show obvious negative anomalies of Nb, Ta and Ti for all the samples, but slightly negative Zr- and Hf- anomalies and positive Sm-anomalies for three samples (31-10 from Min-Gan area, 34-4 from Luomadi area and 41-1 from Tianjingping area). The close similarity among the paragneiss samples from three areas in the Tianjingping Complex in both REE patterns and spidergrams attests similar sedimentary sources for the protoliths.

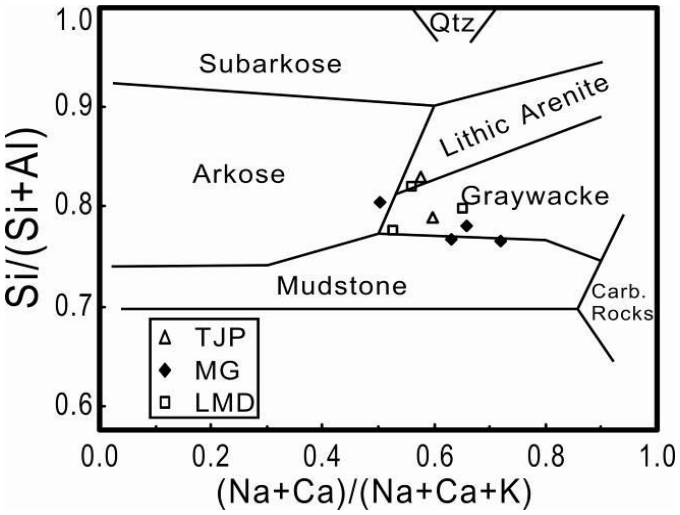

Figure 4.31 Atomic proportions of (Na + Ca) / (Na + Ca + K) vs. Si / (Si + Al)[143] for protoliths of paragneiss samples. Abbreviations: TJP = Tianjingping area; MG = Min-Gan area; LMD = Luomadi area

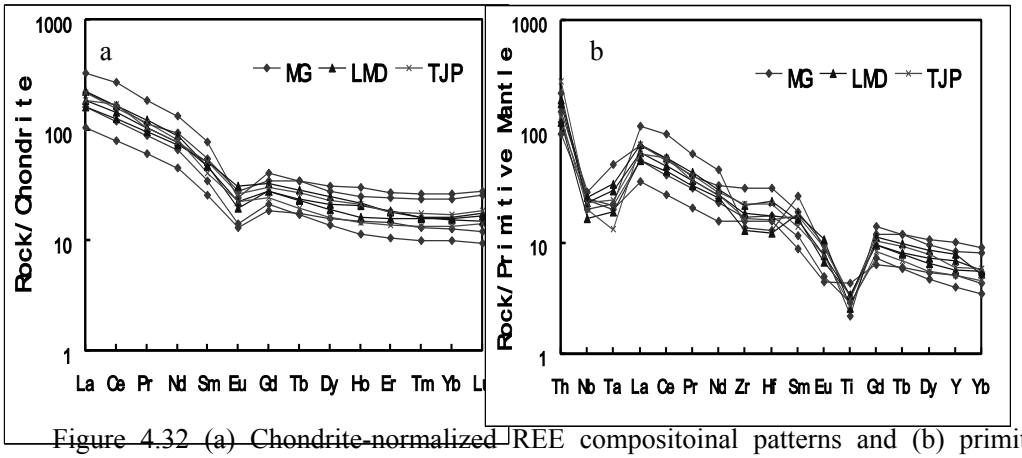

Figure 4.32 (a) Chondrite-normalized REE compositoinal patterns and (b) primitive mantle-normalized trace element distribution diagrams for paragneiss rocks from the Tianjingping Complex. Chondrite and primitive mantle values are from reference [135] (not including Rb, Ba, U, K, Pb, Sr). Abbreviations: MG = Min-Gan area; LMD = Luomadi area; TJP = Tianjingping area

In zircon, the titanium content is dependent on the temperature of its crystallization, thus can be used as geothermometer. Titanium-in-zircon (hereafter called Ti-in-zircon) thermometer[144-145] provide a link between the chronologic and geochemical information preserved in zircon.

The contents of trace element ^{49}Ti were analyzed when detect trace elements in zircon grains. In the Tianjingping Complex, ^{49}Ti contents of zircon grains are similar from either mafic (4-27 ppm) or felsic (3-38 ppm) samples (APPENDIX C). Then the formula Log (Ti_{zircon}) = (6.01 ± 0.03) − (5080 ± 30) / [T (K) / a_{TiO2}][144, 146-147] is used to calculate the mean crystallization temperature of these zircons. The thermometer was calibrated under rutile-saturated conditions (a_{TiO2} = 1). Since there are no rutile discovered in those samples, the ideal equation is adjust to reflect a_{TiO2} ≈

0.6[144], appropriate for titanite and titanomagnetite saturation, as follows: T (°C) = (5080 ± 30) / [(6.01 ± 0.03) − Log (Ti_{zircon} / 0.6)] − 273. The calculated crystallization temperatures for zircons with ages of about 450 to 440 Ma ranged from 608 ºC to 779 ºC (APPENDIX C), which is consistent with the upper amphibolite facies metamorphism or anatexis as defined by petrologic observations.

§ 4.4 Pressure-Temperature conditions estimation of the Tianjingping Complex

4.4.1 Ti-in-zircon geothermometer

In zircon, the titanium content is dependent on the temperature of its crystallization, thus can be used as geothermometer. Titanium-in-zircon (hereafter called Ti-in-zircon) thermometer[144-145] provide a link between the chronologic and geochemical information preserved in zircon.

The contents of trace element ^{49}Ti were analyzed when detect trace elements in zircon grains. In the Tianjingping Complex, ^{49}Ti contents of zircon grains are similar from either mafic (4 - 27 ppm) or felsic (3 - 38 ppm) samples (APPENDIX C). Then the formula Log (Ti_{zircon}) = (6.01 ± 0.03) − (5080 ± 30) / [T (K) / a_{TiO2}][144, 146-147] is used to calculate the mean crystallization temperature of these zircons. The thermometer was calibrated under rutile-saturated conditions (a_{TiO_2} = 1). Since there are no rutile discovered in those samples, the ideal equation is adjust to reflect $a_{TiO_2} \approx$ 0.6[144], appropriate for titanite and titanomagnetite saturation, as follows: T (°C) = (5080 ± 30) / [(6.01 ± 0.03) − Log (Ti_{zircon} / 0.6)] − 273. The calculated crystallization temperatures for zircons with ages of about 450 to 440 Ma ranged from 608 ºC to 779 ºC (APPENDIX C), which is consistent with the upper amphibolite facies metamorphism or anatexis as defined by petrologic observations.

4.4.2 Mineral assemblages geothermobarometer

In the Tianjingping Complex, three samples (paragneiss 34-4 and biotite-amphibole-plagioclase gneiss 125-4 and amphibole-plagioclase gneiss 39-1) have been selected for pressure-temperature analyses. Since plagioclase grains are almost altered to clay minerals in sample 125-4, no reasonable result can be calculated. Following touched mineral assemblages are found for microprobe analysis: biotite + garnet and amphibole + garnet in sample 34-4 (Figure 4.33a) and amphibole + plagioclase in sample 39-1 (Figure 4.33b). For each sample, analytical spots close to each other are matched as pairs to calculate the pressure-temperature conditions. Because of the lack of plagioclase in sample 34-4 and most of which has been

altered, pressure was hardly calculated.

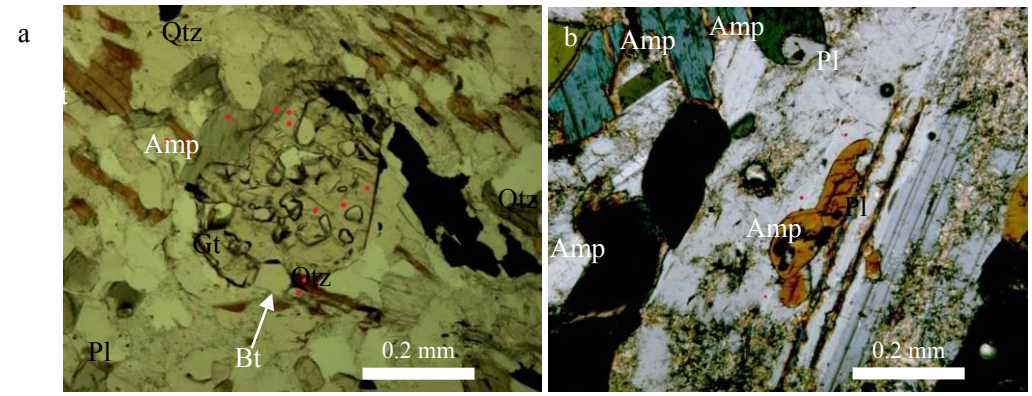

Figure 4.33 Typical mineral assemblages in sample 34-4 (a) and 39-1 (b) under plane polarized (a) and cross polarized (b) light. (a) amphibole + garnet, biotite + garnet; (b) amphibole + plagioclase; Red dots stand for analytical spots. Abbreviations: Gt = garnet, Pl = plagioclase, Amp = amphibole, Bt = biotite, Qtz = quartz.

In sample 34-4, four garnet grains surrounded by biotite and amphibole are found, and totally 26 spots are selected for analyses including 14, 7 and 5 spots for garnet, amphibole and biotite, respectively. Garnet grains are less than 300 μm in length, pale pink, anhedral crystals with tiny quartz inclusions and similar in element content without obvious zoning. Based on the EPMA data, slightly different Mg# values (Mg / (Mg+Fe)) between 0.082 and 0.099, and four garnet end members (X_{alm} = 53.7% - 58.0%, X_{pyr} = 9.0% - 11.4%, X_{gros} = 16.2% - 21.1% and X_{sps} = 14.5% - 19.3%) are calculated (APPENDIX G). Amphibole grains are much smaller either in matrix or touched by garnet, commonly less than 200 μm in length and 50 μm in width (Figure 4.2, 4.33). They can be easily observed by their obvious poly chroism, dark green-pale yellow. According to the EMPA data of amphiboles, Mg# values slightly vary from 0.396 to 0.442 (APPENDIX G). The obtained temperature data from the garnet-biotite grains are slightly higher, varying from 645 to 765 ºC (mean T = 696 ºC), whereas results from garnet-amphibole are lower between 469 and 529 ºC (mean T = 498 ºC).

In sample 39-1, 9 spots are selected for both amphibole and plagioclase. Amphibole grains are lager than the ones in sample 34-4, generally from 50 to 500 in length (Figure 4.24, 4.33). According to the EMPA data of amphiboles, Mg # values slightly vary from 0.462 to 0.481 (APPENDIX G). Both pressure and temperature could be calculated by the Amp-Pl geothermobarometer. Yielded pressure results are quite high, 8 - 14 kbar (mean P = 11 kbar), and the temperature data ranging from 722 to 799 ºC (mean T = 757 ºC).

§ 4.5 Discussions on the Tianjingping Complex

4.5.1 Depositional ages of protoliths and reworking

The Tianjingping Complex has been believed as the oldest metamorphic rock series in the NE Cathaysia Block since early 1990s from the viewpoint of geochronology study[33, 35, 101-102]. According to the U–Pb ages combined with the Hf isotopic features of zircons from both felsic and mafic gneiss, protliths of the Tianjingping Complex are evidently multi-sources formed in different periods. As shown in Figure 4.34, the majority of the zircons have Th/U > 0.4, characteristic of an igneous origin[114, 148].

Fiftiy-five zircon grains with Precambrian ages (~2700 - ~740 Ma) have been identified, all of which are from paragneiss samples, and one of them is dated as old as Archean age (2696 ± 7 Ma, Spot 34-4-07t). The oscillatory zoning, together with high Th/U ratios of 0.26 - 2.44, suggests that these zircons are of igneous origin. The youngest cluster of these zircons is at ~680 Ma (Figure 4.34), suggesting a maximum depositional age no older than middle Neoproterozoic.

Among the zircons from felsic samples, 42 of the 43 grains measured for Hf isotopes have negative $\varepsilon_{Hf}(t)$ values in the range from -24.0 to -1.5 and the other one has positive $\varepsilon_{Hf}(t)$ value of +4.6. The zircon with positive $\varepsilon_{Hf}(t)$ value yields T_{DM} of 2.42 Ga, suggesting juvenile crustal additions during early Paleoproterozoic. The zircon grains with negative $\varepsilon_{Hf}(t)$ values produce T_{DM}^{UC} varying from 3.13 to 1.70 Ga, indicating that their source rocks are recycled ancient continental crust materials formed from Neoarchean to late Paleoproterozoic.

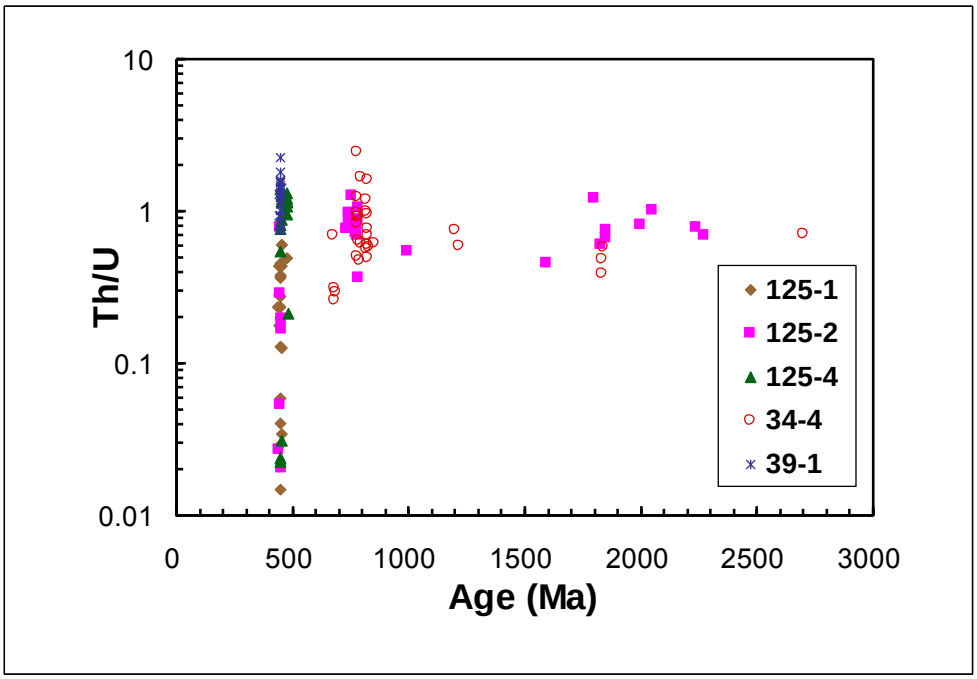

Figure 4.34 Plots of Th/U ratios vs. U–Pb ages of all concordant zircons in the Tianjingping Complex

For the zircons from mafic samples, 27 grains are measured for Hf isotopes and 22 of them have negative $\varepsilon_{Hf}(t)$ values between -16.6 to -0.3 and the other five have positive $\varepsilon_{Hf}(t)$ value ranging from +0.3 to +7.1. All the five grains with positive $\varepsilon_{Hf}(t)$ values are from sample 125-4, and yields T_{DM} between 1121 to 853 Ma, implying depleted mantle materials input during late Mesoproterozoic to early Neoproterozoic. The zircon grains with negative $\varepsilon_{Hf}(t)$ values produce T_{DM}^{LC} varying from 3.33 to 1.88 Ga, suggesting that their source rocks are recycled ancient crust materials formed during Paleoarchean to late Paleoproterozoic, slightly earlier than the protoliths of felsic rocks.

Typical metamorphic Th/U ratios (< 0.1) occur sporadically only for the youngest zircons of ~440 - ~451 Ma old (Figure 4.35), indicating metamorphism possibly occurred later. Thus, considering all the concordant U-Pb zircon ages with either high or low Th/U ratios from the Tianjingping Complex, the main peaks of most samples in the Min-Gan boundary or Luomadi areas are 445 ± 3 Ma (125-1), 445 ± 4 Ma (125-2), 448 ± 3 Ma (125-4) and 444 ± 3 Ma (39-1), which are consistent within error, implying a widespread anatectic reworking during Late Ordovician.

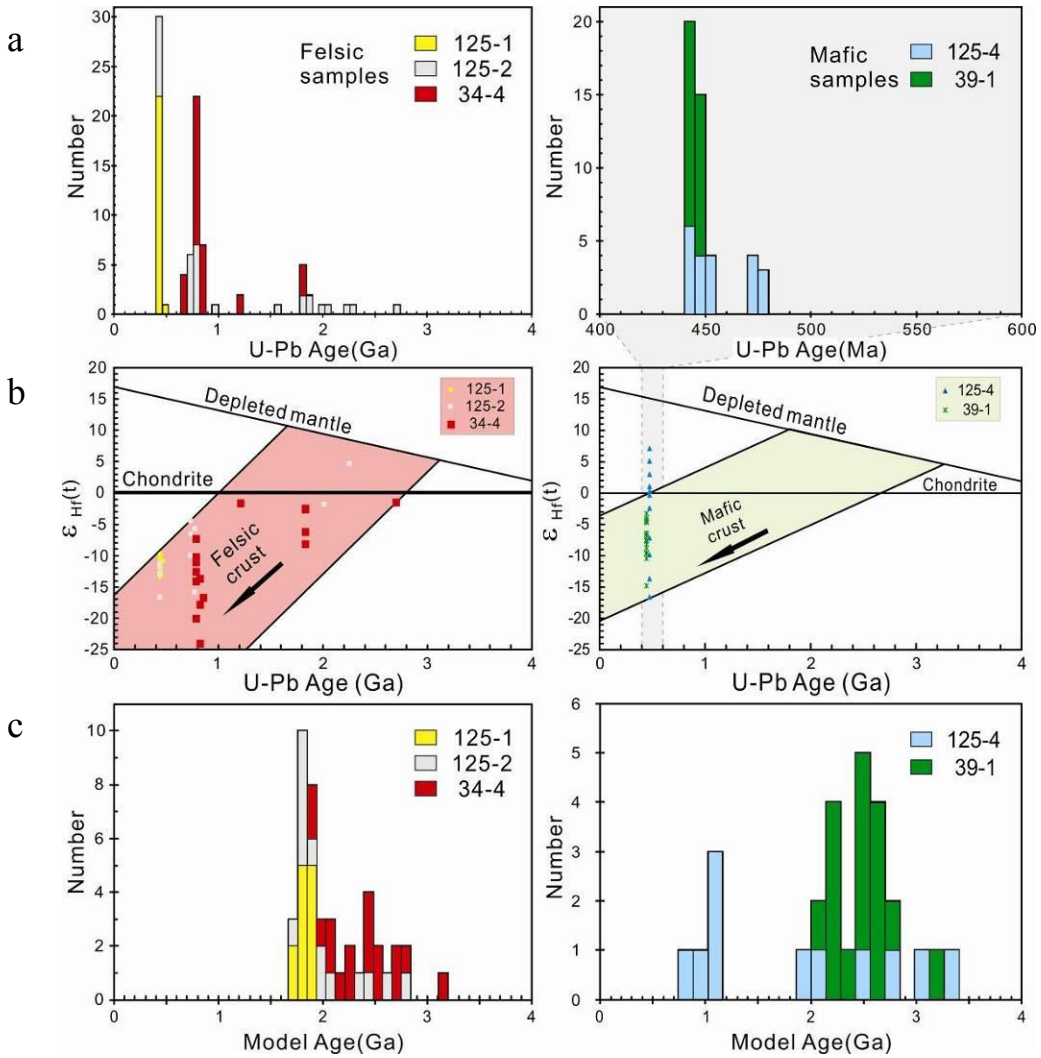

Figure 4.35 U–Pb age histograms (a), $\varepsilon_{Hf}(t)$ vs. U–Pb ages (b), crustal model age histograms (c) of zircons from typical felsic and mafic samples in the Tianjingping Complex

Although the rocks in the Tianjingping Complex are represented by high-grade gneisses or migmatites, the chemical signatures are regular and consistent, showing that the migmatization did not produce major alteration, especially in the immobile trace elements and REE patterns. The metamafic rocks are identified as subalkaline basalt including both tholeiitic and calc-alkaline compositions (Figure 4.29). The felsic paragneiss samples are ploted in the fields of arkose, lithic arenite and greywacke (Figure 4.31), which are immature sedimentations. Therefore, sedimentary-volcanic series probably developed during late Neoproterozoic. After that, a wide range of migmatization and anataxis occurred from Late Ordovician to Early Silurian, around ~440 - ~451 Ma. As Figure 4.26 shown, almost all the leucosomes in the Tianjingping Complex are peraluminous, varying along the tendency in granodiorite field from higher to lower content of anorthite, then towards granite with high content of orthoclase and the lowest content of anorthite.

4.5.2 Cooling history of the Tianjingping Complex

Based on the U-Pb zircon, $^{40}Ar/^{39}Ar$ amphibole and biotite ages dated in this study, as well as the temperature range of thermochronometers and themobarometers, the T-t path of the Tianjingping Complex could be established (Figure 4.36).

The crystalline temperatures range calculated for zircons from Samples 125-1, 125-2, 125-4 and 39-1, which are dated from ~450 - ~441 Ma, is ~648 - ~837 ºC (APPENDIX C). This would be the max temperature of migmatization or anatexis. The calculated temperature data from the garnet-biotite and garnet-amphibole geothermometers vary from 645 to 765 ºC (mean T = 696 ºC) and 469 to 529 ºC (mean T = 498 ºC), respectively (Figure 4.36). Since the last two steps of the $^{40}Ar/^{39}Ar$ amphibole age for sample 39-1 are the youngest ones (~430 Ma), the real amphibole age of 39-1 should be no older than ~430 Ma. Because both samples 39-1 and 34-4 were collected from Luomadi area, the cooling history for the two samples should be comparable. Although the metamorphic rims of the zircons in sample 34-4 are hardly detected, the biotite-garnet assemblages were probably formed between ~450 and ~430 Ma, and the amphibole-garnet assemblages could grew at the same time (~430 Ma) when amphibole in sample 39-1 reached its closure temperature (450 - 525 ºC[149]). Finally, $^{40}Ar/^{39}Ar$ biotite ages obtained from sample 31-7 and 125-4 are 392 and 370 Ma, respectively, and the temperature decreased to the closure temperature of biotite (about 300 ± 50 ºC[150]).

On the basis of above chronological data with corresponding closure or metamorphic tepratures, an estimated cooling T-t path in the range of ~800 - ~300 ºC for the Tianjingping Complex can be obtained. As illustrated in Figure 4.35, it is significant that a rapid cooling occurred during ~450 and ~392 Ma, and then a relative isothermal stage from ~392 to ~370 Ma.

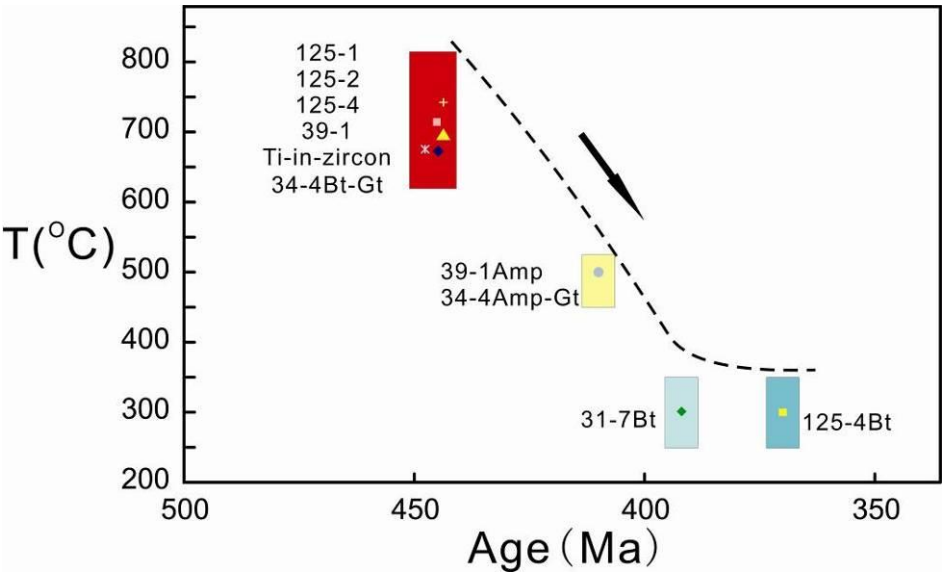

Figure 4.36 Cooling trace of the Tianjingping Complex according to geochronology and temperature calculation; Ti-in-zircon, Bt-Gt and Amp-Gt stand for the geothermometer, Amp and Bt stand for the ^{40}Ar-^{39}Ar analyses of samples 39-1, 31-7 and 125-4, respectively.

Chapter 5 Reworking of the Precambrian crustal components in the Jiaoxi and Mayuan complexes

§ 5.1 Petrography

Twenty-nine rock samples were collected from the Jiaoxi and Mayuan complexes (for sampling localities see Figures 2.1, 2.6 and 2.9 and Table 2.2), including two leocosome samples, twenty-four felsic paragneiss samples and three mafic samples. The leucosome samples are massive with a porphyritic texture. The phenocrysts are mainly K-feldspar (0.5 - 1.2 mm, partly altered) and quartz (0.5 - 0.8 mm). The matrix is composed of plagioclase, quartz and K-feldspar, with minor accessory minerals (Figure 5.1). Felsic paragneiss samples are grey in color and consist of biotite + plagioclase + quartz ± amphibole ± garnet ± sillimanite ± muscovite, with minor epidote, apatite, zircon, titanite and opaque minerals (Figure 5.2). Their compositions range from intermediate to acid, s with an increase in the quartz content. Mafic gneiss samples are dark green and massive, granoblastic, with the mineral assemblage of amphibole + plagioclase + quartz and minor titanite (Figure 5.3).

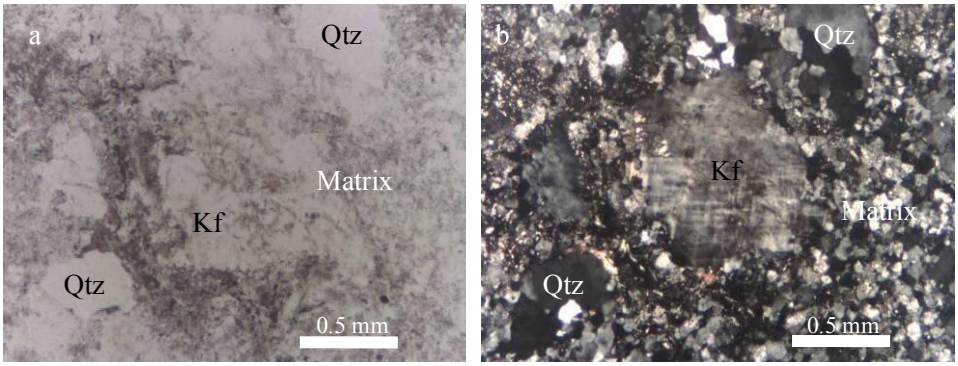

Figure 5.1 Typical porphyric texture of leucosome (sample 59-2) under both (a) plane polarized and (b) cross polarized light. The phenocrysts are mainly K-feldspar (Kf, partly altered) and quartz (Qtz), with lesser amounts of biotite (Bt, partly altered to chlorite).

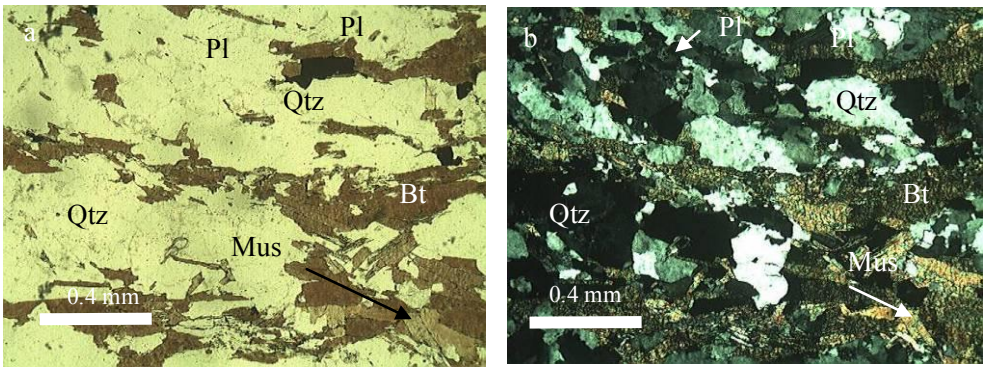

Figure 5.2 Typical gneissic structure of muscovite-bearing biotite-plagioclase gneiss (sample 65-2) under both (a) plane polarized and (b) cross polarized light. The composition is dominated by quartz (Qtz), biotite (Bt) and plagioclase (Pl), with lesser amounts of muscovite (Mus) and opaque minerals.

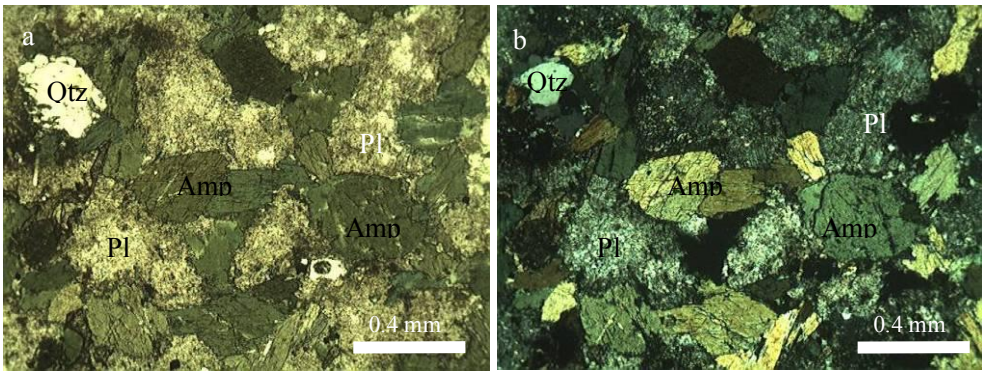

Figure 5.3 Typical amphibolite (sample 61-3) under both (a) plane polarized and (b) cross polarized light. The composition is dominated by amphibole (Amp), plagioclase (Pl, partly altered) and quartz (Qtz).

§ 5.2 Geochronology

5.2.1 Zircon U-Pb ages

Three samples from the Mayuan and Jiaoxi Complexes were selected for determining the ages of the amphibole-plagioclase gneiss (sample 61-3), the upper age limit for the deposition of the meta-sediments, and time of their reworking (samples 59-1 and 65-1).

1) Meta-sedimentary samples

Fine-grained biotite-plagioclase gneiss (sample 59-1)

Sample 59-1 is a dark grey, fine-grained (grain sizes 0.1 - 0.5 mm) felsic gneiss. It consists of biotite (5%), plagioclase (28%, altered), quartz (65%), and minor apatite, zircon and opaque minerals. Zircon grains are up to 150 μm in length, generally subhedral, with some crystal fragments shorter than 50 μm, and are colorless to pale brown under plane polarized light. Representative CL images of the zircon grains are shown in Figure 5.4a, and they commonly display core/rim structures. The rims generally show fine oscillatory zonation whereas the cores do not. Some grains are brighter in CL images, indicating lower thorium and uranium contents[114]. In addition, many grains show sponge-like structures (e.g. Spot 6t in Figure 5.4a), indicating that they had experienced fluid-rich conditions[128].

Figure 5.4b shows the concordia diagram of thirty-nine LA-ICP-MS zircon U-Pb analyses, with the analytical results listed in APPENDIX B. The Th/U ratios are

variable, ranging from 0.17 to 2.66, but most higher than 0.40. Th and U contents are 4 - 1614 ppm and 22 - 1456 ppm, respectively (APPENDIX B). Since the rims with fine oscillatory zoning are too narrow to analyze, all the ages are from the cores or single grains. Most of the analytical data plot on or near the concordia (Figure 5.4b) and yield a range of ages between 718 and 2360 Ma ($^{206}Pb/^{238}U$ ages are used for analyses younger than 1000 Ma, and $^{207}Pb/^{206}Pb$ ages for the others) with the main age population between 840 and 718 Ma (Figure 5.5). This suggests that there was a significant sedimentary input of Neoproterozoic materials, with rare Paleoproterozoic material, indicating the ~1.8 Ga ages are found to be more common in the South China Block other than being restricted to the North China Block. The two main Neoproterozoic populations gave mean ages of 722 ± 9 (95% conf., MSWD = 0.17) and 758 ± 3 Ma (95% conf., MSWD = 0.17), respectively (Figure 5.4c, 5.5). The youngest age of 722 ± 9 Ma provides the upper age limit for the deposition of the protolith of the paragneiss.

Although the thin rims with fine oscillatory zoning were too narrow to analyze, they indicate that the protolith of sample 59-1 has been strongly reworked by later tectono-thermal events, when the sedimentary protolith was converted into a paragneiss.

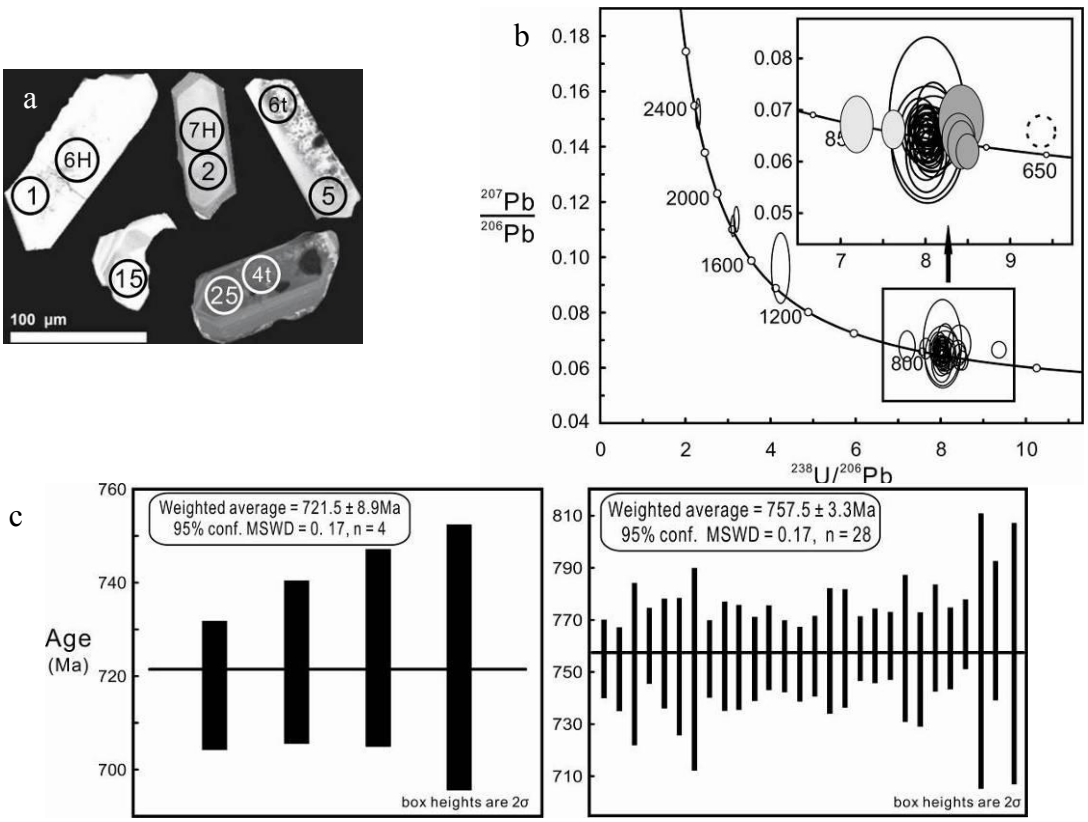

Figure 5.4 (a) Typical CL images and(b) Tera-Wasserburg concordia diagram of zircon grains in sample 59-1 (Laser ICPMS U-Pb analyses). Numbers and letters in circles (such as 1, 6H and 4t) in (a) represent analytical spots for U-Pb, trace elements and Hf isotopes

(see data in APPENDICES B, C and D, respectively). The main age population is 758 ± 3 Ma (c)

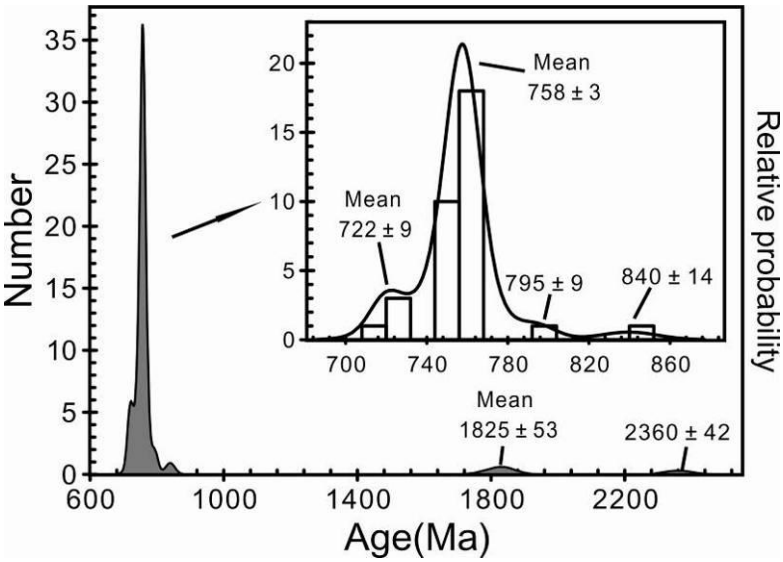

Figure 5.5 Probability histogram of U-Pb ages from sample 59-1. The principal age peak is at 758 Ma.

Biotite-plagioclase gneiss (sample 65-1)

Sample 65-1 is a dark brown, massive and medium-grained (grain sizes 2 - 3 mm) intermediate rock, consisting of biotite, plagioclase (partly altered), quartz, and minor sillimanite, apatite, zircon and opaque minerals. Zircon grains are commonly subhedral to euhedual, most of which are 50 - 200 μm in length, with length/width ratios between 1:1 and 6:1. The internal structures, as revealed by CL imaging, normally display core/rim structures, although no rim was formed on several elongated prismatic crystals (Figure 5.6a). Fine oscillatory zonation is present in the rims around older (>720 Ma) cores, but not on younger (<450 Ma) cores. In addition, some cores are locally penetrated by the rims, forming embayments (Figure 5.6a).

Thirty-one zircon U-Pb analyses are plotted on a Tera-Wasserburg concordia diagram (Figure 5.6b), and the analytical results are listed in APPENDIX B. Th/U ratios for zircons from sample 65-1 vary over a wide range, from 0.03 to 1.97, all but one analysis are higher than 0.1. The Th and U contents also show great variations, from 24 to 7972 ppm and 196 to 4045 ppm, respectively (APPENDIX B). Almost all the analytical data are concordant, although two grains have greater than 10% discordance (89% and 87%). The population shows an age range from 420 - 1382 Ma ($^{206}Pb/^{238}U$ ages are used for analyses younger than 1000 Ma, and $^{207}Pb/^{206}Pb$ ages for the others), which include four discrete populations of ~420 Ma, 440- 450 Ma, 724 - 904 Ma and 1114 - 1397 Ma. The two youngest populations have weighted

mean ages of 423 ± 3 (95% conf., MSWD = 0.93) and 445 ± 2 Ma (95% conf., MSWD = 0.99), respectively (Figure 5.6c, 5.6d, 5.7a). Generally, the Th/U ratios for the spots with ages older than 720 Ma are below 1.1 (0.03 - 1.08), and for the youngest population are relatively high (0.11 - 1.97) (Figure 5.7b). This indicates that the protolith of the paragneiss was probably formed no older than ca. 724 Ma, and has experienced significant reworking during two thermal events (migmatization), one in the Late Ordovician and the other in the Silurian.

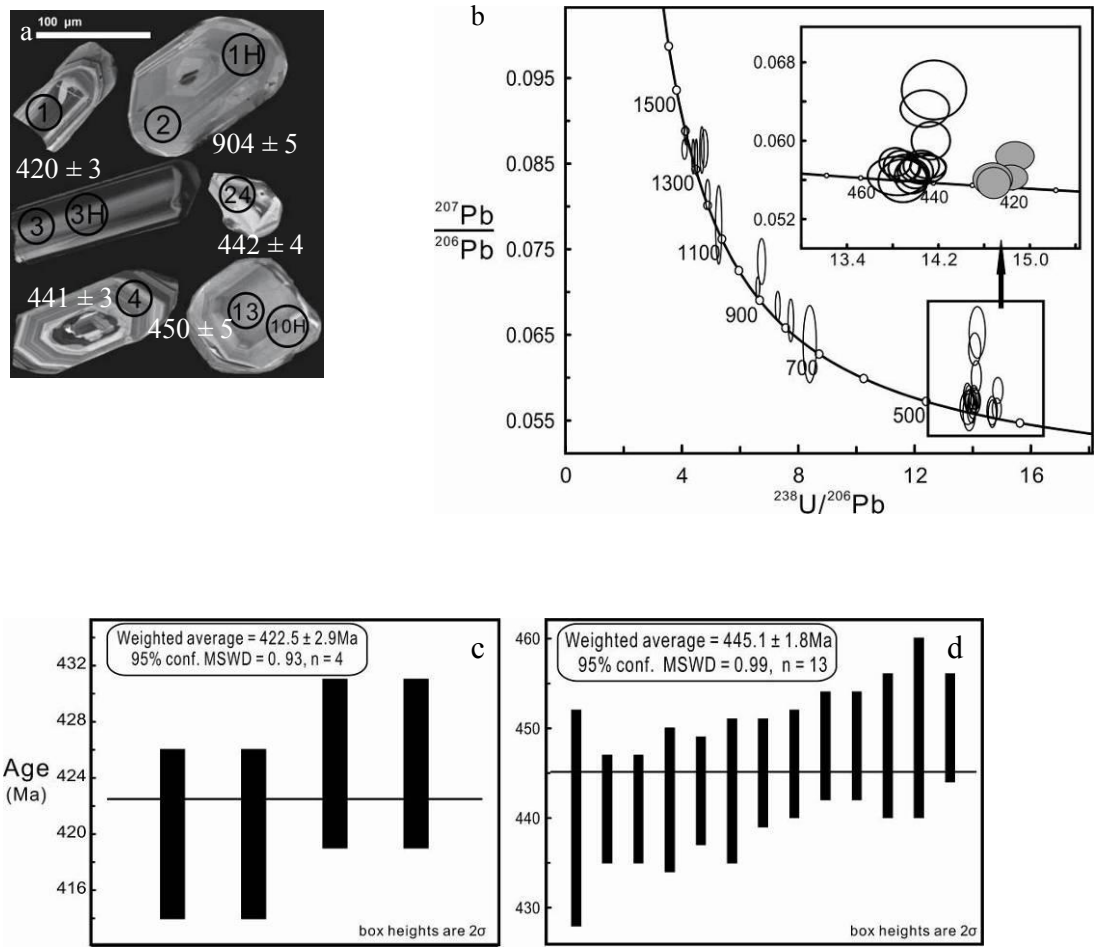

Figure 5.6. (a) Typical CL images and (b) Tera-Wasserburg concordia diagram of zircon grains in sample 65-1 (LA ICP-MS U-Pb analyses). Numbers and letters in circles (such as 1 and 1H) in (a) represent analysis spots for U-Pb and Hf isotopes (the data are listed in APPENDICES B and D, respectively). The two youngest populations in (b) have weighted mean ages of 423 ± 3 (c) and 445 ± 2 Ma (d), respectively

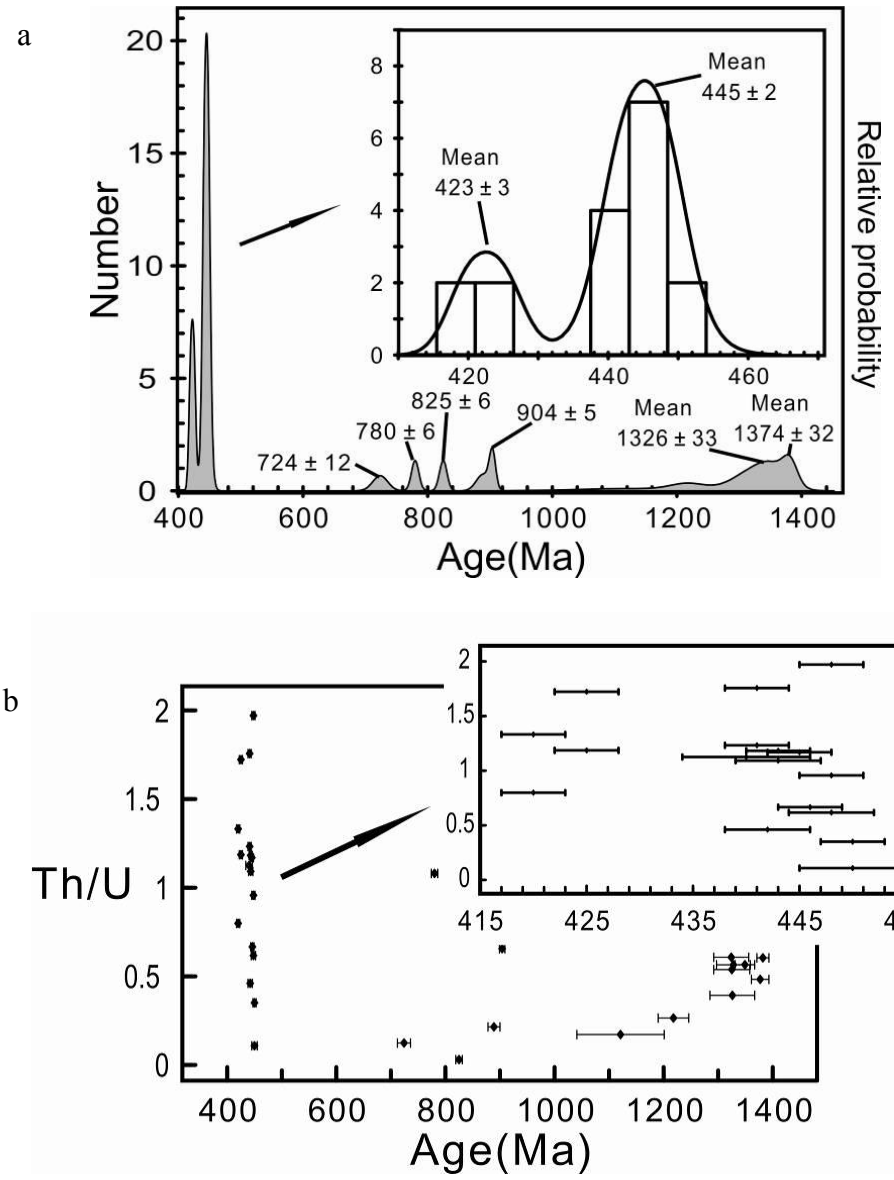

Figure 5.7 (a) Probability histogram of U-Pb ages; $^{206}Pb/^{238}U$ ages are used for analyses <1000 Ma, and $^{207}Pb/^{206}Pb$ ages >1000 Ma. (b) Th/U ratio vs. age plot for zircons from sample 65-1. The plot shows a large spread of ages and Th/U ratios and almost all zircons (except one) older than 700 Ma have Th/U ratios lower than 1.0.

Amphibolie (sample 61-3)

Sample 61-3 is a medium-grained (grain sizes 0.8 - 1.5 mm) meta-basic rock, consisting of amphibole (40%), plagioclase (50%), quartz (5%), and accessory titanite, zircon and opaque minerals. The zircon grains are prismatic, near euhedral, colorless, up to 100 - 200 μm in length with length/width ratios of 2:1 to 7:1. CL images reveal that most grains have core/rim structures, with strongly planar and oscillatory zoned cores surrounded by thin unzoned rims that may transgress the zones (Figure 5.8a). A total of 32 analyses were undertaken on the zircon cores, the rims being too narrow to analyze. The Th and U contents of the zircons vary between 3 and 5099 ppm and 196 and 7584 ppm, respectively, with a positive correlation.

Th/U ratios are between 0.02 and 0.75, but mostly higher than 0.16, indicating that the majority of the zircon grains are of possible igneous origin. All but one analysis plot on concordia (Figure 5.8b) and yield a range of $^{206}Pb/^{238}U$ ages between 440 and 453 Ma, with a weighted mean age of 445 ± 2 Ma (95% conf., MSWD = 1.2) (Figure 5.8b).

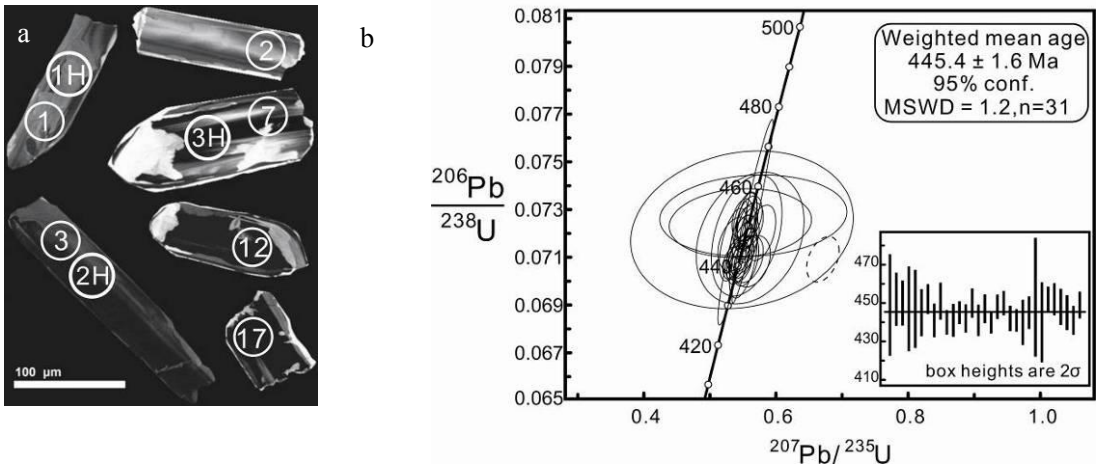

Figure 5.8. (a) Cathodoluminescence (CL) images and (b) LA-ICP-MS U-Pb isotopes of zircon grains in sample 61-3. Numbers and letters in circles (such as 1, 1H) represent analysis spots of U-Pb and Hf isotopes, respectively. The data are listed in APPENDICES B and D

5.2.3 Zircon REE geochemistry

As shown in the APPENDIX C and Figure 5.9, most zircons show similar REE distributions, with slight differences between the felsic and mafic rocks. Similar to samples from the Tianjingping Complex, the REE patterns are characterized by strong fractionation in both light REE (LREE) and heavy REE (HREE), with relatively smooth increases in chondrite-normalized abundances from La to Lu, punctuated by excess Ce and Eu depletion. The intermediate and heavy REE patterns are comparability with typical magmatic zircons[130, 151]. Anomalous analyses 65-1-04t and 65-1-06t in sample 65-1 have $^{206}Pb/^{238}U$ ages of 440 ± 6 and 448 ± 4 (APPENDIX B), respectively, the same as the main zircon population with a mean age 445 ± 2 Ma within error (Figure 5.7), but show lower HREE contents than the others, which are dated as 1218 - 1382 Ma. It suggests that a simultaneous crystallization of garnet might occurred with the later metamorphism/anatexis other than in the middle Mesoproterozoic, when the gneiss protolithes formed. Analytical spot 59-1-08t (759 ± 8 Ma) in sample 59-1 displays greater enrichment of LREE. This probably indicates that some small phosphatic inclusions with higher LREE contents were present at the analytical site, since the Th and U contents are relatively lower compared with the other spots[128, 152]. Strong positive Ce anomalies are found

in all analyzed sites (δCe = 2 - 212).

Zircons from mafic sample 61-3 display weaker Eu negative anomalies (δEu = 0.38 - 1.71) than those of the felsic paragneiss samples 59-1 and 65-1 (Figure 5.9). In the δCe vs. δEu diagram for all three samples, the felsic samples overlap with mafic sample (Figure 5.10). It is probable that some of the zircon spots analyzed in 59-1 are strongly influenced by fluids, such as spots 2t, 5t, 6t and 7t, which results in their ploting near mafic samples. The same two younger zircons in Sample 65-1 (65-1-04t and 65-1-06t) for the trace elements analyses also show different δCe-δEu features (Figure 5.10).

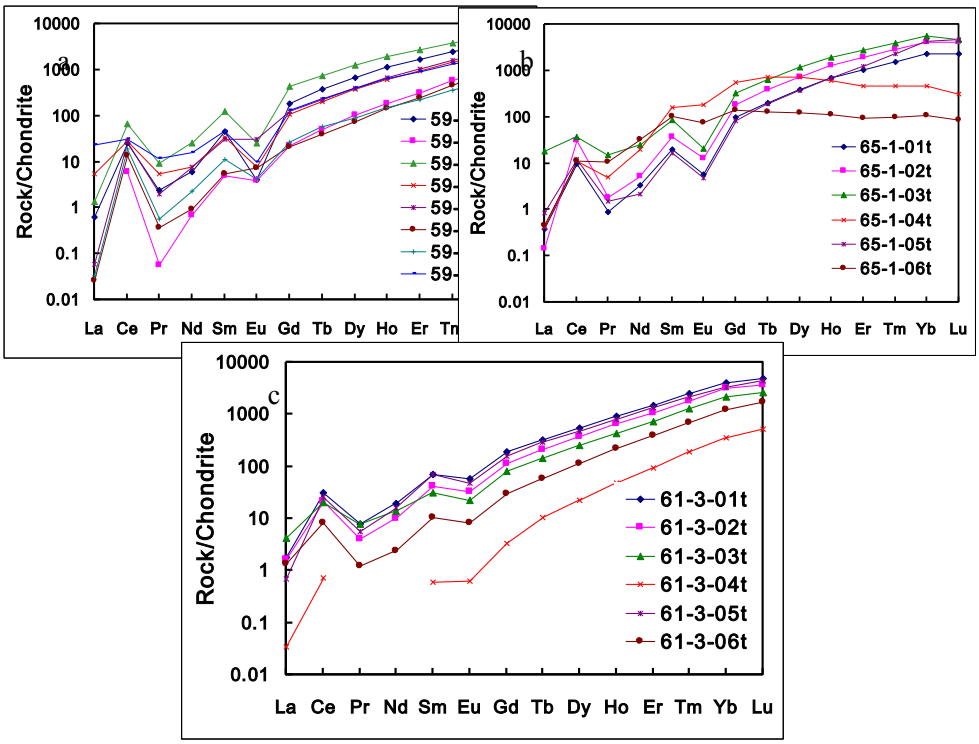

Figure 5.9 Chondrite-normalized REE distributions of the zircon grains from (a) 59-1, (b) 65-1 and (c) 61-3 in the Jiaoxi and Mayuan complexes. Positive Ce anomalies are shown in all analyzed grains. Negative Eu anomalies are strongly developed in felsic samples and weaker in the mafic sample.

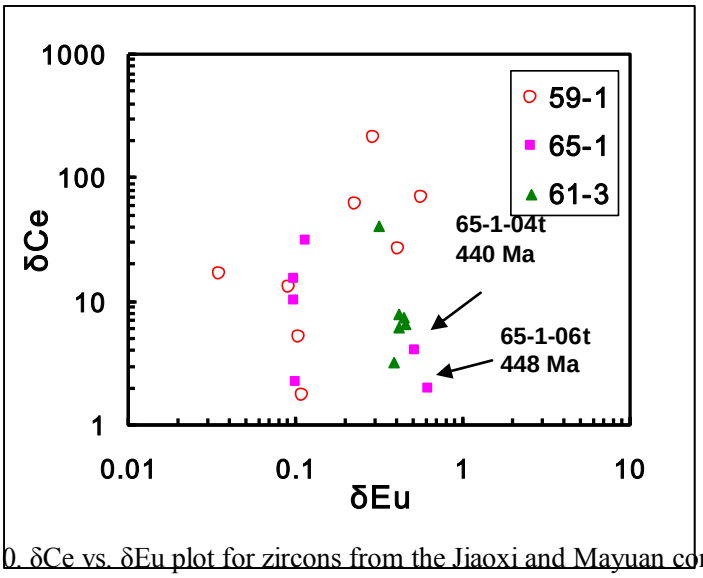

Figure 5.10. δCe vs. δEu plot for zircons from the Jiaoxi and Mayuan complexes

5.2.3 Zircon Hf isotopes

Paragneiss 59-1

For sample 59-1, *in-situ* Lu-Hf isotopes of 15 zircon grains were analyzed simultaneous with the U-Pb data collection. The $^{176}Hf/^{177}Hf$ ratios of the zircons fall between 0.281326 and 0.2822215, calculated from two different age populations of 722 and 758 Ma and single age data of 1668 and 1843 Ma according to the U-Pb results. The younger zircons (< 760 Ma) have slightly higher $^{176}Hf/^{177}Hf$ ratios than the older ones (> 1600 Ma), suggesting that the former contained more radiogenic Hf. The $\varepsilon_{Hf}(t)$ values ranging from -14.2 to -3.8, implying that the protolith consists of recycled old crust. Since all the grains gave negative $\varepsilon_{Hf}(t)$ values, two-stage Hf model ages (T_{DM}^{UC}) were calculated and range from 1678 to 2929 Ma (Figure 5.11), suggesting the protolith was mostly derived from crust materials no younger than late Paleoproterozoic.

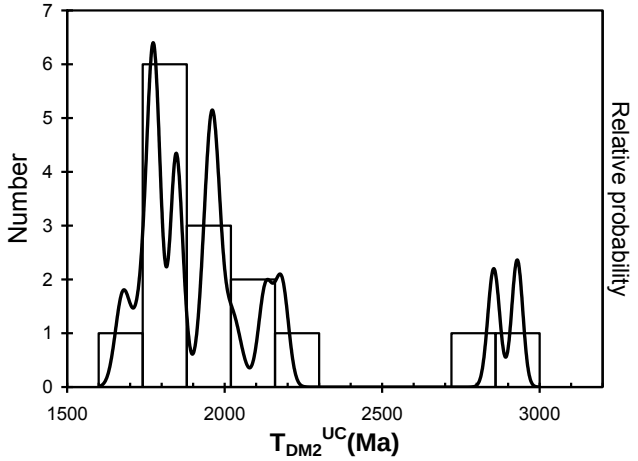

Figure 5.11 Probability histogram of T_{DM}^{UC} ages for sample 59-1.

Paragneiss 65-1

In-situ Lu-Hf isotopes of 14 zircon grains from sample 65-1 were analyzed at the same time as the U-Pb data collection. The $^{176}Hf/^{177}Hf$ ratios are generally higher than from paragneiss sample 59-1, ranging from 0.281943 to 0.282442. The $^{176}Hf/^{177}Hf$ ratios were calculated using different age populations of 445, 825 and 1326 Ma and single ages of 889 and 1374 Ma, on the basis of the U-Pb results. The $\varepsilon_{Hf}(t)$ values are mostly in the range of -20.6 to -1.9, with four high positive values between +5.5 and +17.8, implying that the protolith may have been derived from a mixture of ancient crust or enriched mantle, with some addition of depleted mantle materials. Hf model ages (T_{DM}) for zircon grains with positive $\varepsilon_{Hf}(t)$ values range between 1152 and 1595 Ma (Figure 5.12). For the grains with negative $\varepsilon_{Hf}(t)$ values, two-stage Hf model ages (T_{DM}^{UC}) spread from 1330 to 2278 Ma (Figure 5.12). This indicates that during the late Mesoproterozoic, mantle materials were added into early to middle Mesoproterozoic crust.

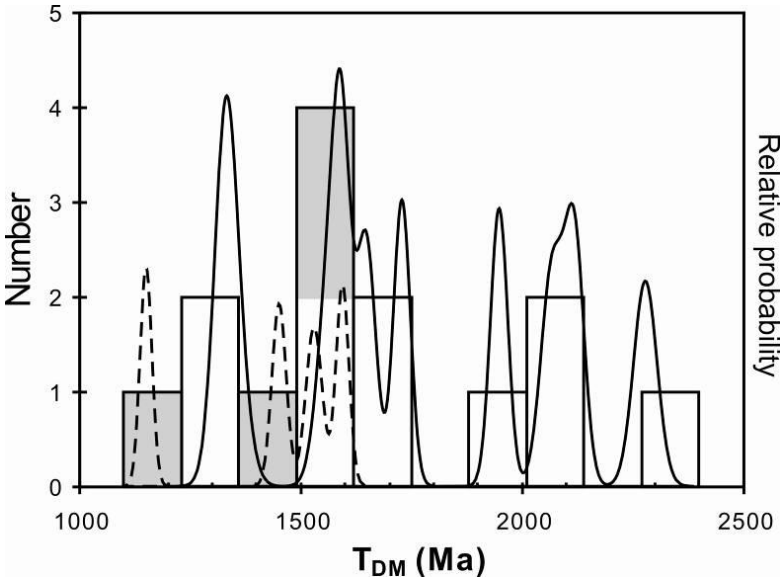

Figure 5.12 Probability histogram of T_{DM} and T_{DM}^{UC} ages for sample 65-1. The grey boxes and dashed curves are T_{DM} whereas the open boxes and solid lines are T_{DM}^{UC}

Amphibole-plagioclase gneiss 61-3

In-situ Lu-Hf isotopes analyses of 16 zircon grains separated from amphibole-plagioclase gneiss sample 61-3 were measured along with the U-Pb analyses. The 176Hf/177Hf ratios of the zircons range from 0.281944 to 0.282511, calculated for the age of 445 Ma. Most of the $\varepsilon_{Hf}(t)$ values are between –20.0 and –0.6, except for one positive value of 0.2 (spot 61-3-04H), suggesting that the protolith of the sample was derived from old crustal materials with some mantle input. For all the analytical spots, two-stage Hf model ages (T_{DM}^{LC}) were calculated and values show a large variation of between 1818 Ma and 3613 Ma (Figure 5.13), in which the youngest age

(1818 Ma) is from spot 61-3-04H (T_{DM} = 1057 Ma). This implies a protolith derived from crustal materials formed during the Archean to Paleoproterozoic, with some input of mantle material during the Paleoproterozoic.

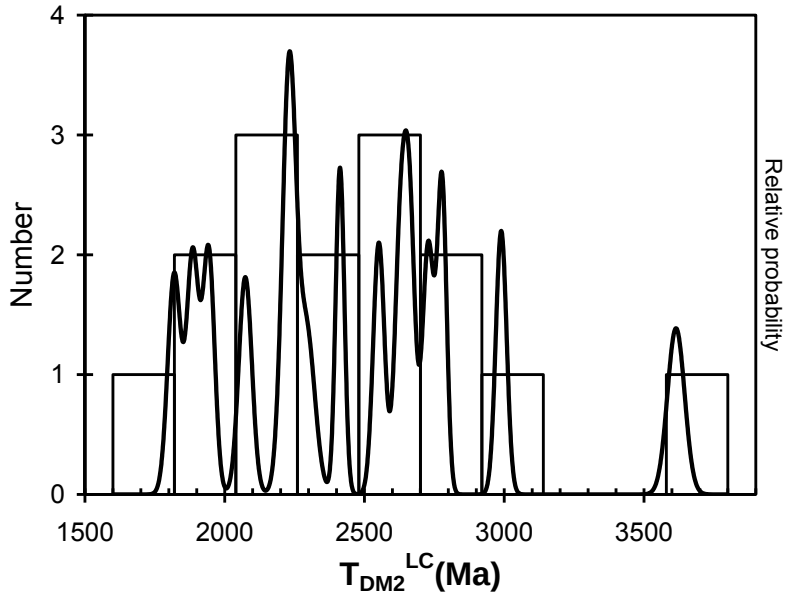

Figure 5.13 Probability histogram of T_{DM}^{LC} ages for sample 61-3.

5.2.4 Amphibole and biotite $^{40}Ar/^{39}Ar$ thermochronology

Three samples (61-3, 65-2 and 122-1) from the Jiaoxi and Mayuan complexes were selected for amphibole and biotite $^{40}Ar/^{39}Ar$ geochronology. The locations of these samples are shown in Figure 2.9. Amphibole and biotite separated from the two mafic rocks (61-3 and 122-1) yielded satisfactory plateau ages, but biotite from the felsic gneiss (65-2) produced no plateau age.

1) Sample from the Jiaoxi Complex

Amphibole-plagioclase gneiss 61-3

Multiple amphibole grains (3 mg) were selected from sample 61-3 (Figure 5.14a) and were filled in a package (described in Chapter 3.2.4) with a size of 4088 × 3242 μm. They yielded a weighted mean mini-plateau age of 380.9 ± 2.3 Ma (2σ, MSWD = 0.8, probability of fit = 0.52, including J-error), defined by five consecutive gas fractions comprising 63% of the released ^{39}Ar (Figure 5.14b and APPENDIX E). The lowest temperature steps exhibit younger apparent ages, but together represent only 25% of the ^{39}Ar released. The plateau age is considered to represent the timing of cooling through the closure temperature for argon diffusion in amphibole (ca. 450 - 525 °C[149]).

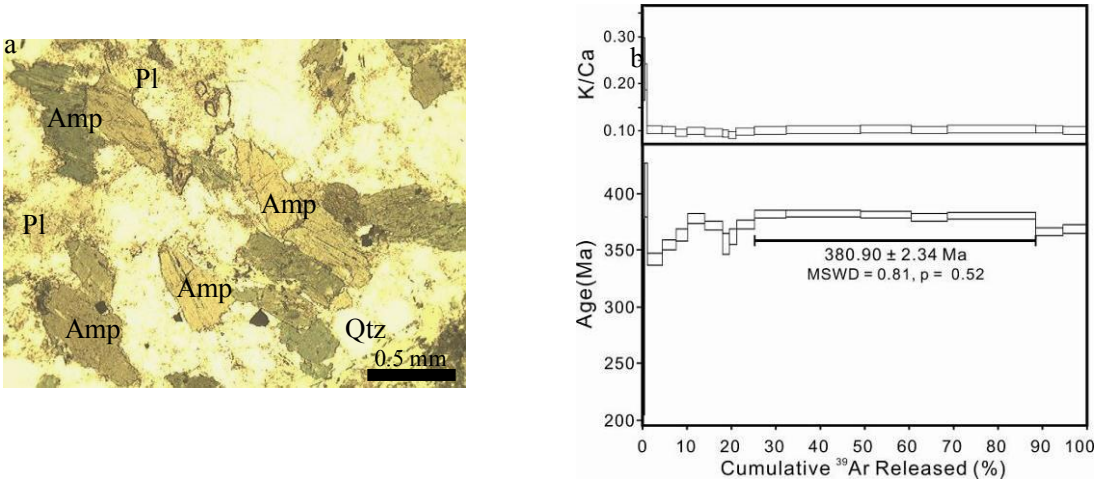

Figure 5.14 (a) Photomicrograph of sample 61-3 in plane light and (b) associated amphibole $^{40}Ar/^{39}Ar$ age spectrum. Mineral abbreviations: amphibole (Amp), plagioclase (Pl), quartz (Qtz).

2) Samples from the Mayuan Complex

Biotite-amphibole-plagioclase gneiss 122-1

Multiple amphibole grains (3 mg, package size 4330 × 3122 μm) and a biotite flake (440 × 380 μm) were separated from sample 122-1 (Figure 5.15a). The amphibole grains yielded a discordant age spectrum with apparent ages varying with increasing temperature (Figure 5.15b): no age could be obtained. The biotite yielded a weighted mean plateau age of 152.1 ± 1.8 (2σ, MSWD = 0.76, probability of fit = 0.66, including J-error), which was established by ten successive gas fractions incorporating 89% of the released ^{39}Ar (Figure 5.15c and APPENDIX E). The first two steps show older apparent ages. The plateau age is considered to reflect the time of biotite cooling through ca. 300 °C[132]. Considering the Ar ispotopic age of the biotite flake, the complicated variation of the amphibole Ar isotopic pattern from this sample might indicate incomplete reworking by younger thermal events.

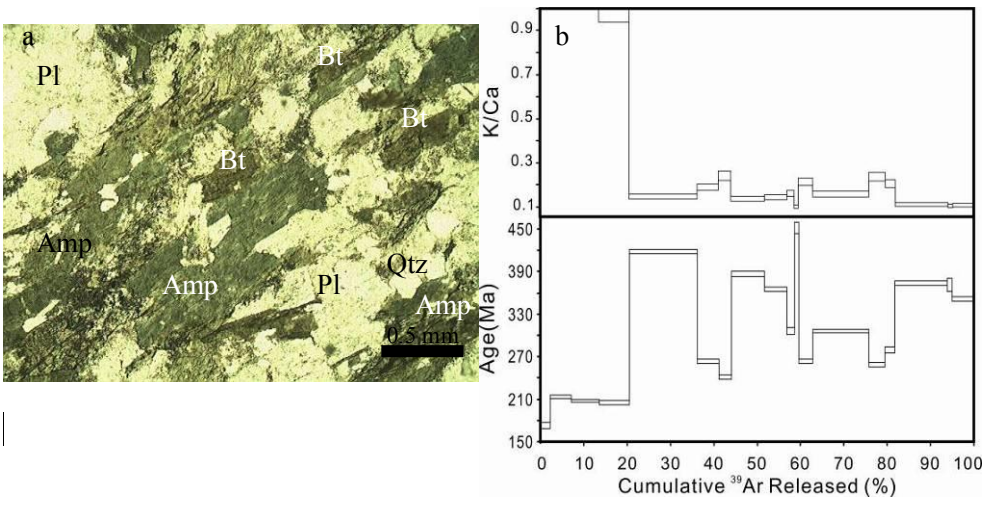

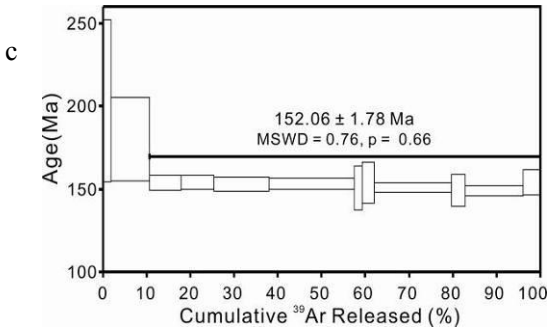

Figure 5.15 (a) Photomicrograph of sample 122-1 in plane polarised light, (b) associated amphibole and (c) biotite $^{40}Ar/^{39}Ar$ age spectra. Mineral abbreviations biotite (Bt), amphibole (Amp), plagioclase (Pl), quartz (Qtz).

Biotite-plagioclase gneiss 65-2

A biotite flake (630 × 420 μm) separated from sample 65-2 (Figure 5.16a) was analyzed. With increasing laser power, it produced decreasing ages from ~295 Ma to ~243 Ma. In the last three steps, the age increased again to about 274 Ma. No plateau age could be obtained from this sample.

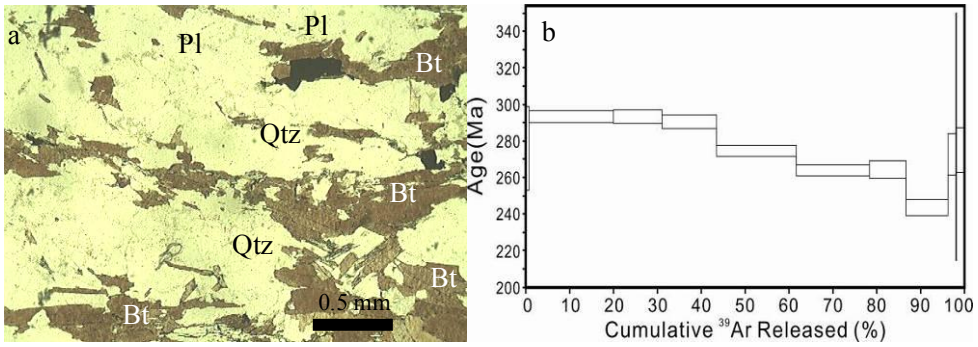

Figure 5.16 (a) Photomicrograph of sample 65-2 in plane polarized light and (b)associated biotite $^{40}Ar/^{39}Ar$ age spectrum. Mineral abbreviations biotite (Bt), plagioclase (Pl), quartz (Qtz).

§ 5.3 Whole-rock geochemical analyses

5.3.1 Geochemistry of the metamafic rocks

Since meta-mafic rocks are rare in the Jiaoxi and Mayuan complexes, only three samples were analyzed in this study, and their major and trace element compositions are listed in APPENDIX F. Petrographic features indicate that these rocks underwent varying degrees of alteration, consistent with their relatively high LOI (loss of ignition) values of 5.95 - 9.91%. So the alteration effects on chemical compositions of these rocks also need to be evaluated, as for samples analyzed from the Tianjingping Complex. Only the immobile elements are therefore used for rock classification and further petrogenetic discussions.

The mafic rocks have low SiO_2 (48.62 - 58.70%), relatively high MgO (2.78 - 5.81%) and total alkalis ($Na_2O + K_2O$ = 4.99 - 6.42%) (APPENDIX F). On the Zr/TiO_2 vs. Nb/Y diagram of Pearce (1996), all samples plot in the subalkaline basalt field (Figure 5.17a). On the Jensen diagram[153] (Figure 5.17b), they plot in the calc-alkaline field. All the mafic rocks are highly evolved in composition with low Mg# ranging from 15 to 17. The samples have a range of total REE contents between 127 and 236 ppm. Their REE and trace element characteristics are similar, showing strong enrichment in LREEs relative to HREEs (LREE/HREE = 6.71 to 8.41) in the chondrite-normalized REE patterns (Figure 5.18a) and with negligible Eu anomalies (δEu = 0.74 to 1.00). The primitive mantle-normalized spidergrams of these rocks are characterized by moderate enrichments in most trace elements (Figure 5.18b), with slight depletions in Nb and Ta relative to La and Th, in P relative to Pr and Nd, in Zr and Hf relative to Nd and Sm, and in Ti relative to Eu and Gd.

a

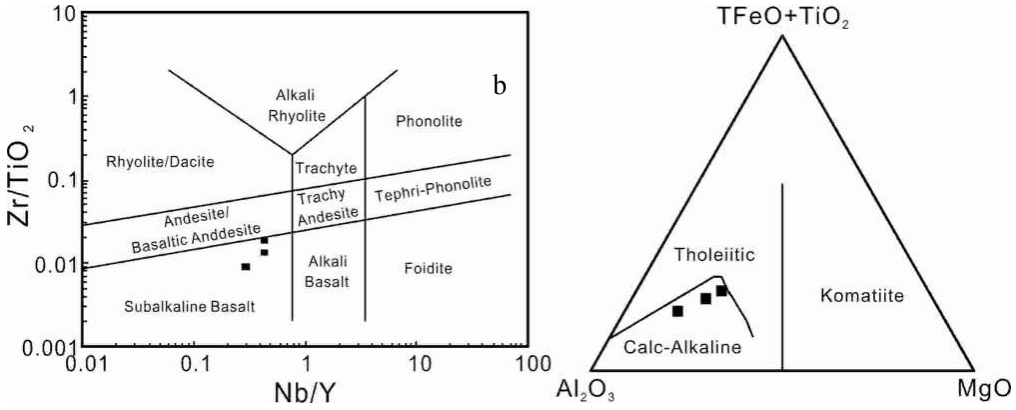

Figure 5.17 (a) Zr/TiO_2 vs. Nb/Y classification diagram[140] and (b) Jensen diagram[153] for the meta-mafic rocks in the Jiaoxi and Mayuan complexes.

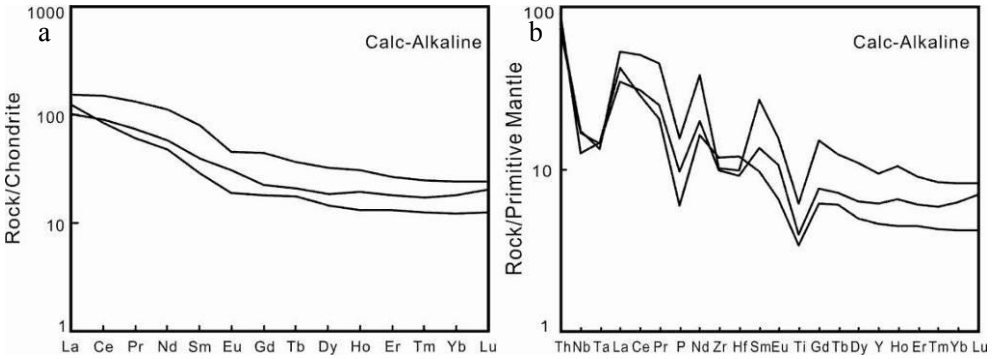

Figure 5.18 (a) Chondrite-normalized REE patterns and (b) primitive mantle-normalized trace element distribution diagrams for meta-mafic rocks in the Jiaoxi and Mayuan complexes. Chondrite and Primitive Mantle values are from reference [135] (excluding Rb, Ba, U, K, Pb, Sr).

5.3.2 Geochemical characteristics of the paragneisses

Major and trace element compositions of nine paragneiss samples from the Jiaoxi and Mayuan complexes are listed in APPENDIX F. These rocks have variable SiO_2 (63.84 - 78.90%), Al_2O_3 (9.61 - 17.00%) and relatively high Na_2O (1.30 - 7.09%), K_2O (1.65 - 4.54%) and low MgO (0.86 - 2.68%). In a Si / (Si + Al) versus (Na + Ca) / (Na + Ca + K) plot (atomic proportions; Figure 5.19) that defines compositional fields for various sedimentary rocks[143], all the samples from the Jiaoxi Complex plot in the greywacke field and the samples from the Mayuan Complex fall into a greater range including the arkose and the lithic arenite fields.

The samples have a range of total REE contents between 161 and 510 ppm. Chondrite-normalized REE patterns (Figure 5.20a) show that the samples are enriched in LREEs relative to HREEs (LREE / HREE = 6.32 - 30.59) and display well- developed negative Eu-anomalies (δEu = 0.24 - 0.97). Primitive mantle-normalized spidergrams (Figure 5.20b) show negative anomalies of Nb, Ta and Ti for all the samples, but weak negative Zr and Hf anomalies and positive Sm-anomalies in three samples. The close similarity among the paragneiss samples from three areas in the Jiaoxi and Mayuan complexes in both REE patterns and spidergrams attests to similar sedimentary sources for the protoliths.

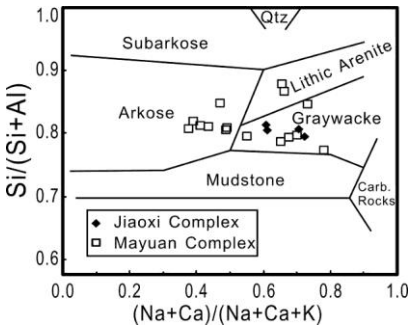

Figure 5.19 The atomic proportion of Si / (Si + Al) vs. (Na + Ca) / (Na + Ca + K) showing likely protoliths for the paragneiss samples[143].

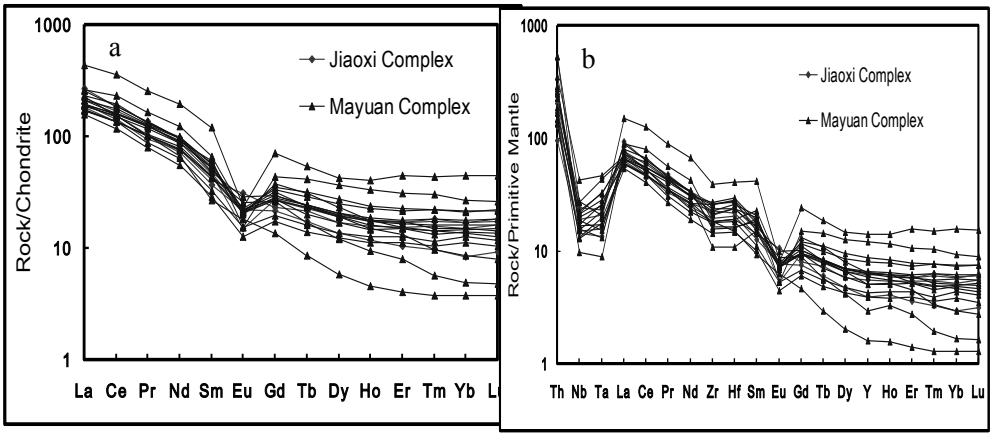

Figure 5.20 (a) Chondrite-normalized REE patterns and (b) primitive mantle-normalized trace element distribution diagrams for paragneisses from the Jiaoxi and Mayuan complexes. Chondrite and primitive mantle values are from reference [135].

§ 5.4 Estimation of Pressure-temperature conditions in the Jiaoxi and Mayuan complexes

5.4.1 Ti-in-zircon geothermometer

^{49}Ti was analyzed in zircon grains in order to determine the zircon crystallization temperatures. The ^{49}Ti contents in the Jiaoxi and Mayuan complex zircons are broadly similar (5 - 19 ppm), except for four grains where ^{49}Ti = 31 - 127 ppm (APPENDIX C). The formula T (°C) = (5080 ± 30) / [(6.01 ± 0.03) − Log (Ti_{zircon} / 0.6)] − 273[144, 146-147] was used to calculate the mean crystallization temperature of these zircons. Since there are four groups of ages, the calculated crystallization temperatures were related to this age subdivision. The temperatures ranged from 639 to 744 ºC for zircons with ages of 452 - 440 Ma, from 700 to 792 ºC for zircons with ages of 795 - 756 Ma, 731 to 788 ºC for zircons with ages of 1218 - 1389 Ma, and as high as 950 ºC for a zircon with the age of 1843 Ma (APPENDIX C; Figure 5.21). The very high temperature of the zircon with the age of 1843 Ma may contain the Paleoproterozoic information about adjacent blocks which would be the provenance of the sedimentary protoliths. The temperatures for the youngest zircon group are consistent with upper amphibolite facies metamorphism or anatexis as defined by petrologic observations.

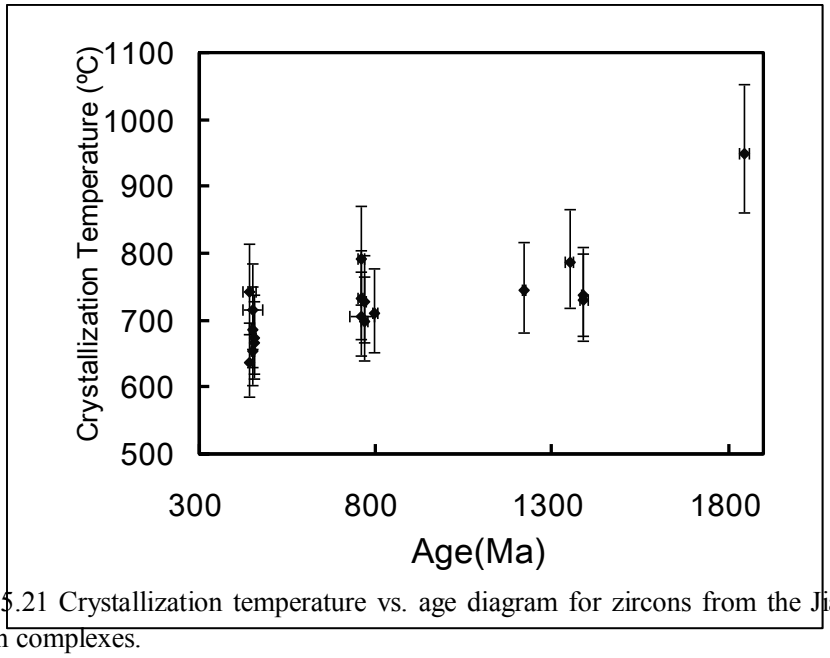

Figure 5.21 Crystallization temperature vs. age diagram for zircons from the Jiaoxi and Mayuan complexes.

5.4.2 Mineral assemblage geothermobarometer

In the Jiaoxi and Mayuan complexes, three samples (paragneisses 65-2 and 66-3 and amphibole-plagioclase gneiss 61-3) were selected for pressure-temperature analyses. The following contiguous mineral assemblages were subjected to microprobe analysis: biotite + muscovite in samples 65-2 and 66-3 (Figure 5.22a) and amphibole + plagioclase in sample 61-3 (Figure 5.22b). For each sample, analytical spots close to each other were matched as pairs for calculating the pressure-temperature conditions. Because of the lack of suitable plagioclase in samples 65-2 and 66-3 (most were altered), pressure estimation was not possible for these samples.

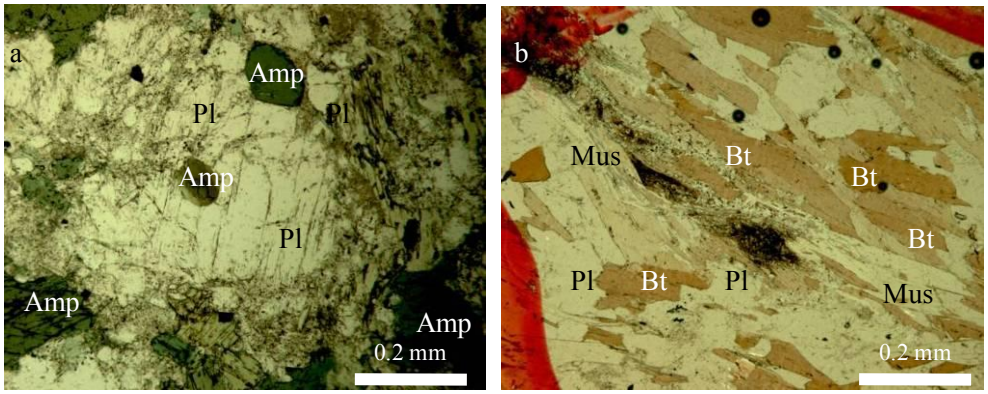

Figure 5.22 Typical mineral assemblages in (a) sample 61-3 with amphibole + plagioclase, in plane polarized light and (b) sample 66-3 with biotite + muscovite, in cross polarized light. Abbreviations: Pl = plagioclase, Amp = amphibole, Bt = biotite, Qtz = quartz.

In sample 61-3, 14 sites were selected for the analyses of both amphibole and plagioclase. Amphibole grains are generally 50 to 500 in length (Figure 5.3, 5.22a). EMPA data for the amphiboles revealed slightly variable Mg # values of between 0.308 and 0.409 (APPENDIX G). Pressure and temperature estimations using the Amp-Pl geothermobarometer yielded a pressure range of 3 - 11 kbar (mean P = 6 kbar), and a temperature range of 700 to 783 ºC (mean T = 746 ºC).

In samples 65-2 and 66-3, 8 sites on the biotite and muscovite assemblages were selected for each sample. According to the EMPA data (APPENDIX G), Mg# values of biotite and muscovite for sample 65-2 are 0.413 - 0.467 and 0.469 - 0.513 respectively, which are slightly higher than those for sample 66-3, which range from 0.369 to 0.408 and from 0.454 to 0.474, respectively. The temperature calculated by the biotite-muscovite assemblages[154] from samples 65-2 and 66-3 are similar: 339 - 347 ºC (mean T = 343 ºC) and 339 - 344 ºC (mean T = 341 ºC), respectively.

§ 5.5 Discussion of the Jiaoxi and Mayuan complexes

5.5.1 Depositional ages of protoliths and their reworking

The metamorphic rocks of the Jiaoxi and Mayuan complexes have been considered to be younger than the Tianjingping Complex, with deposition age of the protoliths being no older than 0.8 Ga based on the latest geochronological study[33]. As shown in Figure 5.23, the majority of the zircons have Th/U > 0.4, characteristic of an igneous origin (Rubatto and Gebauer, 2000; Hanchar and Hoskin, 2003), whereas most zircons with Th/U ratios less than 0.1 yield younger ages.

Sixty-seven zircon grains, including fifteen grains from leucosomes (Liu, 2009) and fifty-two grains from mafic and felsic gneisses with Precambrian ages (~2425 - ~718 Ma) have been identified. Most of the zircon grains show oscillatory zoning and relatively high Th/U ratios of 0.12 - 2.66 (with only sixteen analyses < 0.1), suggesting an igneous origin for most zircons. The youngest cluster of inherited zircons/cores is at ~722 Ma (Figure 5.24), suggesting a maximum depositional age no older than middle Neoproterozoic.

Among the zircons from felsic samples, including the leucosomes, 46 of 51 grains measured for Hf isotopes have negative $\varepsilon_{Hf}(t)$ values in the range from -27.2 to -1.9 and the other five grains yield positive $\varepsilon_{Hf}(t)$ value from 0 to +17.8. T_{DM} model ages of ~1.15 - ~1.60 Ga were recorded by the zircons with positive $\varepsilon_{Hf}(t)$ value and 1.89 Ga for the zircon with $\varepsilon_{Hf}(t) = 0$, suggesting some juvenile crustal additions during the Mesoproterozoic and early Paleoproterozoic. The zircon grains with negative $\varepsilon_{Hf}(t)$ values record T_{DM}^{UC} varying from 3.08 to 1.33 Ga, indicating that their source rocks were recycled ancient continental crustal materials formed from the Neoarchean to middle Mesoproterozoic.

For zircons from mafic sample 61-3, 15 grains are measured for Hf isotopes and almost all of them yield negative $\varepsilon_{Hf}(t)$ values between -20.0 to -0.6, although one grain has a positive $\varepsilon_{Hf}(t)$ value of +0.2 ± 0.4. The zircon grains have T_{DM}^{LC} ranging from 3.61 to 1.82 Ga, suggesting that their source rocks are recycled ancient crustal materials formed during the Paleoarchean to late Paleoproterozoic, slightly earlier than the protoliths of the felsic rocks.

Overall, typical metamorphic Th/U ratios (< 0.1) mostly occur in the youngest zircons, with ages of ~412 - ~448 Ma (leucosomes) and ~441 - ~447 Ma (gneiss). A few zircons with ages of ~817, ~822 (leucosomes) and ~825 (paragneiss) Ma (Figure 5.23) also record values <0.1, indicating that metamorphism possibly occurred in the

source area at ~820 Ma. Considering the concordant U-Pb zircon ages of gneiss samples 61-3 (mafic) and 65-1 (felsic) with both high and low Th/U ratios, but their main age peaks are both 445 ± 2 Ma, which is consistent within these of the Tianjingping Complex. It is most likely that as in the Tianjingping Complex, anatectic reworking also occurred in the Jiaoxi and Mayuan complexes during the Late Ordovician. The zircons from leucosome samples yield a weighted mean age of 437 ± 5 Ma[155], younger than the main peak age from the gneiss samples, indicating that the leucosomes probably formed slightly later than the main anatectic event.

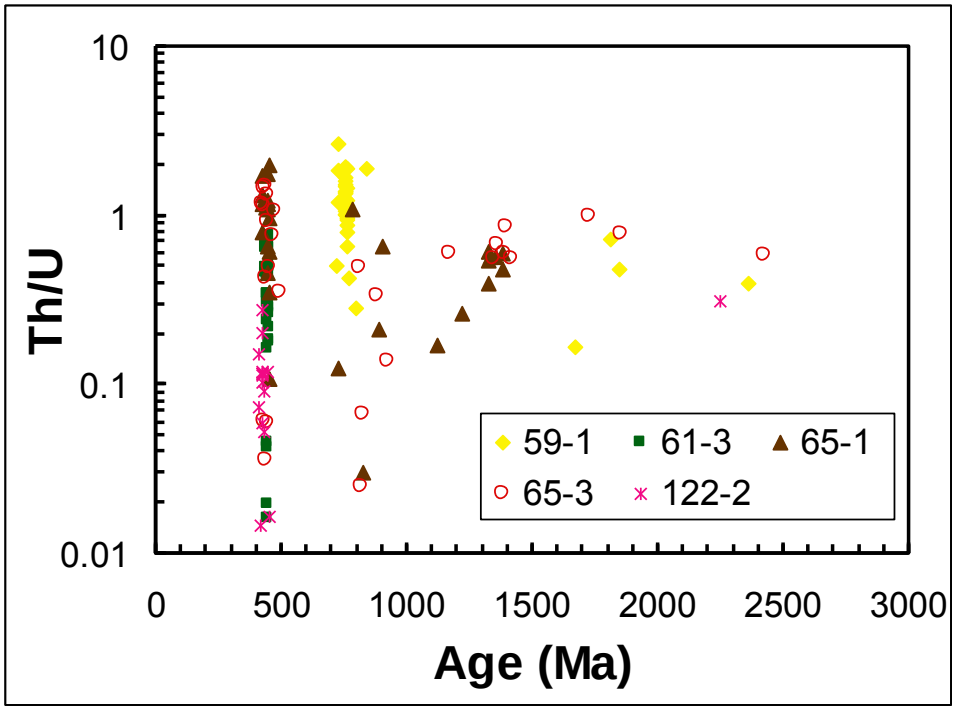

Figure 5.23 Plots of Th/U ratios vs. U–Pb ages of concordant zircons in the Jiaoxi and Mayuan complexes; Samples 59-1, 61-3 and 65-1 are gneisses; samples 65-3 and 122-2 are leucosomes in the Mayuan Complex[155]

Although the rocks of the Jiaoxi and Mayuan complexes are typically high-grade gneisses or migmatites, their chemical signatures are consistent, indicating that migmatization did not produce major alteration, especially with respect to the immobile trace and REE elements. The meta-mafic rocks are identified as subalkaline basalts with calc-alkaline compositions (Figure 5.17, 5.18). The felsic paragneiss samples plot in the fields of arkose, lithic arenite and greywacke, (Figure 5.19), which are immature sediments, similar to the protoliths of the Tianjingping Complex (Figure 4.30). Therefore, it is interpreted that late Neoproterozoic sedimentary-volcanic series were also the protoliths of the Jiaoxi and Mayuan complexes. A major migmatization and anatectic event occurred between the Late

Ordovician and the Early Silurian, to form leucosomes and granites. As determined[155], almost all the leucosomes in the Jiaoxi and Mayuan complexes are peraluminous, plotting in the granite field but with variable contents of orthoclase; one sample falls in the tonalite field.

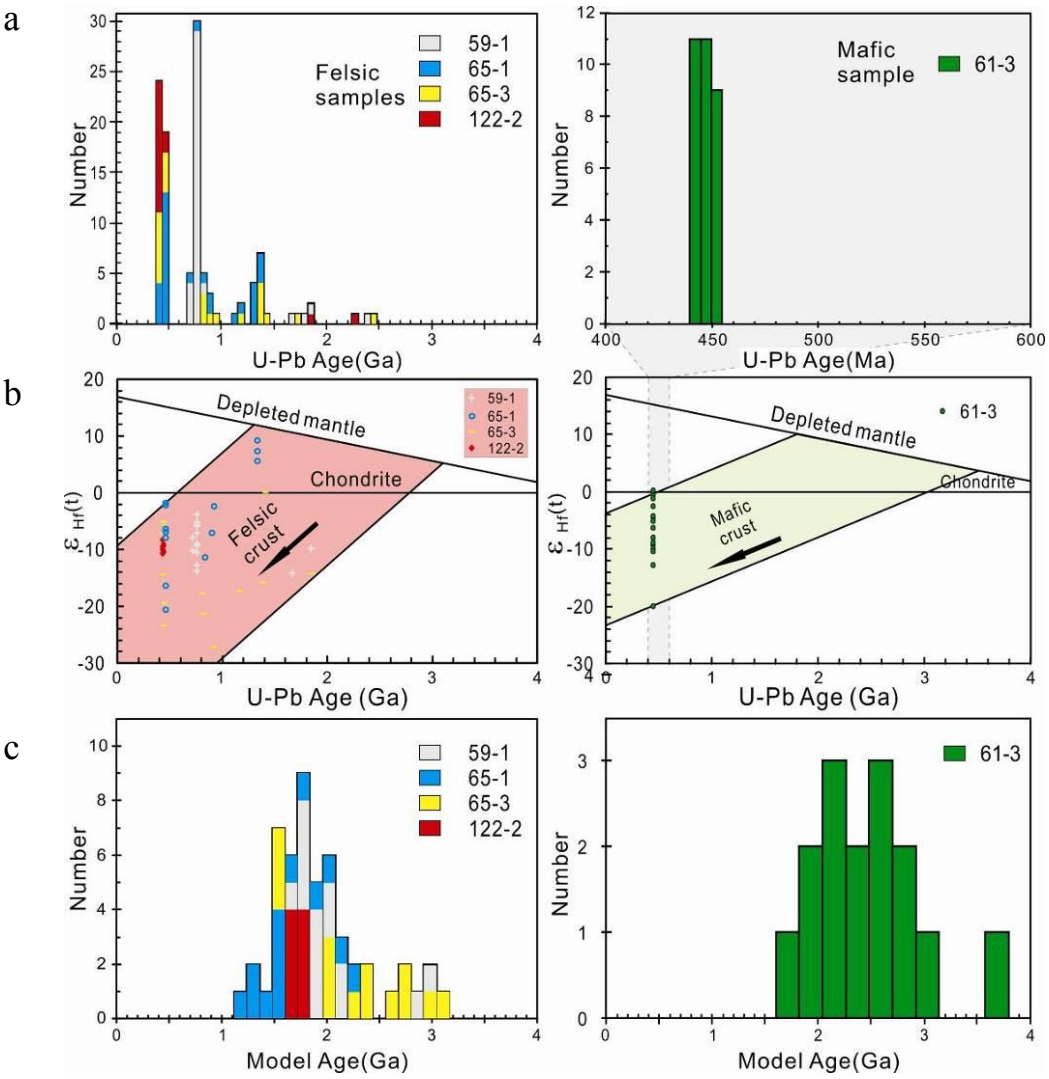

Figure 5.24 (a) U–Pb age histograms, (b) $\varepsilon_{Hf}(t)$ vs. U–Pb ages, and (c) crustal model age histograms of zircons from typical felsic and mafic samples in the Jiaoxi and Mayuan complexes

5.5.1 Cooling history of the Jiaoxi and Mayuan complexes

Based on the U-Pb zircon ages, together with the $^{40}Ar/^{39}Ar$ amphibole and biotite ages obtained during this study, as well as the temperature data provided by the thermochronometers and themobarometers, the T-t path of the Jiaoxi and Mayuan complexes can be established (Figure 5.25).

The crystallization temperature ranges calculated for zircons from the mafic and felsic gneisses (samples 61-3 and 65-1), with ages of ~452 - ~440 Ma, is 639 - 744 ºC, which are slightly lower than for samples from the Tianjingping Complex (APPENDIX C). As for zircons from the leucosomes (samples 65-3 and 122-2), which are dated at ~448 - ~410 Ma (Liu, 2009), the temperatures are calculated at ~598 - ~874 ºC (APPENDIX C). This indicates that the leucosomes in the Mayuan Complex were probably developed slightly later as temperature increased. The calculated pressure and temperature from the amphibole-plagioclase geothermobarometer are 3 - 11 kbar (mean P = 6 kbar) and 700 - 783 ºC (mean T = 746 ºC). Since the $^{40}Ar/^{39}Ar$ amphibole age of sample 61-3 is ~381 Ma and the Ar closure temperature of amphibole is about 450 - 525 ºC[149], the time taken for the temperature to drop below ca. 700 - 783 ºC and for the amphibole-plagioclase assemblage to reach equilibrium should be approximately 65 Ma, i.e. before ~381 Ma but younger than the U-Pb zircon age of ca. 445 Ma for sample 61-3.

The $^{40}Ar/^{39}Ar$ biotite age of sample 122-1 is ~152 Ma, which might record the later activation/reactivation of the fault near the sampling site. It might be the reason for the decreasing ages in each step of the biotite $^{40}Ar/^{39}Ar$ analysis of sample 65-2, which was collected in the same area as sample 122-1, near the shear zone. Thus ~290 Ma, which is the oldest age with the initial four steps of analysis (44% of released ^{39}Ar), would be closer to the thermal event recorded by biotite in sample 65-2 (biotite closure temperature is about 300 ± 50 ºC[156]) (Figure 5.25). Therefore, the estimated time at which the calculated temperature of ~339 - ~347 ºC (mean T = ~342 ºC; biotite-muscovite geothermometer in samples 65-2 and 66-3) was recorded would be between ~381 Ma and ~290 Ma (Figure 5.25).

On the basis of the above chronological data with corresponding closure or metamorphic tepratures, an estimated cooling T-t path in the range of ~850 - ~250 ºC for the Jiaoxi and Mayuan complexes has been obtained (Figure 5.25). It is significant that relatively rapid cooling occurred between ~445 and ~330 Ma, followed by a more isothermal stage between ~330 and ~300 Ma.

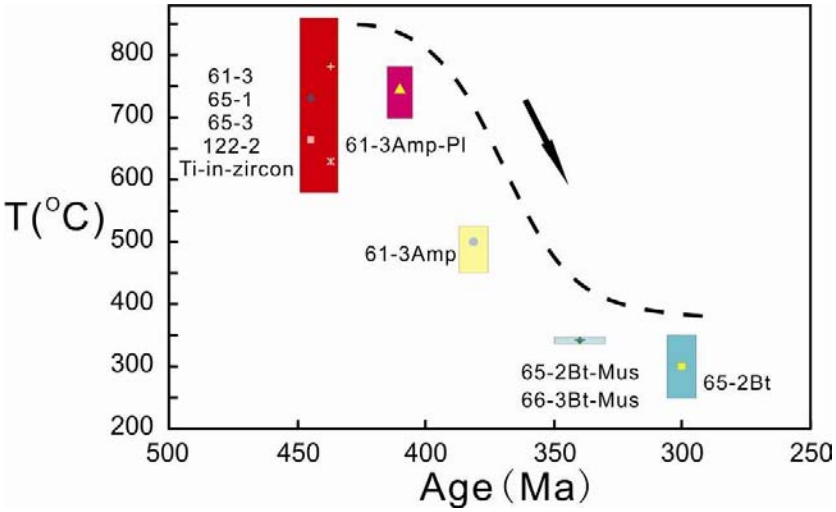

Figure 5.25 Cooling ages of the rocks from the Jiaoxi and Mayuan complexes, based on geochronology and temperature calculations. Ti-in-zircon, Amp-Pl and Bt-Mus stand for the geothermometers, Amp and Bt are the minerals used in the ^{40}Ar-^{39}Ar analyses of samples 61-3 and 65-2, respectively.

Chapter 6 Tectonic interpretation

§ 6.1 Provenance of the sedimentary protoliths

As discussed in Chapters 4 and 5, abundant inherited zircons with Precambrian ages are found in leucosome and paragneiss samples, and these results are used for estimating the depositional ages and for analysing the provenance of their sedimentary protoliths. The youngest cluster of inherited zircons found in the studied rocks are dated at ~680 Ma (Figure 4.34), with oscillatory zoning and Th/U ratios of 0.26 - 0.69. They suggest an igneous origin for these young zircons and a maximum deposition age of ca. 680 Ma for the protolith of the Tianjingping Complex.

Determination of the provenance of the sedimentary protolithes for the paragneisses of the Tianjingping, Jiaoxi and Mayuan complexes will help to understand the tectonic evolution of Precambrian NE Cathaysia Block. Figure 6.1a shows a relative probability plot based on $^{206}Pb/^{238}U$ (< 1.0 Ga) and $^{207}Pb/^{206}Pb$ (>1.0 Ga) zircon ages for 127 inherited zircons analysed during this study (the Tianjingping, Jiaoxi and Mayuan complexes), which can be compared with the age histogram of Precambrian magmatic and metamorphic zircon ages from rocks in northeastern Cathaysia (Figure 6.1b), southwestern Cathaysia (Figure 6.1c), the Yangtze Block (Figure 6.1d), and Laurentia (Figure 6.1e, f).

Although the detrital zircons from this study exhibit a broad age spectrum, they cluster at three major populations of 1850 - 1727 Ma (11 spots), 1416 - 1327 Ma (12 spots) and 922 - 677 Ma (81 spots), with several minor populations or singular ages of ~2700 Ma, ~2440 Ma, ~2300 Ma, ~2030 Ma, ~1580 Ma, ~1200 Ma and ~1050 Ma (Figure 6.1a). The main age peaks of ~1850 Ma and ~800 - ~750 Ma are consistent with crustal ages of igneous[34, 157], meta-sedimentary rocks[33] and river sands[158] from the NE Cathaysia Block. Besides, the age population of ~1420 - ~1210 Ma, which however were not detected by previous study in NE Cathaysia, are consistent with major crustal growth events during Mesoproterozoic in SW Cathaysia[27, 32, 59, 158] (Figure 6.1c) and the Yangtze Block (Jiangnan Orogen[159], Kongling[31], Western margin[160], Figure 6.1d). One zircon grain as old as 2696 ± 7 Ma indicates that Archean components may present in the NW Fujian area. Differing from the previous investigation in the NE Cathaysia, the absence of zircons population of ~2500 Ma or zircons > 2700 Ma in this study is probably due to the

low number of analyzed spots. Therefore, the basement rocks in NE and SW Cathaysia are consistent according to the Precambrian zircon age data.

Obvious zircon age peaks of ~1800 Ma suggest that the protoliths be comparable to the basements of North America (Figure 6.1e, f) rather than those of Eastern India and East Antarctica[32, 161-163]. Although zircon age peaks of ~1800 Ma are present in Western Australia[32, 164-165], their $^{176}Hf/^{177}Hf$ ratios (0.280706 - 0.281510)[164] are apparently lower than those of zircons from SW Cathaysia (0.281515 - 0.282098)[32] and from this study (0.281232 - 0.282213, NE Cathaysia) (Figure 6.2). Besides, analyses of Hf isotope in zircons from this study, SW Cathaysia and Yangtze show different crustal growth episodes from that in Western Australia. For example, in Western Australia, model ages (T_{DM}) of the zircons having positive $\varepsilon_{Hf}(t)$ values (+0.2 - +14.7) are ~3800 Ma, ~ 3300 Ma, ~3200 - 2700 Ma, ~2400 Ma, ~1300 - 820 Ma, but there is a gap between ~2400 ma and 1300 Ma[164]. There is no such a gap in data from detrital zircons from Yangtze (Kongling[31], west margin[160]), SW Cathaysia[32] and NE Cathaysia (APPENDIC D). Thus, detrital zircons in Cathaysia and NW Yangtze indicate significant juvenile input during Paleo- to Mesoproterozoic, which are distinctly different from Western Australia. So the Rodinia reconstruction[32], in which Western Australia, India and East Antarctica are adjacent to South China, is not supported by these results.

On the other hand, abundant zircons with positive $\varepsilon_{Hf}(t)$ values (+0.1 - +14.7) and Paleo- to Mesoproterozoic model ages (~2250 - 1310 Ma) have been found in southwestern North America [166-167], which supports the relation between Laurentia and Cathaysia. Therefore, the Rodinia configuration[59], in which Cathaysia was next to western Laurentia before and during the late Mesoproterozoic assembly of Rodinia, is more consistent zircon U-Pb ages and Hf isotopic evidence.

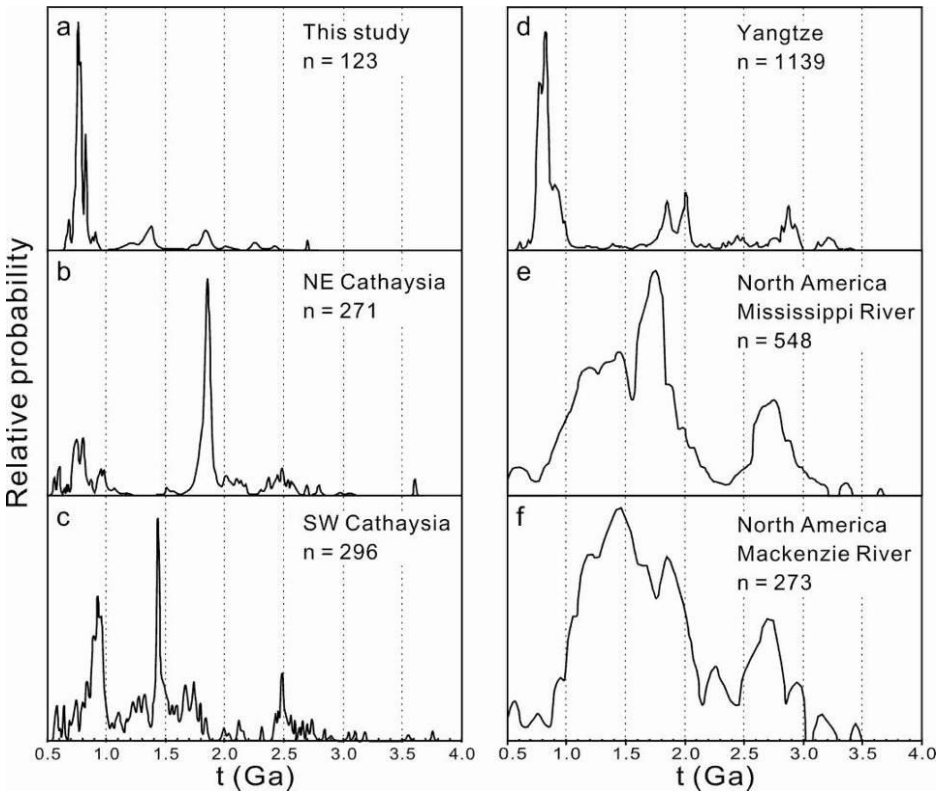

Figure 6.1 Relative probability plots of detrital zircon ages from this study and for other locations, using $^{206}Pb/^{238}U$ ages for ages < 1.0 Ga and $^{207}Pb/^{206}Pb$ ages for ages > 1.0 Ga. Data with < 10% discordance are used here. Data sources for age comparison are: references [33-34, 157-158] for NE Cathaysia; [32, 158, 168] for SW Cathaysia; [45-46, 160, 169-175] for Yangtze; [176] for North America (Mississippi and Mackenzie rivers).

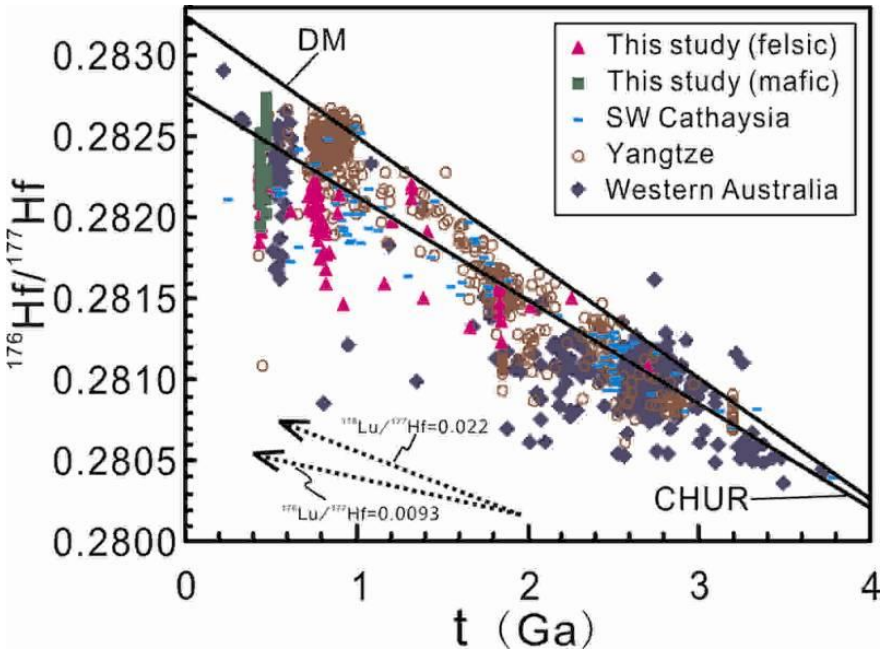

Figure 6.2 Hf isotopic evolution diagram with comparative data from SW Cathaysia[32], Yangtze[159-160, 172, 174, 177] and Western Australia[164].

§ 6.2 Crustal reworking of the Cathaysia Block during the "Caledonian" events between Early Ordovician and Early Devonian

The high-grade metamorphic rocks exposed in the NE Cathaysia have been believed to be Proterozoic due to the lack of reliable geochronological constraints on the metamorphic/anatectic and magmatic events[105, 178]. In this study, new La-ICPMS U-Pb anatectic zircon data from the NW Fujian area (Table 6.1) suggest that the tectonothermal events occurred during Ordovician and Silurian, consisting of at least three main episodes (~473 Ma, ~445 Ma, ~423 Ma). It indicates that the duration of the orogeny in the NW Fujian area was no shorter than ~50 Myr, starting at ~473 Ma (~Early Ordovician) or earlier, and terminating at ~423 Ma (~Middle Silurian) or later. Considering the age data of granitoids as mentioned in Chapter 1.1.3 and earlier geological observations, the orogeny may have started during the Middle Cambrian and lasted until the Middle Devonian, with major orogeny events (including syn- to post-orogenic melting) constrained between ~473 Ma and ~407 Ma in the NE Cathaysia, and between ~468 Ma and ~415 Ma in the SW Cathaysia (Figure 6.3).

Most of the "Caledonian" granitoids in the Cathaysia Block are S-type, the magma of which were derived from partial melting of the continental crust. A few of the granites show characteristics of I-type granitoids, with the magma containing mantle materials[76-82, 155, 179-180]. There is no evidence for large-scale "Caledonian" I-type granitoids related to plate subduction, or synchronous island arc-type volcanic rocks in the study area. As shown by the Hf isotope results, the protoliths of the mafic gneisses were basaltic rocks with mantle input that formed no later than Neoproterozoic (Figure 4.34, 5.24), although their anatectic zircon U-Pb ages are during the "Caledonian" orogeny. Combined with the low $\varepsilon_{Nd}(t)$ values of −18.4 to −2.1 and high $(^{87}Sr/^{86}Sr)_i$ values of 0.7071 to 0.7287 for most "Caledonian" granitoids[87, 180], it appears that the "Caledonian" orogenic event in the Cathaysia Block was likely due to an intracontinental collision rather than the subduction of oceanic crust or arc-continental collision.

Comparing with the Paleozoic magmatic zircon ages from the Qinling-Tongbai-Dabie orogen along the northern margin of the South China Block[181-187], the age peaks in the Cathaysia Block (ca. 488, 471, 455, 440 and 415 Ma) are within the age range of the Qinling-Tongbai-Dabie orogen (Figure 6.3). This suggests a possible linkage or interaction of the two orogens.

Table 6.1 La-ICPMS anatectic zircon U-Pb data of metamorphic rocks in NW Fujian area

Sample No.	Rock	Age (Ma)	Number	Complex
125-1	leucosome	471 ± 4 445 ± 3	1 22	Tianjingping
125-2	felsic gneiss	445 ± 4	8	Tianjingping
125-4	mafic gneiss	448 ± 3 473 ± 4	14 7	Tianjingping
39-1	mafic gneiss	444 ± 3	26	Tianjingping
65-1	felsic gneiss	445 ± 2 423 ± 3	13 4	Mayuan
61-3	mafic gneiss	445 ± 2	31	Mayuan

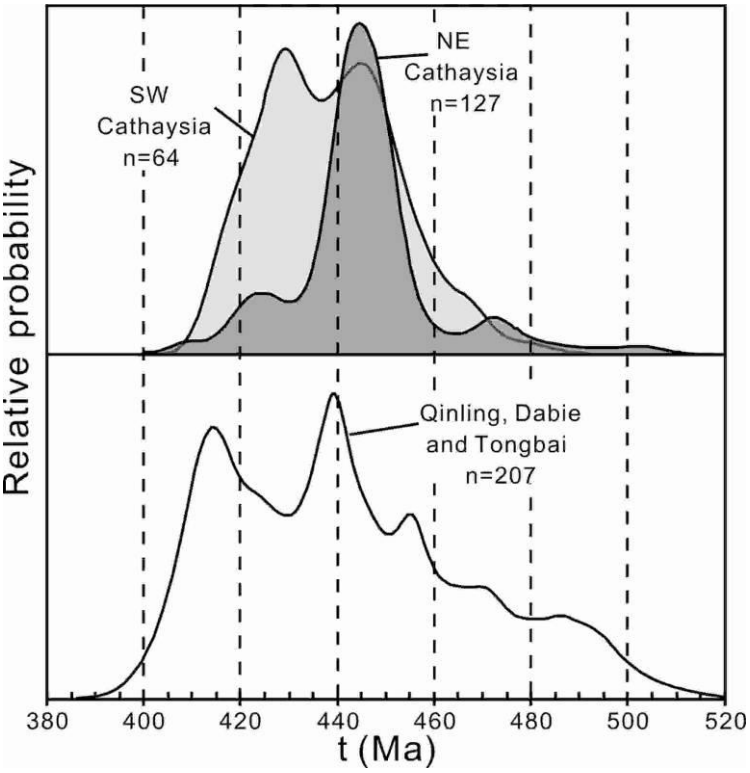

Figure 6.3 Relative probability plots for Paleozoic zircon $^{206}Pb/^{238}U$ ages from the NE and SW Cathaysia, and the Qingling-Tongbai-Dabie Orogen. Data with < 10% discordance are used here. Data sources for age comparison are: references [33, 155] and this study for NE Cathaysia; [80, 82] for SW Cathaysia; [179, 181, 183-187] for the Qingling-Tongbai-Dabie Orogen.

In the cooling paths discussed in Chapters 4 and 5 (Figure 4.35 and 5.25), the temperature of the Tianjingping Complex might have already dropped below the Ar closure temperature of biotite (about 300 ± 50 ºC[156]) by ca. 392 Ma (Figure 4.23), whereas the temperature of the Jiaoxi and Mayuan complexes just dropped below the closure temperature of amphibole (about 450 - 525 ºC[149]) at ca. 381 Ma (Figure 5.14). However, magmatic events were still occurring in Hainan, which is located in SW Cathaysia, at ca. 370 Ma[77]. This indicates not only the longevity of the

"Caledonian" tectono-thermal events (over 50 Mys), but also the localization of the events and their inhomogeneous cooling rates.

§ 6.3 Conclusions

(1) New La-ICPMS U-Pb zircon ages presented here and in previous study suggest that the original litho-stratigraphy should be abandoned and the terminology "Complex" should be used instead of "Group" and "Formation" for the high grade metamorphic rock series in northwestern Fujian, where the protoliths were strongly reworked by Early Paleozoic tectono-thermal events.

(2) Zircon U-Pb ages and Hf isotopic evidence suggest that the bmasement of the Cathaysia share similarities with that of North America[166-167, 176], lending support for the Rodinia configuration proposed by Li et al.[59].

(3) The protoliths of the felsic paragneiss in the NW Fujian area are immature sediments, probably deposited not early than middle Neoproterozoic (~680 Ma). Many metamorphic rocks contain 0.99 - 0.72 Ga detrital zircons, which are interpreted as reflecting the tectono-thermal events related to the assembly and break-up of the Rodinia supercontinent during the Neoproterozoic[27].

(4) The intense and widespread Palaeozoic tectono-thermal events in Cathaysia between 504 Ma and 408 Ma[33, 80, 82, 155] (and this study) were probably related to those occurred in the Qinling-Tongbai-Dabie orogen during 512 - 406 Ma[181-187].

(5) The "Caledonian" tectono-thermal events in the Cathaysia Block lasted over 50 Mys, but vary between different segments of the orogen.

§ 6.4 Suggestions for future work

To further advance our understanding of the nature and tectonic history of the NE Cathaysia Block, the following aspects of research are recommended.

(1) There is a need for geochronological studies on the of the zircon rims from the plagioclase-amphibole gneisses. The narrow rims show no zoning structure and likely recorded metamorphic events either during the "Caledonian" orogeny, or during later events.

(2) A systematic geochronological, petrological and geochemical study of the Early-Middle Paleozoic granites in the region will help to define the relationship between

the igneous activity and the anatexis events in the NE Cathaysia Block as reported in this study.

(3) More detailed U-Pb and Lu-Hf isotopic research on the inherited zircons/cores in the metamorphic rocks are necessary for studying the evolving history of the Cathaysia Block during the Neoproterozoic, and its possible connection to other continents through comparisons with the isotopic characteristics of zircons from continental blocks like Western Australia, India, East Antarctica and North America.

(4) There is a need for systematic and more in-depth investigations of the metamorphic P-T-t of the region.

References

[1] Huang Q Z, Song Y X, Zhuang J M, et al. Geological Map of Fujian Province. 1998, Fujian Province Map Press: Sanming.

[2] Metcalfe I. Gondwanaland dispersion, Asian accretion and evolution of eastern Tethys. Australian Journal of Earth Sciences, 1996, 43(6): 605-623.

[3] Metcalfe I. Paleozoic and Mesozoic tectonic evolution and palaeogeography of East Asian crustal fragments: The Korean Peninsula in context. Gondwana Research, 2006, 9(1-2): 24-46.

[4] Hoffman P F. The break-up of Rodinia, birth of Gondwana, true polar wander and the snowball Earth. Journal of African Earth Sciences, 1999, 28(1): 17-33.

[5] Veevers J J. Tectonic climatic supercycle in the billion-year plate-tectonic Eon-Permian Pangean icehouse alternates with Cretaceous dispersed-continents greenhouse. Sedimentary Geology, 1990, 68(1-2): 1-16.

[6] Veevers J J. Gondwanaland from 650-500 Ma assembly through 320 Ma merger in Pangea to 185-100 Ma breakup: supercontinental tectonics via stratigraphy and radiometric dating. Earth-Science Reviews, 2004, 68(1-2): 1-132.

[7] Hoffman P F. Did the breakout of Laurentia turn Gondwanaland inside-out? Science, 1991, 252(5011): 1409-1412.

[8] Dalziel I W D. Neoproterozoic-Paleozoic geography and tectonics: Review, hypothesis, environmental speculation. Geological Society of America Bulletin, 1997, 109(1): 16-42.

[9] Weil A B, Van der Voo R, Mac Niocaill C, et al. The Proterozoic supercontinent Rodinia: paleomagnetically derived reconstructions for 1100 to 800 Ma. Earth and Planetary Science Letters, 1998, 154(1-4): 13-24.

[10] Karlstrom K, Harlan S, Williams M, et al. Refining Rodinia: Geologic evidence for the Australia-western US connection in the Proterozoic. GSA Today, 1999, 9(10): 1-7.

[11] Piper J D A. The Neoproterozoic Supercontinent: Rodinia or Palaeopangaea? Earth and Planetary Science Letters, 2000, 176(1): 131-146.

[12] Rogers N, Macdonald R, Fitton J G, et al. Two mantle plumes beneath the east African rift system: Sr, Nd and Pb isotope evidence from Kenya Rift basalts. Earth and Planetary Science Letters, 2000, 176(3-4): 387-400.

[13] Li Z and Powell C. An outline of the palaeogeographic evolution of the Australasian region since the beginning of the Neoproterozoic. Earth-Science Reviews, 2001, 53(3-4): 237-277.

[14] Meert J. Paleomagnetic evidence for a Paleo-Mesoproterozoic supercontinent

Columbia. Gondwana Research, 2002, 5(1): 207-215.
[15] Ross G M and Eaton D W. Proterozoic tectonic accretion and growth of western Laurentia: results from Lithoprobe studies in northern Alberta. Canadian Journal of Earth Sciences, 2002, 39(3): 313-329.
[16] Condie K C. The supercontinent cycle: are there two patterns of cyclicity? Journal of African Earth Sciences, 2002, 35(2): 179-183.
[17] Sears J and Price R. The hypothetical Mesoproterozoic supercontinent Columbia: implications of the Siberian-west Laurentian connection. Gondwana Research, 2002, 5(1): 35-39.
[18] Wilde S and Youssef K. A re-evaluation of the origin and setting of the Late Precambrian Hammamat Group based on SHRIMP U-Pb dating of detrital zircons from Gebel Umm Tawat, North Eastern Desert, Egypt. Journal of the Geological Society, 2002, 159(5): 595.
[19] Zhao G, Sun M, Wilde S, et al. Assembly, accretion and breakup of the Paleo-Mesoproterozoic Columbia supercontinent: records in the North China Craton. Gondwana Research, 2003, 6(3): 417-434.
[20] Li Z, Wang J, Li X, et al. From Sibao orogenesis to Nanhua rifting: late Precambrian tectonic history of eastern South China¨Can overview and field guide. 2003, Beijing: Geological Publishing House.
[21] Grabau A W. Stratigraphy of China, Part I: Paleozoic and Older. 1924, Beijing: The Geological Survey of Agriculture and Commerce. 1-528
[22] Huang B, Sun M Z, and Wu S X. Studies on genesis and characters of Caledonian migmatites in middle Wuyi Montains. Acta Petrologica Sinica, 1994, 10(4): 427-439.
[23] Ren J S. On the geotectonics of southern China. Acta Geologica Sinica-English Edition, 1990, 64(4): 275-287.
[24] Hsü K J, Shu S, Jiliang L, et al. Mesozoic overthrust tectonics in south China. Geology, 1988, 16(5): 418.
[25] Hsü K J, Li J, Chen H, et al. Tectonics of South China: key to understanding West Pacific geology. Tectonophysics, 1990, 183(1-4): 9-39.
[26] Li Z, Zhang L, and Powell C. South China in Rodinia: Part of the missing link between Australia, East Antarctica and Laurentia? Geology, 1995, 23(5): 407.
[27] Li Z, Li X, Zhou H, et al. Grenvillian continental collision in south China: New SHRIMP U-Pb zircon results and implications for the configuration of Rodinia. Geology, 2002, 30(2): 163.
[28] Li Z. Tectonic history of the major East Asian lithospheric blocks since the mid-Proterozoic: A synthesis. Mantle dynamics and plate interactions in East Asia, 1998, 27: 221-243.
[29] Qiu Y, Gao S, McNaughton N, et al. First evidence of> 3.2 Ga continental crust in the Yangtze craton of south China and its implications for Archean crustal

evolution and Phanerozoic tectonics. Geology, 2000, 28(1): 11.

[30] Zhang S, Zheng Y, Wu Y, et al. Zircon U-Pb age and Hf isotope evidence for 3.8 Ga crustal remnant and episodic reworking of Archean crust in South China. Earth and Planetary Science Letters, 2006, 252(1-2): 56-71.

[31] Zheng J, Griffin W, O'Reilly S, et al. Widespread Archean basement beneath the Yangtze craton. Geology, 2006, 34(6): 417.

[32] Yu J H, O'Reilly S Y, Wang L J, et al. Where was South China in the Rodinia supercontinent? Evidence from U-Pb geochronology and Hf isotopes of detrital zircons. Precambrian Research, 2008, 164(1-2): 1-15.

[33] Wan Y, Liu D, Xu M, et al. SHRIMP U-Pb zircon geochronology and geochemistry of metavolcanic and metasedimentary rocks in Northwestern Fujian, Cathaysia block, China: Tectonic implications and the need to redefine lithostratigraphic units. Gondwana Research, 2007, 12(1-2): 166-183.

[34] Liu R, Zhou H W, Zhang L, et al. Paleoproterozoic reworking of ancient crust in the Cathaysia Block, South China: Evidence from zircon trace elements, U-Pb and Lu-Hf isotopes. Chinese Science Bulletin, 2009, 54(9): 1543-1554.

[35] Li X H. Timing of the Cathaysia block formation: Constraints from SHRIMP U-Pb zircon geochronology. Episodes, 1997, 20(3): 188-192.

[36] Ma D Q, Huang D X, Xiao Z F, et al. eds. The crystalline basement of the Hainan Island - Stratigraphy and geochronology of the Baoban Group. 1998, China University of Geosciences Press: Wuhan. 60

[37] Li W, Li X, and Li Z. Neoproterozoic bimodal magmatism in the Cathaysia Block of South China and its tectonic significance. Precambrian Research, 2005, 136(1): 51-66.

[38] Jahn B M. Geochemical and isotopic characteristics of UHP eclogites and ultramafic rocks of the Dabie orogen: implications for continental subduction and collisional tectonics. When Continents Collide: Geodynamics and Geochemistry of Ultrahigh-Pressure Rocks, 1998: 203-239.

[39] Li X H. SHRIMP ion microprobe zircon U-Pb age of the NE Jiangxi ophiolite and its tectonic implications. Geochimica, 1994, 23(2): 125-131.

[40] Li W X and Li X H. Adakitic granites within the NE Jiangxi Ophiolites, South China--geochemical and Nd isotopic evidence. Precambrian Research, 2003, 122: 29-44.

[41] Lee K, Chang H, and Park K. Neoproterozoic bimodal volcanism in the central Ogcheon belt, Korea: age and tectonic implication. Precambrian Research, 1998, 89(1): 47-57.

[42] Lee S, Cho M, Cheong C, et al. Age, geochemistry, and tectonic significance of Neoproterozoic alkaline granitoids in the northwestern margin of the Gyeonggi massif, South Korea. Precambrian Research, 2003, 122(1): 297-310.

[43] Li X. U-Pb zircon ages of granites from the southern margin of the Yangtze

Block: timing of Neoproterozoic Jinning: Orogeny in SE China and implications for Rodinia Assembly. Precambrian Research, 1999, 97(1): 43-57.

[44] Li X, Li Z, Zhou H, et al. U-Pb zircon geochronology, geochemistry and Nd isotopic study of Neoproterozoic bimodal volcanic rocks in the Kangdian Rift of South China: implications for the initial rifting of Rodinia. Precambrian Research, 2002, 113(1): 135-154.

[45] Li X, Li Z, Ge W, et al. Neoproterozoic granitoids in South China: crustal melting above a mantle plume at ca. 825 Ma? Precambrian Research, 2003, 122(1): 45-83.

[46] Li Z, Li X, Kinny P, et al. Geochronology of Neoproterozoic syn-rift magmatism in the Yangtze Craton, South China and correlations with other continents: evidence for a mantle superplume that broke up Rodinia. Precambrian Research, 2003, 122(1): 85-109.

[47] Ling W, Gao S, Zhang B, et al. Neoproterozoic tectonic evolution of the northwestern Yangtze craton, South China: implications for amalgamation and break-up of the Rodinia Supercontinent. Precambrian Research, 2003, 122(1): 111-140.

[48] Ma G G, Li H Q, and Zhang Z C. On the time constraint of the Sinian in South China. Journal of Yichang Institute of Geology and Mineral Resources, 1984, 8: 1-29.

[49] Zhou H W, Li X H, Wang H R, et al. U-Pb zircon geochronology of basic volcanic rocks of the Yingyangguan Group in Hezhou, Guangxi, and its tectonic implications. Geological Review, 2002, 48 (Supplement): 22-25.

[50] Wang J, Li X, Duan T, et al. Zircon SHRIMP U-Pb dating for the Cangshuipu volcanic rocks and its implications for the lower boundary age of the Nanhua strata in South China. Chinese Science Bulletin, 2003, 48(16): 1663-1669.

[51] Wang J, Li Z, Duan T, et al. Stratigraphic and sedimentological records of the Neoproterozoic rift basins in southern China. Li ZX, Wang J, Li XH, Zhang S. From Sibao Orogenesis to Nanhua Rifting: Late Precambrian Tectonic History of Eastern South China-An Overview and Field Guide, 2003: 26-39.

[52] Zeng W, Zhou H W, Zhong Z Q, et al. Single zircon U-Pb ages and their tectonic implications of Neoproterozoic magmatic rocks in southeastern Guizhou, China. Geochimica, 2005, 34(6): 548-556.

[53] Li Z C, Wang G H, and Zhang Z C. Isotopic age spectrum of the Huangling granitic batholith , western Hubei. Geology and Mineral Resources of South China, 2002(3): 19-28.

[54] Ge W C, Li X H, Li Z X, et al. Mafic intrusions in Longsheng arcs: Age and its geological implications. Chines Journal of Geology, 2001, 36(1): 112-118.

[55] Valentine J W and Moores E M. Plate-tectonic Regulation of Faunal Diversity and Sea Level: a Model. Nature, 1970, 228(5272): 657-659.

[56] McMenamin M and McMenamin D. The emergence of animals: the Cambrian breakthrough. 1990, New York: Columbia University Press

[57] Dalziel I. Pacific margins of Laurentia and East Antarctica-Australia as a conjugate rift pair: evidence and implications for an Eocambrian supercontinent. Geology, 1991, 19(6): 598.

[58] Moores E. Southwest US¨CEast Antarctic (SWEAT) connection: a hypothesis: Geology, v. 19. doi, 1991, 10: 0091-7613.

[59] Li Z, Bogdanova S, Collins A, et al. Assembly, configuration, and break-up history of Rodinia: A synthesis. Precambrian Research, 2008, 160(1-2): 179-210.

[60] Piper J. Palaeomagnetism and the continental crust. 1987: John Wiley and Sons Inc., New York, NY

[61] Li Z, Evans D, and Zhang S. A 90 spin on Rodinia: possible causal links between the Neoproterozoic supercontinent, superplume, true polar wander and low-latitude glaciation. Earth and Planetary Science Letters, 2004, 220(3-4): 409-421.

[62] Li Z, Zhang L, and Powell C. South China in Rodinia: Part of the missing link between Australia¨CEast Antarctica and Laurentia? Geology, 1995, 23(5): 407.

[63] Li Z, Li X, Kinny P, et al. The breakup of Rodinia: did it start with a mantle plume beneath South China? Earth and Planetary Science Letters, 1999, 173(3): 171-181.

[64] Jiang G, Sohl L, and Christie-Blick N. Neoproterozoic stratigraphic comparison of the Lesser Himalaya (India) and Yangtze block (south China): Paleogeographic implications. Geology, 2003, 31(10): 917.

[65] Yang Z, Sun Z, Yang T, et al. A long connection (750-380 Ma) between South China and Australia: paleomagnetic constraints. Earth and Planetary Science Letters, 2004, 220(3-4): 423-434.

[66] Chen J F, Foland K A, Xing F M, et al. Magmatism along the southeast margin of the Yangtze block: Precambrian collision of the Yangtze and Cathysia blocks of China. Geology, 1991, 19(8): 815.

[67] Zhou M, Yan D, Kennedy A, et al. SHRIMP U-Pb zircon geochronological and geochemical evidence for Neoproterozoic arc-magmatism along the western margin of the Yangtze Block, South China. Earth and Planetary Science Letters, 2002, 196(1-2): 51-67.

[68] Zhou M, Kennedy A, Sun M, et al. Neoproterozoic arc©\related mafic intrusions along the northern margin of South China: implications for the accretion of Rodinia. The Journal of Geology, 2002, 110: 611-618.

[69] Zhou J C, Wang X L, Qiu J S, et al. Lithogeochemistry of Meso- and Neoproterozoic mafic-ultramafic rocks from northern Guangxi. Acta Geologica Sinica, 2003, 19(1): 9-18.

[70] Zhou J, Wang X, Qiu J, et al. Geochemistry of Meso-and Neoproterozoic

mafic-ultramafic rocks from northern Guangxi, China: Arc or plume magmatism? Geochemical Journal-Japan-, 2004, 38(2): 139-152.
[71] Huang J Q, Ren J S, Jiang C F, et al. eds. Geotectonic Evolution of China. 1980, Science Press: Beijing. 124
[72] Liu B J and Xu X S. eds. Atlas of lithofacies and paleogeography of South China. 1994, Science Press: Beijing. 188
[73] Su W, Huff W, Ettensohn F, et al. K-bentonite, black-shale and flysch successions at the Ordovician-Silurian transition, South China: Possible sedimentary responses to the accretion of Cathaysia to the Yangtze Block and its implications for the evolution of Gondwana. Gondwana Research, 2009, 15(1): 111-130.
[74] Sun T. A new map showing the distribution of the granites in South China and its explanatory notes. Geological Bulletin of China, 2006, 25(3): 332-335.
[75] Shu L S. Predevonian tectonic evolution of south China: from Cathaysian Block to Caledonian period folded orogenic belt. Geological Journal of China Universities, 2006, 12(4): 418-431.
[76] Ding X, Zhou X, and Sun T. The episodic growth of the continental crustal basement in south China: single zircon LA-ICPMS U-Pb dating of Guzhai granodiorite in Guangdong. Geologcial Review, 2005, 51(4): 382-392.
[77] Ding S, Hu J, Song B, et al. U-Pb dating of zircon fromthe bed parallel anatectic granitic intrusion in the Baoban group in Hainan Island and the tectonic implication. Science in China Series D: Earth Sciences, 2005, 48(12): 2092-2103.
[78] Lou F, Shen W, Wang D, et al. Zircon U-Pb Isotopic Chronology of the Wugongshan Dome Compound Granite in Jiangxi Province. Acta Geologica Sinica, 2005, 79(5): 636-644.
[79] Sun T. The Mesozoic magmatic rocks assemblages and their petrogenesis, South China. 2005, Report of Postdoctoral Research of Nanjing University: Nanjing. 41
[80] Geng H Y, Xu X S, O'Reilly S Y, et al. Cretaceous volcanic-intrusive magmatism in western Guangdong and its geological significance. Science in China: Series D Earth Sciences, 2006, 49(7): 696-713.
[81] Peng S, Jin Z, Liu Y, et al. Petrochemistry, Chronology and Tectonic Setting of Strong Peraluminous Anatectic Granitoids in Yunkai Orogenic Belt, Western Guangdong Province, China. Journal of China University of Geosciences, 2006, 17(1): 1-12.
[82] Wang Y, Fan W, Zhao G, et al. Zircon U-Pb geochronology of gneissic rocks in the Yunkai massif and its implications on the Caledonian event in the South China Block. Gondwana Research, 2007, 12(4): 404-416.
[83] Zeng Y and Liao Q A. Caledonian granites in the western Wuyi and inversion of the Orogenic process. Regional Geology of China, 2000, 19(4): 344-349.
[84] Wang J, Tu X, and Sun D. U-Pb dating of anatectic migmatites at Gaozhou in

the Yunkai Block, western Guangdong, China. Geochimica, 1999, 28(3).

[85] Zeng W, Zhang L, Zhou H W, et al. Caledonian reworking of Paleoproterozoic basement in the Cathaysia Block: Constraints from zircon U-Pb dating, Hf isotopes and trace elements. Chinese Science Bulletin, 2008, 53(6): 895-904.

[86] Li C F. Fundamental features of migmatites in Guangzhou district. Guangdong Geology, 1991, 6(1): 17-31.

[87] Wang D Z and Shen W Z. Genesis of granitoids and crustal evolution in southeast China. Earth Science Frontiers (China University of Geosciences, Beijing), 2003, 10(3): 209-220.

[88] Ren J S. Thoughts on the study of tectonics of China. Geological Review, 1996, 42(4): 290-294.

[89] Cocks L. Ordovician and Silurian global geography. Journal of the Geological Society, 2001, 158: 197-210.

[90] Burrett C, Long J, and Stait B. Early-Middle Palaeozoic biogeography of Asian terranes derived from Gondwana. Geological Society London Memoirs, 1990, 12(1): 163.

[91] Zheng Y F. The location of the South China in the reconstructions of the Neoproterozoic supercontinent. Chinese Science Bulletin, 2004, 49(8): 715-717.

[92] Van der Voo R. Paleomagnetism of the Atlantic, Tethys, and Iapetus oceans. 1993: Cambridge University Press

[93] Nie S Y. Paleoclimatic and paleomagnetic constraints on the Paleozoic reconstructions of South China, North China and Tarim. Tectonophysics, 1991, 196(3-4): 279-308.

[94] Zhao X, Coe R, Gilder S, et al. Palaeomagnetic constraints on the palaeogeography of China: implications for Gondwanaland. Australian Journal of Earth Sciences, 1996, 43(6): 643-672.

[95] Li Z and Powell C. Late Proterozoic to early Paleozoic paleomagnetism and the formation of Gondwanaland. Gondwana Eight: Rotterdam, Balkema, 1993: 9-21.

[96] Hu X J, Xu J K, Tong Z X, et al. The Precambrian Geology of Southwestern Zhejiang Province. 1991, Beijing: Geological Publishing House

[97] Jin W S, Zhuang J M, Yang C X, et al. Characteristics of Petrology, Geochemistry and Metamorphism of the Precaledonian Regional Metamorphic Rocks in Fujian Province. Geology of Fujian, 1992, 11(4): 241-261.

[98] Chen J and Jahn B. Crustal evolution of southeastern China: Nd and Sr isotopic evidence. Tectonophysics, 1998, 284(1-2): 101-133.

[99] Chen J F, Guo X S, Tang J F, et al. Nd isotopic model ages: implications of the growth of the continental crust of southeastern China. Journal of Nanjing University, 1999, 35(6): 649-658.

[100] Hong D, Xie X, and Zhang J. An exploration on the composition, nature and evolution of mid-lower crust in South China based on the Sm-Nd isotopic data of

granites. Geological Journal of China Universities (in Chinese), 1999, 5: 361-371.
[101] Fu S C, Chen J M, and Lin W S. Geological characteristics of late Archean metamorphic rocks in the Qiuyuan area of Pucheng county, Fujian Province. Geology of Fujian, 1991, 10(2): 103-113.
[102] Li X H, Sun M, Wei G J, et al. Geochemical and Sm-Nd isotopic study of amphibolites in the Cathaysia Block, southeastern China: evidence for an extremely depleted mantle in the Paleoproterozoic. Precambrian Research, 2000, 102(3-4): 251-262.
[103] Mei H L, Zhuang J M, and Yang C X. P-T-t paths and geodynamic implication of Precambrian metamorphic rocks in northern Fujian. Geology of Fujian, 1993, 12(3): 182-194.
[104] Jin W S and Sun D Z. Deep crustal structure and its evolution of South China. 1997, Beijing: Geological Publishing House
[105] Zhao G and Cawood P. Tectonothermal evolution of the Mayuan assemblage in the Cathaysia Block: Implications for Neoproterozoic collision-related assembly of the South China Craton. American Journal of Science, 1999, 299(4): 309.
[106] Zhuang J M, Huang Q Z, Deng B Z, et al. Study on Strata Unit Division of Precambrian Metamorphic Rocks in Fujian Province. 2000, Xiamen: Xiamen University Press
[107] Zhao F Q, Chen Y Z, and Li R A. Study on the multiple deformations and structural levels of the Precaledonian metamorphic basement in Northern Fujian. Geology of Fujian, 1993, 12(1): 33-44.
[108] Gan X C, Li H M, Sun D Z, et al. Single zircon U-Pb age and its geological significance of the "Hexi Group", southwestern Zhejiang Province. Journal of Nanjing university (Earth Sciences), 1993, 5(3): 361-364.
[109] Gan X C, Li H M, Sun D Z, et al. A geochronologicaI study on Early Proterozoic granitic rocks,southwestern Zhejiang. Acta Petrologica Et Mineralogica, 1995, 14(1): 1-8.
[110] Dickin A P. Radiogenic Isotope Geology. 2006; Available from: http://www.onafarawayday. com/Radiogenic/Ch2/Ch2-2.htm
[111] Worley J and Kvech S. ICP-MS. 2000; Available from: http://www.cee.vt.edu/ ewr/environmental/teach/smprimer/icpms/icpms.htm
[112] Hanchar J and Miller C. Zircon zonation patterns as revealed by cathodoluminescence and backscattered electron images: implications for interpretation of complex crustal histories. Chemical Geology, 1993, 110(1-3): 1-13.
[113] Hanchar J and Rudnick R. Revealing hidden structures: the application of cathodoluminescence and back-scattered electron imaging to dating zircons from lower crustal xenoliths. Lithos, 1995, 36(3-4): 289-303.
[114] Rubatto D and Gebauer D. Use of cathodoluminescence for U-Pb zircon dating by ion microprobe: Some examples from the western Alps.

Cathodoluminescence in Geosciences, ed. M. Pagel, V. Barbin, P. Blanc, et al. 2000. 373-400

[115] Corfu F, Hanchar J, Hoskin P, et al. Atlas of zircon textures. Reviews in Mineralogy and Geochemistry, 2003, 53(1): 469.

[116] Yuan H, Gao S, Liu X, et al. Accurate U-Pb age and trace element determinations of zircon by laser ablation-inductively coupled plasma-mass spectrometry. Geostandards and geoanalytical Research, 2007, 28(3): 353-370.

[117] Ludwig K R. Isoplot 4.0. Berkeley Geochronology Center Special Publication No. 4, 2008: 77.

[118] Dodson M. Closure temperature in cooling geochronological and petrological systems. Contributions to Mineralogy and Petrology, 1973, 40(3): 259-274.

[119] Bottomley R and York D. 40Ar-39Ar age determinations on the Owyhee basalt of the Columbia Plateau. Earth and Planetary Science Letters, 1976, 31(1): 75-84.

[120] Steiger R and J ger E. Subcommission on geochronology: convention on the use of decay constants in geochronology and cosmochronology. Earth and Planetary Science Letters, 1977, 36: 359-362.

[121] Griffin W, Wang X, Jackson S, et al. Zircon chemistry and magma mixing, SE China: In-situ analysis of Hf isotopes, Tonglu and Pingtan igneous complexes. Lithos, 2002, 61(3-4): 237-269.

[122] DeBievre P and Taylor P D P. Table of the isotopic composition of the elements. International Journal of Mass Spectrometry and Ion Processes, 1993, 123: 1-149.

[123] Chu M, Chung S, Song B, et al. Zircon U-Pb and Hf isotope constraints on the Mesozoic tectonics and crustal evolution of southern Tibet. Geology, 2006, 34(9): 745.

[124] Scherer E, Munker C, and Mezger K. Calibration of the lutetium-hafnium clock. Science, 2001, 293(5530): 683.

[125] Blichert-Toft J and Albar¨¨de F. The Lu-Hf isotope geochemistry of chondrites and the evolution of the mantle-crust system. Earth and Planetary Science Letters, 1997, 148(1-2): 243-258.

[126] Vervoort J and Blichert-Toft J. Evolution of the depleted mantle: Hf isotope evidence from juvenile rocks through time. Geochimica Et Cosmochimica Acta, 1999, 63(3-4): 533-556.

[127] Vervoort J and Patchett J. Behavior of hafnium and neodymium isotopes in the crust: constraints from Precambrian crustally derived granites. Geochimica Et Cosmochimica Acta, 1996, 60(19): 3717-3733.

[128] Wu Y B and Zheng Y F. Genesis of zircon and its constraints on interpretation of U-Pb age. Chinese Science Bulletin, 2004, 49(15): 1554-1569.

[129] Hoskin P and Ireland T. Rare earth element chemistry of zircon and its use as a provenance indicator. Geology, 2000, 28(7): 627.
[130] Belousova E, Griffin W, O'Reilly S, et al. Igneous zircon: trace element composition as an indicator of source rock type. Contributions to Mineralogy and Petrology, 2002, 143(5): 602-622.
[131] Taylor S and McLennan S. The continental crust: its composition and evolution. New York: Oxford, 1985.
[132] Grove M and Harrison T. 40Ar* diffusion in Fe-rich biotite. The American mineralogist, 1996, 81(7-8): 940-951.
[133] Maniar P D and Piccoli P M. Tectonic discrimination of granitoids. Bulletin of the Geological Society of America, 1989, 101(5): 635.
[134] Barker F. Trondhjemite: definition, environment and hypotheses of origin. Trondhjemites, dacites, and related rocks, 1979: 1¨C12.
[135] Sun S and McDonough W. Chemical and isotopic systematics of oceanic basalts: implications for mantle composition and processes. Geological Society London Special Publications, 1989, 42(1): 313.
[136] Pearce J. Role of the sub-continental lithosphere in magma genesis at active continental margins. Continental basalts and mantle xenoliths, 1983, 249.
[137] Rudnick R and Gao S. Composition of the continental crust, Rudnick, RL (ed.) Treatise in Geochemistry, Vol. 3, The Crust. 2003, Elsevier, Amsterdam.
[138] Wood D, Joron J, and Treuil M. A re-appraisal of the use of trace elements to classify and discriminate between magma series erupted in different tectonic settings. Earth and Planetary Science Letters, 1979, 45(2): 326-336.
[139] Gibson S A, Kirkpatrick R J, Emmerman R, et al. The trace element composition of the lavas and dykes from a 3 km vertical section through a lava pile of Eastern Iceland. Journal of Geophysics Research, 1982, 87: 6532-6546.
[140] Pearce J A. ed. A users guide to basalt discrimination diagram. Trace element geochemistry of volcanic rocks: Applications for massive sulphide exploration., ed. D. A. Wyman. Vol. 12. 1996, Geological Association of Canada, Short Course Notes. 79-113
[141] Miyashiro A. Volcanic rock series in island arcs and active continental margins. American Journal of Science, 1974, 274(4): 321.
[142] Pearce N and Leng M. The origin of carbonatites and related rocks from the Igaliko Dyke Swarm, Gardar Province, South Greenland: field, geochemical and CO-Sr-Nd isotope evidence. Lithos, 1996, 39(1-2): 21-40.
[143] Wintsch R and Kvale C. Differential mobility of elements in burial diagenesis of siliciclastic rocks. Journal of Sedimentary Research-Section A-Sedimentary Petrology and Processes, 1994, 64(2): 349-361.
[144] Watson E and Harrison T. Zircon thermometer reveals minimum melting conditions on earliest Earth. Science, 2005, 308(5723): 841.

[145] Watson E, Wark D, and Thomas J. Crystallization thermometers for zircon and rutile. Contributions to Mineralogy and Petrology, 2006, 151(4): 413-433.
[146] Bea F, Montero P, Gonzalez-Lodeiro F, et al. Zircon thermometry and U-Pb ion-microprobe dating of the gabbros and associated migmatites of the Variscan Toledo Anatectic Complex, Central Iberia. Journal of Geological Society, 2006, 163(5): 847.
[147] Baldwin J, Brown M, and Schmitz M. First application of titanium-in-zircon thermometry to ultrahigh-temperature metamorphism. Geology, 2007, 35(4): 295.
[148] Hanchar J and Hoskin P. Zircon. 2003: Mineralogical Society of America
[149] McDougall I and Harrison T. Geochronology and Thermochronology by the 40Ar/39Ar Method. 1999: Oxford University Press, USA
[150] Butler R F, Gehrels G E, Baldwin S L, et al. Paleomagnetism and geochronology of the Ecstall pluton in the Coast Mountains of British Columbia: Evidence for local deformation rather than large-scale transport. Journal of Geophysical Research-Solid Earth, 2002, 107(B1).
[151] Hoskin P W O and Ireland T R. Rare earth element chemistry of zircon and its use as a provenance indicator. Geology, 2000, 28(7): 627-630.
[152] Whitehouse M and Kamber B. On the overabundance of light rare earth elements in terrestrial zircons and its implication for Earth's earliest magmatic differentiation. Earth and Planetary Science Letters, 2002, 204(3-4): 333-346.
[153] Rickwood P. Boundary lines within petrologic diagrams which use oxides of major and minor elements. Lithos, 1989, 22(4): 247-263.
[154] Hoisch T D. A muscovite-biotite geothermometer. American Mineralogist, 1989, 74: 565-572.
[155] Liu R. Pre-Hercynian crustal anatexis in the Cathaysia Block: A case study from Zhejiang and Fujian provinces, in *China University of Geosciences*. 2009, China University of Geosciences: Wuhan. 97
[156] Gehrels G E. Detrital zircon geochronology of the Taku terrane, southeast Alaska. Canadian Journal of Earth Sciences, 2002, 39(6): 921-931.
[157] Xiang H, Zhang L, Zhou H W, et al. U-Pb zircon geochronology and Hf isotope study of metamorphosed basic-ultrabasic rocks from metamorphic basement in southwestern Zhejiang: The response of the Cathaysia Block to Indosinian orogenic event. Science in China Series D-Earth Sciences, 2008, 51(6): 788-800.
[158] Xu X S, O'Reilly S Y, Griffin W L, et al. The crust of Cathaysia: Age, assembly and reworking of two terranes. Precambrian Research, 2007, 158(1-2): 51-78.
[159] Wu R, Zheng Y, Wu Y, et al. Reworking of juvenile crust: Element and isotope evidence from Neoproterozoic granodiorite in South China. Precambrian Research, 2006, 146(3-4): 179-212.
[160] Sun W H, Zhou M F, Gao J F, et al. Detrital zircon U-Pb geochronological

and Lu-Hf isotopic constraints on the Precambrian magmatic and crustal evolution of the western Yangtze Block, SW China. Precambrian Research, 2009, 172(1-2): 99-126.

[161] Boger S, Wilson C, and Fanning C. Early Paleozoic tectonism within the East Antarctic craton: The final suture between east and west Gondwana? Geology, 2001, 29(5): 463.

[162] Jayananda M, Moyen J F, Martin H, et al. Late Archaean (2550-2520 Ma) juvenile magmatism in the Eastern Dharwar craton, southern India: constraints from geochronology, Nd-Sr isotopes and whole rock geochemistry. Precambrian Research, 2000, 99(3-4): 225-254.

[163] Liu R, Zhang B R, Zhang H F, et al. U-Pb Zircon Age, Geochemical and Sr-Nd-Hf Isotopic Compositions of Neoproterozoic Granitoids in Northwestern Margin of Yangtze Block (South China): Implications for Neoproterozoic Tectonic Evolution. Journal of Earth Science, 2009, 20(4): 659-680.

[164] Griffin W, Belousova E, Shee S, et al. Archean crustal evolution in the northern Yilgarn Craton: U-Pb and Hf-isotope evidence from detrital zircons. Precambrian Research, 2004, 131(3-4): 231-282.

[165] Veevers J, Saeed A, Belousova E, et al. U-Pb ages and source composition by Hf-isotope and trace-element analysis of detrital zircons in Permian sandstone and modern sand from southwestern Australia and a review of the paleogeographical and denudational history of the Yilgarn Craton. Earth-Science Reviews, 2005, 68(3-4): 245-279.

[166] Bickford M E, Mueller P A, Kamenov G D, et al. Crustal evolution of southern Laurentia during the Paleoproterozoic: Insights from zircon Hf isotopic studies of ca. 1.75 Ga rocks in central Colorado. Geology, 2008, 36(7): 555-558.

[167] Wang C, Campbell I, Allen C, et al. Rate of growth of the preserved North American continental crust: Evidence from Hf and O isotopes in Mississippi detrital zircons. Geochimica Et Cosmochimica Acta, 2009, 73(3): 712-728.

[168] Li Z, Wartho J, Occhipinti S, et al. Early history of the eastern Sibao Orogen (South China) during the assembly of Rodinia: New mica 40Ar/39Ar dating and SHRIMP U-Pb detrital zircon provenance constraints. Precambrian Research, 2007, 159(1-2): 79-94.

[169] Wang X L, Zhou J C, Qiu J S, et al. LA-ICP-MS U-Pb zircon geochronology of the Neoproterozoic igneous rocks from Northern Guangxi, South China: Implications for tectonic evolution. Precambrian Research, 2006, 145(1-2): 111-130.

[170] Zhang S, Zheng Y, Wu Y, et al. Zircon U-Pb age and Hf-O isotope evidence for Paleoproterozoic metamorphic event in South China. Precambrian Research, 2006, 151(3-4): 265-288.

[171] Zhang S, Zheng Y, Wu Y, et al. Zircon isotope evidence for>= 3.5 Ga continental crust in the Yangtze craton of China. Precambrian Research, 2006,

146(1-2): 16-34.
[172] Zheng Y F, Zhao Z F, Wu Y B, et al. Zircon U-Pb age, Hf and O isotope constraints on protolith origin of ultrahigh-pressure eclogite and gneiss in the Dable orogen. Chemical Geology, 2006, 231(1-2): 135-158.
[173] Ye M, Li X, Li W, et al. SHRIMP zircon U-Pb geochronological and whole-rock geochemical evidence for an early Neoproterozoic Sibaoan magmatic arc along the southeastern margin of the Yangtze Block. Gondwana Research, 2007, 12(1-2): 144-156.
[174] Xiong Q, Zheng J P, Yu C M, et al. Zircon U-Pb age and Hf isotope of Quanyishang A-type granite in Yichang: signification for the Yangtze continental cratonization in Paleoproterozoic. Chinese Science Bulletin, 2009, 54(3): 436-446.
[175] Wu Y B, Gao S, Gong H J, et al. Zircon U-Pb age, trace element and Hf isotope composition of Kongling terrane in the Yangtze Craton: refining the timing of Palaeoproterozoic high-grade metamorphism. Journal of Metamorphic Geology, 2009, 27(6): 461-477.
[176] Rino S, Komiya T, Windley B, et al. Major episodic increases of continental crustal growth determined from zircon ages of river sands; implications for mantle overturns in the Early Precambrian. Physics of the Earth and Planetary Interiors, 2004, 146(1-2): 369-394.
[177] Jiao W F, Wu Y B, Yang S H, et al. The oldest basement rock in the Yangtze Craton revealed by zircon U-Pb age and Hf isotope composition. Science in China Series D-Earth Sciences, 2009, 52(9): 1393-1399.
[178] Shui T. Tectonic framework of the continental basement of southeast China. Science in China Series B, 1988, 31: 885-896.
[179] Wang K L, O'Reilly S Y, Griffin W L, et al. Sulfides in mantle peridotites from Penghu Islands, Taiwan: Melt percolation, PGE fractionation, and the lithospheric evolution of the South China block. Geochimica Et Cosmochimica Acta, 2009, 73(15): 4531-4557.
[180] Zhang F R, Shu L S, Wang D Z, et al. Discussions on the tectonic setting of Caledonian granitoids in the eastern segment of South China. Earth Science Frontiers, 2009, 16(1): 248-260.
[181] Wang H L, Xu X Y, Chen J L, et al. Dating and geochemical characteristics of the Yanwan Paleozoic collisional intrusion in the west segment of Northern Qinling Mts. Acta Geologica Sinica, 2009, 83(3): 353-364.
[182] Wang T, Wang X, Tian W, et al. North Qinling Paleozoic granite associations and their variation in space and time: Implications for orogenic processes in the orogens of central China. Science in China Series D: Earth Sciences, 2009, 52(9): 1359-1384.
[183] Wu Y B, Hanchar J M, Gao S, et al. Age and nature of eclogites in the Huwan shear zone, and the multi-stage evolution of the Qinling-Dabie-Sulu orogen,

central China. Earth and Planetary Science Letters, 2009, 277(3-4): 345-354.
[184] Zhang L, Zhong Z Q, Zhang H, et al. The formation of foliated (garnet-bearing) granites in the Tongbai-Dabie orogenic belt: partial melting of subducted continental crust during exhumation. Journal of Metamorphic Geology, 2009, 27(9): 789-803.
[185] Sun W, Li S, Chen Y, et al. Timing of Synorogenic Granitoids in the South Qinling, Central China: Constraints on the Evolution of the Qinling-Dabie Orogenic Belt. The Journal of Geology, 2002, 110: 457-468.
[186] Lu X P, Wu F Y, Zhao C B, et al. Triassic U-Pb age for zircon from granites in the Tonghua area and its response to the Dabie-Sulu ultrahigh-pressure collisional orogenesis. Chinese Science Bulletin, 2003, 48(15): 1616-1623.
[187] Chen W F, Chen P R, Zhou X M, et al. Single Zircon LA-ICP-MS U-Pb Dating of the Guandimiao and Wawutang Granitic Plutons in Hunan, South China and Its Petrogenetic Significance. Acta Geologica Sinica, 2007, 81(1).

APPENDIX A: List of samples collected in this study

Sample Number	Sample Name	Minerals for Geochronology			P	T	GPS
		Zr	Hb	Bt			
The Tianjingping Complex							
31-1	Leucogranite						N 26°53′18.6″ E 116°35′14.0″
31-2	Leucogranite						N 26°53′18.6″ E 116°35′14.0″
31-3	Leucogranite						N 26°53′18.6″ E 116°35′14.0″
31-4	Chl-Pl gneiss						N 26°53′18.6″ E 116°35′14.0″
31-5	Bt-Pl gneiss						N 26°53′18.6″ E 116°35′14.0″
31-6	Bt-Hb-Pl gneiss			X			N 26°53′18.6″ E 116°35′14.0″
31-6-1	Quartzofelsdparic vein						N 26°53′18.6″ E 116°35′14.0″
31-7	Bi-Hb-Pl gneiss						N 26°53′18.6″ E 116°35′14.0″
31-8	Chl-Pl gneiss						N 26°53′18.6″ E 116°35′14.0″
31-9	Leucogranite						N 26°53′18.6″ E 116°35′14.0″
31-10	Bi-Pl gneiss						N 26°53′18.6″ E 116°35′14.0″
34-1	Quartzofelsdparic vein						N 26°52′13.0″ E 116°42′27.2″
34-3	Bi-Pl gneiss						N 26°52′13.0″ E 116°42′27.2″
34-4	Hb-Pl gneiss	X				X	N 26°52′13.0″ E 116°42′27.2″
35-1	Bi-Pl gneiss						N 26°52′22.7″ E 116°42′37.5″
38	Leucogranodiorite						N 26°54′27.8″ E 116°44′46.7″
39-1	Amphibolite		X		X	X	N 26°54′23.3″ E 116°44′52.3″
39-2	Amphibolite						N 26°54′23.3″ E 116°44′52.3″
39-4	Amphibolite						N 26°54′23.3″ E 116°44′52.3″
40-2	Bi-Pl gneiss						N 26°40′22.2″ E 116°42′41.0″
41-1	Fine-grained Bi-Pl gneiss						N 26°40′38.0″ E 116°43′11.8″
41-3	Pl-Hb gneiss						N 26°40′38.0″ E 116°43′11.8″
125-1	Leucogranite	X					N 26°53′12.1″ E 116°35′05.0″
125-2	Leucogranite	X					N 26°53′12.1″ E 116°35′05.0″
125-3	Hb-Bi-Pl gneiss						N 26°53′12.1″ E 116°35′05.0″
125-4	Bi-Pl gneiss	X		X			N 26°53′12.1″ E 116°35′05.0″
125-5	Leucogranite						N 26°53′12.1″ E 116°35′05.0″
The Mayuan Complex							
53	Bi-Pl gneiss						N 26°46′07.4″ E 118°29′47.4″
54	Mica gneiss						N 26°45′49.1″ E 118°29′10.9″
55	Bi gneiss						N 26°45′19.5″ E 118°28′13.8″
56-2	Bi gneiss						N 26°45′15.6″ E 118°27′24.1″
57-2	Mica gneiss						N 26°44′52.1″ E 118°26′04.5″
59-4	Bi-Pl gneiss						N 27°33′50.6″ E 117°38′30.0″
59-5	Quartzofelsdparic vein						N 27°33′50.6″ E 117°38′30.0″
65-1	Bi-Pl gneiss	X					N 27°27′27.7″ E 117°45′37.4″
65-2	Bi-Pl gneiss					X	N 27°27′27.7″ E 117°45′37.4″
65-3	Granitic vein						N 27°27′27.7″ E 117°45′37.4″
65-4-1	Gt-bearing Sill-Mica-Pl gneiss						N 27°27′27.7″ E 117°45′37.4″
65-4-2	Gt-bearing Sill-Mica-Pl gneiss						N 27°27′27.7″ E 117°45′37.4″
65-5	Bi-Pl gneiss						N 27°27′27.7″ E 117°45′37.4″
66-2	Bi-Pl gneiss						N 27°24′21.2″ E 117°49′36.5″
Sample Number	**Sample Name**	**Minerals for Geochronology**			**P**	**T**	**GPS**

Sample Number	Sample Name	Minerals for Geochronology			P	T	GPS
		Zr	Hb	Bt			
The Mayuan Complex							
66-3	Bi-Pl gneiss					X	N 27°24′21.2″ E 117°49′36.5″
117-2	Gneiss						N 27°52′23.5″ E 118°46′29.8″
122-1	Bi-Pl gneiss		X	X			N 27°28′01.1″ E 117°36′22.1″
122-2	Quartzofelsdparic vein	X					N 27°28′01.1″ E 117°36′22.1″
122-3	Bi-Pl gneiss						N 27°28′01.1″ E 117°36′22.1″
134-1	Granitic gneiss						N 27°42′25.8″ E 118°47′49.2″
134-2	Granitic gneiss						N 27°42′25.8″ E 118°47′49.2″
135	Mica gneiss						N 27°40′29.0″ E 118°49′28.4″
The Jiaoxi Complex							
59-1	Fine-grained Bi-Pl gneiss	X					N 27°33′50.6″ E 117°38′30.0″
59-2	Leocogranite						N 27°33′50.6″ E 117°38′30.0″
59-3	Fine-grained Bi-Pl gneiss						N 27°33′50.6″ E 117°38′30.0″
60-1	Pl gneiss						N 27°32′02.7″ E 117°38′33.4″
61-1	Fine-grained Bi-Pl gneiss						N 27°32′02.7″ E 117°38′33.4″
61-2	Amphibolite						N 27°32′02.7″ E 117°38′33.4″
61-3	Hb-Pl gneiss	X	X		X	X	N 27°32′02.7″ E 117°38′33.4″
61-4	Leocogranite						N 27°32′02.7″ E 117°38′33.4″
The Mamianshan Complex							
1-6	Fine-grained Bi-Pl gneiss						N 27°23'27.0" E 118°59'26.7"
15-1	Hb schist						N 27°20′43.4″ E 118°43′32.8″
15-2	Qtz-Hb schist		X				N 27°20′43.4″ E 118°43′32.9″
16-1	Mica-Qtz schist						N 27°20′43.4″ E 118°43′32.9″
18-1	Hb schist						N 27°28'43.4" E 118°45'32.1"
19-2	Greenschist						N 27°22′26.7″ E 118°54′30.8″
58-2	Mica-Qtz schist		X				N 26°43′22.0″ E 117°23′02.9″
69-1	Hb schist		X				N 27°20′43.4″ E 118°43′32.9″
69-2	Hb schist						N 27°20′43.4″ E 118°43′32.9″
69-2	Hb schist						N 27°20′43.4″ E 118°43′32.9″
71-1	Bi granite		X				N 27°23'27.0" E 118°59'26.7"
119-1	Fine-grained Bi-Pl gneiss						N 27°27′11.6″ E 118°21′48.2″
124-1	Mico-Qtz schist		X				N 26°55′11.5″ E 117°00′01.6″
124-2	Bi schist						N 26°55′11.5″ E 117°00′01.6″
124-3	Mica schist						N 26°55′11.5″ E 117°00′01.6″
126-1	Ms-Qtz schist						N 26°44′55.4″ E 118°24′12.9″
126-4	Qtz schist						N 26°44′55.4″ E 118°24′12.9″
126-5	Greenschist						N 26°44′55.4″ E 118°24′12.9″
127-1	Greenschist						N 26°43′24.0″ E 118°22′55.1″
127-2	Ms-Qtz schist						N 26°43′24.0″ E 118°22′55.1″
128-1	Mylonitic Gt-bearing gneiss						N 27°02′14.3″ E 118°14′17.0″
131	Greenschist						N 27°12′29.5″ E 118°40′47.2″
132	Ms-Qtz schist						N 27°19′47.7″ E 118°42′23.0″
The Wanquan Complex							
43-1	Bi-Pl gneiss		X				N 26°35′35.9″ E 117°09′41.1″
45-2	Fine-grained Chl-Ep-Ms-Kf-Pl gneiss						N 26°35′55.3″ E 117°09′47.1″

		Zr	Hb	Bt		
The Wanquan Complex						
46-1	Fine-grained Chl-Ep-Ms-Kf-Pl gneiss					N 26°36′56.0″ E 117°09′35.7″
47-1	Fine-grained Mica-Pl gneiss					N 26°37′37.9″ E 117°10′30.9″
48-2	Bi-Pl gneiss					N 26°39′40.9″ E 117°11′17.5″
49	Bi-Ep-Pl gneiss					N 26°39′59.9″ E 117°14′25.7″
50	Ep-Ms-Pl gneiss					N 26°39′44.1″ E 117°14′49.1″
51	Ep-Ms-Pl gneiss					N 26°42′03.3″ E 117°17′26.4″
62-1	Finegrained Bi-Pl gneiss					N 27°29′47.6″ E 117°39′50.1″
64-1	Bi-Pl gneiss					N 27°28′13.0″ E 117°43′16.4″
64-2	Gt-bearing Bi-Pl gneiss				X	X N 27°28′09.0″ E 117°43′26.9″
64-3	Fine-grained Bi-Pl gneiss					N 27°29′12.5″ E 117°43′15.9″
121-1	Fine-grained Bi-Pl gneiss					N 27°28′11.4″ E 117°43′33.2″

APPENDIX B: LA-ICP-MS zircon U-Pb isotope data

Spot No.	Content (ppm)		Isotopic ratio											Age (Ma)								
	^{232}Th	^{238}U	^{232}Th/^{238}U	^{207}Pb/^{206}Pb	1σ	^{207}Pb/^{235}U	1σ	^{206}Pb/^{238}U	1σ	^{208}Pb/^{232}Th	1σ	$\frac{^{207}Pb}{^{206}Pb}$	1σ	$\frac{^{207}Pb}{^{235}U}$	1σ	$\frac{^{206}Pb}{^{238}U}$	1σ	$\frac{^{208}Pb}{^{232}Th}$	1σ
The Tianjingping Complex																						
125-1-01	447	1167	0.38	0.05769	0.00090	0.56942	0.01130	0.07140	0.00062	0.02769	0.00043	518	40	458	7	445	4	552	8
125-1-02	1211	2428	0.50	0.05646	0.00095	0.59299	0.01156	0.07583	0.00067	0.03012	0.00040	471	39	473	7	471	4	600	8
125-1-03	843	1927	0.44	0.05728	0.00064	0.56182	0.00746	0.07076	0.00049	0.02652	0.00026	502	26	453	5	441	3	529	5
125-1-04	229	977	0.23	0.05512	0.00087	0.54408	0.00885	0.07160	0.00069	0.02737	0.00048	417	30	441	6	446	4	546	10
125-1-05	137	764	0.18	0.05717	0.00107	0.56091	0.01053	0.07083	0.00057	0.02431	0.00059	498	38	452	7	441	3	485	12
125-1-06	718	1556	0.46	0.05743	0.00068	0.56681	0.00669	0.07118	0.00047	0.02394	0.00023	508	22	456	4	443	3	478	5
125-1-07	38	638	0.06	0.05713	0.00123	0.56335	0.01183	0.07143	0.00059	0.02742	0.00108	497	44	454	8	445	4	547	21
125-1-08	350	1736	0.20	0.05566	0.00071	0.55048	0.00756	0.07131	0.00056	0.02733	0.00040	439	26	445	5	444	3	545	8
125-1-09	993	2254	0.44	0.05593	0.00055	0.55952	0.00573	0.07232	0.00056	0.02609	0.00023	450	15	451	4	450	3	521	5
125-1-10	1954	3251	0.60	0.05590	0.00052	0.55706	0.00629	0.07215	0.00069	0.02452	0.00019	449	13	450	4	449	4	490	4
125-1-11	1688	2785	0.61	0.05586	0.00053	0.55968	0.00588	0.07237	0.00049	0.02464	0.00023	447	18	451	4	450	3	492	4
125-1-12	39	1313	0.03	0.05479	0.00071	0.54305	0.00742	0.07177	0.00050	0.02645	0.00092	404	27	440	5	447	3	528	18
125-1-13	461	1230	0.37	0.05550	0.00067	0.55158	0.00784	0.07184	0.00047	0.02426	0.00027	432	29	446	5	447	3	485	5
125-1-14	209	745	0.28	0.05603	0.00088	0.55202	0.01015	0.07118	0.00049	0.02463	0.00036	454	39	446	7	443	3	492	7
125-1-15	17	1137	0.02	0.05506	0.00078	0.54019	0.00979	0.07098	0.00048	0.03370	0.00129	415	38	439	6	442	3	670	25
125-1-01t	142	1085	0.13	0.05552	0.00099	0.54740	0.01595	0.07149	0.00069	0.02869	0.00119	433	63	443	10	445	4	572	23
125-1-02t	290	1025	0.28	0.05490	0.00145	0.53578	0.01883	0.07049	0.00073	0.02928	0.00095	408	77	436	12	439	4	583	19
125-1-03t	31	902	0.03	0.05486	0.00110	0.54804	0.01603	0.07231	0.00081	0.04186	0.00206	406	62	444	11	450	5	829	40
125-1-04t	162	1270	0.13	0.05588	0.00098	0.55724	0.01526	0.07224	0.00067	0.02960	0.00096	448	59	450	10	450	4	590	19
125-1-05t	31	757	0.04	0.05462	0.00140	0.53889	0.01869	0.07133	0.00072	0.02765	0.00143	397	76	438	12	444	4	551	28
125-1-06t	655	1482	0.44	0.05403	0.00143	0.52568	0.01903	0.07029	0.00060	0.02122	0.00057	372	81	429	13	438	4	424	11
125-1-07t	444	1210	0.37	0.05467	0.00134	0.53596	0.01963	0.07133	0.00077	0.02573	0.00094	399	80	436	13	444	5	514	18
125-1-08t	217	918	0.24	0.05531	0.00109	0.53637	0.02078	0.07001	0.00080	0.02413	0.00052	425	85	436	14	436	5	482	10
125-2-01	113	2104	0.05	0.05662	0.00094	0.55891	0.01121	0.07183	0.00137	0.03359	0.00139	477	14	451	7	447	8	668	27
125-2-02	177	216	0.82	0.06610	0.00134	1.14937	0.02622	0.12744	0.00177	0.04348	0.00059	810	39	777	12	773	10	860	11
125-2-03	117	192	0.61	0.11165	0.00145	4.96483	0.09058	0.32720	0.00505	0.10441	0.00122	1826	18	1813	15	1825	25	2007	22

Spot No.	Content (ppm)		Isotopic ratio									Age (Ma)							
	^{232}Th	^{238}U	^{232}Th/^{238}U	^{207}Pb/^{206}Pb	1	^{207}Pb/^{235}U	1	^{206}Pb/^{238}U	1	^{208}Pb/^{232}Th	1	$\frac{^{207}Pb}{^{206}Pb}$	1	$\frac{^{207}Pb}{^{235}U}$	1	$\frac{^{206}Pb}{^{238}U}$	1	$\frac{^{208}Pb}{^{232}Th}$	1

125-2-03	117	192	0.61	0.11165	0.00145	4.96483	0.09058	0.32720	0.00505	0.10441	0.00122	1826	18	1813	15	1825	25	2007	22
Spot No.	Content (ppm)		Isotopic ratio									Age (Ma)							
	^{232}Th	^{238}U	$^{232}Th/^{238}U$	$^{207}Pb/^{206}Pb$	1σ	$^{207}Pb/^{235}U$	1σ	$^{206}Pb/^{238}U$	1σ	$^{208}Pb/^{232}Th$	1σ	$\frac{^{207}Pb}{^{206}Pb}$	1σ	$\frac{^{207}Pb}{^{235}U}$	1σ	$\frac{^{206}Pb}{^{238}U}$	1σ	$\frac{^{208}Pb}{^{232}Th}$	1σ
The Tianjingping Complex																			
125-2-04	93	141	0.67	0.11302	0.00158	5.14297	0.10464	0.33203	0.00415	0.10686	0.00148	1849	30	1843	17	1848	20	2052	27
125-2-05	57	125	0.46	0.09813	0.00259	3.81564	0.14051	0.28263	0.00642	0.10226	0.00257	1589	55	1596	30	1605	32	1968	47
125-2-06	167	203	0.82	0.12282	0.00163	6.00857	0.14333	0.35886	0.00655	0.11352	0.00139	1998	28	1977	21	1977	31	2173	25
125-2-07	129	187	0.69	0.14358	0.00190	8.37165	0.17939	0.42425	0.00651	0.14008	0.00182	2271	26	2272	19	2280	29	2650	32
125-2-08	324	411	0.79	0.14089	0.00155	8.22808	0.18149	0.41462	0.00698	0.13532	0.00131	2238	25	2256	20	2236	32	2565	23
125-2-09	35	1713	0.02	0.05651	0.00070	0.56069	0.01111	0.07222	0.00088	0.02927	0.00094	473	35	452	7	450	5	583	18
125-2-10	196	259	0.76	0.11298	0.00288	5.13125	0.16702	0.32901	0.00565	0.12023	0.00269	1848	51	1841	28	1834	27	2295	49
125-2-11	222	254	0.87	0.06334	0.00124	1.11332	0.03063	0.12853	0.00213	0.04243	0.00054	720	48	760	15	779	12	840	11
125-2-12	626	491	1.28	0.06407	0.00130	1.08882	0.02623	0.12330	0.00110	0.04273	0.00047	744	48	748	13	750	6	846	9
125-2-13	469	579	0.81	0.06456	0.00103	1.08985	0.02349	0.12224	0.00126	0.04066	0.00049	760	41	748	11	743	7	806	10
125-2-14	762	974	0.78	0.05622	0.00098	0.55449	0.01286	0.07124	0.00065	0.02352	0.00029	461	48	448	8	444	4	470	6
125-2-15	398	448	0.89	0.06420	0.00136	1.13554	0.03086	0.12805	0.00122	0.04187	0.00056	748	55	770	15	777	7	829	11
125-2-16	177	894	0.20	0.05575	0.00081	0.55605	0.01155	0.07213	0.00054	0.02479	0.00042	443	44	449	8	449	3	495	8
125-2-17	575	597	0.96	0.06283	0.00135	1.05544	0.02578	0.12166	0.00106	0.04039	0.00052	702	50	732	13	740	6	800	10
125-2-18	184	335	0.55	0.08376	0.01014	1.66850	0.10841	0.16638	0.00383	0.07624	0.00514	1287	122	997	41	992	21	1485	97
125-2-19	606	1663	0.36	0.06241	0.00075	1.11073	0.02071	0.12862	0.00097	0.04163	0.00047	688	37	759	10	780	6	824	9
125-2-20	208	171	1.22	0.10997	0.00365	4.76724	0.18348	0.31452	0.00524	0.09868	0.00194	1799	65	1779	32	1763	26	1902	36
125-2-21	517	672	0.77	0.06427	0.00117	1.06090	0.02495	0.11969	0.00091	0.03944	0.00049	751	48	734	12	729	5	782	10
125-2-22	639	606	1.05	0.06432	0.00087	1.14182	0.02302	0.12838	0.00105	0.04162	0.00039	752	40	773	11	779	6	824	7
125-2-23	486	693	0.70	0.06497	0.00101	1.14490	0.02339	0.12743	0.00092	0.04039	0.00048	773	41	775	11	773	5	800	9
125-2-24	999	1019	0.98	0.06436	0.00065	1.08287	0.01835	0.12175	0.00076	0.03895	0.00031	753	34	745	9	741	4	772	6
125-2-25	622	667	0.93	0.06585	0.00109	1.11069	0.02516	0.12215	0.00096	0.04167	0.00045	802	46	759	12	743	6	825	9
125-2-03t	370	1275	0.29	0.05804	0.00154	0.56297	0.01881	0.07168	0.00205	0.02417	0.00065	531	39	453	12	446	12	483	13
125-2-04t	204	202	1.01	0.12621	0.00289	6.36528	0.17068	0.36553	0.00478	0.11391	0.00192	2046	42	2027	24	2008	23	2180	35
125-2-05t	4	902	0.00	0.05798	0.00142	0.56481	0.01571	0.07066	0.00071	0.10194	0.00615	529	58	455	10	440	4	1962	113
125-2-06t	31	1161	0.03	0.05737	0.00125	0.56116	0.01535	0.07074	0.00064	0.02690	0.00171	506	58	452	10	441	4	536	34
125-2-07t	289	1719	0.17	0.05629	0.00120	0.55865	0.01642	0.07201	0.00093	0.02516	0.00066	464	60	451	11	448	6	502	13
125-2-08t	619	848	0.73	0.06604	0.00119	1.15595	0.03380	0.12652	0.00129	0.04432	0.00070	808	59	780	16	768	7	876	13
125-4-01	7378	8317	0.89	0.05543	0.00040	0.55345	0.00841	0.07209	0.00050	0.02239	0.00015	430	31	447	5	449	3	448	3
125-4-02	17685	13826	1.28	0.05586	0.00040	0.55881	0.00794	0.07223	0.00053	0.02261	0.00015	447	28	451	5	450	3	452	3
125-4-03	17289	12263	1.41	0.06036	0.00051	0.59716	0.01062	0.07106	0.00062	0.02410	0.00021	616	34	475	7	443	4	481	4
125-4-04	131	4179	0.03	0.05639	0.00058	0.56632	0.00943	0.07254	0.00044	0.02279	0.00050	468	35	456	6	451	3	455	10
Spot No.	Content (ppm)		Isotopic ratio									Age (Ma)							
	^{232}Th	^{238}U	$^{232}Th/^{238}U$	$^{207}Pb/^{206}Pb$	1	$^{207}Pb/^{235}U$	1	$^{206}Pb/^{238}U$	1	$^{208}Pb/^{232}Th$	1	$\frac{^{207}Pb}{^{206}Pb}$	1	$\frac{^{207}Pb}{^{235}U}$	1	$\frac{^{206}Pb}{^{238}U}$	1	$\frac{^{208}Pb}{^{232}Th}$	1

125-4-04	131	4179	0.03	0.05639	0.00058	0.56632	0.00943	0.07254	0.00044	0.02279	0.00050	468	35	456	6	451	3	455	10
Spot No.	Content (ppm)		Isotopic ratio									Age (Ma)							
	^{232}Th	^{238}U	$^{232}Th/^{238}U$	$^{207}Pb/^{206}Pb$	1σ	$^{207}Pb/^{235}U$	1σ	$^{206}Pb/^{238}U$	1σ	$^{208}Pb/^{232}Th$	1σ	$\frac{^{207}Pb}{^{206}Pb}$	1σ	$\frac{^{207}Pb}{^{235}U}$	1σ	$\frac{^{206}Pb}{^{238}U}$	1σ	$\frac{^{208}Pb}{^{232}Th}$	1σ
The Tianjingping Complex																			
125-4-06	3993	7299	0.55	0.06812	0.00081	0.66868	0.01556	0.07125	0.00120	0.02800	0.00037	872	34	520	9	444	7	558	7
125-4-07	17129	12846	1.33	0.05624	0.00035	0.59228	0.00946	0.07596	0.00053	0.02527	0.00017	462	33	472	6	472	3	504	3
125-4-08	9561	12301	0.78	0.05793	0.00076	0.56860	0.01242	0.07167	0.00143	0.02530	0.00078	527	20	457	8	446	9	505	15
125-4-09	10188	10533	0.97	0.05627	0.00040	0.59144	0.00881	0.07610	0.00071	0.02662	0.00017	463	26	472	6	473	4	531	3
125-4-10	15885	13121	1.21	0.05603	0.00039	0.59419	0.00886	0.07670	0.00067	0.02691	0.00017	453	27	474	6	476	4	537	3
125-4-11	15119	13013	1.16	0.05662	0.00045	0.59853	0.01142	0.07640	0.00105	0.02736	0.00022	477	30	476	7	475	6	546	4
125-4-12	256	1199	0.21	0.05501	0.00090	0.58012	0.01238	0.07701	0.00110	0.03283	0.00064	413	36	465	8	478	7	653	12
125-4-13	13982	11869	1.18	0.05584	0.00050	0.55494	0.00977	0.07196	0.00105	0.02542	0.00020	446	23	448	6	448	6	507	4
125-4-14	12161	11222	1.08	0.05535	0.00043	0.58167	0.00890	0.07627	0.00087	0.02769	0.00021	427	23	466	6	474	5	552	4
125-4-15	12372	10604	1.17	0.05496	0.00038	0.57683	0.00885	0.07581	0.00064	0.02618	0.00016	411	29	462	6	471	4	522	3
125-4-01t	13324	11573	1.15	0.05419	0.00041	0.54509	0.00577	0.07239	0.00050	0.02287	0.00017	379	18	442	4	451	3	457	3
125-4-02t	2	1146	0.00	0.05455	0.00144	0.54494	0.01471	0.07212	0.00063	0.16997	0.01401	394	59	442	10	449	4	3173	242
125-4-03t	166	7333	0.02	0.05726	0.00070	0.56289	0.01380	0.07106	0.00150	0.04084	0.00158	502	28	453	9	443	9	809	31
125-4-04t	48	5097	0.01	0.05615	0.00081	0.55883	0.01418	0.07223	0.00148	0.06968	0.00331	458	34	451	9	450	9	1362	63
125-4-05t	3	1019	0.00	0.06280	0.00119	0.61485	0.01930	0.07106	0.00149	0.61623	0.03089	701	51	487	12	443	9	9704	386
125-4-06t	444	18479	0.02	0.06022	0.00100	0.59584	0.01535	0.07135	0.00082	0.06980	0.00259	611	51	475	10	444	5	1364	49
125-4-07t	5841	7194	0.81	0.05637	0.00069	0.55633	0.01323	0.07114	0.00078	0.02328	0.00031	467	48	449	9	443	5	465	6
34-4-01	445	484	0.92	0.06756	0.00146	1.19721	0.04089	0.12809	0.00118	0.04433	0.00061	855	70	799	19	777	7	877	12
34-4-02	156	328	0.48	0.06577	0.00167	1.17686	0.04047	0.12961	0.00135	0.04517	0.00087	799	70	790	19	786	8	893	17
34-4-03	516	831	0.62	0.06608	0.00101	1.19014	0.03118	0.13041	0.00122	0.04467	0.00058	809	52	796	14	790	7	883	11
34-4-04	1469	3768	0.39	0.11199	0.00101	4.65488	0.11219	0.30039	0.00262	0.09661	0.00110	1832	42	1759	20	1693	13	1864	20
34-4-05	54	108	0.50	0.07114	0.00446	1.31829	0.08182	0.13635	0.00278	0.05178	0.00250	961	123	854	36	824	16	1020	48
34-4-06	767	803	0.96	0.06700	0.00125	1.24636	0.03817	0.13572	0.00157	0.04622	0.00056	838	60	822	17	820	9	913	11
34-4-07	468	563	0.83	0.06854	0.00128	1.21209	0.03531	0.12821	0.00115	0.04358	0.00057	885	59	806	16	778	7	862	11
34-4-08	59	98	0.60	0.06990	0.00254	1.30215	0.05313	0.13629	0.00162	0.04678	0.00126	925	82	847	23	824	9	924	24
34-4-09	284	410	0.69	0.06647	0.00230	1.00641	0.03994	0.11036	0.00185	0.04454	0.00097	821	77	707	20	675	11	881	19
34-4-10	396	786	0.50	0.06569	0.00108	1.15865	0.03501	0.12796	0.00102	0.04557	0.00068	796	63	781	16	776	6	901	13
34-4-11	343	456	0.75	0.08005	0.00184	2.08974	0.07496	0.18886	0.00225	0.06603	0.00135	1198	68	1145	25	1115	12	1292	26
34-4-12	333	568	0.59	0.06857	0.00155	1.29549	0.03956	0.13731	0.00157	0.05272	0.00107	886	60	844	17	829	9	1038	21
34-4-13	1019	2099	0.49	0.11197	0.00113	4.11892	0.11063	0.26572	0.00352	0.10129	0.00122	1832	43	1658	22	1519	18	1950	22
34-4-14	1234	992	1.24	0.06424	0.00117	1.13167	0.03384	0.12761	0.00143	0.04453	0.00054	749	60	769	16	774	8	881	11
34-4-15	462	804	0.57	0.06618	0.00172	1.23467	0.04580	0.13479	0.00130	0.04100	0.00080	812	77	816	21	815	7	812	15
Spot No.	Content (ppm)		Isotopic ratio									Age (Ma)							
	^{232}Th	^{238}U	$^{232}Th/^{238}U$	$^{207}Pb/^{206}Pb$	1	$^{207}Pb/^{235}U$	1	$^{206}Pb/^{238}U$	1	$^{208}Pb/^{232}Th$	1	$\frac{^{207}Pb}{^{206}Pb}$	1	$\frac{^{207}Pb}{^{235}U}$	1	$\frac{^{206}Pb}{^{238}U}$	1	$\frac{^{208}Pb}{^{232}Th}$	1

34-4-15	462	804	0.57	0.06618	0.00172	1.23467	0.04580	0.13479	0.00130	0.04100	0.00080	812	77	816	21	815	7	812	15
Spot No.	Content (ppm)		Isotopic ratio									Age (Ma)							
	^{232}Th	^{238}U	$^{232}Th/^{238}U$	$^{207}Pb/^{206}Pb$	1σ	$^{207}Pb/^{235}U$	1σ	$^{206}Pb/^{238}U$	1σ	$^{208}Pb/^{232}Th$	1σ	$\frac{^{207}Pb}{^{206}Pb}$	1σ	$\frac{^{207}Pb}{^{235}U}$	1σ	$\frac{^{206}Pb}{^{238}U}$	1σ	$\frac{^{208}Pb}{^{232}Th}$	1σ
The Tianjingping Complex																			
34-4-16	274	927	0.30	0.06279	0.00137	0.96636	0.03014	0.11157	0.00129	0.04194	0.00091	701	63	687	16	682	7	830	18
34-4-17	425	694	0.61	0.06780	0.00162	1.32268	0.04627	0.14076	0.00207	0.04850	0.00115	862	67	856	20	849	12	957	22
34-4-18	144	457	0.32	0.06211	0.00205	0.95243	0.03876	0.11081	0.00175	0.04333	0.00098	678	82	679	20	677	10	857	19
34-4-19	1982	1167	1.70	0.06629	0.00085	1.19801	0.03054	0.13070	0.00137	0.04400	0.00038	816	50	800	14	792	8	870	7
34-4-20	1684	1035	1.63	0.06636	0.00109	1.25094	0.03723	0.13597	0.00110	0.04455	0.00041	818	61	824	17	822	6	881	8
34-4-21	864	937	0.92	0.06582	0.00102	1.17968	0.03449	0.12937	0.00109	0.04233	0.00042	801	60	791	16	784	6	838	8
34-4-23	394	402	0.98	0.06749	0.00203	1.18968	0.04290	0.12770	0.00155	0.04315	0.00076	853	55	796	20	775	9	854	15
34-4-24	249	387	0.64	0.06824	0.00153	1.21558	0.03438	0.12920	0.00145	0.04696	0.00075	876	40	808	16	783	8	928	15
34-4-25	5657	2321	2.44	0.06578	0.00104	1.16436	0.03158	0.12757	0.00137	0.04236	0.00052	799	39	784	15	774	8	839	10
34-4-26	368	524	0.70	0.06867	0.00170	1.28740	0.04040	0.13577	0.00146	0.04732	0.00085	889	47	840	18	821	8	934	16
34-4-27	170	655	0.26	0.06250	0.00216	0.96878	0.04305	0.11147	0.00178	0.04984	0.00159	691	67	688	22	681	10	983	31
34-4-02t	261	448	0.58	0.11230	0.00190	5.03130	0.14560	0.32230	0.00320	0.10740	0.00170	1837	50	1825	25	1801	16	2062	31
34-4-03t	346	451	0.77	0.06600	0.00150	1.23430	0.03000	0.13540	0.00140	0.04600	0.00080	806	47	816	14	819	8	909	15
34-4-04t	268	454	0.59	0.08060	0.00170	2.31130	0.05430	0.20650	0.00240	0.06520	0.00150	1212	41	1216	17	1210	13	1277	28
34-4-05t	569	569	1.00	0.06590	0.00150	1.22860	0.02890	0.13490	0.00120	0.04350	0.00060	803	47	814	13	816	7	861	12
34-4-06t	935	779	1.20	0.06640	0.00120	1.24190	0.02150	0.13530	0.00110	0.04160	0.00050	819	33	820	10	818	6	824	10
34-4-07t	278	392	0.71	0.18480	0.00160	13.30950	0.11380	0.52060	0.00390	0.14160	0.00150	2696	7	2702	8	2702	17	2677	27
39-1-01	445	347	0.78	0.05669	0.00329	0.56044	0.03258	0.07182	0.00120	0.02284	0.00072	479	126	452	21	447	7	456	14
39-1-02	174	276	1.59	0.05833	0.00196	0.57602	0.02128	0.07147	0.00078	0.02332	0.00057	542	79	462	14	445	5	466	11
39-1-03	200	226	1.13	0.05739	0.00202	0.56202	0.02016	0.07164	0.00079	0.02122	0.00053	506	77	453	13	446	5	424	10
39-1-04	151	216	1.43	0.05733	0.00175	0.56236	0.01868	0.07118	0.00074	0.02276	0.00050	504	71	453	12	443	4	455	10
39-1-05	134	207	1.54	0.05592	0.00172	0.54870	0.01809	0.07149	0.00061	0.02263	0.00042	449	72	444	12	445	4	452	8
39-1-06	155	251	1.62	0.06051	0.00168	0.58753	0.01738	0.07114	0.00069	0.02245	0.00041	622	62	469	11	443	4	449	8
39-1-07	489	402	0.82	0.06157	0.00344	0.60129	0.03496	0.07117	0.00116	0.02153	0.00071	659	123	478	22	443	7	431	14
39-1-08	200	289	1.45	0.05755	0.00197	0.55987	0.01963	0.07111	0.00073	0.02182	0.00044	513	75	451	13	443	4	436	9
39-1-09	263	327	1.25	0.05762	0.00145	0.56421	0.01553	0.07122	0.00062	0.02278	0.00036	515	59	454	10	443	4	455	7
39-1-10	147	212	1.45	0.05759	0.00201	0.56268	0.02061	0.07158	0.00076	0.02276	0.00055	514	79	453	13	446	5	455	11
39-1-11	372	343	0.92	0.05623	0.00258	0.54769	0.02586	0.07118	0.00076	0.02138	0.00044	461	105	443	17	443	5	428	9
39-1-12	410	421	1.03	0.05739	0.00124	0.56580	0.01384	0.07183	0.00056	0.02141	0.00027	507	52	455	9	447	3	428	5
39-1-13	172	225	1.31	0.05541	0.00292	0.53866	0.02728	0.07108	0.00109	0.02078	0.00066	429	110	438	18	443	7	416	13
39-1-14	402	376	0.93	0.05465	0.00165	0.53425	0.01653	0.07133	0.00064	0.02338	0.00032	398	68	435	11	444	4	467	6
Spot No.	Content (ppm)		Isotopic ratio									Age (Ma)							
	^{232}Th	^{238}U	$^{232}Th/^{238}U$	$^{207}Pb/^{206}Pb$	1	$^{207}Pb/^{235}U$	1	$^{206}Pb/^{238}U$	1	$^{208}Pb/^{232}Th$	1	$\frac{^{207}Pb}{^{206}Pb}$	1	$\frac{^{207}Pb}{^{235}U}$	1	$\frac{^{206}Pb}{^{238}U}$	1	$\frac{^{208}Pb}{^{232}Th}$	1

39-1-14	402	376	0.93	0.05465	0.00165	0.53425	0.01653	0.07133	0.00064	0.02338	0.00032	398	68	435	11	444	4	467	6
Spot No.	Content (ppm)		Isotopic ratio									Age (Ma)							
	^{232}Th	^{238}U	^{232}Th/^{238}U	^{207}Pb/^{206}Pb	1σ	^{207}Pb/^{235}U	1σ	^{206}Pb/^{238}U	1σ	^{208}Pb/^{232}Th	1σ	$\frac{^{207}Pb}{^{206}Pb}$	1σ	$\frac{^{207}Pb}{^{235}U}$	1σ	$\frac{^{206}Pb}{^{238}U}$	1σ	$\frac{^{208}Pb}{^{232}Th}$	1σ
The Tianjingping Complex																			
39-1-15	125	227	1.82	0.05721	0.00209	0.55755	0.02120	0.07117	0.00080	0.02205	0.00062	499	82	450	14	443	5	441	12
39-1-16	545	653	1.20	0.05646	0.00148	0.55208	0.01579	0.07119	0.00063	0.02098	0.00033	470	62	446	10	443	4	420	7
39-1-01t	752	712	0.95	0.05793	0.00201	0.56516	0.02315	0.07086	0.00072	0.02615	0.00043	527	89	455	15	441	4	522	8
39-1-02t	157	204	1.30	0.07859	0.00826	0.76499	0.08313	0.07078	0.00224	0.02656	0.00195	1162	215	577	48	441	13	530	38
39-1-03t	226	339	1.50	0.05578	0.00291	0.54434	0.03087	0.07150	0.00114	0.02686	0.00079	444	124	441	20	445	7	536	16
39-1-04t	135	210	1.55	0.05989	0.00321	0.58544	0.03461	0.07170	0.00122	0.02793	0.00092	600	126	468	22	446	7	557	18
39-1-05t	150	215	1.44	0.05671	0.00327	0.55054	0.03515	0.07204	0.00131	0.02798	0.00090	480	139	445	23	448	8	558	18
39-1-06t	60	137	2.27	0.05331	0.00483	0.52114	0.04836	0.07121	0.00168	0.02244	0.00180	342	206	426	32	443	10	449	36
39-1-07t	183	231	1.26	0.05738	0.00257	0.56364	0.02867	0.07161	0.00115	0.02271	0.00071	506	109	454	19	446	7	454	14
39-1-08t	708	531	0.75	0.05652	0.00299	0.55332	0.03146	0.07113	0.00104	0.02437	0.00071	473	125	447	21	443	6	487	14
39-1-09t	260	346	1.33	0.05509	0.00200	0.54023	0.02232	0.07155	0.00077	0.02326	0.00045	416	91	439	15	446	5	465	9
39-1-10t	390	519	1.33	0.06174	0.00639	0.60710	0.06590	0.07118	0.00068	0.02375	0.00037	665	242	482	42	443	4	474	7
The Jiaoxi and Mayuan complexes																			
59-1-01	275	541	0.51	0.06170	0.00152	1.00322	0.03791	0.11774	0.00119	0.03812	0.00089	664	80	705	19	718	7	756	17
59-1-02	341	268	1.27	0.06458	0.00178	1.10652	0.04112	0.12418	0.00130	0.03996	0.00059	761	77	756	20	755	7	792	11
59-1-03	530	503	1.05	0.06370	0.00132	1.08364	0.03278	0.12361	0.00139	0.03821	0.00063	732	61	745	16	751	8	758	12
59-1-04	205	284	0.72	0.11072	0.00151	4.98011	0.12413	0.32604	0.00339	0.09503	0.00159	1811	42	1816	21	1819	16	1835	29
59-1-05	107	106	1.01	0.06553	0.00464	1.09458	0.07498	0.12388	0.00269	0.03542	0.00132	791	140	751	36	753	15	704	26
59-1-06	531	281	1.89	0.06494	0.00210	1.12313	0.04492	0.12511	0.00126	0.03628	0.00067	772	83	764	21	760	7	720	13
59-1-07	4	22	0.17	0.10242	0.01213	3.13376	0.29782	0.23792	0.00805	0.11189	0.01315	1668	170	1441	73	1376	42	2144	239
59-1-08	533	1325	0.40	0.15127	0.00194	9.29547	0.26513	0.44413	0.00675	0.12515	0.00289	2360	42	2368	26	2369	30	2383	52
59-1-09	243	209	1.16	0.06408	0.00238	1.09334	0.05002	0.12458	0.00182	0.03878	0.00096	744	94	750	24	757	10	769	19
59-1-10	101	63	1.60	0.06421	0.00386	1.07589	0.07351	0.12375	0.00228	0.03768	0.00107	749	143	742	36	752	13	748	21
59-1-11	272	197	1.38	0.06536	0.00489	1.11227	0.08704	0.12360	0.00336	0.04066	0.00125	786	159	759	42	751	19	806	24
59-1-12	474	353	1.34	0.06611	0.00173	1.13102	0.03935	0.12427	0.00128	0.03794	0.00052	810	71	768	19	755	7	753	10
59-1-13	671	588	1.14	0.06288	0.00235	1.07845	0.04722	0.12445	0.00181	0.03680	0.00094	704	90	743	23	756	10	730	18
59-1-14	38	36	1.06	0.07087	0.01062	1.17452	0.18318	0.12471	0.00458	0.03982	0.00350	954	331	789	86	758	26	789	68
59-1-15	405	240	1.69	0.06350	0.00222	1.09312	0.04965	0.12425	0.00139	0.03875	0.00063	725	96	750	24	755	8	768	12
59-1-16	106	75	1.40	0.06414	0.00762	1.08423	0.13386	0.12461	0.00434	0.03848	0.00206	746	263	746	65	757	25	763	40
59-1-17	1461	747	1.96	0.06266	0.00142	1.07669	0.03415	0.12445	0.00119	0.03661	0.00047	697	66	742	17	756	7	727	9
59-1-18	1614	1456	1.11	0.06068	0.00106	1.04096	0.02900	0.12394	0.00123	0.03808	0.00049	628	57	724	14	753	7	755	10
59-1-19	539	360	1.50	0.06396	0.00183	1.09504	0.03872	0.12442	0.00133	0.03845	0.00063	740	73	751	19	756	8	763	12
Spot No.	Content (ppm)		Isotopic ratio									Age (Ma)							
	^{232}Th	^{238}U	^{232}Th/^{238}U	^{207}Pb/^{206}Pb	1	^{207}Pb/^{235}U	1	^{206}Pb/^{238}U	1	^{208}Pb/^{232}Th	1	$\frac{^{207}Pb}{^{206}Pb}$	1	$\frac{^{207}Pb}{^{235}U}$	1	$\frac{^{206}Pb}{^{238}U}$	1	$\frac{^{208}Pb}{^{232}Th}$	1

59-1-19	539	360	1.50	0.06396	0.00183	1.09504	0.03872	0.12442	0.00133	0.03845	0.00063	740	73	751	19	756	8	763	12
Spot No.	Content (ppm)		Isotopic ratio									Age (Ma)							
	^{232}Th	^{238}U	$^{232}Th/^{238}U$	$^{207}Pb/^{206}Pb$	1σ	$^{207}Pb/^{235}U$	1σ	$^{206}Pb/^{238}U$	1σ	$^{208}Pb/^{232}Th$	1σ	$\frac{^{207}Pb}{^{206}Pb}$	1σ	$\frac{^{207}Pb}{^{235}U}$	1σ	$\frac{^{206}Pb}{^{238}U}$	1σ	$\frac{^{208}Pb}{^{232}Th}$	1σ
The Jiaoxi and Mayuan complexes																			
59-1-20	322	121	2.66	0.06783	0.00444	1.11154	0.07728	0.11880	0.00245	0.03730	0.00128	863	142	759	37	724	14	740	25
59-1-21	680	632	1.08	0.06671	0.00215	1.14436	0.04430	0.12478	0.00208	0.03962	0.00083	829	75	775	21	758	12	785	16
59-1-22	97	101	0.96	0.06164	0.00311	1.04967	0.05636	0.12493	0.00197	0.03873	0.00102	662	113	729	28	759	11	768	20
59-1-23	429	541	0.79	0.06390	0.00142	1.10656	0.03338	0.12503	0.00107	0.03857	0.00068	738	63	757	16	759	6	765	13
59-1-24	375	202	1.86	0.06311	0.00299	1.03219	0.05219	0.11875	0.00150	0.03565	0.00069	712	107	720	26	723	9	708	14
59-1-25	620	701	0.88	0.06628	0.00121	1.14524	0.03353	0.12510	0.00124	0.03712	0.00048	815	59	775	16	760	7	737	9
59-1-26	803	704	1.14	0.06370	0.00122	1.09945	0.03288	0.12504	0.00112	0.03913	0.00051	732	62	753	16	760	6	776	10
59-1-27	119	82	1.46	0.06114	0.00497	1.05079	0.08416	0.12489	0.00244	0.03571	0.00159	644	172	729	42	759	14	709	31
59-1-28	816	429	1.90	0.06710	0.00353	1.28575	0.07331	0.13913	0.00245	0.04498	0.00081	841	116	839	33	840	14	889	16
59-1-29	408	342	1.19	0.06438	0.00308	1.05980	0.05317	0.11921	0.00182	0.03609	0.00081	754	103	734	26	726	11	717	16
59-1-30	218	142	1.54	0.07034	0.00329	1.19393	0.06020	0.12358	0.00190	0.04016	0.00087	938	101	798	28	751	11	796	17
59-1-31	147	118	1.24	0.06713	0.00306	1.14322	0.05677	0.12558	0.00178	0.03737	0.00102	842	102	774	27	763	10	742	20
59-1-01t	424	752	0.56	0.06546	0.00103	0.96778	0.03184	0.10685	0.00125	0.03684	0.00045	789	33	687	16	654	7	731	9
59-1-02t	34	120	0.28	0.06592	0.00197	1.19487	0.04723	0.13121	0.00157	0.04939	0.00123	804	62	798	22	795	9	974	24
59-1-03t	300	290	1.03	0.06612	0.00152	1.13993	0.03778	0.12495	0.00136	0.04080	0.00067	810	48	772	18	759	8	808	13
59-1-04t	138	210	0.66	0.06546	0.00132	1.13930	0.03329	0.12590	0.00115	0.04012	0.00062	789	42	772	16	764	7	795	12
59-1-05t	80	80	1.00	0.06671	0.00270	1.13891	0.05051	0.12436	0.00174	0.04243	0.00103	829	84	772	24	756	10	840	20
59-1-06t	30	70	0.43	0.06783	0.00445	1.14695	0.07387	0.12614	0.00231	0.04334	0.00228	863	136	776	35	766	13	858	44
59-1-07t	36	74	0.49	0.11266	0.00226	4.94375	0.14621	0.31655	0.00383	0.11936	0.00335	1843	36	1810	25	1773	19	2279	60
59-1-08t	67	71	0.95	0.06761	0.00223	1.15635	0.04518	0.12500	0.00141	0.04051	0.00069	857	69	780	21	759	8	803	13
61-3-01	397	1371	0.29	0.05602	0.00151	0.54890	0.11080	0.07210	0.00218	0.02839	0.00063	453	411	444	73	449	13	566	12
61-3-02	5099	7584	0.67	0.05640	0.00078	0.56602	0.09309	0.07269	0.00113	0.02880	0.00044	468	356	455	60	452	7	574	9
61-3-03	1375	2651	0.52	0.05444	0.00114	0.54675	0.07098	0.07238	0.00095	0.02826	0.00050	389	292	443	47	450	6	563	10
61-3-04	153	944	0.16	0.05748	0.00148	0.56138	0.05396	0.07175	0.00182	0.04205	0.00138	510	211	452	35	447	11	832	27
61-3-05	385	1261	0.31	0.05666	0.00128	0.55606	0.03488	0.07186	0.00168	0.03197	0.00066	478	132	449	23	447	10	636	13
61-3-06	1328	2959	0.45	0.05438	0.00067	0.53564	0.01397	0.07148	0.00100	0.02823	0.00026	387	51	436	9	445	6	563	5
61-3-07	1350	2726	0.50	0.05580	0.00067	0.56011	0.01263	0.07257	0.00063	0.02570	0.00033	444	47	452	8	452	4	513	6
61-3-08	30	722	0.04	0.05758	0.00161	0.56395	0.01840	0.07078	0.00071	0.03032	0.00159	514	70	454	12	441	4	604	31
61-3-09	1636	3661	0.45	0.05524	0.00072	0.55355	0.01197	0.07247	0.00078	0.02940	0.00033	422	43	447	8	451	5	586	6
61-3-10	4005	6186	0.65	0.05583	0.00048	0.54686	0.01136	0.07068	0.00051	0.02805	0.00023	446	44	443	7	440	3	559	5
61-3-11	3504	4895	0.72	0.05665	0.00074	0.55541	0.01242	0.07078	0.00069	0.02463	0.00031	478	46	449	8	441	4	492	6
61-3-12	2680	4188	0.64	0.05631	0.00048	0.55747	0.00984	0.07145	0.00048	0.02719	0.00023	465	37	450	6	445	3	542	4
Spot No.	Content (ppm)		Isotopic ratio									Age (Ma)							
	^{232}Th	^{238}U	$^{232}Th/^{238}U$	$^{207}Pb/^{206}Pb$	1	$^{207}Pb/^{235}U$	1	$^{206}Pb/^{238}U$	1	$^{208}Pb/^{232}Th$	1	$\frac{^{207}Pb}{^{206}Pb}$	1	$\frac{^{207}Pb}{^{235}U}$	1	$\frac{^{206}Pb}{^{238}U}$	1	$\frac{^{208}Pb}{^{232}Th}$	1

61-3-12	2680	4188	0.64	0.05631	0.00048	0.55747	0.00984	0.07145	0.00048	0.02719	0.00023	465	37	450	6	445	3	542	4

Spot No.	Content (ppm)		Isotopic ratio									Age (Ma)							
	^{232}Th	^{238}U	^{232}Th/^{238}U	^{207}Pb/^{206}Pb	1σ	^{207}Pb/^{235}U	1σ	^{206}Pb/^{238}U	1σ	^{208}Pb/^{232}Th	1σ	$\frac{^{207}Pb}{^{206}Pb}$	1σ	$\frac{^{207}Pb}{^{235}U}$	1σ	$\frac{^{206}Pb}{^{238}U}$	1σ	$\frac{^{208}Pb}{^{232}Th}$	1σ
The Jiaoxi and Mayuan complexes																			
61-3-13	429	1260	0.34	0.05572	0.00091	0.54759	0.01225	0.07096	0.00060	0.04447	0.00240	441	47	443	8	442	4	879	47
61-3-14	171	939	0.18	0.05608	0.00092	0.56140	0.01296	0.07232	0.00062	0.03457	0.00090	456	49	452	8	450	4	687	18
61-3-15	15	767	0.02	0.05699	0.00128	0.55710	0.01575	0.07088	0.00066	0.05200	0.00337	491	60	450	10	441	4	1025	65
61-3-16	23	512	0.05	0.05608	0.00113	0.55341	0.01404	0.07178	0.00061	0.03396	0.00139	455	54	447	9	447	4	675	27
61-3-17	1609	3272	0.49	0.05473	0.00068	0.53483	0.00990	0.07072	0.00046	0.02602	0.00028	401	40	435	7	440	3	519	6
61-3-18	410	1569	0.26	0.05584	0.00084	0.55364	0.01065	0.07195	0.00051	0.02866	0.00043	446	41	447	7	448	3	571	8
61-3-19	528	1849	0.29	0.05557	0.00060	0.55411	0.00984	0.07232	0.00051	0.02901	0.00040	435	37	448	6	450	3	578	8
61-3-20	979	2066	0.47	0.06855	0.00116	0.67090	0.01608	0.07086	0.00063	0.03745	0.00066	885	47	521	10	441	4	743	13
61-3-21	975	2181	0.45	0.05565	0.00096	0.54681	0.01353	0.07105	0.00053	0.02778	0.00104	438	54	443	9	442	3	554	20
61-3-22	599	1730	0.35	0.05528	0.00069	0.53921	0.01019	0.07074	0.00047	0.02652	0.00029	424	40	438	7	441	3	529	6
61-3-23	1171	2556	0.46	0.05633	0.00097	0.55090	0.01364	0.07069	0.00096	0.02788	0.00043	465	47	446	9	440	6	556	9
61-3-24	370	1543	0.24	0.05601	0.00084	0.55023	0.01087	0.07139	0.00069	0.02815	0.00049	453	39	445	7	445	4	561	10
61-3-25	333	1526	0.22	0.05670	0.00126	0.56466	0.02069	0.07288	0.00255	0.05232	0.00196	480	24	455	13	453	15	1031	38
61-3-26	4141	6295	0.66	0.05552	0.00081	0.53483	0.01443	0.07070	0.00171	0.02853	0.00034	433	27	435	10	440	10	569	7
61-3-01t	845	1123	0.75	0.05443	0.00064	0.54906	0.01014	0.07259	0.00053	0.02302	0.00022	389	39	444	7	452	3	460	4
61-3-02t	544	856	0.64	0.05517	0.00084	0.55632	0.00998	0.07266	0.00068	0.02391	0.00042	419	35	449	7	452	4	478	8
61-3-03t	327	663	0.49	0.05765	0.00133	0.57738	0.01482	0.07198	0.00077	0.02557	0.00042	516	52	463	10	448	5	510	8
61-3-04t	3	196	0.02	0.05408	0.00155	0.53804	0.01659	0.07150	0.00074	0.04860	0.00276	374	67	437	11	445	4	959	53
61-3-05t	690	923	0.75	0.05529	0.00115	0.54291	0.01108	0.07074	0.00061	0.02143	0.00027	424	42	440	7	441	4	429	5
61-3-06t	98	546	0.18	0.05597	0.00089	0.55943	0.00884	0.07218	0.00057	0.02384	0.00053	451	31	451	6	449	3	476	11
65-1-01	1140	1427	0.80	0.05825	0.00108	0.54085	0.00999	0.06724	0.00050	0.02085	0.00023	539	38	439	7	420	3	417	5
65-1-02	494	754	0.66	0.07035	0.00081	1.46242	0.01883	0.15058	0.00097	0.04657	0.00044	939	23	915	8	904	5	920	8
65-1-03	2943	1675	1.76	0.05704	0.00064	0.55944	0.00856	0.07086	0.00052	0.02153	0.00019	493	30	451	6	441	3	431	4
65-1-04	87	803	0.11	0.05615	0.00117	0.56088	0.01473	0.07222	0.00090	0.02189	0.00071	458	52	452	10	450	5	438	14
65-1-05	242	1125	0.21	0.07282	0.00125	1.49672	0.04059	0.14788	0.00192	0.05531	0.00168	1009	49	929	17	889	11	1088	32
65-1-06	1809	1890	0.96	0.05723	0.00073	0.56933	0.01126	0.07204	0.00053	0.02272	0.00023	500	41	458	7	448	3	454	5
65-1-07	2304	1948	1.18	0.05728	0.00076	0.56284	0.01076	0.07115	0.00052	0.02310	0.00034	502	40	453	7	443	3	462	7
65-1-08	5518	3203	1.72	0.05583	0.00097	0.52574	0.01122	0.06813	0.00053	0.02062	0.00020	446	45	429	7	425	3	412	4
65-1-09	401	710	0.57	0.08554	0.00086	2.67440	0.04602	0.22629	0.00160	0.06954	0.00064	1328	31	1321	13	1315	8	1359	12
65-1-10	412	1048	0.39	0.08546	0.00106	2.52402	0.05931	0.21181	0.00228	0.07082	0.00100	1326	41	1279	17	1238	12	1383	19
65-1-11	636	589	1.08	0.06645	0.00141	1.18065	0.03076	0.12869	0.00110	0.04091	0.00055	821	53	792	14	780	6	810	11

Spot No.	Content (ppm)		Isotopic ratio									Age (Ma)							
	^{232}Th	^{238}U	^{232}Th/^{238}U	^{207}Pb/^{206}Pb	1	^{207}Pb/^{235}U	1	^{206}Pb/^{238}U	1	^{208}Pb/^{232}Th	1	$\frac{^{207}Pb}{^{206}Pb}$	1	$\frac{^{207}Pb}{^{235}U}$	1	$\frac{^{206}Pb}{^{238}U}$	1	$\frac{^{208}Pb}{^{232}Th}$	1

65-1-11	636	589	1.08	0.06645	0.00141	1.18065	0.03076	0.12869	0.00110	0.04091	0.00055	821	53	792	14	780	6	810	11
Spot No.	Content (ppm)		Isotopic ratio									Age (Ma)							
	^{232}Th	^{238}U	$^{232}Th/^{238}U$	$^{207}Pb/^{206}Pb$	1σ	$^{207}Pb/^{235}U$	1σ	$^{206}Pb/^{238}U$	1σ	$^{208}Pb/^{232}Th$	1σ	$\frac{^{207}Pb}{^{206}Pb}$	1σ	$\frac{^{207}Pb}{^{235}U}$	1σ	$\frac{^{206}Pb}{^{238}U}$	1σ	$\frac{^{208}Pb}{^{232}Th}$	1σ
The Jiaoxi and Mayuan complexes																			
65-1-12	24	196	0.12	0.06410	0.00319	1.04503	0.05209	0.11887	0.00210	0.10252	0.00529	745	101	726	26	724	12	1973	97
65-1-13	264	435	0.61	0.08536	0.00100	2.60701	0.04553	0.22082	0.00143	0.06727	0.00071	1324	32	1303	13	1286	8	1316	13
65-1-14	1248	1067	1.17	0.05679	0.00091	0.55868	0.01175	0.07141	0.00052	0.02188	0.00039	484	45	451	8	445	3	438	8
65-1-15	86	2819	0.03	0.06774	0.00051	1.28435	0.02369	0.13661	0.00106	0.05366	0.00140	861	36	839	11	825	6	1056	27
65-1-16	3815	3216	1.19	0.05536	0.00071	0.52194	0.01049	0.06808	0.00045	0.02068	0.00018	427	43	426	7	425	3	414	4
65-1-17	7972	4045	1.97	0.05691	0.00056	0.56640	0.00964	0.07191	0.00047	0.02253	0.00019	488	36	456	6	448	3	450	4
65-1-18	715	2039	0.35	0.05754	0.00073	0.57583	0.01022	0.07233	0.00048	0.02233	0.00026	512	37	462	7	450	3	446	5
65-1-19	845	686	1.23	0.06005	0.00117	0.58429	0.01332	0.07073	0.00056	0.02220	0.00026	605	47	467	9	441	3	444	5
65-1-20	2389	2189	1.09	0.05698	0.00079	0.55935	0.01137	0.07109	0.00067	0.02467	0.00053	491	41	451	7	443	4	493	10
65-1-21	561	842	0.67	0.05613	0.00090	0.55539	0.01222	0.07156	0.00051	0.02342	0.00032	457	47	449	8	446	3	468	6
65-1-22	4828	3624	1.33	0.05601	0.00061	0.52196	0.00858	0.06740	0.00044	0.02025	0.00016	453	34	426	6	420	3	405	3
65-1-23	1134	2108	0.54	0.08542	0.00081	2.48463	0.05531	0.20796	0.00306	0.06972	0.00089	1325	33	1268	16	1218	16	1362	17
65-1-24	480	1043	0.46	0.06306	0.00100	0.61855	0.01368	0.07100	0.00071	0.02392	0.00036	710	43	489	9	442	4	478	7
65-1-25	350	2042	0.17	0.07699	0.00074	2.02149	0.08346	0.18873	0.00245	0.05872	0.00103	1121	80	1123	28	1114	13	1153	20
65-1-01t	123	255	0.48	0.08773	0.00096	2.91204	0.03348	0.23960	0.00191	0.07891	0.00082	1377	16	1385	9	1385	10	1535	15
65-1-02t	484	800	0.60	0.08798	0.00066	2.93450	0.03198	0.24047	0.00228	0.08111	0.00080	1382	11	1391	8	1389	12	1576	15
65-1-03t	313	553	0.57	0.08647	0.00135	2.88741	0.04776	0.24198	0.00334	0.08373	0.00110	1349	18	1379	12	1397	17	1625	21
65-1-04t	707	628	1.13	0.06484	0.00208	0.63371	0.02110	0.07060	0.00093	0.02863	0.00046	769	66	498	13	440	6	571	9
65-1-05t	150	567	0.26	0.08087	0.00133	2.27905	0.03928	0.20342	0.00201	0.08340	0.00155	1218	28	1206	12	1194	11	1619	29
65-1-06t	152	246	0.62	0.05575	0.00157	0.55399	0.01534	0.07198	0.00073	0.02680	0.00058	443	59	448	10	448	4	535	12

APPENDIX C: LA-ICP-MS zircon trace element data

Spot No.	Content (ppm)																				T (°C)	Ratio	
	Y	Nb	La	Ce	Pr	Nd	Sm	Eu	Gd	Tb	Dy	Ho	Er	Tm	Yb	Lu	Hf	Ta	^{49}Ti	∑REE		Eu/Eu*	Ce/Ce*
The Tianjingping Complex																							
125-1-01t	931	2.97	0.043	4.05	0.17	3.24	5.16	0.78	20.1	7.13	82.6	32.1	153	39.3	452	79.0	29183	2.46	4	879	656	0.20	6.81
125-1-02t	1562	4.95	0.054	8.23	0.20	5.22	9.18	1.24	37.2	12.2	148	54.8	245	60.8	630	94.5	27854	2.56	8	1306	716	0.18	11.5
125-1-03t	497	2.60	0.024	1.61	0.0060	0.16	0.64	0.21	5.24	2.41	37.5	16.0	84.9	24.3	297	52.9	30590	2.39	5	523	690	0.24	32.2
125-1-04t	1091	5.51	0.00	4.72	0.097	1.41	4.30	0.51	20.8	7.08	90.1	37.1	184	47.8	522	91.3	26129	4.60	6	1011	701	0.14	15.1
125-1-05t	527	2.32	0.011	1.58	0.029	0.23	0.88	0.24	6.61	2.72	37.1	16.8	89.9	24.5	286	50.6	31251	2.25	5	517	691	0.22	14.7
125-1-06t	3501	8.13	0.034	18.8	0.75	12.7	25.4	2.97	109	33.1	364	130	554	121	1163	186	20809	3.26	20	2721	806	0.15	7.68
125-1-07t	1932	6.06	0.093	9.17	0.61	8.35	13.9	2.03	64.6	19.2	207	71.3	302	68.3	683	100	26133	2.98	7	1550	713	0.17	4.41
125-1-08t	1439	5.46	0.064	8.14	0.16	3.49	5.74	0.96	33.1	10.7	132	50.6	235	57.0	591	93.0	25852	2.69	15	1220	778	0.17	13.7
125-2-01t	1620	15.2	0.044	28.4	0.18	3.58	5.84	1.30	29.3	10.4	142	56.5	278	78.4	932	131	22953	14.1	10	1697	741	0.25	43.6
125-2-02t	2008	24.7	0.17	16.2	0.85	8.28	14.9	0.74	56.4	18.4	209	72.3	322	81.5	969	145	24495	22.7	13	1914	764	0.07	5.47
125-2-03t	1694	5.85	0.018	7.98	0.61	13.4	36.6	1.25	138	34.2	267	62.0	183	31.6	249	28.8	27275	3.46	24	1054	826	0.05	3.99
125-2-04t	1041	4.19	0.080	109	0.25	3.60	6.85	0.87	26.1	8.86	97.6	36.0	162	37.6	367	56.0	22814	1.45	17	912	792	0.17	122
125-2-05t	566	34.6	0.0052	2.08	0.00	0.017	0.057	0.011	0.66	0.91	23.5	16.0	130	54.3	833	149	33585	28.6	3	1210	648	0.11	311
125-2-06t	1172	1.93	0.0097	1.23	0.14	2.38	11.5	1.03	96.7	35.1	255	37.8	75.1	9.81	69.3	7.74	29026	1.38	23	603	818	0.06	2.69
125-2-07t	2664	7.08	0.017	18.9	0.28	4.51	8.58	1.01	48.6	18.4	245	96.5	446	115	1242	187	27841	6.00	11	2432	750	0.12	20.6
125-2-08t	2879	18.9	0.056	81.2	0.29	4.23	10.6	0.96	58.8	21.6	273	102	455	108	1066	158	23669	6.72	12	2340	756	0.09	81.1
125-4-01t	11868	25.7	0.33	90.8	3.46	50.0	64.5	43.3	322	100	1124	398	1588	321	2944	520	15426	4.37	20	7569	803	0.75	7.85
125-4-02t	3516	11.3	0.011	1.01	0.014	0.17	1.68	1.62	22.9	13.3	217	110	615	164	1831	416	38464	11.4	5	3394	684	0.46	16.7
125-4-03t	952	1.59	1.63	15.7	1.09	8.52	5.90	2.00	16.1	6.04	69.5	28.0	146	41.4	513	98.2	30094	3.92	4	953	668	0.59	2.80

Spot No.	Content (ppm)																				T (°C)	Ratio	
	Y	Nb	La	Ce	Pr	Nd	Sm	Eu	Gd	Tb	Dy	Ho	Er	Tm	Yb	Lu	Hf	Ta	^{49}Ti	∑REE		Eu/Eu*	Ce/Ce*

Spot No.	Content (ppm)																				T (°C)	Ratio	
	Y	Nb	La	Ce	Pr	Nd	Sm	Eu	Gd	Tb	Dy	Ho	Er	Tm	Yb	Lu	Hf	Ta	^{49}Ti	∑REE		Eu/Eu*	Ce/Ce*
125-4-03t	952	1.59	1.63	15.7	1.09	8.52	5.90	2.00	16.1	6.04	69.5	28.0	146	41.4	513	98.2	30094	3.92	4	953	668	0.59	2.80
The Tianjingping Complex																							
125-4-04t	11160	30.0	0.71	10.4	0.68	7.06	17.0	9.99	133	58.9	829	335	1558	383	4058	639	40593	40.5	10	8039	744	0.45	3.34
125-4-05t	3419	6.73	0.012	1.04	0.013	0.50	2.02	2.10	25.2	13.7	228	109	595	169	2126	376	28100	8.61	6	3648	695	0.53	17.8
125-4-06t	1229	2.84	0.53	20.6	0.30	3.35	2.55	5.93	21.2	7.02	86.1	37.2	196	52.2	612	131	28311	8.96	4	1176	662	1.71	12.4
125-4-07t	5381	16.8	6.61	71.3	7.60	66.4	48.4	27.1	149	44.6	491	176	733	158	1561	271	14494	3.50	19	3813	798	0.89	2.16
34-4-01t	4168	2.86	0.31	49.1	0.64	11.3	19.5	2.62	97.2	33.6	393	142	620	136	1255	213	28390	2.47	30	2973	848	0.15	20.0
34-4-02t	1513	4.16	0.94	31.7	0.90	11.0	11.4	1.41	48.9	14.7	152	53.1	221	46.5	419	75.2	24359	2.56	38	1088	873	0.16	7.70
34-4-03t	1619	6.12	69.6	204	21.8	98.6	19.9	1.33	42.1	12.1	139	51.9	241	55.4	543	95.8	31132	2.98	12	1596	755	0.14	1.27
34-4-04t	4327	14.8	0.14	41.0	1.10	22.9	35.5	2.96	153	45.2	482	162	630	124	1029	168	23136	5.89	14	2897	774	0.10	11.0
34-4-05t	4881	6.09	0.027	46.3	1.01	16.0	28.1	4.23	141	44.3	493	173	725	152	1345	230	26275	2.71	11	3399	750	0.17	14.0
34-4-06t	5447	6.49	0.97	81.6	1.40	22.8	37.6	7.16	163	49.5	541	192	795	166	1489	262	27581	2.70	36	3808	869	0.24	14.2
34-4-07t	5076	3.02	0.071	19.2	0.75	12.9	26.0	4.76	134	42.8	494	180	750	151	1337	235	25045	1.41	8	3388	724	0.20	7.67
39-1-01t	3212	4.24	0.39	39.8	1.30	22.1	24.9	8.57	83.2	25.1	291	105	476	127	1429	218	14535	2.01	27	2852	837	0.52	8.51
39-1-02t	997	1.12	0.0000	13.2	0.23	6.09	5.23	1.72	23.5	7.06	80.1	33.1	150	39.8	436	75.8	16540	0.55	16	872	785	0.40	17.6
39-1-03t	1086	0.90	0.033	14.8	0.48	6.85	7.31	2.73	20.6	7.82	92.8	36.2	173	48.2	560	85.8	15873	0.73	19	1056	799	0.64	9.28
39-1-04t	847	0.74	0.053	10.8	0.33	3.10	4.63	2.07	19.6	5.70	72.9	27.7	131	35.5	418	66.8	16377	0.54	22	798	817	0.57	9.56
39-1-05t	975	0.90	0.048	12.4	0.46	4.42	5.05	2.33	20.5	6.90	86.0	32.0	152	41.8	465	76.5	17086	0.56	17	905	791	0.61	8.03
39-1-06t	464	0.71	0.021	7.50	0.00	0.15	2.27	0.45	5.51	2.42	33.7	14.2	75.1	22.2	280	48.3	18356	0.64	16	492	782	0.38	282
39-1-07t	1182	0.77	0.053	13.2	0.44	5.66	5.99	2.84	25.3	8.19	100	37.5	183	47.5	517	92.0	18331	0.70	17	1039	792	0.60	8.93
39-1-08t	3024	3.51	0.16	36.9	1.34	19.3	19.3	8.28	78.7	24.5	269	95.7	440	106	1137	193	16634	1.21	23	2430	819	0.56	8.14
39-1-09t	1310	1.04	0.058	14.9	0.49	5.80	6.97	2.62	24.9	8.86	107	41.8	202	53.8	621	110	19220	0.96	15	1199	779	0.54	8.91
39-1-10t	1434	1.35	0.094	18.5	0.56	6.95	6.84	3.06	28.3	9.81	116	45.8	222	59.2	680	124	20303	1.01	11	1322	751	0.58	9.64

Spot No.	Content (ppm)																				T (°C)	Ratio	
	Y	Nb	La	Ce	Pr	Nd	Sm	Eu	Gd	Tb	Dy	Ho	Er	Tm	Yb	Lu	Hf	Ta	^{49}Ti	∑REE		Eu/Eu*	Ce/Ce*

Spot No.	Content (ppm)																				T (°C)	Ratio	
	Y	Nb	La	Ce	Pr	Nd	Sm	Eu	Gd	Tb	Dy	Ho	Er	Tm	Yb	Lu	Hf	Ta	^{49}Ti	∑REE		Eu/Eu*	Ce/Ce*
39-1-10t	1434	1.35	0.094	18.5	0.56	6.95	6.84	3.06	28.3	9.81	116	45.8	222	59.2	680	124	20303	1.01	11	1322	751	0.58	9.64
The Jiaoxi and Mayuan complexes																							
59-1-01t	5338	29.7	0.44	46.1	0.68	8.23	20.5	0.70	114	42.1	515	193	851	189	1779	282	27036	10.6	89	4040	978	0.03	16.8
59-1-02t	964	1.93	0.00	11.2	0.016	0.99	2.28	0.68	13.5	5.67	77.3	31.2	158	44.3	502	85.6	27886	1.97	12	933	761	0.29	212
59-1-03t	8927	16.9	0.96	124	2.60	36.4	57.0	4.43	267	83.8	954	330	1329	288	2642	392	19101	3.46	31	6510	851	0.09	12.9
59-1-04t	3000	8.83	3.88	51.0	1.52	10.5	15.3	1.30	67.4	23.2	283	105	468	108	1070	171	23685	4.45	15	2379	780	0.11	5.15
59-1-05t	3209	3.01	0.042	48.8	0.56	10.5	14.3	5.48	75.2	24.9	297	114	505	120	1232	193	17781	0.96	16	2642	786	0.41	26.4
59-1-06t	766	2.08	0.018	25.6	0.11	1.31	2.46	1.28	12.9	4.50	55.1	24.0	124	35.0	444	77.9	21595	1.17	11	808	748	0.56	69.9
59-1-07t	727	4.67	0.024	34.9	0.17	3.26	5.09	0.75	16.7	6.42	69.4	26.0	110	27.9	287	40.9	19707	2.40	127	629	1028	0.23	61.9
59-1-08t	2924	3.59	16.8	57.6	3.42	21.9	21.1	1.66	80.2	26.0	297	107	454	99.5	940	151	16732	0.96	12	2277	757	0.11	1.76
61-3-01t	5007	11.1	1.27	57.8	2.22	26.9	31.8	10.1	116	36.1	421	157	745	188	2053	371	23228	4.43	8	4217	722	0.45	6.59
61-3-02t	3569	9.34	1.13	38.3	1.14	14.2	19.3	5.82	68.5	23.4	284	112	531	139	1580	277	28572	3.95	7	3095	713	0.44	7.45
61-3-03t	2395	5.91	3.03	37.0	2.29	19.1	14.5	3.81	51.0	16.2	195	73.6	363	96.3	1113	196	25935	3.45	9	2185	735	0.38	3.28
61-3-04t	287	2.00	0.024	1.30	0.00	0.00	0.27	0.11	2.07	1.15	17.2	8.10	46.6	14.5	180	40.1	32207	2.97	0.71	311	552	0.31	41.7
61-3-05t	4411	8.59	0.49	46.5	1.63	22.4	31.5	8.16	97.0	33.1	365	137	652	163	1736	338	25726	3.68	5	3632	681	0.42	7.88
61-3-06t	1212	3.35	0.98	14.7	0.35	3.26	4.82	1.44	18.4	6.43	86.4	36.8	193	53.5	629	128	30409	2.62	6	1177	700	0.41	6.15
65-1-01t	3182	8.08	0.27	17.6	0.25	4.68	9.07	0.99	59.6	22.9	292	117	517	119	1149	172	24031	4.18	17	2480	792	0.10	15.4
65-1-02t	6019	24.2	0.10	56.5	0.52	7.45	16.8	2.20	112	43.4	557	216	957	219	2121	305	25377	13.7	16	4613	783	0.12	31.3
65-1-03t	8522	15.4	13.0	68.8	4.40	34.7	39.1	3.55	199	70.1	880	330	1351	295	2808	356	22550	7.35	30	6453	846	0.10	2.22
65-1-04t	3035	17.3	0.30	20.3	1.42	27.6	73.0	31.6	336	80.4	553	102	232	35.2	236	23.4	28069	2.68	18	1752	797	0.52	4.09
65-1-05t	3382	60.8	0.59	22.4	0.44	3.04	7.74	0.84	50.4	21.2	286	119	606	175	2203	364	27877	85.3	19	3859	800	0.10	10.3
65-1-06t	527	4.88	0.33	20.2	3.01	44.4	48.0	13.1	86.0	14.6	94.1	18.8	45.8	7.67	54.2	6.42	25707	1.55	13	456	767	0.62	1.99

APPENDIX D: LA-ICP-MS zircon Hf isotope data

Spot No.	Isotopic ratio				t (Ma)	$\varepsilon_{Hf}(0)$	$\varepsilon_{Hf}(t)$	2σ	$f_{Lu/Hf}$	Hf model age (Ma)					
	$^{176}Hf/^{177}Hf$	2σ	$^{176}Lu/^{177}Hf$	2σ						T_{DM}	2σ	T_{DM}^{UC}	2σ	T_{DM}^{LC}	2σ
125-1-01H	0.282186	0.000032	0.001723	0.000108	471	-20.7	-10.9	1.1	-0.95	1533	91	1808	142	-	-
125-1-02H	0.282219	0.000028	0.000551	0.000062	445	-19.5	-9.9	1	-0.98	1441	77	1739	124	-	-
125-1-03H	0.282141	0.000038	0.001657	0.000028	445	-22.3	-13	1.3	-0.95	1594	108	1895	168	-	-
125-1-04H	0.282205	0.000038	0.00047	0.000036	445	-20	-10.4	1.3	-0.99	1457	105	1763	169	-	-
125-1-05H	0.282224	0.000034	0.000446	0.000024	445	-19.4	-9.7	1.2	-0.99	1430	94	1728	151	-	-
125-1-06H	0.282145	0.000026	0.000631	0.000026	445	-22.2	-12.6	0.9	-0.98	1546	72	1872	115	-	-
125-1-07H	0.282159	0.000022	0.000471	0.000096	445	-21.7	-12	0.8	-0.99	1520	60	1845	98	-	-
125-1-08H	0.282155	0.000028	0.002121	0.000092	445	-21.8	-12.7	1	-0.94	1594	80	1876	124	-	-
125-1-09H	0.282162	0.00004	0.000786	0.00005	445	-21.6	-12	1.4	-0.98	1529	111	1844	177	-	-
125-1-10H	0.282199	0.000028	0.001569	0.00048	445	-20.3	-10.9	1	-0.95	1508	79	1790	124	-	-
125-1-11H	0.282132	0.000026	0.000188	0.000008	445	-22.6	-12.9	0.9	-0.99	1546	71	1889	115	-	-
125-1-12H	0.282121	0.000034	0.000321	0.000015	445	-23	-13.3	1.2	-0.99	1566	93	1911	151	-	-
125-2-01H	0.282146	0.000032	0.001587	0.00004	616	-22.1	-9.2	1.1	-0.95	1584	91	1839	142	-	-
125-2-02H	0.282045	0.00004	0.001168	0.000026	616	-25.7	-12.6	1.4	-0.96	1707	112	2011	177	-	-
125-2-03H	0.281856	0.000034	0.001065	0.000052	776	-32.4	-15.8	1.2	-0.97	1965	94	2300	150	-	-
125-2-04H	0.281408	0.00003	0.000589	0.000012	1832	-48.2	-8.2	1.1	-0.98	2550	81	2764	131	-	-
125-2-05H	0.282046	0.00004	0.00132	0.000102	740	-25.7	-10	1.4	-0.96	1713	112	1978	177	-	-
125-2-06H	0.282178	0.00004	0.000585	0.0002	445	-21	-11.4	1.4	-0.98	1498	110	1812	177	-	-
125-2-07H	0.282173	0.000028	0.001102	0.000046	445	-21.2	-11.7	1	-0.97	1526	78	1829	124	-	-
125-2-08H	0.282139	0.000032	0.001056	0.000046	776	-22.4	-5.8	1.1	-0.97	1571	89	1796	142	-	-
125-2-09H	0.282027	0.000034	0.00054	0.000064	445	-26.3	-16.7	1.2	-0.98	1704	93	2082	150	-	-
125-2-10H	0.281498	0.000098	0.000487	0.000038	2254	-45	4.6	3.5	-0.99	2422	265	2472	427	-	-
125-2-11H	0.282141	0.000034	0.001332	0.000052	445	-22.3	-12.9	1.2	-0.96	1580	96	1890	151	-	-
125-2-12H	0.281456	0.00003	0.000172	0.000004	2013	-46.5	-1.9	1.1	-0.99	2459	80	2598	131	-	-
125-2-13H	0.282152	0.000036	0.001924	0.00024	776	-21.9	-5.8	1.3	-0.94	1590	103	1795	159	-	-
125-2-14H	0.282203	0.000042	0.001339	0.000052	740	-20.1	-4.5	1.5	-0.96	1493	118	1698	186	-	-
125-4-01H	0.28229	0.00001	0.001641	0.000031	473	-17.1	-7.2	0.4	-0.95	1383	29	-	-	2493	46
125-4-02H	0.282437	0.000014	0.003061	0.000014	473	-11.8	-2.4	0.5	-0.91	1219	43	-	-	2067	65
125-4-03H	0.282103	0.000017	0.001247	0.00002	473	-23.7	-13.7	0.6	-0.96	1631	48	-	-	3072	76
125-4-04H	0.282543	0.000011	0.003941	0.00002	473	-8.1	1.1	0.4	-0.88	1090	35	-	-	1757	51
125-4-05H	0.28252	0.00001	0.005721	0.000012	473	-8.9	-0.3	0.4	-0.83	1185	32	-	-	1880	45
125-4-06H	0.282203	0.000007	0.000292	0.000005	473	-20.1	-9.8	0.2	-0.99	1454	19	-	-	2731	31
125-4-07H	0.282014	0.000008	0.000518	0.000004	473	-26.8	-16.6	0.3	-0.98	1722	22	-	-	3332	35
125-4-08H	0.282734	0.000014	0.006203	0.000013	473	-1.3	7.1	0.5	-0.81	853	47	-	-	1212	65
125-4-09H	0.282613	0.000014	0.005674	0.000014	473	-5.6	3	0.5	-0.83	1034	46	-	-	1583	65
125-4-10H	0.282521	0.000013	0.00388	0.000028	473	-8.9	0.3	0.5	-0.88	1121	41	-	-	1824	60
125-4-11H	0.282665	0.000015	0.004799	0.000012	473	-3.8	5.1	0.5	-0.86	926	46	-	-	1392	66
34-4-01H	0.281943	0.000009	0.000799	0.000007	781	-29.3	-12.5	0.3	-0.98	1833	26	2138	41	-	-
34-4-02H	0.281551	0.00001	0.00014	0.000001	1833	-43.2	-2.5	0.4	-1	2330	26	2486	43	-	-
34-4-03H	0.281993	0.000013	0.001328	0.000003	781	-27.5	-11	0.5	-0.96	1788	37	2062	58	-	-
34-4-04H	0.281596	0.000013	0.000783	0.000001	820	-41.6	-24	0.5	-0.98	2308	35	2741	56	-	-
34-4-05H	0.281978	0.000009	0.000411	0.000002	1208	-28.1	-1.7	0.3	-0.99	1766	25	1935	40	-	-

Spot No.	Isotopic ratio				t (Ma)	$\varepsilon_{Hf}(0)$	$\varepsilon_{Hf}(t)$	2σ	$f_{Lu/Hf}$	Hf model age (Ma)					
	$^{176}Hf/^{177}Hf$	2σ	$^{176}Lu/^{177}Hf$	2σ						T_{DM}	2σ	T_{DM}^{UC}	2σ	T_{DM}^{LC}	2σ
34-4-06H	0.281476	0.00001	0.000979	0.000003	1833	-45.8	-6.2	0.4	-0.97	2483	28	2668	45	-	-
34-4-07H	0.281783	0.000012	0.000657	0.000005	849	-35	-16.6	0.4	-0.98	2044	32	2398	51	-	-
34-4-08H	0.28177	0.00001	0.000721	0.000002	820	-35.4	-17.8	0.4	-0.98	2066	27	2431	44	-	-
34-4-09H	0.281418	0.000013	0.000793	0.000002	1833	-47.9	-8.1	0.5	-0.98	2551	36	2760	57	-	-
34-4-10H	0.281744	0.000011	0.001505	0.000006	781	-36.4	-19.9	0.4	-0.95	2145	31	2509	48	-	-
34-4-11H	0.282015	0.000012	0.001059	0.000013	781	-26.8	-10.1	0.4	-0.97	1745	34	2017	55	-	-
34-4-12H	0.281076	0.00001	0.001103	0.000007	2697	-60	-1.4	0.4	-0.97	3038	28	3133	44	-	-
34-4-13H	0.281896	0.00001	0.001239	0.000009	820	-31	-13.6	0.3	-0.96	1919	27	2222	43	-	-
34-4-14H	0.281584	0.000008	0.000986	0.000009	1833	-42	-2.4	0.3	-0.97	2336	23	2480	37	-	-
34-4-15H	0.281992	0.00001	0.000449	0.000002	781	-27.6	-10.6	0.3	-0.99	1748	26	2041	42	-	-
34-4-16H	0.281909	0.000009	0.001436	0.000004	781	-30.5	-14.1	0.3	-0.96	1911	26	2215	42	-	-
34-4-17H	0.282085	0.000013	0.000402	0.000001	781	-24.3	-7.3	0.5	-0.99	1619	37	1874	60	-	-
39-1-01H	0.282272	0.000013	0.000638	0.000002	444	-17.7	-8.1	0.5	-0.98	1372	36	-	-	2560	58
39-1-01H	0.282206	0.000013	0.000638	0.000002	444	-20	-10.4	0.4	-0.98	1462	35	-	-	2766	56
39-1-01H	0.282386	0.000015	0.001192	0.000011	444	-13.7	-4.3	0.5	-0.96	1232	41	-	-	2214	65
39-1-02H	0.282394	0.000016	0.001091	0.000001	444	-13.4	-3.9	0.5	-0.97	1217	44	-	-	2186	69
39-1-03H	0.282253	0.00001	0.000652	0.000005	444	-18.3	-8.8	0.3	-0.98	1397	26	-	-	2618	43
39-1-04H	0.282316	0.000011	0.000917	0.000011	444	-16.1	-6.6	0.4	-0.97	1320	30	-	-	2427	48
39-1-05H	0.282408	0.000014	0.000462	0.000001	444	-12.9	-3.3	0.5	-0.99	1177	39	-	-	2125	63
39-1-06H	0.282289	0.000008	0.000675	0.000002	444	-17.1	-7.5	0.3	-0.98	1349	23	-	-	2507	37
39-1-07H	0.282287	0.000009	0.0009	0.000008	444	-17.2	-7.7	0.3	-0.97	1360	26	-	-	2519	41
39-1-08H	0.282375	0.00001	0.000836	0.000002	444	-14	-4.5	0.3	-0.97	1235	27	-	-	2239	43
39-1-09H	0.282305	0.000011	0.000688	0.000001	444	-16.5	-6.9	0.4	-0.98	1327	29	-	-	2455	47
39-1-10H	0.282322	0.000011	0.000719	0	444	-15.9	-6.4	0.4	-0.98	1305	30	-	-	2404	48
39-1-11H	0.282086	0.000016	0.000898	0.000002	444	-24.3	-14.8	0.6	-0.97	1639	44	-	-	3153	71
39-1-11H	0.282229	0.000017	0.000746	0.000003	444	-19.2	-9.7	0.6	-0.98	1435	48	-	-	2699	76
39-1-12H	0.282233	0.000011	0.000698	0.000005	444	-19.1	-9.5	0.4	-0.98	1428	31	-	-	2684	50
39-1-12H	0.282369	0.000014	0.000764	0.000004	444	-14.2	-4.7	0.5	-0.98	1240	38	-	-	2254	61
61-3-01H	0.281944	0.000014	0.001547	0.000035	445	-29.3	-20	0.5	-0.95	1868	39	-	-	3613	61
61-3-02H	0.282397	0.00001	0.003371	0.000016	445	-13.3	-4.5	0.4	-0.9	1290	30	-	-	2234	44
61-3-03H	0.282498	0.00001	0.002229	0.000055	445	-9.7	-0.6	0.3	-0.93	1104	28	-	-	1884	43
61-3-04H	0.282511	0.00001	0.001243	0.000012	445	-9.2	0.2	0.4	-0.96	1057	29	-	-	1818	46
61-3-05H	0.282484	0.000009	0.002764	0.000023	445	-10.2	-1.2	0.3	-0.92	1140	28	-	-	1942	42
61-3-06H	0.282373	0.000014	0.002563	0.000046	445	-14.1	-5.1	0.5	-0.92	1297	40	-	-	2290	61
61-3-07H	0.282316	0.000007	0.000307	0.000003	445	-16.1	-6.5	0.2	-0.99	1299	19	-	-	2411	31
61-3-08H	0.282278	0.000009	0.001043	0.000007	445	-17.5	-8	0.3	-0.97	1378	25	-	-	2550	41
61-3-09H	0.282134	0.000009	0.000504	0.000005	445	-22.5	-12.9	0.3	-0.98	1556	24	-	-	2988	39
61-3-10H	0.282245	0.000009	0.001372	0.000026	445	-18.6	-9.2	0.3	-0.96	1435	25	-	-	2660	39
61-3-11H	0.282222	0.000009	0.001104	0.000013	445	-19.4	-10	0.3	-0.97	1458	26	-	-	2727	41
61-3-12H	0.282202	0.000007	0.000514	0.000011	445	-20.2	-10.5	0.3	-0.98	1463	21	-	-	2776	33
61-3-13H	0.282389	0.000011	0.001953	0.000009	445	-13.5	-4.3	0.4	-0.94	1252	33	-	-	2222	50
61-3-14H	0.282252	0.000009	0.000903	0.000016	445	-18.4	-8.9	0.3	-0.97	1408	26	-	-	2628	41
61-3-15H	0.282432	0.000011	0.00143	0.000028	445	-12	-2.7	0.4	-0.96	1174	30	-	-	2073	47
59-1-01H	0.282215	0.000011	0.001545	0.000007	758	-19.7	-3.8	0.4	-0.95	1485	31	1678	48	-	-
59-1-02H	0.282127	0.000007	0.001787	0.000021	758	-22.8	-7	0.3	-0.95	1620	21	1842	32	-	-
59-1-03H	0.282154	0.00001	0.001302	0.000002	758	-21.9	-5.8	0.3	-0.96	1561	28	1781	44	-	-
59-1-04H	0.282181	0.000013	0.003015	0.000014	758	-20.9	-5.7	0.5	-0.91	1596	39	1777	59	-	-
59-1-05H	0.282185	0.000013	0.002097	0.000015	758	-20.8	-5.1	0.5	-0.94	1551	37	1746	57	-	-
59-1-06H	0.282137	0.000009	0.002845	0.000006	722	-22.5	-7.9	0.3	-0.91	1653	25	1858	39	-	-
59-1-07H	0.282164	0.000008	0.00171	0.000006	758	-21.5	-5.6	0.3	-0.95	1564	23	1773	36	-	-
59-1-08H	0.28136	0.000009	0.000747	0.000004	1843	-49.9	-9.8	0.3	-0.98	2625	23	2854	38	-	-
59-1-09H	0.281326	0.000008	0.000071	0.000001	1668	-51.1	-14.2	0.3	-1	2626	21	2929	35	-	-
59-1-10H	0.281949	0.00001	0.000654	0.000004	758	-29.1	-12.7	0.4	-0.98	1817	28	2130	45	-	-

Spot No.	Isotopic ratio				t (Ma)	$\varepsilon_{Hf}(0)$	$\varepsilon_{Hf}(t)$	2σ	$f_{Lu/Hf}$	Hf model age (Ma)					
	$^{176}Hf/^{177}Hf$	2σ	$^{176}Lu/^{177}Hf$	2σ						T_{DM}	2σ	T_{DM}^{UC}	2σ	T_{DM}^{LC}	2σ
59-1-11H	0.282054	0.00001	0.001203	0.000002	758	-25.4	-9.3	0.4	-0.96	1697	28	1958	44	-	-
59-1-12H	0.281928	0.00001	0.001165	0.000009	758	-29.9	-13.8	0.3	-0.96	1871	27	2181	43	-	-
59-1-13H	0.282052	0.00001	0.00114	0.000006	722	-25.5	-10.1	0.3	-0.97	1697	27	1970	43	-	-
59-1-14H	0.282019	0.000014	0.001266	0.000006	758	-26.6	-10.6	0.5	-0.96	1749	38	2021	60	-	-
59-1-15H	0.282072	0.000011	0.001996	0.000004	758	-24.7	-9	0.4	-0.94	1707	32	1944	50	-	-
65-1-01H	0.282147	0.000009	0.000526	0.000006	904	-22.1	-2.4	0.3	-0.98	1539	23	1729	38	-	-
65-1-02H	0.282428	0.00001	0.000579	0.000002	1374	-12.1	17.8	0.3	-0.98	1152	27	1086	43	-	-
65-1-03H	0.282266	0.00001	0.000055	0.000001	445	-17.9	-8.1	0.3	-1	1359	27	1648	44	-	-
65-1-04H	0.282035	0.000009	0.000983	0.000004	889	-26.1	-7	0.3	-0.97	1714	24	1948	39	-	-
65-1-05H	0.282296	0.000009	0.000032	0	445	-16.8	-7.1	0.3	-1	1317	24	1594	39	-	-
65-1-06H	0.281914	0.000012	0.000126	0.000003	445	-30.3	-20.6	0.4	-1	1840	32	2278	53	-	-
65-1-07H	0.282124	0.00001	0.00109	0.000002	1326	-22.9	5.5	0.4	-0.97	1595	29	1670	46	-	-
65-1-08H	0.282213	0.000012	0.000632	0.000005	1326	-19.8	9.1	0.4	-0.98	1452	32	1489	52	-	-
65-1-09H	0.282031	0.000011	0.000044	0.000001	445	-26.2	-16.4	0.4	-1	1677	31	2068	50	-	-
65-1-10H	0.282185	0.000013	0.001632	0.000012	1326	-20.7	7.2	0.5	-0.95	1531	37	1584	58	-	-
65-1-11H	0.28194	0.00001	0.000317	0.000001	825	-29.4	-11.4	0.4	-0.99	1814	27	2118	44	-	-
65-1-12H	0.282311	0.000012	0.000032	0	445	-16.3	-6.5	0.4	-1	1297	32	1567	53	-	-
65-1-13H	0.282442	0.000011	0.000029	0	445	-11.7	-1.9	0.4	-1	1117	30	1330	48	-	-
65-1-14H	0.282435	0.000014	0.00014	0.000001	445	-11.9	-2.2	0.5	-1	1130	37	1344	60	-	-

APPENDIX E: $^{40}Ar/^{39}Ar$ step heating results

Complex	Sample No.	Mineral	Total fusion age (Ma)	2σ	Plateau characteristics					Isochron characteristics					
					Plateau age (Ma)	2σ	Total ^{39}Ar released	Attribute	MSWD	Isochron age (Ma)	2σ	n	$^{40}Ar/^{36}Ar$ intercept	1σ	MSWD
Tianjingping	31-7	Biotite	384.2	3.6	391.8	3.8	84%	Plateau	0.92	395.9	4.4	8	39	117	0.52
	39-1	Amphible	472.7	3.2	-	-	-	-	-	-	-	-	-	-	-
	125-4	Biotite	366.6	2.6	370.1	3.0	86%	Plateau	1.29	376.0	2.6	7	-91	15	1.40
	61-3	Amphible	375.1	2.2	380.9	2.3	63%	Mini-plateau	0.81	379.5	9.4	18	353	368	1.01
Mayuan	65-2	Biotite	276.8	2.4	-	-	-	-	-	-	-	-	-	-	-
	122-1	Amphible	318.4	1.6	-	-	-	-	-	-	-	-	-	-	-
	122-1	Biotite	155.6	3.0	152.1	1.8	89%	Plateau	0.76	151.2	4.7	12	301	43	0.85

Laser intensity (%)	^{36}Ar (V)	σ	^{37}Ar (V)	σ	^{38}Ar (V)	σ	^{39}Ar (V)	σ	^{40}Ar (V)	σ	^{40}Ar* (%)	^{40}Ar*/^{39}Ar$_K$	σ	Age (Ma)	σ
				J=0.008759				*D=1.0041*							
31-7				***± 0.000029***				*± 0.0038*							
				-0.33%											
54.7	0.000023	0.000002	0.000017	0.000004	0.000009	0.000002	0.000364	0.000008	0.011356	0.000085	82.4	19.00	4.26	277.71	115.29
54.8	0.000139	0.000005	0.000039	0.000003	0.000154	0.00001	0.011371	0.000053	0.314051	0.001098	88.7	24.35	0.25	348.83	6.57
54.9	0.000048	0.000007	0.000029	0.000004	0.000101	0.000006	0.008492	0.000066	0.242613	0.001116	96.4	27.31	0.39	386.90	9.85
55.0	0.000073	0.000003	0.000052	0.000003	0.000516	0.000008	0.043077	0.000082	1.212326	0.002258	98.7	27.80	0.13	393.13	3.42
55.3	0.000031	0.000003	0.000031	0.000003	0.000065	0.000006	0.00459	0.000053	0.131197	0.000343	97.2	27.22	0.47	385.78	12.03
55.2	0.000025	0.000003	0.000027	0.000003	0.000014	0.000002	0.000434	0.000011	0.015198	0.000104	81.7	22.73	3.61	327.49	95.05
55.4	0.000024	0.000003	0.000035	0.000005	0.000071	0.000004	0.005027	0.000028	0.143396	0.000461	98.8	27.65	0.38	391.27	9.64
55.6	0.000022	0.000002	0.000019	0.000003	0.000021	0.000004	0.001044	0.000008	0.032842	0.000171	96.0	27.26	1.34	386.28	34.21
				J=0.008891				*D=1.0054*							
39-1				***± 0.000030***				*± 0.0035*							
				-0.34%											
62.0	0.000194	0.000007	0.000077	0.000005	0.000057	0.000005	0.000726	0.000013	0.474466	0.001103	89.6	634.20	53.52	3414.96	258.63
65.0	0.000097	0.000004	0.000112	0.000004	0.000033	0.000005	0.000993	0.000006	0.061850	0.000439	62.5	37.12	4.38	514.55	105.68
68.0	0.000261	0.000006	0.000255	0.000007	0.000094	0.000005	0.002994	0.000027	0.214350	0.000884	67.4	48.02	1.68	641.45	37.68
69.0	0.000396	0.000009	0.001265	0.000012	0.000182	0.000006	0.007960	0.000034	0.395227	0.001096	73.4	36.41	0.67	505.98	16.27
69.3	0.000212	0.000004	0.003028	0.000033	0.000230	0.000012	0.012123	0.000014	0.439392	0.000950	89.8	32.50	0.25	457.98	6.27
69.5	0.000123	0.000004	0.002257	0.000020	0.000147	0.000010	0.008973	0.000042	0.307063	0.001075	93.0	31.58	0.34	446.46	8.58
69.8	0.000291	0.000007	0.006580	0.000055	0.000425	0.000007	0.023035	0.000041	0.839420	0.000533	93.4	34.25	0.20	479.55	4.95
70.0	0.000492	0.000010	0.015519	0.000073	0.000954	0.000014	0.054023	0.000092	1.842460	0.002738	95.5	32.89	0.17	462.81	4.10
70.1	0.000248	0.000004	0.007481	0.000025	0.000433	0.000012	0.026187	0.000058	0.855235	0.000744	95.4	31.36	0.17	443.70	4.32
70.2	0.000130	0.000003	0.002989	0.000020	0.000184	0.000010	0.010265	0.000039	0.358726	0.001279	94.4	32.93	0.31	463.25	7.77
70.4	0.000125	0.000004	0.003460	0.000015	0.000206	0.000007	0.012158	0.000028	0.424302	0.001140	96.1	33.56	0.27	471.03	6.60
70.6	0.000399	0.000007	0.011841	0.000029	0.000666	0.000007	0.038419	0.000052	1.464204	0.003072	95.4	36.75	0.19	510.02	4.62
70.8	0.000803	0.000007	0.028608	0.000088	0.001703	0.000024	0.096103	0.000097	3.217715	0.003212	96.1	32.55	0.14	458.57	3.54
71.0	0.000440	0.000012	0.015795	0.000055	0.000905	0.000009	0.053591	0.000096	1.772434	0.002142	96.4	32.22	0.17	454.40	4.13
71.5	0.000680	0.000011	0.020394	0.000082	0.001239	0.000015	0.071062	0.000117	2.255099	0.000895	94.8	30.41	0.14	431.73	3.66
72.5	0.000211	0.000007	0.002873	0.000030	0.000187	0.000006	0.009389	0.000038	0.325721	0.000657	86.8	30.29	0.37	430.18	9.36
Laser intensity (%)	^{36}Ar (V)	σ	^{37}Ar (V)	σ	^{38}Ar (V)	σ	^{39}Ar (V)	σ	^{40}Ar (V)	σ	^{40}Ar* (%)	^{40}Ar*/^{39}Ar$_K$	σ	Age (Ma)	σ

72.5	0.000211	0.000007	0.002873	0.000030	0.000187	0.000006	0.009389	0.000038	0.325721	0.000657	86.8	30.29	0.37	430.18	9.36
Laser intensity (%)	^{36}Ar (V)	σ	^{37}Ar (V)	σ	^{38}Ar (V)	σ	^{39}Ar (V)	σ	^{40}Ar (V)	σ	^{40}Ar* (%)	^{40}Ar*/^{39}Ar$_K$	σ	Age (Ma)	σ
				J=0.008855				*D=1.0041*							
125-4				***± 0.000020***				*± 0.0038*							
				-0.23%											
54.7	0.000146	0.000005	0.000094	0.000008	0.000112	0.000004	0.006651	0.000039	0.179319	0.000968	79.9	21.24	0.33	310.88	8.92
54.8	0.000118	0.000004	0.000061	0.000005	0.000247	0.000009	0.018777	0.000053	0.499069	0.001170	94.6	25.05	0.16	361.49	4.09
54.9	0.000027	0.000003	0.000022	0.000003	0.000005	0.000002	0.000223	0.000006	0.009235	0.000067	94.7	26.00	7.41	373.86	192.37
55.2	0.000207	0.000007	0.000065	0.000003	0.001530	0.000017	0.125495	0.000084	3.261881	0.000756	98.4	25.64	0.10	369.07	2.62
55.3	0.000031	0.000004	0.000031	0.000002	0.000050	0.000003	0.004198	0.000020	0.110502	0.000328	98.9	25.35	0.38	365.41	9.85
55.4	0.000025	0.000002	0.000025	0.000004	0.000105	0.000007	0.008490	0.000041	0.224285	0.000873	100.2	26.18	0.23	376.20	5.94
55.6	0.000030	0.000002	0.000028	0.000003	0.000085	0.000004	0.007278	0.000068	0.190628	0.000639	99.2	25.63	0.31	369.02	8.08
55.8	0.000024	0.000004	0.000018	0.000003	0.000035	0.000005	0.002940	0.000041	0.080933	0.000243	99.5	26.40	0.62	378.93	16.18
56.0	0.000026	0.000004	0.000025	0.000004	0.000014	0.000002	0.001193	0.000012	0.034614	0.000201	101.0	26.70	1.14	382.90	29.48
				J=0.008827				*D=1.0054*							
61-3				***± 0.000025***				*± 0.0035*							
				-0.28%											
66.0	0.000134	0.000005	0.000110	0.000007	0.000061	0.000006	0.002365	0.000018	0.092451	0.000397	62.4	23.28	1.52	337.21	40.28
67.0	0.000103	0.000006	0.000113	0.000010	0.000050	0.000003	0.001997	0.000013	0.063994	0.000209	58.3	17.15	1.79	254.35	49.51
68.0	0.000218	0.000008	0.000252	0.000009	0.000114	0.000006	0.004645	0.000040	0.192638	0.000543	69.6	28.38	0.94	403.35	23.92
69.0	0.000356	0.000008	0.002779	0.000018	0.000602	0.000006	0.026456	0.000076	0.715127	0.001674	87.7	23.68	0.20	342.41	5.26
69.1	0.000154	0.000004	0.002656	0.000013	0.000566	0.000011	0.024967	0.000054	0.644666	0.000663	95.4	24.62	0.17	354.72	4.51
69.2	0.000122	0.000004	0.002415	0.000015	0.000484	0.000010	0.021386	0.000045	0.562152	0.000842	96.3	25.28	0.19	363.40	5.01
69.4	0.000146	0.000006	0.003351	0.000035	0.000720	0.000017	0.031231	0.000034	0.846957	0.000875	97.2	26.39	0.16	377.81	4.01
69.6	0.000148	0.000005	0.003544	0.000041	0.000726	0.000009	0.031863	0.000067	0.847505	0.001252	97.2	25.90	0.16	371.38	4.08
69.7	0.000082	0.000006	0.001345	0.000014	0.000265	0.000008	0.011776	0.000078	0.304914	0.001035	96.1	24.68	0.37	355.50	9.62
69.8	0.000079	0.000002	0.001623	0.000027	0.000318	0.000007	0.013739	0.000039	0.357750	0.001200	97.2	25.15	0.27	361.75	7.14
69.9	0.000140	0.000007	0.003510	0.000014	0.000765	0.000010	0.032328	0.000051	0.859609	0.000829	97.5	25.97	0.16	372.35	4.07
70.0	0.000230	0.000006	0.006089	0.000060	0.001316	0.000018	0.057580	0.000110	1.567985	0.001995	97.5	26.66	0.13	381.31	3.38
70.1	0.000489	0.000009	0.014017	0.000041	0.003063	0.000022	0.134592	0.000239	3.667791	0.002451	97.6	26.75	0.11	382.46	2.91
70.2	0.000268	0.000006	0.009374	0.000049	0.002075	0.000019	0.091175	0.000124	2.459479	0.002304	98.4	26.67	0.11	381.42	2.90
70.4	0.000227	0.000007	0.006861	0.000023	0.001488	0.000015	0.065410	0.000107	1.760836	0.001997	97.9	26.47	0.12	378.80	3.19
71.0	0.000513	0.000006	0.016301	0.000055	0.003729	0.000025	0.159374	0.000089	4.300754	0.004417	98.0	26.59	0.10	380.35	2.67
72.5	0.000345	0.000010	0.005150	0.000028	0.001185	0.000012	0.049878	0.000060	1.346120	0.002615	94.2	25.51	0.14	366.34	3.68
72.6	0.000348	0.000011	0.004557	0.000020	0.001014	0.000008	0.043199	0.000095	1.187478	0.001993	93.1	25.69	0.16	368.77	4.17
Laser intensity (%)	^{36}Ar (V)	σ	^{37}Ar (V)	σ	^{38}Ar (V)	σ	^{39}Ar (V)	σ	^{40}Ar (V)	σ	^{40}Ar* (%)	^{40}Ar*/^{39}Ar$_K$	σ	Age (Ma)	σ

72.6	0.000348	0.000011	0.004557	0.000020	0.001014	0.000008	0.043199	0.000095	1.187478	0.001993	93.1	25.69	0.16	368.77	4.17
Laser intensity (%)	^{36}Ar (V)	σ	^{37}Ar (V)	σ	^{38}Ar (V)	σ	^{39}Ar (V)	σ	^{40}Ar (V)	σ	^{40}Ar* (%)	^{40}Ar*/^{39}Ar$_K$	σ	Age (Ma)	σ
				J=0.008758				*D=1.0041*							
65-2				***± 0.000033***				*± 0.0038*							
				-0.38%											
54.5	0.000030	0.000002	0.000026	0.000003	0.000017	0.000004	0.001549	0.000015	0.034832	0.000196	92.1	18.88	0.84	276.03	22.89
54.7	0.000145	0.000004	0.000043	0.000004	0.000469	0.000014	0.037382	0.000070	0.790028	0.002562	95.5	20.16	0.12	293.37	3.14
54.8	0.000050	0.000004	0.000032	0.000004	0.000257	0.000007	0.021545	0.000072	0.444453	0.001195	98.2	20.17	0.13	293.45	3.60
54.9	0.000041	0.000005	0.000035	0.000003	0.000296	0.000012	0.024099	0.000090	0.487989	0.001464	98.9	19.96	0.14	290.62	3.90
55.0	0.000042	0.000003	0.000047	0.000004	0.000415	0.000009	0.035428	0.000061	0.671856	0.002164	99.2	18.77	0.11	274.62	2.91
55.2	0.000046	0.000004	0.000039	0.000005	0.000405	0.000021	0.032394	0.000057	0.591144	0.002405	98.9	17.99	0.12	264.01	3.17
55.4	0.000034	0.000003	0.000033	0.000005	0.000209	0.000010	0.016102	0.000110	0.295802	0.001255	99.1	18.03	0.18	264.52	4.98
55.5	0.000031	0.000005	0.000039	0.000004	0.000238	0.000012	0.018715	0.000096	0.313623	0.001339	99.4	16.51	0.16	243.69	4.45
55.6	0.000031	0.000003	0.000029	0.000004	0.000047	0.000001	0.003421	0.000021	0.068869	0.000314	97.5	18.64	0.42	272.77	11.46
55.7	0.000022	0.000003	0.000019	0.000004	0.000004	0.000002	0.000466	0.000011	0.012216	0.000085	112.3	20.68	3.20	300.32	85.63
55.8	0.000028	0.000004	0.000039	0.000005	0.000046	0.000006	0.003321	0.000006	0.066557	0.000329	98.8	18.80	0.46	275.01	12.40
				J=0.008756				*D=1.0054*							
122-1-A				***± 0.000024***				*± 0.0035*							
				-0.24%											
65.0	0.000093	0.000005	0.000106	0.000003	0.000321	0.000005	0.024919	0.000085	0.311151	0.000739	93.1	11.47	0.14	172.70	4.03
66.0	0.000191	0.000005	0.000134	0.000007	0.000692	0.000010	0.052552	0.000039	0.805516	0.001209	93.7	14.34	0.08	213.37	2.31
67.0	0.000227	0.000008	0.000227	0.000008	0.000961	0.000012	0.072364	0.000135	1.068871	0.001570	94.3	13.92	0.08	207.49	2.23
68.0	0.000266	0.000008	0.000848	0.000022	0.001075	0.000017	0.077509	0.000339	1.135887	0.003390	93.8	13.74	0.10	204.97	2.85
68.5	0.000649	0.000013	0.013053	0.000039	0.003382	0.000024	0.173363	0.000267	5.274683	0.005987	97.3	29.78	0.12	417.98	3.12
68.6	0.000149	0.000002	0.003220	0.000011	0.000934	0.000009	0.055040	0.000107	1.016943	0.002302	97.2	17.97	0.10	263.57	2.73
68.7	0.000088	0.000004	0.001499	0.000034	0.000537	0.000011	0.032339	0.000065	0.547249	0.000807	97.1	16.32	0.12	240.97	3.28
69.0	0.000233	0.000006	0.006897	0.000036	0.001652	0.000025	0.085194	0.000330	2.354591	0.004144	98.3	27.29	0.16	386.60	4.03
69.1	0.000163	0.000005	0.004400	0.000038	0.001091	0.000014	0.057159	0.000096	1.485834	0.002425	98.2	25.60	0.13	364.88	3.24
69.2	0.000071	0.000005	0.001329	0.000022	0.000333	0.000009	0.019025	0.000043	0.415387	0.000757	97.7	21.12	0.20	306.09	5.34
69.5	0.000037	0.000005	0.001202	0.000018	0.000248	0.000010	0.010930	0.000050	0.356785	0.000849	100.0	32.53	0.33	452.10	8.05
69.6	0.000099	0.000004	0.001934	0.000026	0.000624	0.000009	0.036880	0.000099	0.681573	0.000839	97.9	17.96	0.12	263.52	3.27
70.0	0.000297	0.000011	0.010086	0.000075	0.002724	0.000037	0.143851	0.000171	3.072465	0.003155	98.6	21.12	0.09	306.17	2.34
70.1	0.000128	0.000004	0.001941	0.000026	0.000693	0.000011	0.041078	0.000057	0.749714	0.000590	97.1	17.61	0.10	258.70	2.84
70.2	0.000109	0.000005	0.001386	0.000020	0.000421	0.000006	0.025203	0.000051	0.504893	0.000896	96.4	19.11	0.16	279.12	4.21
71.0	0.000465	0.000005	0.013429	0.000058	0.002862	0.000021	0.135027	0.000177	3.614103	0.001753	97.7	26.29	0.10	373.81	2.69
71.1	0.000080	0.000006	0.001297	0.000014	0.000254	0.000008	0.011972	0.000049	0.326906	0.000610	96.2	26.11	0.35	371.39	8.91
72.5	0.000362	0.000006	0.005732	0.000024	0.001193	0.000015	0.055226	0.000063	1.432341	0.001762	94.3	24.58	0.12	351.63	3.10
Laser intensity (%)	^{36}Ar (V)	σ	^{37}Ar (V)	σ	^{38}Ar (V)	σ	^{39}Ar (V)	σ	^{40}Ar (V)	σ	^{40}Ar* (%)	^{40}Ar*/^{39}Ar$_K$	σ	Age (Ma)	σ

72.5	0.000362	0.000006	0.005732	0.000024	0.001193	0.000015	0.055226	0.000063	1.432341	0.001762	94.3	24.58	0.12	351.63	3.10
Laser intensity (%)	^{36}Ar (V)	σ	^{37}Ar (V)	σ	^{38}Ar (V)	σ	^{39}Ar (V)	σ	^{40}Ar (V)	σ	$^{40}Ar^*$ (%)	$^{40}Ar^*/^{39}Ar_K$	σ	Age (Ma)	σ
				J=0.008758				*D=1.0041*							
122-1-B				***± 0.000033***				*± 0.0038*							
				-0.38%											
54.7	0.000676	0.000014	0.000045	0.000003	0.000171	0.000005	0.003093	0.000026	0.236031	0.001082	17.9	13.63	1.74	203.42	49.02
54.9	0.002722	0.000024	0.000116	0.000008	0.000730	0.000018	0.015834	0.000040	0.978010	0.002070	19.4	11.99	0.88	180.11	25.21
54.9	0.000199	0.000003	0.000102	0.000006	0.000192	0.000011	0.012787	0.000086	0.184664	0.000850	71.5	10.17	0.16	153.89	4.75
54.9	0.000089	0.000004	0.000102	0.000006	0.000177	0.000005	0.013289	0.000045	0.158072	0.000576	87.4	10.19	0.15	154.26	4.33
54.9	0.000150	0.000008	0.000308	0.000010	0.000295	0.000013	0.022443	0.000091	0.266781	0.000965	85.9	10.11	0.14	152.99	4.04
55.0	0.000243	0.000008	0.000610	0.000020	0.000455	0.000013	0.034560	0.000142	0.416319	0.001636	84.5	10.13	0.11	153.29	3.16
55.1	0.000051	0.000002	0.000041	0.000005	0.000057	0.000004	0.003134	0.000031	0.043158	0.000114	78.4	9.95	0.46	150.70	13.30
55.3	0.000050	0.000006	0.000074	0.000005	0.000072	0.000006	0.005068	0.000025	0.063075	0.000240	86.3	10.17	0.42	153.92	12.24
55.6	0.000209	0.000005	0.000709	0.000017	0.000434	0.000005	0.031387	0.000126	0.369558	0.001594	85.3	9.98	0.10	151.11	2.87
55.7	0.000070	0.000004	0.000134	0.000007	0.000076	0.000007	0.005675	0.000037	0.073258	0.000329	79.9	9.85	0.32	149.30	9.41
55.9	0.000203	0.000005	0.000838	0.000018	0.000320	0.000013	0.023274	0.000072	0.283919	0.001031	81.4	9.84	0.11	149.13	3.28
56.1	0.000053	0.000004	0.000294	0.000006	0.000094	0.000005	0.007056	0.000027	0.083900	0.000625	89.1	10.18	0.26	154.02	7.58

APPENDIX F: Whole rock geochemistry analytical data

Leucogranotoid in the Tianjingping Complex										
Samples	31-1	31-2	31-3	31-6-1	31-9	34-1	38	125-1	125-2	125-5
Major elements (%)										
SiO_2	72.20	72.73	60.40	65.69	70.14	72.89	57.38	62.54	68.61	68.41
TiO_2	0.37	0.19	1.22	0.58	0.28	0.05	1.47	0.77	0.30	0.31
Al_2O_3	14.09	14.50	17.57	14.29	14.08	14.41	16.73	16.51	14.93	15.30
Fe_2O_3	1.14	0.30	2.82	0.96	0.32	0.03	4.13	0.86	0.83	0.52
FeO	1.55	0.87	3.50	2.53	1.75	0.25	4.35	3.11	2.51	1.98
MgO	0.79	0.54	2.47	2.87	0.83	0.18	2.71	1.71	0.97	0.89
MnO	0.07	0.04	0.10	0.18	0.07	0.00	0.16	0.09	0.12	0.09
CaO	1.77	1.42	4.83	3.61	1.45	0.51	4.88	3.61	1.99	1.67
Na_2O	3.64	3.43	2.79	1.17	3.49	2.21	3.08	3.18	3.94	3.75
K_2O	3.33	4.72	2.55	4.03	5.60	8.62	2.61	2.95	4.23	5.59
P_2O_5	0.05	0.09	0.26	0.17	0.11	0.10	0.19	0.18	0.20	0.14
LOI	0.52	0.81	0.84	3.37	1.66	0.42	1.44	4.32	1.14	1.13
Total	99.52	99.78	99.35	99.45	99.78	99.77	99.78	99.83	99.77	99.78
TFeO	2.58	1.14	6.04	3.39	2.04	0.28	8.07	3.88	3.26	2.45
Na_2O+K_2O	6.97	8.15	5.34	5.20	9.09	10.83	5.69	6.13	8.17	9.34
K_2O/Na_2O	0.60	0.91	0.60	2.27	1.06	2.57	0.56	0.61	0.71	0.98
$\frac{(Na_2O+K_2O)}{Al_2O_3}$	0.68	0.74	0.42	0.44	0.84	0.90	0.47	0.51	0.74	0.80
δ	1.7	2.2	1.6	1.2	3.0	3.9	2.3	1.9	2.6	3.4
A/CNK	1.10	1.09	1.09	1.11	0.97	1.04	1.00	1.10	1.02	1.00
A/NK	1.47	1.35	2.39	2.27	1.19	1.11	2.12	1.96	1.35	1.25
Trace elements (ppm)										
Sc	6.38	3.73	18.1	8.83	6.74	1.42	18.0	14.3	7.20	6.22
V	37.4	14.5	95.0	41.0	26.7	3.90	182	58.6	35.7	32.5
Rb	122	155	157	343	151	221	165	191	123	143
Ba	675	1122	904	1334	967	1296	620	391	945	1242
Th	17.9	16.0	16.0	10.2	15.8	7.05	4.63	14.5	12.1	12.1
U	3.21	3.98	1.37	2.86	3.67	4.53	1.40	7.84	2.19	4.48
Nb	8.33	6.03	14.9	21.4	13.9	1.75	10.6	14.0	5.87	8.07
Ta	1.15	0.77	0.94	3.89	0.87	0.22	0.69	2.78	0.99	1.04
Sr	224	232	381	116	211	223	365	302	222	202
Zr	210	86.3	258	284	177	11.4	109	131	212	217
Hf	6.45	2.67	7.01	8.22	5.27	0.45	3.04	3.35	6.10	5.99
Y	68.1	73.7	31.9	40.8	47.6	44.1	31.9	60.9	15.1	11.3
La	47.9	38.3	55.1	39.6	45.3	11.1	19.2	36.6	54.2	56.0
Ce	93.6	76.4	111	82.6	100	22.4	44.3	78.1	116	115
Pr	10.9	9.07	13.0	10.3	10.2	2.72	6.00	8.43	11.9	11.5
Nd	38.3	32.5	47.4	39.6	36.6	9.94	25.1	32.2	41.0	39.5
Sm	6.95	6.40	8.31	7.69	7.05	2.47	5.43	6.91	7.08	6.40
Eu	1.09	1.15	1.84	1.43	1.16	1.12	1.32	1.27	1.09	1.13
Samples	31-1	31-2	31-3	31-6-1	31-9	34-1	38	125-1	125-2	125-5

Trace elements (ppm)										
Gd	6.76	6.62	6.97	6.75	6.16	3.34	5.45	6.49	5.06	4.33
Tb	1.25	1.31	1.05	1.11	1.07	0.81	0.91	1.26	0.69	0.56
Dy	8.90	9.42	5.79	6.77	7.33	6.17	5.56	9.25	3.67	2.83
Ho	2.16	2.30	1.12	1.42	1.62	1.37	1.18	2.15	0.60	0.46
Er	7.12	7.52	3.07	4.26	5.28	4.42	3.24	7.21	1.54	1.15
Tm	1.20	1.25	0.45	0.70	0.76	0.76	0.50	1.07	0.25	0.16
Yb	8.38	8.70	2.96	5.00	5.47	5.45	3.16	7.41	2.20	1.25
Lu	1.25	1.27	0.43	0.78	0.79	0.82	0.48	0.96	0.32	0.21
∑REE	236	202	258	208	229	73	122	199	245	240
$\frac{\sum LREE}{\sum HREE}$	5.37	4.27	10.82	6.77	7.04	2.15	4.95	4.56	16.11	20.94
δEu	0.48	0.54	0.72	0.59	0.52	1.19	0.74	0.57	0.53	0.62

Paragneiss in the Tianjingping Complex									
Samples	31-4	31-6	31-8	31-10	34-3	34-4	35-1	40-2	41-1
Major elements (%)									
SiO_2	63.77	64.78	62.75	66.81	61.79	67.05	67.47	65.78	67.87
TiO_2	0.63	0.7	0.94	0.48	0.75	0.57	0.75	0.6	0.69
Al_2O_3	17.23	15.95	16.65	14.2	15.64	12.88	15.03	15.41	12.26
Fe_2O_3	1.56	0.71	1.72	0.83	0.47	0.58	0.77	2.12	0.62
FeO	3.57	3.2	4.15	3.5	5.29	4.96	4.23	2.6	5.69
MgO	1.35	2.8	1.74	2.02	3.51	2.8	2.07	1.86	3.5
MnO	0.06	0.15	0.08	0.1	0.1	0.2	0.09	0.08	0.11
CaO	1.55	3.8	1.51	1.77	3.04	4.03	2.2	1.63	1.55
Na_2O	4.85	2.55	3.85	2.61	2.13	0.59	3.42	4.45	2.18
K_2O	2.22	2.88	2.77	3.8	4.05	3.13	2.65	3.63	2.42
P_2O_5	0.19	0.15	0.2	0.34	0.16	0.12	0.09	0.15	0.08
LOI	2.46	1.66	3.08	3.31	2.89	2.89	0.63	1.02	2.66
Total	99.44	99.33	99.44	99.77	99.82	99.8	99.4	99.33	99.63
$\frac{Si}{(Si+Al)}$	0.77	0.78	0.77	0.81	0.78	0.82	0.80	0.79	0.83
$\frac{(Na+Ca)}{(Na+Ca+K)}$	0.72	0.66	0.63	0.50	0.53	0.56	0.65	0.60	0.58
Trace elements (ppm)									
Sc	12.7	11.6	15.1	11.3	15.4	11.1	13.8	10.2	25.7
V	83.4	54.5	76.2	47.3	94.6	65.6	83.5	66.8	98.5
Rb	186	234	228	278	220	136	162	91.2	63.2
Ba	121	1303	281	348	483	1438	529	1466	1838
Th	10.5	13.1	8.04	19.1	15.3	10.3	16.3	11.4	24.2
U	2.09	3.50	1.58	2.62	3.01	1.91	3.26	1.12	7.95
Nb	18.1	20.4	17.6	14.3	16.5	11.8	18.4	14.4	16.5
Ta	0.89	2.08	0.84	0.91	1.21	0.78	1.40	0.55	1.01
Sr	171	179	162	168	174	301	275	147	110
Zr	193	346	177	156	206	145	244	251	188
Hf	5.47	9.68	4.82	4.04	5.46	3.82	7.29	6.91	4.94
Y	18.2	38.3	23.4	46.3	31.4	36.7	26.1	23.4	27.4
La	38.4	52.0	24.8	77.8	44.4	38.2	52.8	52.2	44.1
Ce	73.0	103	48.7	168	89.0	78.4	103	97.7	105

Samples	31-4	31-6	31-8	31-10	34-3	34-4	35-1	40-2	41-1
Trace elements (ppm)									
Pr	8.57	11.0	5.79	17.5	10.1	9.13	11.8	11.2	10.0
Nd	30.9	44.5	21.2	62.5	36.9	35.0	41.6	38.8	36.4
Sm	5.25	8.52	3.99	11.9	7.32	8.04	7.12	6.33	7.89
Eu	0.83	1.61	0.75	1.42	1.15	1.82	1.30	1.31	1.52
Gd	4.38	7.13	3.81	8.40	5.78	6.76	5.68	4.97	6.31
Tb	0.64	1.30	0.65	1.31	0.89	1.06	0.86	0.74	1.01
Dy	3.49	7.02	4.02	7.89	5.39	6.33	4.84	4.17	5.94
Ho	0.65	1.42	0.84	1.72	1.17	1.25	0.93	0.82	1.20
Er	1.75	4.05	2.39	4.56	3.09	3.04	2.60	2.31	3.02
Tm	0.25	0.61	0.33	0.67	0.42	0.41	0.41	0.34	0.45
Yb	1.72	4.03	2.14	4.51	2.79	2.59	2.73	2.30	2.95
Lu	0.24	0.65	0.30	0.72	0.45	0.38	0.42	0.36	0.48
∑REE	170	247	120	369	209	192	236	224	226
$\frac{\sum LREE}{\sum HREE}$	11.95	8.44	7.26	11.40	9.45	7.82	11.77	12.96	9.58
δEu	0.52	0.61	0.58	0.41	0.52	0.73	0.60	0.69	0.64

Metamafic rocks in the Tianjingping Complex							
Samples	31-5	31-7	39-1	39-2	41-3	125-3	125-4
Major elements (%)							
SiO_2	47.99	42.67	51.87	54.89	46.93	55.54	52.32
TiO_2	3.98	5.61	0.68	0.84	4.06	0.41	0.39
Al_2O_3	14.24	13.80	19.54	14.99	12.93	12.71	12.02
Fe_2O_3	9.15	15.86	1.97	2.10	4.42	0.99	1.33
FeO	6.90	2.60	4.90	6.25	13.10	5.09	4.86
MgO	4.39	5.12	5.73	6.30	3.58	9.00	10.56
MnO	0.24	0.22	0.13	0.25	0.24	0.16	0.15
CaO	3.82	5.22	8.58	7.65	8.29	4.96	5.51
Na_2O	1.78	1.39	2.81	2.45	2.84	0.49	0.34
K_2O	4.08	4.22	1.55	1.37	1.05	5.17	4.56
P_2O_5	0.81	0.67	0.11	0.22	0.68	0.08	0.06
LOI	1.59	1.94	1.25	2.09	0.28	5.11	7.60
Total	98.97	99.32	99.12	99.40	98.40	99.71	99.70
TFeO	15.14	16.87	6.67	8.14	17.08	5.98	6.06
Mg#	18	19	40	37	14	54	57
Trace elements (ppm)							
Sc	22.2	39.8	24.3	23.0	31.3	14.9	36.2
V	199	323	141	140	223	123	135
Rb	342	322	66.5	75.3	17.1	318	331
Ba	2297	662	293	702	265	348	347
Th	3.71	2.56	1.82	7.54	3.29	4.20	3.54
U	3.18	1.64	0.46	3.27	0.60	1.57	1.51
Nb	27.9	21.1	5.64	10.6	40.9	6.07	5.35

Ta	1.89	1.43	0.32	0.75	2.56	0.45	0.56
Samples	31-5	31-7	39-1	39-2	41-3	125-3	125-4
Trace elements (ppm)							
Sr	212	209	454	219	441	59.5	75.4
Zr	320	213	73.2	99.1	275	75.1	66.9
Hf	8.15	5.76	1.94	2.78	7.41	2.02	1.89
Y	55.8	44.6	15.7	25.4	69.7	14.4	12.8
La	41.7	29.5	12.3	19.4	36.4	14.9	12.2
Ce	91.1	66.9	26.0	41.1	82.4	30.2	24.9
Pr	12.5	9.14	3.07	4.82	10.1	3.48	2.89
Nd	53.2	39.5	12.6	20.8	48.1	13.0	10.5
Sm	11.4	8.80	2.67	4.92	11.9	2.91	2.39
Eu	3.53	2.71	0.85	1.66	3.35	0.85	0.68
Gd	11.1	8.74	2.43	4.52	11.8	2.51	2.05
Tb	1.75	1.40	0.45	0.80	2.18	0.40	0.33
Dy	9.92	8.21	2.66	4.23	12.2	2.44	2.11
Ho	1.92	1.55	0.56	0.87	2.47	0.54	0.47
Er	5.22	4.34	1.63	2.48	6.89	1.47	1.33
Tm	0.77	0.64	0.25	0.39	1.05	0.22	0.20
Yb	5.25	4.26	1.59	2.51	6.68	1.48	1.46
Lu	0.79	0.64	0.25	0.38	1.00	0.24	0.23
∑REE	250	186	67	109	236	75	62
∑LREE/∑HREE	5.82	5.26	5.85	5.73	4.35	7.03	6.55
δEu	0.95	0.94	1.01	1.06	0.85	0.94	0.91

Paragneiss in the Jiaoxi and Mayuan complexes																			
Sample No.	59-1	59-3	60-1	61-1	10-1	7-1	8-1	65-2	65-5	66-2	66-3	122-3	134-1	134-2	135	53	54	55	56-2
Major elements (%)																			
SiO_2	68.05	70.64	66.84	69.27	67.13	68.62	65.6	75.8	78.9	65.79	63.8	64	67.12	68.36	68.8	73.89	68.85	72.82	64.97
TiO_2	0.47	0.32	0.68	0.43	0.76	0.72	0.87	0.55	0.43	0.54	1.08	0.77	0.6	0.69	0.47	0.56	0.82	0.64	0.79
Al_2O_3	15.44	14.34	14.14	14.73	14.35	14.51	15.1	10.3	9.61	17	14.6	15.3	14.06	14.05	14	11.87	13.41	11.6	14.66
Fe_2O_3	1.64	1.32	1.75	1.29	0.73	0.47	2.47	0.19	0.12	0.21	0.49	0.7	0.35	0.3	0.28	1	1.33	0.91	1.47
FeO	1.75	1.07	2.12	1.6	4.45	3.32	4.05	3.95	2.77	3.2	6.2	4.88	4.79	4.21	3.6	3	4.15	3.2	5.3
MgO	1.04	0.92	1.06	0.92	1.77	1.25	1.98	1.3	0.86	1.68	2.15	2.45	2.09	1.51	1.46	1.6	2.45	1.72	2.68
MnO	0.07	0.06	0.08	0.06	0.12	0.08	0.17	0.1	0.09	0.03	0.07	0.1	0.06	0.06	0.04	0.06	0.11	0.06	0.18
CaO	2.99	2.05	1.49	2.23	2.4	1.43	2.68	1.81	2.48	4.44	2.49	3.42	1.74	1.63	1.02	2.56	1.19	1.27	2.02
Na_2O	4.84	4.64	7.09	4.7	1.3	2.31	2.98	2.45	1.32	3.48	2.64	3.08	2.1	2.4	2.57	2.62	1.67	2.23	3.23
K_2O	2.62	3.79	3.19	3.87	3.36	5.45	2.36	1.89	1.72	1.93	3.65	3.03	3.47	4.6	4.5	1.65	3.9	3.46	1.95
P_2O_5	0.11	0.09	0.15	0.11	0.21	0.15	0.18	0.09	0.08	0.18	0.05	0.22	0.11	0.24	0.15	0.08	0.17	0.17	0.19
LOI	0.53	0.17	0.85	0.24	2.79	1.2	0.81	1.46	1.5	1.06	2.57	1.78	3.28	1.7	2.89	0.64	1.3	1.43	1.7
Total	99.55	99.41	99.44	99.45	99.37	99.51	99.2	99.9	99.88	99.54	99.8	99.8	99.77	99.75	99.8	99.53	99.35	99.51	99.14
Si/(Si+Al)	0.8	0.81	0.81	0.81	0.81	0.81	0.79	0.87	0.88	0.77	0.79	0.79	0.81	0.81	0.81	0.85	0.82	0.85	0.8
$\frac{(Na+Ca)}{(Na+Ca+K)}$	0.72	0.61	0.7	0.61	0.49	0.38	0.68	0.66	0.66	0.78	0.55	0.65	0.49	0.44	0.41	0.73	0.39	0.47	0.7
Sc	7.81	6.13	11.5	7.35	11.8	9.18	14.2	7.9	6.55	5.38	20.7	15.8	11.4	10.9	8.62	12.4	13.9	9.74	13.4
V	43.1	27.7	55.6	42.8	91.4	64.2	111	48.6	40.3	56.1	102	150	67.7	48.9	43	53	96.2	66.2	87.2
Rb	80.2	103	87.2	98.9	193	243	123	84.6	77.3	135	154	192	142	191	152	126	205	133	115
Ba	1379	1131	1439	1315	759	808	567	291	158	535	486	540	768	816	902	86.2	462	920	314
Th	14.3	17.4	8.08	11.1	12.7	21.9	14.2	12.5	11.6	11.5	45.1	16.1	24.8	22.3	45.1	30.1	19.5	21.1	23.4
U	1.89	1.29	0.86	0.73	2.35	4.5	2.59	2.39	2.09	0.92	3.18	0.87	2.59	2.49	5.5	2.89	3.63	3.3	4.11
Nb	13.6	17.3	10.4	10.9	15.4	15.5	14.2	9.52	9.26	6.97	19.6	12.1	11.2	13.3	11	30.4	19.5	12.2	16.4
Ta	0.87	0.96	0.55	0.64	1.17	1.37	1.03	0.8	0.72	0.37	0.85	0.7	0.55	0.64	0.92	1.92	1.8	1.07	1.32
Sr	314	238	244	323	228	149	407	234	247	318	116	231	190	185	223	137	95	168	183
Zr	299	234	258	219	205	238	265	200	163	204	442	121	183	178	205	256	307	288	290
Hf	8.44	7.42	6.73	6.26	5.95	7.4	7.43	5.73	4.6	4.71	12.7	3.4	5.1	4.93	5.99	8.01	9.19	8.55	8.71
Y	28.3	29.2	25.4	18	26.9	29.3	28.6	19.7	18	7.3	63.7	13.4	23	28.5	23.2	55.8	39.7	29.8	36.5
La	64.5	53	46.4	43.2	41.2	45.6	61.7	40.9	37.3	53.5	103	44.3	55.4	50.1	62.3	47.2	45.2	41.8	50
Ce	115	105	87.4	84.1	83.7	98.7	114	84.6	72.8	95.1	224	94.8	119	110	143	97.7	92.9	84.3	99.6
Pr	13.1	12.1	9.1	9.7	9.83	12.1	12.9	8.51	7.56	9.65	24.7	10.1	12.6	12.3	15.6	11.7	11.2	9.83	11.8
Nd	45.3	41.9	36.1	34	36.8	45.8	45.7	30.1	26.1	32	91.9	38.5	45.9	46.6	58	42.2	41.8	35.9	43.2
Sm	7.17	7.03	6.31	5.63	6.47	8.96	7.33	4.97	4.49	4.17	18.5	6.74	8.11	8.51	10.1	9.36	8.21	6.66	8.04
Eu	1.22	0.89	1.8	1.29	1.21	1.17	1.69	0.89	0.74	1.06	1.34	1.48	1.28	1.29	1.27	0.9	1.23	1.23	1.31
Gd	5.62	5.65	4.77	4.47	5.55	7.83	6.12	4.05	3.62	2.79	14.5	5.35	5.74	6.14	6.58	9.04	7.29	5.77	6.92
Tb	0.85	0.88	0.8	0.65	0.86	1.17	0.91	0.6	0.53	0.32	2.02	0.63	0.76	0.91	0.9	1.56	1.19	0.91	1.09
Dy	4.89	5.1	4.29	3.5	4.88	5.91	5.06	3.51	3.18	1.51	11	3.12	4.38	5.23	4.84	9.39	7	5.24	6.38
Ho	1.01	1.02	0.89	0.67	0.92	1.01	0.98	0.72	0.63	0.26	2.33	0.54	0.83	1.01	0.86	1.91	1.37	1.05	1.29
Er	2.82	2.81	2.59	1.72	2.48	2.55	2.78	2.09	1.88	0.68	7.53	1.33	2.49	2.92	2.21	5.15	3.74	2.98	3.58
Tm	0.47	0.45	0.4	0.25	0.36	0.37	0.41	0.29	0.27	0.1	1.11	0.15	0.34	0.38	0.25	0.77	0.57	0.47	0.57
Yb	2.9	2.88	2.59	1.45	2.48	2.32	2.79	2.16	1.91	0.64	7.72	0.83	2.39	2.54	1.46	4.57	3.69	3.03	3.6
Lu	0.45	0.46	0.41	0.24	0.38	0.33	0.41	0.3	0.26	0.1	1.14	0.12	0.35	0.37	0.21	0.67	0.55	0.46	0.56
∑ REE	918	753	737	761	670	665	976	646	598	740	1135	584	664	648	772	710	683	697	761
$\frac{\sum LREE}{\sum HREE}$	2.27	1.96	2.39	2.8	2.17	1.67	2.51	2.34	2.5	2.6	1.1	1.72	1.44	1.46	1.41	1.59	1.76	2.24	1.96
δ Eu	5.42	6.39	3.66	4.6	5.37	6.68	4.71	5.43	5.67	4.04	8.63	5.06	5.63	5.59	6.07	7.37	6.02	5.4	5.76

Metamafic rocks in the Jiaoxi and Mayuan complexes			
Samples	61-2	61-3	122-1
Major elements (%)			
SiO_2	58.70	53.07	48.62
TiO_2	0.74	0.86	1.33
Al_2O_3	17.84	17.18	17.74
Fe_2O_3	2.83	3.35	2.78
FeO	3.40	4.94	7.41
MgO	2.78	4.40	5.81
MnO	0.13	0.21	0.21
CaO	6.71	7.37	8.44
Na_2O	4.94	4.94	1.62
K_2O	0.89	1.48	3.37
P_2O_5	0.13	0.21	0.34
LOI	0.23	1.85	2.06
Total	99.32	99.86	99.73
TFeO	5.95	7.96	9.91
Mg#	27	30	31
Trace elements (ppm)			
Sc	17.0	15.6	29.3
V	98.3	184	259
Rb	24.7	40.7	144
Ba	546	192	653
Th	7.89	6.35	6.83
U	2.12	2.28	1.54
Nb	8.94	12.0	12.4
Ta	0.60	0.59	0.55
Sr	265	323	291
Zr	132	110	113
Hf	3.73	2.81	3.04
Y	20.9	27.8	42.8
La	29.2	24.1	36.6
Ce	50.9	54.9	91.3
Pr	5.68	6.90	12.4
Nd	22.0	27.0	51.8
Sm	4.29	5.99	12.0
Eu	1.09	1.78	2.62
Gd	3.64	4.52	8.98
Tb	0.65	0.77	1.35
Dy	3.64	4.68	8.06
Ho	0.73	1.08	1.71
Er	2.13	2.92	4.33
Tm	0.32	0.44	0.62
Yb	2.06	3.06	4.04

Lu	0.31	0.51	0.60
∑REE	127	139	236
∑LREE/∑HREE	8.41	6.71	6.96
δEu	0.28	0.34	0.25

Leucogranotoid in the Jiaoxi and Mayuan complexes				
Samples	59-2	61-4	59-5	65-3
Major elements (%)				
SiO_2	73.70	69.53	69.15	71.49
TiO_2	0.10	0.30	0.02	0.16
Al_2O_3	13.68	14.64	15.44	15.09
Fe_2O_3	0.01	0.76	0.10	0.10
FeO	0.92	1.72	0.71	1.65
MgO	0.02	0.07	0.01	0.03
MnO	0.25	0.83	0.08	0.53
CaO	1.54	2.01	1.91	2.14
Na_2O	4.05	3.95	4.06	3.73
K_2O	5.01	4.68	5.54	3.88
P_2O_5	0.04	0.09	0.03	0.07
LOI	0.34	1.20	2.90	1.06
Total	99.65	99.78	99.85	99.83
TFeO	0.93	2.40	0.80	1.74
Na_2O+K_2O	9.06	8.63	9.60	7.61
K_2O/Na_2O	0.82	0.78	0.90	0.69
$(Na_2O+K_2O)/ Al_2O_3$	0.88	0.79	0.82	0.69
δ	2.7	2.8	3.5	2.0
A/CNK	0.92	0.96	0.95	1.06
A/NK	1.13	1.26	1.22	1.46
Trace elements (ppm)				
Sc	2.51	6.03	1.03	4.38
V	13.8	28.5	3.29	14.4
Rb	109	115	140	80.3
Ba	1805	1290	2157	1589
Th	11.6	9.68	0.091	4.39
U	0.67	0.78	0.030	1.84
Nb	3.41	4.57	0.26	4.01
Ta	0.20	0.14	0.016	0.47
Sr	297	280	392	440
Zr	134	163	0.54	77.5
Hf	4.31	4.55	0.023	2.83
Y	9.86	6.74	0.71	7.16
La	48.2	43.1	2.29	14.8
Ce	94.4	92.5	3.86	30.9
Pr	10.7	9.39	0.38	3.34
Nd	36.9	33.0	1.28	11.9
Sm	5.50	5.27	0.20	2.32
Eu	1.19	1.13	0.47	1.89
Gd	3.60	3.49	0.14	1.70

Tb	0.46	0.40	0.019	0.24
Dy	2.16	1.75	0.11	1.27
Ho	0.37	0.28	0.018	0.25
Er	0.93	0.69	0.069	0.81
Samples	59-2	61-4	59-5	65-3
Trace elements (ppm)				
Tm	0.14	0.082	0.010	0.12
Yb	0.84	0.51	0.070	0.97
Lu	0.13	0.098	0.011	0.14
∑REE	205	192	9	71
∑LREE/∑HREE	22.81	25.27	18.99	11.85
δEu	0.26	0.26	2.77	0.94

A/CNK = molar $Al_2O_3/(CaO+Na_2O+K_2O)$, A/NK= molar $Al_2O_3/(Na_2O+K_2O)$,
δ Eu=2$(Eu)_n/(Sm+Gd)_n$, δ = w% $(Na_2O+K_2O)^2/(SiO_2-43)$ (%),δ Eu=2$(Eu)_n/(Sm+Gd)_n$.

APPENDIX G: Mineral geochemistry analytical data

Mafic Sample	P (kbar)	error (kbar)	T (°C)	error (°C)
39-1	13.7	0.1	798.7	10.0
1	12.2	0.1	774.9	8.6
2	14.0	0.1	796.2	4.9
3	9.1	0.0	737.4	2.5
4	9.6	0.0	733.0	4.7
5	10.8	0.0	749.9	7.5
6	10.3	0.0	744.3	2.0
7	8.1	0.0	722.1	1.0
Average	10.5	0.0	756.8	6.6
61-3	6.3	0.1	753.6	8.3
1	11.5	0.0	783.8	89.4
2	3.3	0.1	700.3	40.1
3	4.2	0.0	745.8	24.8
Average	6.3	0.0	745.9	40.6

Sample No.	61-3	61-3	61-3	61-3	61-3	61-3	61-3	61-3	61-3	61-3	61-3	61-3
Mineral	Amp	Amp	Amp	Amp	Amp	Amp	Pl	Pl	Pl	Pl	Pl	Pl
Analysis No.	1A-1	1A-2	1A-3	2A-1	2A-2	2A-3	1P-1	1P-2	1P-3	2P-1	2P-2	2P-3
SiO_2	42.24	59.48	41.66	41.69	50.03	41.69	60	58.3	60.91	63.16	58.8	59
TiO_2	0.64	0.06	0.89	0.63	0.12	0.88	0.01	0	0.01	0	0.02	0.02
Al_2O_3	10.32	22.29	9.74	9.92	1.66	9.62	23.3	23.6	19.52	20.91	22.9	22.9
FeO	17.99	1.09	16.85	16.65	16.88	17.09	0.17	0.16	0.06	0.12	0.14	0.23
MgO	10.19	0.49	10.37	10.61	11.7	10.36	0.01	0	0.03	0.01	0	0.01
MnO	0.63	0.06	0.6	0.55	0.7	0.58	0.05	0.05	0.06	0.05	0.06	0.04
CaO	12.43	5.73	11.88	11.76	12.11	11.79	5.71	6.34	1.73	2.89	5.8	5.72
Na_2O	1.18	7.93	1.18	1.21	0.16	1.27	8.25	7.55	4.45	9.07	8	8.02
K_2O	1.1	0.2	1.19	1.16	0.13	1.23	0.1	0.26	7.52	0.25	0.15	0.12
Total	96.74	97.32	94.35	94.18	93.49	94.51	97.6	96.3	94.29	96.44	95.9	96.1
Si	6.35	2.72	6.44	6.43	7.71	6.44	2.73	2.7	2.91	2.88	2.72	2.73
Ti	0.07	0	0.1	0.07	0.01	0.1	0	0	0	0	0	0
Al	1.83	1.2	1.77	1.8	0.3	1.75	1.25	1.29	1.1	1.12	1.25	1.25
Fe^{2+}	1.26	0	1.48	1.39	1.94	1.52	0	0	0	0	0	0
Fe^{3+}	1	0.04	0.69	0.76	0.24	0.69	0.01	0.01	0	0	0.01	0.01
Mg	2.28	0.03	2.39	2.44	2.69	2.39	0	0	0	0	0	0
Mn	0.08	0	0.08	0.07	0.09	0.08	0	0	0	0	0	0
Ca	2	0.28	1.97	1.94	2	1.95	0.28	0.31	0.09	0.14	0.29	0.28
Na	0.35	0.7	0.35	0.36	0.05	0.38	0.73	0.68	0.41	0.8	0.72	0.72
K	0.21	0.01	0.23	0.23	0.03	0.24	0.01	0.02	0.46	0.01	0.01	0.01
Total	15.44	5	15.52	15.51	15.05	15.54	5	5	4.98	4.97	5	5
Mg/(Mg+Fe)	0.362	0.308	0.381	0.389	0.409	0.377	-	-	-	-	-	-

Sample No.	39-1	39-1	39-1	39-1	39-1	39-1	39-1	39-1	39-1	39-1	39-1	39-1	39-1	39-1	39-1	39-1	39-1	39-1
Mineral	Amp	Amp	Amp	Amp	Amp	Amp	Amp	Amp	Amp	Pl	Pl	Pl	Pl	Pl	Pl	Pl	Pl	Pl
Analysis No.	1A-1	1A-2	1A-3	1A-4	2A-1	2A-2	2A-3	2A-4	2A-5	1P-1	1P-2	1P-3	1P-4	2P-1	2P-2	2P-3	2P-4	2P-5
SiO_2	44.18	43.93	44.11	42.61	44.94	45.00	45.13	44.61	44.99	53.16	53.54	53.21	55.01	54.39	53.84	53.78	56.98	53.91
TiO_2	0.91	0.92	0.85	0.87	0.80	0.86	0.83	0.86	0.83	0.01	0.06	0.01	0.05	0.04	0.01	0.01	0.00	0.01
Al_2O_3	10.03	9.96	10.05	8.56	8.87	8.94	8.71	9.33	9.05	27.35	27.04	27.17	26.00	26.40	26.93	26.71	23.71	26.61
FeO	14.14	14.32	14.00	13.28	13.69	13.91	13.65	14.08	13.89	0.11	0.12	0.18	0.24	0.27	0.14	0.09	0.07	0.09
MgO	12.28	12.34	12.28	11.92	12.67	12.71	12.92	12.50	12.89	0.00	0.00	0.02	0.01	0.01	0.01	0.01	0.00	0.00
MnO	0.28	0.36	0.30	0.35	0.34	0.32	0.28	0.46	0.34	0.06	0.01	0.00	0.00	0.06	0.04	0.03	0.01	0.02
CaO	12.14	12.09	11.97	11.57	12.32	12.15	12.29	11.54	12.14	11.07	10.39	10.55	9.28	9.81	10.28	10.30	6.54	10.00
Na_2O	1.05	1.11	1.08	0.96	0.97	0.98	0.94	1.19	1.06	5.35	5.57	5.41	6.21	5.97	5.64	5.61	7.23	5.74
Total	95.01	95.01	94.64	90.12	94.60	94.88	94.76	94.58	95.18	97.10	96.73	96.55	96.78	96.95	96.89	96.53	94.53	96.40
Si	6.58	6.55	6.59	6.70	6.72	6.71	6.73	6.67	6.68	2.47	2.49	2.48	2.55	2.52	2.50	2.51	2.68	2.51
Ti	0.10	0.10	0.10	0.10	0.09	0.10	0.09	0.10	0.09	0.00	0.00	0.00	0.00	0.00	0.00	0.00	0.00	0.00
Al	1.76	1.75	1.77	1.59	1.56	1.57	1.53	1.64	1.58	1.50	1.48	1.49	1.42	1.44	1.47	1.47	1.32	1.46
Fe^{2+}	1.03	0.98	1.02	1.06	1.05	1.02	1.01	1.02	0.98	0.00	0.00	0.00	0.00	0.00	0.00	0.00	0.00	0.00
Fe^{3+}	0.73	0.80	0.73	0.68	0.67	0.71	0.70	0.74	0.74	0.00	0.00	0.01	0.01	0.01	0.01	0.00	0.00	0.00
Mg	2.73	2.74	2.74	2.79	2.83	2.82	2.87	2.79	2.85	0.00	0.00	0.00	0.00	0.00	0.00	0.00	0.00	0.00
Mn	0.04	0.04	0.04	0.05	0.04	0.04	0.04	0.06	0.04	0.00	0.00	0.00	0.00	0.00	0.00	0.00	0.00	0.00
Ca	1.94	1.93	1.92	1.95	1.97	1.94	1.96	1.85	1.93	0.55	0.52	0.53	0.46	0.49	0.51	0.51	0.33	0.50
Na	0.30	0.32	0.31	0.29	0.28	0.28	0.27	0.35	0.31	0.48	0.50	0.49	0.56	0.54	0.51	0.51	0.66	0.52
Total	15.22	15.23	15.22	15.21	15.21	15.20	15.20	15.21	15.22	5.00	5.00	5.00	5.00	5.00	5.00	5.00	4.99	5.00
Mg/(Mg+Fe)	0.46	0.46	0.47	0.47	0.48	0.48	0.49	0.47	0.48	-	-	-	-	-	-	-	-	-

Sample No.	34-4	34-4	34-4	34-4	34-4	34-4	34-4	34-4	34-4	34-4	34-4	34-4	34-4	34-4	34-4	34-4
Mineral	Gt	Gt	Gt	Gt	Gt	Gt	Gt	Gt	Gt	Gt	Gt	Gt	Gt	Gt	Gt	Gt
Analysis No.	3G-5	3G-1	4G-1	4G-3	4G-4	1G-2	1G-4	2G-1	2G-2	2G-3	3G-2	3G-3	3G-4	5G-1	5G-2	5G-6
SiO_2	37.70	37.60	37.21	37.08	37.46	37.19	36.93	36.83	37.41	37.27	37.32	37.16	36.90	37.07	36.88	37.24
TiO_2	0.05	0.03	0.01	0.08	0.03	0.05	0.03	0.03	0.03	0.05	0.04	0.05	0.05	0.03	0.02	0.04
$Al2O_3$	21.01	21.02	20.80	20.82	21.16	20.97	20.87	20.52	20.99	21.03	21.07	20.89	20.74	20.80	20.55	21.07
Cr_2O_3	0.05	0.08	0.10	0.13	0.00	0.05	0.07	0.03	0.04	0.01	0.05	0.09	0.07	0.07	0.11	0.10
FeO	26.69	26.34	26.51	26.90	26.54	25.41	25.60	25.92	26.84	26.35	26.41	26.12	25.95	25.20	25.13	25.80
MnO	7.48	8.74	6.68	6.69	7.54	7.31	7.06	7.13	6.41	7.72	6.92	6.50	6.98	7.10	7.12	6.76
MgO	2.62	2.32	2.82	2.85	2.44	2.32	2.43	2.41	2.82	2.35	2.70	2.86	2.84	2.37	2.44	2.60
CaO	5.81	5.80	5.84	5.89	6.04	7.56	6.75	6.29	5.70	5.69	5.91	6.12	5.78	6.52	6.98	6.71
Na_2O	0.00	0.00	0.01	0.01	0.00	0.00	0.01	0.01	0.00	0.00	0.00	0.00	0.00	0.00	0.00	0.00
K_2O	0.04	0.02	0.02	0.02	0.01	0.00	0.01	0.01	0.00	0.01	0.03	0.01	0.02	0.00	0.01	0.02
NiO	0.09	0.03	0.10	0.00	0.04	0.00	0.06	0.03	0.04	0.03	0.12	0.01	0.06	0.06	0.03	0.07
P_2O_5	0.08	0.00	0.00	0.00	0.04	0.06	0.02	0.05	0.00	0.00	0.08	0.06	0.04	0.00	0.01	0.00
Total	101.61	101.97	100.10	100.48	101.30	100.92	99.84	99.26	100.28	100.50	100.64	99.87	99.42	99.23	99.28	100.40
Si	2.97	2.96	2.97	2.95	2.96	2.95	2.96	2.97	2.98	2.97	2.97	2.97	2.97	2.99	2.97	2.96
Ti	0.00	0.00	0.00	0.00	0.00	0.00	0.00	0.00	0.00	0.00	0.00	0.00	0.00	0.00	0.00	0.00
Al	1.95	1.95	1.96	1.95	1.97	1.96	1.97	1.95	1.97	1.98	1.98	1.97	1.97	1.97	1.95	1.98
Cr	0.00	0.00	0.01	0.01	0.00	0.00	0.00	0.00	0.00	0.00	0.00	0.01	0.00	0.00	0.01	0.01
Fe^{2+}	1.67	1.62	1.68	1.66	1.66	1.54	1.61	1.65	1.73	1.69	1.68	1.67	1.65	1.66	1.59	1.63
Fe^{3+}	0.09	0.12	0.09	0.13	0.10	0.14	0.11	0.10	0.06	0.07	0.08	0.08	0.09	0.04	0.10	0.09
Mg	0.31	0.27	0.34	0.34	0.29	0.27	0.29	0.29	0.33	0.28	0.32	0.34	0.34	0.28	0.29	0.31
Mn	0.50	0.58	0.45	0.45	0.51	0.49	0.48	0.49	0.43	0.52	0.47	0.44	0.48	0.48	0.49	0.46
Ca	0.49	0.49	0.50	0.50	0.51	0.64	0.58	0.54	0.49	0.49	0.50	0.52	0.50	0.56	0.60	0.57
Na	0.00	0.00	0.00	0.00	0.00	0.00	0.00	0.00	0.00	0.00	0.00	0.00	0.00	0.00	0.00	0.00
K	0.00	0.00	0.00	0.00	0.00	0.00	0.00	0.00	0.00	0.00	0.00	0.00	0.00	0.00	0.00	0.00
Total	8.00	8.00	8.00	8.00	8.00	8.00	8.00	8.00	8.00	8.00	8.00	8.00	8.00	8.00	8.00	8.00
Mg/(Mg+Fe)	0.09	0.08	0.10	0.10	0.08	0.08	0.09	0.09	0.09	0.08	0.09	0.10	0.10	0.09	0.09	0.09
X_{Alm}	0.568	0.556	0.572	0.573	0.566	0.537	0.552	0.562	0.58	0.57	0.569	0.565	0.563	0.553	0.543	0.555
X_{Prp}	0.102	0.09	0.112	0.112	0.096	0.09	0.096	0.096	0.112	0.093	0.107	0.114	0.113	0.096	0.097	0.103
X_{Grs}	0.163	0.162	0.166	0.166	0.17	0.211	0.192	0.18	0.163	0.163	0.168	0.175	0.166	0.189	0.199	0.191
X_{Sps}	0.166	0.193	0.15	0.149	0.168	0.161	0.159	0.162	0.145	0.174	0.156	0.147	0.158	0.163	0.161	0.152

Sample No.	34-4	34-4	34-4	34-4	34-4	34-4	34-4	34-4	34-4	34-4	34-4	34-4	34-4
Mineral	Bt	Bt	Bt	Bt	Amp	Amp	Amp	Amp	Amp	Amp	Amp	Amp	Amp
Analysis No.	3B-9	3B-11	4B-8	4B-5	1A-1	1A-3	2A-4	3A-6	3A-7	3A-8	5A-3	5A-4	5A-5
SiO_2	34.66	35.47	34.78	33.31	47.64	47.21	47.1	48.8	47.65	48.28	47.8	46.9	46.82
TiO_2	2.29	2.41	1.86	2.06	0.55	0.53	0.48	0.4	0.52	0.43	0.52	0.57	0.54
$Al2O_3$	16.08	15.38	16.61	16.38	7.81	8.05	7.75	6.97	7.82	7.1	7.98	8.07	7.38
Cr_2O_3	0.08	0.05	0.06	0.07	0.14	0.06	0.1	0	0.03	0.04	0.08	0.07	0.11
FeO	19.46	19.04	20.66	20.04	16.41	16.48	16.1	15.5	16.14	15.75	16.5	16.9	16.65
MnO	0.27	0.38	0.26	0.33	0.76	0.87	0.74	0.84	0.83	0.9	0.78	0.75	0.76
MgO	11.03	10.74	11.77	11.22	11.56	11.33	11.3	12.3	11.63	11.85	11.5	11.1	11.07
CaO	0.2	0.07	0.05	0.11	11.23	11.42	11.9	11.3	11.54	11.28	11.4	11.6	11.15
Na_2O	0.05	0.06	0.07	0.06	0.59	0.67	0.63	0.55	0.59	0.57	0.65	0.63	0.62
K_2O	8.17	9.47	7.99	7.15	0.3	0.3	0.29	0.29	0.32	0.3	0.28	0.4	0.31
NiO	0.05	0	0.01	0.02	0.01	0.1	0.09	0.05	0.09	0.02	0.01	0.04	0.05
P_2O_5	0.12	0	0.07	0.11	0.05	0.01	0	0.06	0	0.06	0.06	0.01	0.05
Total	92.46	93.07	94.18	90.85	97.04	97.03	96.5	97	97.14	96.55	97.5	97	95.52
Si	2.73	2.78	2.69	2.67	7.04	6.98	7	7.18	7.02	7.16	7.02	6.95	7.05
Ti	0.14	0.14	0.11	0.12	0.06	0.06	0.05	0.04	0.06	0.05	0.06	0.06	0.06
Al	1.49	1.42	1.52	1.55	1.36	1.4	1.36	1.21	1.36	1.24	1.38	1.41	1.31
Cr	0	0	0	0	0.02	0.01	0.01	0	0	0	0.01	0.01	0.01
Fe^{2+}	1.28	1.25	1.34	1.34	1.65	1.58	1.53	1.62	1.58	1.66	1.63	1.62	1.7
Fe^{3+}	0	0	0	0	0.37	0.45	0.46	0.28	0.41	0.29	0.39	0.47	0.39
Mg	1.29	1.26	1.36	1.34	2.55	2.5	2.5	2.69	2.56	2.62	2.51	2.44	2.48
Mn	0.02	0.03	0.02	0.02	0.09	0.11	0.09	0.1	0.1	0.11	0.1	0.09	0.1
Ca	0.02	0.01	0	0.01	1.78	1.81	1.9	1.79	1.82	1.79	1.8	1.85	1.8
Na	0.01	0.01	0.01	0.01	0.17	0.19	0.18	0.16	0.17	0.16	0.19	0.18	0.18
K	0.82	0.95	0.79	0.73	0.06	0.06	0.05	0.05	0.06	0.06	0.05	0.08	0.06
Total	7.8	7.84	7.84	7.8	15.14	15.15	15.2	15.1	15.14	15.14	15.2	15.2	15.15
Mg/(Mg+Fe)	0.36	0.36	0.36	0.36	0.41	0.41	0.41	0.44	0.42	0.43	0.41	0.4	0.4